Carbon Nanotube Growth on Challenging Substrates: Applications for Carbon-Fiber Composites

by

Stephen Alan Steiner III

B.S., Chemistry Course, University of Wisconsin—Madison (2004)
S.M., Materials Science and Engineering, Massachusetts Institute of Technology (2006)

Submitted to the Department of Aeronautics and Astronautics
in partial fulfillment of the requirements for the degree of

Doctor of Philosophy

at the

MASSACHUSETTS INSTITUTE OF TECHNOLOGY

December 2011

Author .....
Department of Aeronautics and Astronautics
December 15, 2011

Certified by .....
Brian L. Wardle
Associate Professor of Aeronautics and Astronautics
Thesis Supervisor

Certified by .....
A. John Hart
Assistant Professor of Mechanical Engineering, University of Michigan at Ann Arbor

Certified by .....
Carl V. Thompson
Stavros Salapatas Professor of Materials Science and Engineering

Certified by .....
Michael S. Strano
Charles and Hilda Roddey Associate Professor of Chemical Engineering

Accepted by .....
Eytan H. Modiano
Professor of Aeronautics and Astronautics
Chair, Department of Aeronautics and Astronautics Graduate Committee

Carbon Nanotube Growth on Challenging Substrates: Applications for Carbon-Fiber Composites

by

Stephen Alan Steiner III

Submitted to the Department of Aeronautics and Astronautics
on December 15, 2011 in partial fulfillment of the
requirements for the degree of
Doctor of Philosophy

Abstract

Nanoengineered hierarchal fiber architectures are promising approaches towards improving the inter- and intralaminar mechanical properties (e.g., toughness and strength) and non-mechanical properties of advanced fiber-reinforced composites such as graphite/epoxy. One fiber architecture of particular interest is carbon fiber coated with radially-aligned arrays of carbon nanotubes (CNTs), which can enable through-thickness and interply matrix reinforcement of carbon-fiber-reinforced composites while simultaneously providing additional multifunctional benefits such as electrical and thermal conductivity enhancement. Growth of CNTs on carbon fibers can be achieved by chemical vapor deposition (CVD) techniques, however previous processes for doing so have resulted in a significant reduction in the tensile strength and stiffness of the carbon fibers. This thesis aims to develop an understanding of catalyst-substrate and CVD environment-substrate interactions relevant to maintaining fiber mechanical properties in the growth of CNTs on carbon fibers by CVD and to use this understanding to develop practical approaches for growing CNTs on carbon fibers that simultaneously preserve fiber properties. Novel oxide-based catalysts are demonstrated for the first time to be effective for both CNT growth and graphitization of amorphous carbon and are characterized using *in situ* metrology. These catalysts show promise for use on substrates that exhibit sensitivity to conventional metal catalysts (such as carbon fibers). New CVD processing techniques based on materials properties unique to this class of catalysts are presented and explored. Coatings for enabling growth of aligned CNTs on carbon fibers, coatings for improving adhesion of materials to carbon fibers, and coatings for facilitating low-temperature growth of CNTs on carbon fibers are developed. The mechanochemical responses of carbon fibers to high-temperature processing, exposure to CVD gases relevant for CNT growth, and *in situ* tensioning during CVD growth at high temperatures are investigated. Methods for growing CNTs on carbon fibers that enable aligned CNT morphologies and that preserve fiber properties are presented. A new system for optimizing CNT growth on carbon fibers with special considerations for oxide-based catalysts is described. Finally, recommendations for manufacturing hierarchal carbon fibers for composites in an industrially practical way are made.

Thesis Supervisor: Brian L. Wardle
Title: Associate Professor of Aeronautics and Astronautics

Acknowledgements

Thank you to my family, friends, mentors, and colleagues for everything thus far and everything yet to come, and to the Department of Aeronautics and Astronautics for extending the opportunity to pursue a PhD at MIT to a student with a non-traditional Aero/Astro background.

Table of Contents

List of Figures

List of Tables

Abbreviations and Symbols

$AlCl_3$	Aluminum chloride
$Al(NO_3)_3$	Aluminum nitrate
Al_2O_3	Alumina (aluminum oxide)
$_{(aq)}$	Aqueous
Ar	Argon
AS4	A commercial aerospace-grade high tenacity carbon fiber
ATI	Aluminum triisopropoxide, $Al(OC_3H_7)_3$
ATSB	Aluminum tri-*sec*-butoxide, $Al(OC_4H_9)_3$
C	Carbon
C/C	Carbon/carbon composite
CF	Carbon fiber
CFRP	Carbon-fiber reinforced polymer (or plastic)
CH_4	Methane
C_2H_4	Ethylene (ethene)
C_2H_2	Acetylene (ethyne)
CO	Carbon monoxide
CO_2	Carbon dioxide
CO_2/C_2H_2	Chemical vapor deposition with carbon dioxide and acetylene
CNT	Carbon nanotube
CVD	Chemical vapor deposition
DAQ	Data acquisition device
E	Tensile modulus
EDAX	Energy-dispersive X-ray spectroscopy
eV	Electron volt
[EMI]Cl	1-ethyl-3-methylimidazolium chloride
$Fe(NO_3)_3$	Iron(III) nitrate
$Fe(NO_3)_3$/IPA	Solution of 0.050 M iron(III) nitrate nonahydrate in 2-propanol
FE-SEM	Field emission scanning electron microscopy
FFRP	Fuzzy-fiber reinforced polymer (or plastic)
GPa	Gigapascals, 10^9 kg s^{-2} m^{-1} = 10^9 N m^{-2}
H_2	Hydrogen

HCl	Hydrochloric acid
HCN	Hydrogen cyanide
He	Helium
H_2O	Water
h-PSMA	Poly(styrene-*alt*-[maleic acid])
HR-	High-resolution-
HTR-40	TohoTenax high tenacity research-grade carbon fiber
ID	Inner diameter
IEC	International Electrotechnical Commission standard
IPA	2-propanol (isopropanol)
IR	Infrared
keV	Kiloelectron volts, 10^3 eV
K-PSMA	Poly(styrene-*alt*-[dipotassium maleate])
LP-CVD	Low-pressure chemical vapor deposition
MANGO	Modular mass flow controller array in new CVD system
MeOEtOH	2-methoxyethanol
MFC	Mass flow controller
$MoSi_2$	Molybdenum disilicide
MPa	Megapascals, 10^6 kg s^{-2} m^{-1} = 10^6 N m^{-2}
MWNT	Multiwall carbon nanotube
N	Nitrogen
NaF	Sodium fluoride
NaOH	Sodium hydroxide
nm	Nanometer, 10^{-9} m
OD	Outer diameter
OLED	Organic light-emitting diode
PAN	Poly(acrylonitrile)
PSMA	Poly(styrene-*alt*-[maleicanhydride])
RF	Resorcinol-formaldehyde polymer
RTMS	Real-time multiple strip (an X-ray detection technology)
S(x)	Standard deviation
sccm	Standard cubic centimeters per minute = cm^3 min^{-1} = mL min^{-1}
SCR	Silicon-controlled rectifier
SEM	Scanning electron microscopy
sFEG	Schottky field emission gun
SiO_2	Silica (silicon oxide)
SSR	Solid-state relay
SWNT	Single-wall carbon nanotube
t	Time
t_{mix}	Mixing time
T	Temperature

TANGO	Table-top all-quartz reactor in new CVD system
TEM	Transmission electron microscopy
Ta_2O_5	Tantala (tantalum oxide)
TGA	Thermogravimetric analysis
TiO_2	Titania (titanium oxide)
USB	Universal serial bus
UV	Ultraviolet
VAC	Volts alternating current
VDC	Volts direct current
XRD	X-ray diffraction
XPS	X-ray photoelectron spectroscopy
Zr	Zirconium
$Zr(acac)_4$	Zirconium acetylacetonate, $Zr(C_5H_7O_2)_4$
ZrC	Zirconium carbide
ZrO_2	Zirconia (zirconium oxide)
$ZrOCl_2$	Zirconium oxychloride, usually as $ZrOCl_2 \cdot 8H_2O$
a	Weibull modulus
β	Weibull location parameter (set equal to mean breaking strength)
μm	Micron (or micrometer), 10^{-6} m
Ξ	Applied tension
$\bar{\Xi}$	Maximum tension that can be practically applied
σ	Tensile strength, fiber breaking strength

Chapter 1

Introduction

Lightweight structural materials are of great technological importance in many industries. The ability to minimize the weight of a structure while simultaneously maintaining suitable strength, stiffness, resistance to fracture, and tolerance to damage for the structure to serve its function benefits many applications where weight and cost are coupled. In aircraft and spacecraft, for example, reduced structural weight translates into improved fuel efficiency and expanded payload capacity, in turn reducing operational costs. Similarly, lightweight structural materials reduce operating costs and reduce fuel consumption in the automotive and marine industries by reducing the fuel needed to transport people and cargo. Numerous other markets, for example, wind energy turbines, also see demand for improved lightweight structural materials.

Over time, the availability of lightweight structural materials has expanded from naturally available materials such as wood, canvas, and cotton fibers to crude metals and basic alloys; engineered materials such as synthetic polymers, advanced alloys, and ceramics; and now engineered material *architectures* such as fibers, foams, thin films, nanoparticles, patterned arrays, and more. Today, advanced materials are engineered through processing techniques that arrange matter into specific configurations at length scales ranging from molecular to macro, often combining multiple substances together to achieve the desired properties in the resulting bulk material. Where in the past a single "default" or "best compromise" material may have been used to make multiple structural elements throughout a vehicle or structure, today specialized, engineered materials can be created to optimally perform the exact physical role demanded by specific points within a structural element. For example, the bending stiffness of a heavy steel I-beam can be achieved at a fraction of the weight by employing a sandwich

structure of graphite/epoxy laminates with a polymeric foam or aluminum honeycomb core. In this configuration, materials optimized for the stress profile experienced at their respective locations in the beam are used—high tensile strength graphite/epoxy to transmit the relatively high normal stresses encountered at the top and bottom of the beam, and rigid foam or honeycomb to transmit the relatively high shear stresses experienced in the middle of the beam.

1.1. Motivation: Nanoengineered Composite Architectures

This thesis is motivated by the already-underway evolution of composite materials, critical to future aerospace and environmental needs, into sophisticated, multifunctional architectures that are engineered not only at macroscopic and microscopic length scales, but also at nanoscopic length scales—the fundamental limit of materials engineering. Nanoengineering offers the promise of being able to address shortcomings that have limited the utility of composites for many applications and to install new, active functionalities into materials that will enable new applications and better performance in critical metrics.

Nanoengineered hierarchal fiber architectures are a promising approach towards improving the fracture toughness, inter- and intralaminar strength, and non-mechanical properties of advanced fiber composites such as graphite/epoxy. One fiber architecture of particular interest is carbon fiber circumferentially coated with arrays of aligned carbon nanotubes (CNTs), which could in principle enable through-thickness and interply matrix reinforcement of carbon fiber reinforced composites with multifunctional additional benefits such as providing electrical and thermal conductivity enhancement. Indeed, previous studies investigating the use of alumina fibers coated with CNT arrays for laminated composites have verified this target fiber architecture to be effective in improving the mechanical, electrical, and thermal properties in alumina fiber reinforced composites.[1-4] Growth of CNTs on carbon fibers, however, has proven to be less straightforward than on alumina fibers, as applying analogous CNT growth methodologies to carbon fibers results in significant degradation of tensile strength and stiffness of carbon fibers and, subsequently, may negatively impact fiber-dominated in-plane properties of composites prepared with such fibers. As such, a methodology for growing CNTs on carbon fibers in a way that does not reduce the tensile strength and stiffness properties of the carbon fibers must be developed. Underlying this technical challenge is a need for better understanding the interactions between catalyst nanoparticles used for CNT

growth and the substrate supporting the catalyst, as well as the response of carbon fibers to the chemical vapor deposition (CVD) growth environment commonly used to grow CNTs.

1.2. Thesis Outline

In this thesis, catalyst-substrate and CVD environment-substrate interactions relevant to CVD growth of CNTs on carbon fibers are explored. These understandings are then used to inform practical approaches for growing CNTs on carbon fibers that simultaneously preserve fiber properties and to challenge previously conceived notions regarding mechanisms underlying CNT growth.

In Chapter 2, an overview of composites and their shortcomings is presented, followed by a discussion of nanoengineered composites as a promising approach towards addressing these shortcomings. Reasons why growth of CNTs on carbon fibers remains an important outstanding challenge in the field of nanoengineered composites are discussed and a review of efforts in this area is presented. Difficulties underlying CNT growth on carbon fibers from a materials chemistry perspective are then discussed.

In Chapter 3, the objectives of this thesis are articulated and the methodology employed for understanding and engineering CNT growth on carbon fibers is described.

In Chapter 4, for the first time, an oxide-based material, zirconia, is demonstrated to be effective in facilitating growth of carbon nanotubes and graphitizing amorphous carbon while remaining an oxide (as characterized using *in situ* metrology). The mechanisms underlying these capabilities of zirconia are explored. Interactions between oxides and carbon and prospects of growing CNTs with oxides are described.

In Chapter 5, a parametric study to understand the relatively low activity of oxide materials towards facilitating CNT growth when compared with legacy metallic CNT catalysts is presented. A critical parameter for enabling CNT growth with oxides is identified and discussed in the context of numerous other less-successful parametric vectors explored. Novel CVD processing techniques based on materials properties unique to this class of catalysts are presented and explored for applicability towards growth of CNTs and possible extension to growth of CNTs on carbon fibers.

In Chapter 6, a new CVD system is developed to accommodate emerging research needs in the arena of oxide-based CNT growth. The system is described and initial experiments using it demonstrate its utility.

In Chapter 7, methods of depositing coatings for facilitating growth of CNTs on carbon fiber are explored and developed. Promising approaches are

reduced to practice and optimized. A method for growing CNTs at low CVD processing temperatures is developed.

In Chapter 8, the mechanochemical responses of carbon fibers to elevated temperatures, CVD processing, and tension are characterized. The origins of tensile properties degradation associated with CNT growth on carbon fibers are elucidated for the first time. Informed by these discoveries, methods for the growth of CNTs on carbon fibers in a way that does not result in degradation of tensile properties are developed and demonstrated.

In Chapter 9, important discoveries of this thesis are summarized and perspectives on these discoveries are provided. Recommendations for future work and for practical implementation of CNT growth on carbon fibers without degradation of fiber properties are made. Next steps and new possibilities for CNT growth enabled by unique aspects of oxide-based CNT growth are presented.

Chapter 2

Background

Composite materials offer numerous advantages for structural applications where weight is of concern, however their adoption for many applications in aerospace engineering and other industries has been impeded by performance limitations including inadequate fracture toughness and damage tolerance. Understanding the microstructural origins of the problems associated with use of composites provides insights into how they could be solved through nanoengineering. Following is an overview of advanced filamentary composites focusing on some of their performance drawbacks, how nanoengineered architectures show potential to address these drawbacks, and challenges underlying the production of carbon fibers needed for such architectures.

This section serves to provide a general background to frame the motivation for the work performed in this thesis. More detailed background in support of the specific efforts undertaken throughout the course of this work is provided in the context of those efforts as they are encountered in the following chapters.

2.1. Overview of Advanced Filamentary Composites

Advanced filamentary composites are a critical materials technology in the production of lightweight structures and vehicles.[5] These materials combine engineered fibers possessing high mass-specific strength and stiffness with a matrix material to afford lightweight structures optimized for specific mechanical, thermal, and other loading configurations. Important examples include fiberglass/epoxy (silica fibers joined by epoxy resin), carbon/carbon (carbon fibers joined by an amorphous pyrolyzed carbon

matrix), and carbon fiber-reinforced plastics (CFRPs) such as graphite/epoxy (carbon fibers joined by epoxy resin). Graphite/epoxy is especially important in aerospace engineering as the macroscopic materials properties of graphite/epoxy laminates, including coefficients of thermal expansion (CTE) and non-isotropic mechanical response, can be tailored through configuration of laminate lay-up and selection of matrix. This capability combined with its superior strength-to-weight ratio, machinability, and structural integrity enables production of sophisticated aeroelastic and zero-CTE structures of tremendous technological value.

CFRP composite laminates can be manufactured several ways.[6] One approach entails winding fiber tow (spooled bundles of thousands of fibers) onto a preform mold while simultaneously spraying or brushing matrix resin as the tow is wound followed by a curing step at elevated temperature, possibly under pressure, to harden the composite. Another approach entails preparing stacks of pre-woven cloth and applying matrix resin as each layer is placed onto the stack followed by a curing step. A related approach, vacuum-assisted resin transfer molding, entails infiltrating a stack of pre-woven cloths with matrix resin using the assistance of a vacuum followed by a curing step. Yet another approach entails preparation of stacks of sheets of aligned or woven fibers impregnated with a partially-cured thermoset matrix or a thermoplastic matrix ("prepreg") and then curing. In all cases, the carbon fibers in the resulting laminate are held together by microscopic expanses of matrix (usually epoxy, although sometimes other thermoset resins such as phenolic resins or thermoplastics such as polyether ether ketone are used) which help to transmit load from fiber to fiber.

While in many cases the superior strength-to-weight ratio of graphite/epoxy and other composite materials enable them to replace aluminum and steel in structures—of great value for aircraft and spacecraft where weight savings translates into greater payload capacity and/or reduced fuel consumption—in some cases composites cannot replace metals due to underperformance.[5] For example, today's graphite/epoxy composites are susceptible to failure in shear due to a lack of reinforcement between laminate plies. Additionally, joining and adhering of composite parts is difficult. These drawbacks are common among many structural composite materials and arise from limitations of the microarchitecture intrinsic to such composites, in that there is no reinforcement other than the matrix, which is relatively weak and compliant, holding fibers together between and within plies of the laminate. While techniques for improving interlaminar strength in the through-thickness direction of the laminate have been demonstrated via three-dimensional reinforcement, for example by three-dimensional weaving or by reinforcement with pins in the through-

thickness direction ("Z-pinning"), these techniques significantly compromise in-plane properties of the laminate.[7]

Thus, methods for improving the mechanical properties of filamentary composites dominated by the matrix (e.g., interlaminar/intralaminar shear strength and fracture toughness) without compromising in-plane laminate properties would be highly valuable to the field of aerospace engineering.

2.2. Nanoengineered Composite Architectures

In analyzing the microarchitecture of laminated composites, it can be seen that the microscopic interstices of matrix that join fiber tows and plies together in the laminate are the primary points of failure for ply delamination and fracture propagation. One promising way to address this is to reinforce these microscopic interstitial expanses of matrix with nanostructured fibers, analogous to the way carbon microfibers reinforce macroscopic volumes of epoxy in a graphite/epoxy composite, or the way macroscopic rods or steel cables reinforce structural concrete in a bridge or building (Figure 2.1). In fact, these microscopic interstitial expanses, typically on the order of 100 to 1000 nm across, provide more than ample space for inclusion of a plurality of nanoscale objects (typically 1-20 nm in diameter). The goal in doing so is to engineer interlaminar and intralaminar reinforcement into the composite at the nano level, thereby leaving the in-plane architecture of the laminate undisturbed and the in-plane properties of the laminate uncompromised.

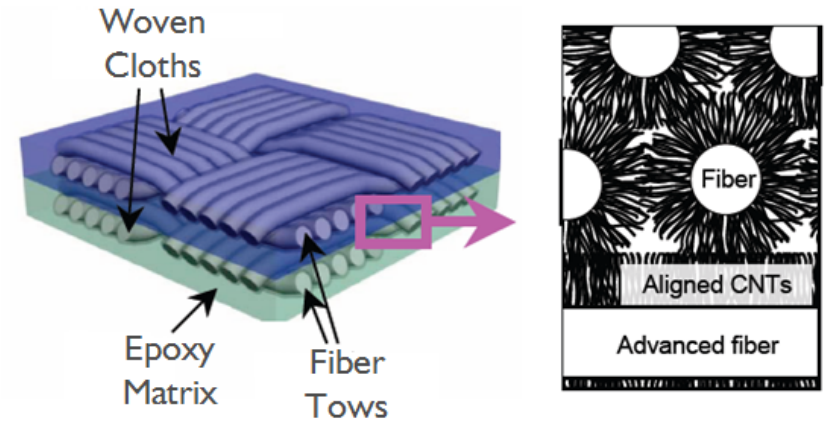

Figure 2.1 Schematic representation of fuzzy-fiber reinforced plastic architecture.[1,2]

A number of different strategies for introducing nanoscale fibers into composite architectures have been attempted, primarily focusing on reinforcing the intralaminar (within a ply) regions of composites through dispersal of unaligned CNTs into the matrix via shear mixing or other means.

These approaches have resulted in marginal reported improvements in mechanical properties in both nanocomposites[8] and microfiber-reinforced composites,[9-11] however, since process difficulties such as poor dispersion, agglomeration, and damage due to mixing arise. Furthermore, such processes result in materials in which the nanoscale fibers are not aligned, thereby limiting the effectiveness of the nanoscale fibers in reinforcing the matrix. Another set of approaches has focused on modification of the interlaminar (between ply) region of composites[12-17] by growing CNTs on the surface of ceramic cloths[13] or by placing unaligned[12,15-17] or aligned[14] CNTs at the interface of plies.

Nanoengineered hierarchal fiber architectures are a promising alternative approach towards improving fracture toughness, interlaminar and intralaminar strength, and wear resistance of advanced fiber composites such as graphite/epoxy and carbon/carbon. One such fiber architecture of particular interest is a carbon fiber circumferentially coated with arrays of aligned carbon nanotubes (CNTs), which can provide interlaminar and intralaminar reinforcement in laminated composites while also providing multifunctional benefits such as electrical and thermal conductivity enhancement. Indeed, this approach has resulted in improvements of mechanical properties (fracture toughness, interlaminar shear strength, and bearing properties) in analogous alumina/epoxy composites[1,2] (see summary data for a model "fuzzy fiber" reinforced plastics (FFRPs) made with alumina fibers, described elsewhere[3]). Notably, a scale effect in fracture toughness has been identified via simple closed-form bridging models,[18] and has been corroborated via interlaminar toughness testing of aligned CNT-reinforced laminates (alumina FFRP system) giving ~1.5 kJ/m^2 toughness enhancement—a value several times that of typical aerospace-grade laminates.[1] Kepple *et al.* have similarly shown that laminates prepared with carbon fiber weaves coated with unaligned CNTs exhibit improvements in fracture toughness of 0.2-0.3 kJ/m^2 and an improvement of ~10% in flexural modulus in three-point bending over control laminates; however, effects on in-plane properties are not addressed.[19] Qian *et al.* have assessed the apparent fiber-matrix adhesion shear strength of unaligned CNT-coated carbon fibers in an epoxy matrix at the single-fiber level and shown an improvement of ~57% in this value in fiber pull-out tests.[20] However, they also show that preparation of such fibers results in a 55% reduction in fiber tensile strength (from 3.5 GPa to 1.6 GPa).[20] Sager *et al.* similarly investigated the interfacial shear strength of unsized Cytek T650 fibers coated with (generally) aligned CNTs deposited through floating catalyst CVD processes and observe a loss in carbon fiber tensile strength of 30-40% and a loss in carbon fiber tensile modulus of 9-13% following CNT

growth.[21] Mathur *et al.* prepared carbon fiber tows coated with unaligned CNTs through a similar floating catalyst approach and investigated laminate-level flexural strength and modulus of unidirectional composites prepared with such fibers and phenolic resin. They observe a reduction of approximately 50% in both properties following CNT growth for fibers with ~3.5 wt % CNT loadings, suggesting the CVD process to be inherently damaging to the tensile properties of the primary fibers. The laminate-level flexural strength and stiffness properties improve with increasing CNT loading and even surpass those of composites prepared with unmodified fibers at loadings above 9 wt %. This, however, is likely due to micromechanical contributions from the CNTs compensating for the apparent loss in carbon fiber tensile strength and stiffness, facilitated by compositing effects (note that the effects of CNT growth on the properties of the carbon fibers were not explicitly characterized in that work).[22] In summary, the approach of using fuzzy carbon fibers for improving intraply, interply, and laminate-level properties appears to be generally promising, however to date these improvements have all only come at the expense of other properties.

Herein lies the fundamental lack of capability in the extant work—growth of CNTs on high-performance carbon fibers by CVD results in a substantial reduction in fiber tensile strength and, in many instances, tensile stiffness as well (i.e., the CNT growth process somehow damages carbon fiber). This is not the case for analogous alumina/epoxy FFRP systems that have been previously explored.[23] Thus, achieving desired laminate-level improvements in fracture toughness and apparent shear strength through incorporation of CNTs onto the surface of carbon fibers while simultaneously preserving the in-plane properties of the laminate remains elusive.

2.3. CNT Growth on Carbon Fibers

To achieve the benefits of "fuzzy carbon fiber" architectures and still attain materials with in-plane properties acceptable for aerospace applications, a methodology for growing CNTs on carbon fibers in a way that does not result in reduction of the tensile properties of the carbon fibers and, subsequently, negatively impact the in-plane properties of composites prepared with such fibers, must be developed. Underlying this is a need for better understanding the interactions between catalyst nanoparticles used for CNT growth and carbon fibers at the conditions required for CNT growth—a need which has largely been unaddressed by researchers interested in using fuzzy carbon fibers.

CNTs can be grown through a number of techniques, however to date the most versatile techniques for doing so have been those based on chemical

vapor deposition (CVD). In these techniques, nanoparticles serve as points of chemical activity from which hollow, seamless cylindrical graphitic fibrils (i.e., CNTs) emerge upon exposure to certain carbon-containing feedstocks (such as ethylene and acetylene) at elevated temperatures (typically 700-900°C).[24,25] In common models of CNT growth, the nanoparticles are believed to both assist in carbon feedstock cracking and facilitate nucleation of nanotubes through some sequence of localized events which may include one or more of adsorption of carbon-containing species onto the nanoparticle surface, dissolution of carbon into the subsurface or bulk of the nanoparticle, and templating of a crystalline carbon protostructure.[24,26-28] By far, the majority of work reporting CVD synthesis of CNTs has focused on nanoparticle catalysts based on Fe, Co, and Ni, although as will be discussed later, it is now known that CNT growth is by no means limited to these three metals.

As indicated, CNT-coated carbon fibers have been prepared by other groups. In fact, numerous works describing methods for growing nanostructured carbon fibrils on carbon fibers exist, dating back to at least 1991[29] (note that growth of SiC whiskers on carbon fibers has been a major area of interest for reinforcing the intralaminar and interlaminar regions of carbon fiber reinforced plastics since the late 1960's[30-34]). Although prior to the coining of the term "carbon nanotube", Downs and Baker published several works in the early 1990's showing carbon nanofibers (CNFs, nanostructured carbon fibrils with non-parallel graphitic walls) and, in some instances, what appear to be CNTs (fibrous carbon nanostructures small as 5 nm in diameter) grown on carbon fibers by catalytic CVD from ethylene employing Ni/Cu catalysts applied to the surface of fibers and fiber weaves through dip-coating with aqueous solutions of the nitrates of these metals (Figure 2-2).[29,35] In a 1995 paper, Downs and Baker demonstrate a 300-fold improvement in fiber surface area (from 1 $m^2\ g^{-1}$ to up to 300 $m^2\ g^{-1}$) and a four-fold improvement in apparent shear strength between single CNF-coated carbon fibers and a polyvinylethylacetate matrix (from 2.9 MPa to 11.8 MPa) with no substantial degradation of tensile properties of their fibers (note that Downs and Baker advise, however, that caution must be exercised in extrapolating these values to other matrix materials).[35] Notably, however, the baseline tensile strength for the fibers used in their work was only ~2.3 GPa, whereas current common intermediate modulus fibers frequently exhibit tensile strengths of 4 GPa or higher.[35,36] Importantly, it has been found that high-performance fibers that are of the greatest interest to the aerospace community all exhibit substantial loss of tensile properties upon CVD growth of CNTs or CNFs, consistent with the report of Qian *et al.*[20] Technological advances in carbon fiber production that have enabled the

higher tensile strengths attainable today invoke important microstructural states into the fiber and the author believes these microstructural states are thermally activated and at room temperature are kinetically trapped. One work reported that CNTs had been grown on high-performance carbon fibers (Cytek T650 and Hexcel IM-7) without substantial reduction in fiber tensile properties based on statistical arguments, however this claim relies on unusually wide error bars in single-fiber tensile strength measurements and notably the reported mean tensile strength and stiffness of the resulting fibers were substantially lower than those of the starting materials.[37] Numerous additional works[19,20,37-46] describing various methods for growing CNTs on carbon fibers[19,20,37-40,44-46] or attaching prefabricated CNTs to carbon fibers[41-43] also exist. These works neglect to characterize effects on fiber tensile properties, however, and, in many cases, utilize low-grade carbon fibers (<3 GPa baseline tensile strengths) and/or involve harsh chemical treatments which damage the carbon fibers, thereby making them of limited utility. As such, the problem of growing CNTs on industrially-important advanced carbon fibers is not resolved.

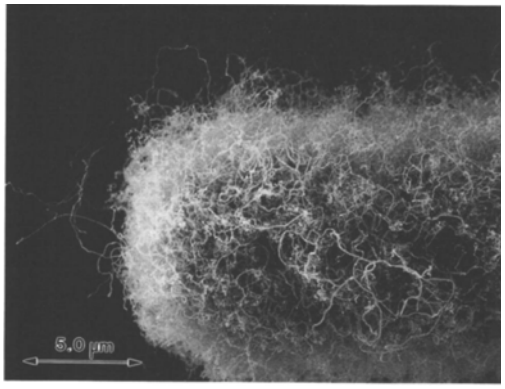

TABLE II. Strength of carbon fibers after growth of carbon nanofibers from the decomposition of ethylene over Cu–Ni catalysts.

Cu–Ni	Fiber	UTS (GPa)
None	T300	2.28 ± 0.52
None	P25	1.58 ± 0.28
3:7	T300	2.18 ± 0.47
3:7	P25	1.31 ± 0.29
2:8	T300	2.32 ± 0.32
2:8	P25	1.46 ± 0.31
1:9	T300	2.34 ± 0.53
1:9	P25	1.50 ± 0.37

Figure 2.2 *(Left)* Nanostructured carbon fibril-coated carbon fiber prepared by Downs and Baker, 1995; *(right)* tensile strength of fibril-coated carbon fibers prepared with low-grade carbon fibers, showing no reduction in tensile strength.[35]

An advantageous morphological feature for fuzzy carbon fibers first introduced by Wardle *et al.* is alignment of the CNTs on the fiber surface.[1-4,18,23] The majority of extant methods result in unaligned ("scraggly") growth of CNTs on fiber surfaces. Wardle *et al.* showed that a high catalyst density on alumina fibers results in aligned CNT arrays ("forests")[2,23] which facilitate capillarity-driven wetting[47] of resins into the microfiber architecture and permit the toughness and strength enhancement observed in alumina/epoxy FFRPs.[1] Achieving this type of growth morphology on carbon fibers would therefore be highly desirable and could serve to replace

the sizings used today (to provide an interphase region for improving adhesion of carbon fibers to matrix resins, among other functions).

2.4. Challenges Specific to Carbon Fiber as a Substrate

Carbon fibers are prepared on an industrial scale from several precursors including polyacrylonitrile (PAN) and mesophase pitch,[48] however the fibers of greatest interest for aerospace applications are those derived from the former (called "ex-PAN" fibers). In the process for making ex-PAN fibers, special (and highly proprietary) formulations of (mostly) polyacrylonitrile are spun into filaments which are then oxidized and subsequently pyrolyzed under extreme tension (i.e., a significant percentage of the fiber's breaking strength), resulting in highly-oriented graphitic carbon fibers.[49] For the purposes of this work, the term "carbon fibers" will hereafter implicitly refer to ex-PAN fibers.

Carbon fibers are challenging substrates upon which to grow CNTs for a number of reasons:

- The majority of the tensile load carried by a carbon fiber is transmitted in the outer skins of the fiber; as such, any disruption to the surface results in a disproportionate loss of tensile properties
- Commonly employed CNT catalysts (metals such as Fe, Ni, etc.) react with or dissolve carbon at CNT growth temperatures (700°C-900°C)—a property which has been speculated to be related to their efficacy in CNT growth
- Carbon reacts with oxygen, water, and hydrogen at temperatures above 400°C
- Many substances common in the environment catalyze microstructural transformations in carbon at these temperatures (e.g., Na^+ and K^+ ions from skin)
- The outer surface of carbon fibers is highly graphitic and therefore presents a low wettability with few active binding sites to which coatings can be applied, frequently involving acid or electrochemical etching surface to overcome
- Aligned growth of CNTs is not natively facilitated on carbon substrates and generally requires the presence of specific support materials

As such, it is challenging to get CNT catalyst materials to adhere to the fiber surface without some added chemical step that circumstantially results

in reduction of fiber tensile properties, and even if the catalyst material can be applied and adhere without such a treatment (for example through *in situ* deposition of floating catalyst particles during CNT growth[22,37,40]), it is likely to damage the fiber at the CNT growth temperatures. Furthermore, attaining the desired aligned CNT morphology on a carbon fiber poses an additional challenge.

2.5. Unconventional CNT Catalysts

While *in situ* observations of CNT growth by CVD using various metrologies have been reported, the mechanism of CVD growth of CNTs is still not fully understood and is likely not limited to one specific mechanism but rather is facilitated by a combination of related phenomena which may be more or less pronounced under different CVD conditions and for different combinations of catalysts and substrates. At a minimum, CVD growth of both single-wall and multi-wall CNTs appears to occur most ready from nanoparticle catalysts[24,27] which we now know are not limited in composition to the commonly-employed transition metals Fe, Co, and Ni, but in fact can be composed of many metals.[24,50-61] This includes Au,[50,56,57] Cu,[54,59,62] and Re,[60,61] which notably have poor bulk solubility for carbon and do not form stable carbides,[63,64] as well as the main group metal Sn[54] and the semiconductors Si, Ge, and SiC.[58] Even nanodiamond[65] can be used as a growth site for CVD growth of CNTs.

Clearly, many candidate nanoparticle catalyst materials exist. A substance that can catalyze CNT growth without dissolving carbon and which is relatively inert on a carbon fiber surface at elevated temperatures would be ideal for use in hierarchical nanoengineered filamentary composites. This is an area unexplored in the extant work and consequently fundamental investigations about this type of CNT growth support the development of solutions for the target engineering application.

2.6. Conclusions

In this chapter, the technological prospects of nanoengineered composites were presented and challenges underlying the growth of CNTs on carbon fibers in a way that preserves fiber tensile properties were established. Previous works in these areas were surveyed and lessons learned from them were summarized. In the next section, the objectives of this thesis are framed and a strategy for meeting those objectives informed by the works reviewed in this chapter is outlined.

Chapter 3

Objectives and Approach

In order to produce fuzzy carbon fibers with properties suitable for the level of performance expected of CFRPs, fundamentals of the CNT growth process and the behavior of carbon fiber during CNT growth must be understood. Additionally, in order to inform the development of practical methods for growing CNTs on carbon fibers, a clear understanding of the engineering boundary conditions must be articulated so that efforts can be focused on addressing specific barriers to progress in an effective way.

3.1. Objectives

The objectives of this thesis were to provide insight into catalyst-substrate and CVD environment-substrate interactions relevant to maintaining fiber properties in the growth of CNTs on carbon fibers by CVD, and to use these understandings to demonstrate practical approaches for growing CNTs on carbon fibers that simultaneously preserve fiber properties with a strong preference for obtaining aligned CNTs. This required developing an understanding of CNT growth in the specific context of carbon fiber substrates as well as understanding the nature of CNT growth by CVD in general.

3.2. Approaches to CNT Growth on Carbon Fibers

Methods of growing CNTs on carbon fibers are classified here as one of two sets of approaches: *direct approaches* and *barrier approaches*. Efforts undertaken to meet the engineering and scientific objectives of this thesis

were performed by exploring possibilities through these two general sets of approaches.

- *"Barrier approaches"* comprise applying a relatively inert metal oxide coating to the carbon fiber prior to application of catalyst in order to protect the fiber from damage that may be caused by interaction of the fiber with the catalyst. The barrier coating also serves the dual role of promoting alignment of CNTs. The effect of the barrier coating on carbon fiber tensile strength is then assessed. Challenges with this approach include development of barrier deposition techniques that do not negatively affect the properties of the carbon fiber, ensuring crack-free coverage, ensuring barrier adhesion to the carbon fiber, and ensuring wettability of the barrier by catalyst precursors.
- *"Direct approaches"* comprise direct application of catalysts that enable CNT growth to the fiber surface without dissolving or reacting with the fiber surface at CNT growth temperatures (as occurs with commonly employed catalysts such as iron, cobalt, and nickel). Challenges with this set of approaches include identification of candidate catalysts, assuring activity of the catalyst on a carbon fiber substrate, and ascertaining how to maximize CNT yield from them. In this work, direct approaches were investigated through the identification and characterization of nanoparticulate zirconia as a novel non-metallic material able to facilitate CNT growth and a promising candidate for enabling direct growth on metal-sensitive substrates such as carbon fibers. A broad study into the fundamentals of CNT growth with zirconia was conducted to better understand how its use could be reduced to practice and transitioned for use towards composites applications.

To assess the viability of methods developed through these two approaches, fundamental investigations were performed to inform the method development process as follows:

- *Viability of barrier approaches.* Carbon fibers were coated and CVD processed with candidate barrier coatings. SEM, Auger spectroscopy, and single-fiber tensile testing provided feedback regarding adhesion, coverage, and effects on carbon fiber tensile properties.
- *Viability of direct approaches.* Parametric investigations of new candidate catalysts (mostly based on zirconia) were performed and progress was assessed with SEM, TEM, XPS, *in situ* XPS during CNT growth, and XRD. Results within the context of parametric investigations provided

feedback for establishing an understanding of how these catalysts work and may be practically implemented.

3.2.1. Barrier Approaches and Supporting Work

Barrier approaches focused primarily on methods for depositing alumina onto carbon fibers. A set of design guidelines was established and put into practice to direct efforts towards a scalable, cost-effective outcome that did not involve methods known to compromise fiber tensile properties (see Section 7.1). This helped ensure that when unexpected sources of tensile property degradation were encountered they could be addressed in isolation from other potential sources of properties degradation. The strategy used for the development of barrier approaches was structured as follows:

- Identification of a candidate deposition method
- Demonstration of a proof-of-concept implementation of the method
- Characterization of coatings deposited from proof-of-concept implementation and their interface with carbon fiber: SEM imaging, Auger spectroscopy, single-fiber tensile tests
- Assess potential, ease of implementation, and probability of success
- If promising, iterate; if not promising, abandon

Candidate deposition methodologies are discussed at greater length in Chapter 7 and included the following:

- Sol-gel-based deposition investigating various processes and alumina precursors
- Electrodeposition of aluminum
- Chemical vapor deposition of alumina: various reactor configurations, processes, and alumina precursors
- Methods of non-covalently enhancing wettability of carbon fiber surfaces
- Direct loading of iron onto a carbon fiber via non-covalent functionalization

To complement engineering-oriented efforts, fundamental investigations of carbon fibers as substrates were performed. These included:

- Characterizing the behavior of carbon fibers at elevated temperatures
- Characterizing the interaction between coatings and carbon fibers

- Contextualizing fiber tensile properties degradation and responding through iterative process refinement

3.2.2. Direct Approaches and Supporting Work

Efforts undertaken for development of direct approaches focused primarily on the identification, characterization, and development of zirconia nanoparticles as promising substitutes for metal-catalyzed CNT growth on carbon fibers. Approaches taken were towards increasing understanding of new candidate catalysts at the catalyst nanoparticle level with the goal of reducing to practice a reliable method for applying them for CNT growth. Fundamental investigations of catalyst behavior and composition were undertaken to inform this development as follows:

- Trial-and-error exploration of new candidate catalyst materials
- Down-selection of promising candidates
- Initial parametric study to identify optimal CNT growth conditions of promising candidates
- Characterization of the catalyst behavior and composition with *ex situ* and *in situ* metrology
- Broader parametric study to optimize CNT yield and improve understanding of how to develop methods of adapting catalyst for practical applications

3.3. Application of Results

The results of these two general approaches were then integrated and used to identify degrees of freedom for engineering practical methods for growth of CNTs on carbon fibers and related interests. Methods that meet the engineering objective of enabling CNT growth on carbon fibers without resulting in degradation of tensile properties were then demonstrated and characterized to show that they meet the engineering objective (see Section 7.3.2 and Section 8.5). Other methods informed by findings and promising results that were demonstrated in combination are then proposed for future research (Section 9.2.1).

Chapter 4

Identification of a Non-Metallic Catalyst for Graphitization of Carbon and CNT Growth

This chapter describes the discovery that an oxide, namely zirconia, can serve as both a catalyst for the solid-state transformation of amorphous carbon into graphitic carbon and for growth of single- and multi-wall CNTs. This study unambiguously demonstrated, for the first time, that a non-metallic substance can catalyze CNT growth while remaining in an oxidized state during the CVD growth process, a process which had previously been believed by many to be limited to metal and/or metal carbide catalysts. The contents of this chapter appeared in a substantially similar form in the *Journal of the American Chemical Society* in August 2009 and represent a collaborative effort among several authors[55] based on discoveries made by the author of this work in the course of thesis studies. Contributors include Dr. Theodore F. Baumann of Lawrence Livermore National Laboratory, Bernhard C. Bayer of the University of Cambridge, Dr. Raoul Blume of the Fritz-Haber-Institut der Max-Planck-Gesellschaft, Dr. Marcus A. Worsley and Warren J. MoberlyChan of Lawrence Livermore National Laboratory, Elisabeth L. Shaw of MIT, Dr. Robert Schlögl of the Fritz-Haber-Institut der Max-Planck-Gesellschaft, Prof. A. John Hart of the University of Michigan, Dr. Stephan Hofmann of the University of Cambridge, and Prof. Brian L. Wardle of MIT (the thesis advisor).

4.1. Introduction and Overview of the Study

Nanoparticulate zirconia (ZrO_2) is found to catalyze both growth of single-wall and multi-wall carbon nanotubes (CNTs) by thermal chemical vapor deposition (CVD) and graphitize solid amorphous carbon. It is observed that silica-, silicon nitride-, and alumina-supported zirconia on silicon nucleate single- and multi-wall carbon nanotubes upon exposure to hydrocarbons at moderate temperatures (750°C). High-pressure, time-resolved X-ray photoelectron spectroscopy (XPS) of these substrates during carbon nanotube nucleation and growth shows that the zirconia catalyst neither reduces to a metal nor forms a carbide. Point-localized energy-dispersive X-ray spectroscopy (EDAX) using scanning transmission electron microscopy (STEM) confirms catalyst nanoparticles attached to CNTs are zirconia. Carbon aerogels prepared through pyrolysis of a Zr(IV)-containing resorcinol-formaldehyde polymer aerogel precursor at 800°C are observed to contain fullerenic cage structures absent in undoped carbon aerogels. Zirconia nanoparticles embedded in these carbon aerogels are further observed to act as nucleation sites for multi-wall carbon nanotube growth upon exposure to hydrocarbons at CVD growth temperatures. This study unambiguously demonstrates, for the first time, that a non-metallic catalyst can catalyze CNT growth by thermal CVD while remaining in an oxidized state and provides new insight into the interactions between nanoparticulate metal oxides and carbon at elevated temperatures.

4.1.1. Legacy CNT Catalysts and Their Properties

Catalyst-assisted transformation of hydrocarbons into graphitic nanostructures is an important tool in the production of emerging electronics and structural materials. Carbon nanotubes (CNTs) in particular are of great interest for these areas and are now commonly produced through well-established thermal chemical vapor deposition (CVD) and other techniques.[25,66,67] The mechanism of CVD growth of CNTs, however, is still not fully understood. At a minimum, CVD growth of both single-wall and multi-wall CNTs requires the use of a nanoparticle catalyst[24,27] which we now know is not limited in composition to the commonly-employed transition metals Fe, Co, and Ni, but in fact can be composed of many metals.[24,50-54,56,58-61,68] This includes Au,[50,56,68] Cu,[54,59,62] and Re,[60,61] which notably have poor bulk solubility for carbon and do not form stable carbides,[63,64] as well as the main group metal Sn[54] and the semiconductors Si, Ge, and SiC.[58] An even larger selection of transition metals (such as Ta), alloys (such as Al-Ti), and non-metal substances

(including $CuSiF_6$ and CeO_2) are known to act as graphitization catalysts for solid-state transformation of amorphous carbon.[69] Although catalytic graphitization is itself a complex process and occurs over a wider temperature range than typical CNT growth by CVD,[69] there is likely substantial mechanistic overlap between the two phenomena, for example in the types of intermediate bonding configurations and surface reactions involved.

In working to understand the necessary and sufficient attributes of effective nanotube catalysts, questions regarding the chemical state of the catalyst during CNT growth arise. The specific case of understanding the chemical state of iron during CNT growth raised the interesting debate of whether iron oxide (of some stoichiometry) or reduced iron (metallic or carbide) was the active catalyst species in that system. Recent direct observation of the chemical state of Fe during CNT growth through *in situ* X-ray photoelectron spectroscopy (XPS) by Mattevi *et al.* and Hofmann *et al.* revealed that it is a reduced species, not an oxide, that is the active catalyst.[26,70] Additionally, *in situ* X-ray diffraction (XRD) of catalyst particles during CNT growth from Fe nanoparticles by Nishimura *et al.* showed that upon introduction of carbon feedstock, the catalyst is deoxidized and that CNT growth is catalyzed by nanoparticles of iron carbides.[71] Sharma *et al.* further demonstrated the applicability of these observations at the single-nanoparticle level by atomic-level *in situ* TEM observations of CNT growth from Fe nanoparticles prepared by electron-beam induced decomposition.[72] Although many metal oxides such as Fe_2O_3 and NiO are used to prepare substrates that do in fact catalyze CNT growth,[25,73] these oxides are almost certainly reduced prior to catalysis, either from being annealed in H_2 during ramp-up to the growth temperature or, as observed by Nishimura *et al.*, by localized carbothermic and/or H_2 reduction upon introduction of CNT feedstock gases.

Recently, Rümmeli *et al.* demonstrated that when placed under typical conditions for CVD growth of CNTs, nanoparticles of certain difficult-to-reduce metal oxides, some of which are often used as catalyst supports in CNT growth (such as alumina), create encapsulating graphene layers.[74] This finding raises questions regarding how commonly-used catalyst supports affect CNT growth, or if materials used for supports, if rendered into nanoparticulate form, could in fact themselves catalyze CNT growth. A recent study reports growth of SWNTs catalyzed by alumina nanoparticles, although it is not clear whether aluminum or an alumina coating on the nanoparticles is the active catalyst.[75] Two recent reports have also described growth of SWNTs from aluminum, but with limited characterization of the nanoparticles.[54,76] Together, these studies suggest

that alumina itself may be a nanotube catalyst. Reports of growth of SWNTs from SiO_2 nanoparticles that result from scratches on SiO_2-coated Si wafers have also recently appeared, although again the identity of the active catalyst species in these cases remains speculative.[77,78]

4.1.2. Summary of Discovery

In this work, nanoparticulate zirconia (ZrO_2) is observed to both catalyze MWNT and SWNT growth by thermal CVD and catalyze transformation of solid amorphous carbon into graphitic nanoshells. Using *in situ* XPS analysis during CVD growth of CNTs from several substrates with zirconia, it is shown unambiguously, for the first time, that an oxide can catalyze CNT growth while remaining in an oxidized state during growth. Si substrates coated with films of ZrO_2 deposited from liquid solutions were studied and found that processing of these substrates by CVD resulted in substantial CNT growth. Depending on temperature and gas flow conditions used during CVD, these substrates demonstrated the ability to grow either SWNTs or MWNTs, including local vertically aligned "forest" morphologies which are indicative of high catalyst particle activity. Solid-state interactions between zirconia and carbon at elevated temperatures were also investigated by preparing zirconia nanoparticle-doped carbon aerogels. Aerogels were produced through pyrolysis of Zr(IV)-containing resorcinol-formaldehyde polymer aerogels at 800°C and exhibited the presence of fullerenic cage structures absent in undoped carbon aerogels. Subsequent CVD processing of zirconia-doped carbon aerogels also resulted in the growth of CNTs, apparently from zirconia particles embedded in the aerogel skeleton. *Ex situ* XRD and XPS analysis of Si and carbon aerogel substrates before and after CNT growth found no metallic zirconium or zirconium carbide present, suggesting that zirconia nanoparticles are not reduced by the hydrogen- and hydrocarbon-rich CVD atmospheres of CNT growth. *In situ* XPS analysis of low-pressure CVD growth of CNTs on Si and carbon aerogel substrates verified that no metallic zirconium or zirconium carbide arises at any point prior to, during, or following CVD growth of CNTs from zirconia nanoparticles.

In addition to demonstrating the interesting result that a metal oxide can exhibit these catalytic behaviors, zirconia offers unique promise as a useful catalyst for CNT growth. First, zirconia is non-magnetic and, as shown here, can catalyze SWNT growth, making it an interesting possible catalyst for electronics applications. It is also relatively inexpensive compared to many other non-magnetic CNT catalysts that have been reported (such as Au, Re, and Pt).[79] Second, zirconia offers the potential for facilitating CNT growth

on historically challenging substrates, such as carbon, metals, and ceramics. Because of their reactivity at elevated temperatures, commonly used CNT catalysts (such as Fe, Co, and Ni) must often be stabilized with a metal oxide barrier to enable CNT growth on these substrates without causing damage to the substrate (see Chapter 7 for how this applies in the context of carbon fiber as a substrate), thereby limiting many potential applications. Zirconia, however, is both a relatively inert oxide and apparently catalyzes CNT growth without dissolving carbon. Hierarchical nano-engineered filamentary composites are one potential application where such a catalyst would be valuable[2,4,20,35] and as a proof-of-concept demonstration, zirconia is shown to catalyze CNT growth on commercially-available carbon fibers without causing pitting of the fibers. Third, ZrO_2 is not susceptible to oxidation, since it is already an oxide, and thus may be an advantageous catalyst for oxidative CNT growth conditions (i.e., water or alcohol growth). Furthermore, we and others[80] have observed that nanoparticulate ZrO_2 appears to be stable against carbothermic reduction at temperatures up to 1050°C, suggesting it is also resistant against poisoning by carburization, which has been hypothesized to be a CNT growth termination mechanism for iron catalysts.

4.2. Methods

In the methods detailed below, great care was taken to prevent contamination by metals, especially iron. Clean, dedicated plastic and glass tools and containers were used for all stages of processing. Pyrolysis of aerogel samples and all CNT growth processes were conducted with an isolated set of new, dedicated quartz process tubes. Null CNT growth on ZrO_2-free Si substrates verified the absence of catalyst contamination in the CVD systems used. XPS analysis of the substrates used also verified that no Fe, Co, Ni, or other obvious potential catalysts were present before or after CVD processing.

4.2.1. Preparation of ZrO_2-Coated Si Substrates

All Si substrates used had a 200-300 nm layer of thermal SiO_2. Si substrates with Al_2O_3 supports were prepared through e-beam evaporation or RF sputter deposition of solid stoichiometric Al_2O_3. Si substrates with oxynitride support were prepared using a vertical thermal reactor followed by annealing. Saturated solutions $ZrOCl_2 \cdot 8H_2O$ in 2-propanol were prepared by adding 322 mg $ZrOCl_2 \cdot 8H_2O$ to 20.0 g 2-propanol, sonicating for ~5 min, and allowing nanoparticles to form over the course of 4-5 d. These solutions

were then stirred and used for dip-coating or drop-casting zirconia nanoparticles onto Si wafers.

4.2.2. Preparation of ZrO_2-Doped Carbon Aerogels

ZrO_2-doped carbon aerogels and undoped control carbon aerogels were prepared using sol-gel processing through the ion-exchange technique developed for preparing metal-doped carbon aerogels, described elsewhere.[81-83] Briefly, the potassium salt of 2,4-dihydroxybenzoic acid was polymerized with formaldehyde in water to form a mesoporous K^+-doped resorcinol-formaldehyde polymer gel. Potassium carboxylate moieties throughout the gel structure act as ion exchange sites, allowing the gel to be doped with other ions (such as transition metal ions) by exchanging the gel liquor with an aqueous ionic salt. Prior to ion exchange, the gel was purified by exchanging the gel liquor with deionized water. Ion exchange of K^+ for zirconyl was then performed by soaking the gel in a solution of aqueous 0.1 M $ZrOCl_2 \bullet 8H_2O$ (Fluka, ≥99.0%, <0.4 μg/mg known CNT catalysts[84]). To serve as a control, an undoped gel was prepared by exchanging K^+ for H^+ through soaking in aqueous 0.1 *N* HCl. The gels were then purified and prepared for supercritical drying through multiple solvent exchanges (3 exchanges per solvent, 1 exchange per 24 h) first with deionized water, then acetone, and then finally liquid CO_2. The gels were then supercritically dried from CO_2 (T_c = 31.1°C, P_c = 72.9 atm, T_{max} = 50°C, P_{max} = 100 atm) to afford zirconyl-doped and undoped resorcinol-formaldehyde polymer aerogels, respectively. Finally, the aerogels were pyrolyzed under a flow of 200 sccm Ar at 800°C or 1050°C for 10.5 h, affording mesoporous carbon aerogel (bulk density approximately 0.1 g cm^{-3}, mean pore size approximately 7 nm, BET surface area approximately 700 m^2 g^{-1}). In the case of the zirconyl-doped samples, the aerogels were found to be homogenously laced with polydisperse ZrO_2 nanoparticles encased in fullerenic nanoshells. The undoped aerogels exhibited a typical amorphous carbon structure only.

4.2.3. ZrO_2-Catalyzed Growth of CNTs

Thermal CVD growth of CNTs was performed on several different substrates, listed in Table 4.1. Atmospheric thermal CVD was performed in a three-zone Lindberg/Blue M furnace with a 62-cm heated length using 50-mm inner diameter fused quartz process tubes with a length of 138 cm. Samples in this system were placed directly in the quartz tube between 50% and 75% of the heated length. Gases used were all ultrahigh purity grades (99.999%, Airgas, US). Low-pressure CVD growth for *in situ* XPS analysis was performed at the BESSY II synchrotron at the Helmholtz-Zentrum Berlin in the

end station of the Fritz-Haber-Institut der Max-Planck-Gesellschaft (FHI-MPG). (*Note that the term "low-pressure" refers to sub-atmospheric CVD, however these same conditions are considered "high-pressure" for XPS*). Samples in this system were transferred into a reaction cell and placed into differentially pumped stages of the lens system of a hemispherical analyzer (Phoibos 150, SPECS) ~2 mm away from the aperture. A focused IR laser was used for sample heating. Temperature readings were taken from a thermocouple spot-welded in the vicinity of the sample and, as such, an underestimation of up to ~100°C may have occurred. The CVD atmosphere was constantly monitored by a mass spectrometer attached via a leak valve.

Substrate Type	**Control Substrate**	**Substrate(s) With Catalyst**
Si wafer, (100) orientation, 200-300 nm thermal SiO_2	Unmodified wafer	Wafer dip-coated or drop-cast with saturated solution of $ZrOCl_2 \cdot 8H_2O$ in 2-propanol
Si wafer, (100) orientation, 200-300 nm thermal SiO_2 and 10 nm alumina	Unmodified wafer	Wafer dip-coated or drop-cast with saturated solution of $ZrOCl_2 \cdot 8H_2O$ in 2-propanol
Si wafer, (100) orientation, 100 nm silicon oxynitride	Unmodified wafer	Wafer dip-coated or drop-cast with saturated solution of $ZrOCl_2 \cdot 8H_2O$ in 2-propanol
Carbon aerogel	Acid-neutralized (undoped) carbon aerogel	ZrO_2-doped carbon aerogel (6-8 nm mean ZrO_2 particle size)
Unsized carbon fibers (AS4 carbon fiber 3k tow)	Unmodified carbon fiber	Carbon fibers dip-coated with saturated solution of $ZrOCl_2 \cdot 8H_2O$ in 2-propanol

Table 4.1 Summary of control and catalyst substrates evaluated for catalytic activity of zirconia nanoparticles towards CNT growth.

CVD processes used for CNT growth were established through process optimization of processes previously established for legacy CNT catalysts (Table 4.2). Atmospheric pressure CVD was performed with methane and

ethylene feedstocks (Table 4.2). Low-pressure CVD employing acetylene was used for the *in situ* XPS analysis (Table 4.2). For atmospheric pressure growths, Si substrates were processed with both methane and ethylene conditions; carbon aerogel and carbon fiber samples were only processed using ethylene growth conditions at atmospheric pressure. *In situ* XPS analysis was performed for zirconia on Si with alumina support and zirconia-doped carbon aerogel.

Feedstock	Pressure	Ramp	Soak	Growth	Cool Down
CH_4	Atmospheric	Ambient to 900°C at 20°C min^{-1}; 400 sccm He	0-10 min; 200 sccm H_2	15 min; 500 sccm CH_4, 100 sccm H_2	400 sccm He
C_2H_4	Atmospheric	Ambient to 750°C at 50°C min^{-1}; 400 sccm He	0-10 min; 400 sccm He, 1600 sccm H_2	10 min; 400 sccm C_2H_4, 400 sccm He, 1600 sccm H_2	400 sccm He
C_2H_2	Low-Pressure	Ambient to ~530°C at ~125°C min^{-1}; 0.1 mbar H_2	15 min; 0.1 mbar H_2, followed by 20 min under 10^{-7} mbar vacuum	10 min; 10^{-2} mbar C_2H_2 only, followed by 20 min C_2H_2:H_2 mixture (1:5 ratio) at 0.2 mbar	Under 10^{-7} mbar vacuum or 0.1 mbar H_2

Table 4.2 Summary of CVD conditions evaluated for CNT growth from zirconia catalysts.

4.2.4. Characterization

Si-based substrates before and after CVD processing were characterized by scanning electron microscopy (SEM), *ex situ* X-ray photoelectron spectroscopy (XPS), *in situ* XPS during CNT growth, transmission electron microscopy (TEM), point-localized energy-dispersive X-ray spectroscopy (EDAX) under scanning transmission electron microscopy (STEM), and Raman spectroscopy. ZrO_2-doped carbon aerogels before and after CVD processing were characterized by powder X-ray diffraction (XRD), *ex situ* XPS,

in situ XPS during CNT growth, SEM, TEM, point-localized EDAX under STEM, and Raman spectroscopy. Carbon fiber substrates before and after CVD processing were analyzed by SEM. XRD patterns were obtained using a PANalytical X'Pert Pro MPD with RTMS detector using Cu K-alpha radiation, a voltage of 45 kV, and a current of 40 mA. Phase identification and crystallite size determination were made using MDI Jade 7 equipped with the ICCD database. *Ex situ* XPS spectra were obtained on an AXIS Ultra DLD Spectrometer (Kratos Analytical Ltd, UK) using Al K-alpha radiation (energy = 1486.6 eV) in a chamber with a base pressure of 5×10^{-9} torr. For the carbon aerogels, XPS samples were prepared either by grinding the material into a fine powder and adhering to adhesive copper tape or by adhering monoliths directly to copper tape. The copper tape was mounted on a sample holder using double-sided adhesive carbon tape. Silicon substrates were directly mounted on the sample holder with carbon tape. All measurements were performed using an X-ray power of 150 W (15 kV and 10 mA), a pass energy of 10 eV, and an analysis area of 750 μm × 350 μm. A charge neutralizer was not used. Charge correction for carbon aerogel samples was not performed as no charging effect was observed; charge correction for silicon substrates was performed using peaks from SiO_2 or Al_2O_3 supports as reference points. High pressure *in situ* XPS spectra were collected in normal emission geometry at photon energies of 500 eV with a spectral resolution of ~0.3-0.4 eV. At these photon energies, the electron mean free path is ~10.5 Å. The analysis area was ~100 μm × 1 mm. Background correction was performed using a Shirley background. Spectra were fitted following the Levenberg-Marquardt algorithm to minimize the χ^2 value. Peak shapes were modelled using asymmetric Doniach-Sunjic functions convolved with Gaussian profiles. High-resolution scanning electron microscopy (HRSEM) was performed with a JEOL 6320 microscope and FEI Philips XL30 sFEG microscope operating at 14 kV for carbon aerogel samples, 5 kV for carbon fiber samples and MWNT Si substrates, and 2.5 kV for samples from the *in situ* XPS analysis. High-resolution transmission electron microscopy (HRTEM) of carbon aerogels and derived nanotube composites was performed on a JEOL JEM-200CX microscope operating at 200 kV. HRTEM and STEM of CNTs grown during *in situ* XPS experiments was performed on a JEOL 2010F microscope operating at 200 kV equipped with an INCA system for performing EDAX. Raman spectra were obtained using a custom-built micro-Raman spectrometer operating at an excitation wavelength of 647 nm with a laser power of 25 mW and a collection time of 5 s. Peak fitting was performed using CasaXPS operating in Raman analysis mode. Peak shapes were modeled using an asymmetric Lorentzian lineshape convolved with a

Gaussian profile with tail exponents α = 1 and β = 1 and Gaussian width *m* = 2 (CasaXPS lineshape LA(1,1,2)).

4.3. Results and Discussion

Growth of CNTs from zirconia on Si substrates was first evaluated by drop-casting a saturated solution of $ZrOCl_2 \cdot 8H_2O$ in 2-propanol onto Si wafers with a silicon oxynitride barrier. Following pre-treatment under hydrogen and CVD processing of these wafers with ethylene feedstock at 750°C, bundles of aligned CNTs ("mini-forests") could be observed at various locations on these wafers with SEM (Figure 4.1). While much of these wafers exhibited no growth, growth was in high yield where it was observed. Also observable on these wafers were cracked platelets, clusters, and films of zirconia, upon which the mini-forests and other long (>5 μm) CNT bundles were observed. Similar results were observed for zirconia on alumina and silica.

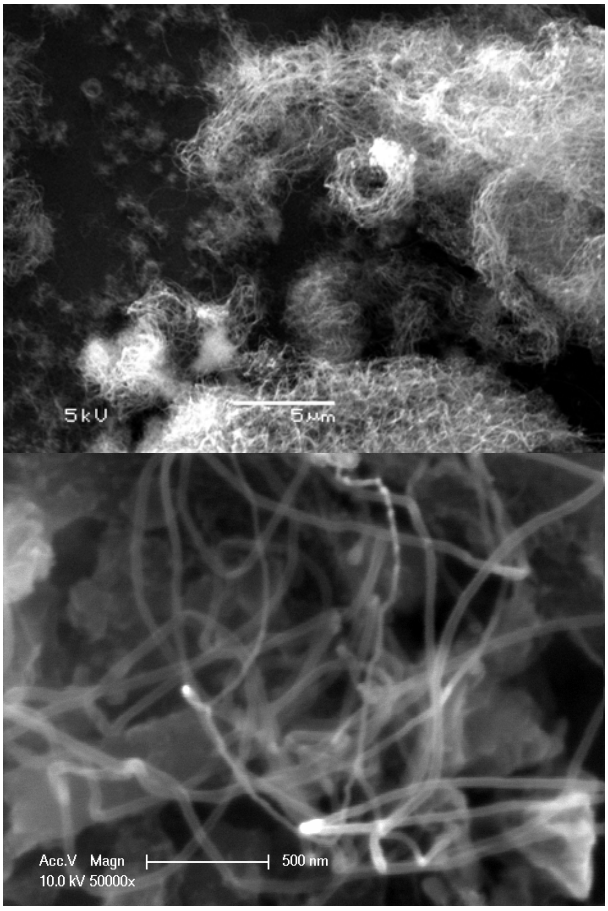

Figure 4.1 (*Top*) SEM of bundles of aligned CNTs catalyzed by ZrO_2 on silicon oxynitride support using ethylene feedstock at 750°C; (*bottom*) close-up of large-diameter MWNTs extending from a cluster of zirconia particles.

To understand whether zirconia or a reduced zirconium species (resulting from high-temperature exposure to hydrogen and hydrocarbons, for example) serves as the CNT growth catalyst on these substrates, zirconia-coated wafers were analyzed by XPS *ex situ* of CVD growth. Both prior to and following exposure of the wafers to the CVD growth conditions, no metallic Zr or ZrC was found to be observable and instead only high-binding energy chemistries in the range expected for ZrO_2 were found. These observations are substantiated by the understanding of ZrO_2 chemistry at high temperatures in the literature. ZrO_2 is known to not be reduced by H_2, even at temperatures of 1500°C and higher.[85] Additionally, carbothermic reduction of ZrO_2 does not yield Zr metal but instead results in the formation of ZrC,[86] and Sacks *et al.* have reported that carbothermic reduction of even nanocrystalline ZrO_2 to ZrC under Ar only begins at temperatures around 1200°C[80]—much higher than the growth temperatures used in this study. Considering the phase diagrams of bulk ZrO_2-Al_2O_3 and ZrO_2-SiO_2, no significant reaction with the support is expected to occur at the conditions for CVD growth of CNTs. The phase diagram for the ZrO_2-SiO_2 system[87] shows that at <1000°C, monoclinic ZrO_2 plus zircon ($ZrSiO_4$) is the favorable phase configuration. However, if zircon were forming during the CVD growth conditions, the XPS spectrum would show an additional silicon chemistry superimposed over the signal for SiO_2 in the Si 2p region, as well as a specific shift in the Zr 3d region to a higher binding energy by ~1 eV,[88,89] neither of which is found. Likely, in the inherently reductive environment of CNT growth, such a reaction between oxides would be inhibited. Similarly in the ZrO_2-Al_2O_3 system,[87] only a mixture of the separate oxides (i.e., no phase transition) is expected at both 750°C and 900°C (up to 1150°C).

To verify the hypothesis that zirconia itself is serving as the CNT growth catalyst, an *in situ* XPS analysis of low-pressure CVD growth of CNTs from ZrO_2 was performed. Figure 4.2 shows SEM images of CNTs grown from ZrO_2 on a Si substrate from this experiment. A substantial yield of CNTs was observed within the XPS analysis area by SEM, easily identifiable atop platelets of zirconia on the substrate surface. Figure 4.3 shows the progression of the C 1s and Zr 3d regions of the XPS spectra from this sample after heating in hydrogen, during growth with acetylene and H_2, and after CVD during cool-down in vacuum. Prior to introduction of hydrogen (not shown), a high-binding energy chemistry of Zr centered at 182.6 eV is initially observed, likely corresponding to the presence of electron-withdrawing oxychloride and/or alkoxide on the surface. Upon introduction of hydrogen, the Zr 3d signal shifts to a lower binding energy, corresponding to formation of zirconia.[90-93] Two pairs of spin-orbit-split peaks corresponding to two phases of zirconia can be resolved, one phase with the Zr $3d_{5/2}$ peak at 182.5

eV and one with the Zr $3d_{5/2}$ peak at 181.8 eV. The lower binding energy signal is attributed to an oxygen-deficient phase of zirconia, while the higher binding energy signal is attributed to stoichiometric ZrO_2.[88] Thus it appears that introduction of H_2 does not reduce the deposited zirconia film to Zr metal but instead pulls off residual chloride and alkoxide groups to yield oxide phases. Subsequent introduction of acetylene invokes an additional temporary, low-lying, high-binding energy signal attributed to a charging effect (also not shown). This signal disappears, and only signals corresponding to two phases of zirconia persist throughout the CVD growth. Upon addition of hydrogen to the acetylene stream, a C 1s peak emerges, which we attribute to nucleation of CNTs and possibly formation of other carbonaceous structures. This peak resolves into several components observed in CNT growth from other catalysts along with a low binding energy component located at 283.4 eV. This peak does not match the expected position for the C 1s peak of zirconium carbide (282 eV)[94,95] and so it is speculated it may be caused by the interaction of a deposited organic with the support. Finally upon cool-down, only the two phases of zirconia observed during growth remain, along with a high binding energy signal attributed to charging effects. At no point prior, during, or after CVD growth of CNTs is metallic zirconium (binding energy 178.6-179.6 eV)[92,93,96] or zirconium carbide (binding energy 179-181.1 eV)[94,95] observed in the Zr 3d region. Thus this confirms that the CNT growth catalyst is the oxide zirconia. Null CNT growth on zirconia-free Si substrates coated with alumina verified that the 10-nm alumina support layer is not serving as the catalyst, consistent with the findings of Mattevi *et al.* that continuous alumina films do not result in the growth of CNTs.[28]

Notably, the C 1s peak in the *in situ* XPS spectrum of the Si substrate did not appear immediately following introduction of acetylene but only after hydrogen was added as well. It has been shown that high-temperature reaction of hydrogen with ethylene,[97] methane,[98] and other hydrocarbons[99] results in the formation of a broad spectrum of organic compounds and that the resulting spectrum of compounds is dependent on the concentration of hydrogen.[97-99] Furthermore, CNT growth rate employing Fe/alumina catalysts has been correlated with concentrations of specific molecules that result from high-temperature reaction of ethylene with hydrogen.[97,100,101] It is speculated that the introduction of hydrogen here aids in transformation of acetylene into other organic precursors that can then be uptaken and catalyzed into CNTs and/or other solid forms of carbon by zirconia. Perhaps common metallic CNT catalysts, such as Fe and Ni, are able to catalyze this hydrocarbon digestive process directly or in a different way, which may explain why zirconia often gives lower areal yields of CNTs.

It should be noted that time-resolved, *in situ* XPS provides the most accurate information about the chemical state of the catalyst during CNT growth at that moment. Nevertheless, the question arises as to whether or not the active species during growth might be missed by XPS due to detection limits of species present in small quantities or because of short, transient changes in the state of a species on a time scale faster than the acquisition time. However, it is argued that if such short and/or small atomic fraction processes do arise and result in traces of metallic or carbidic Zr, these traces would have been detectable at some point in the analysis as reduced Zr would not reoxidize in a vacuum and should not only remain detectable but accumulate and become more detectable with time.

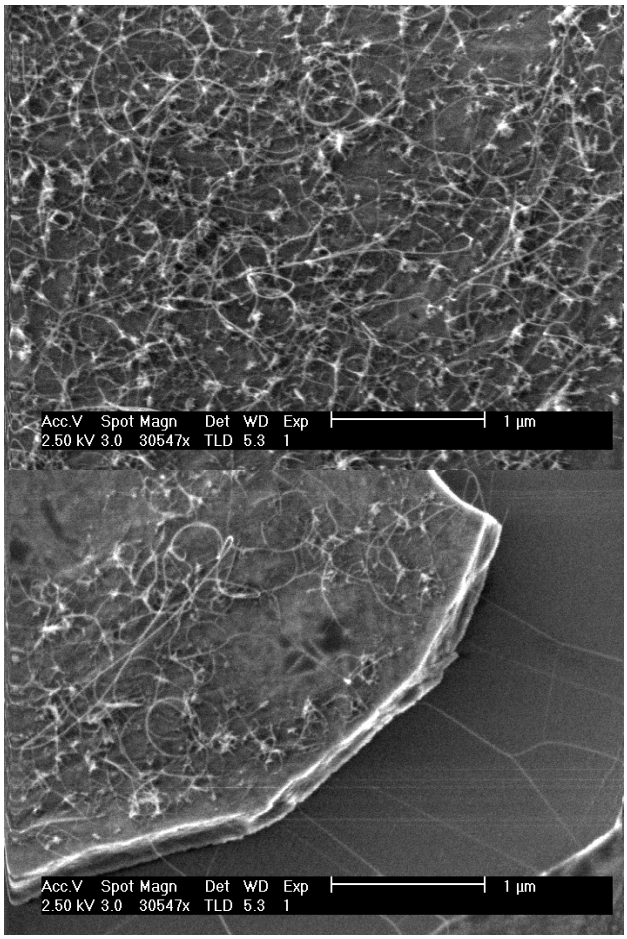

Figure 4.2 SEM images of CNTs grown from zirconia from $ZrOCl_2$/IPA solution on a Si wafer with 10 nm alumina support, analyzed by XPS *in situ* during CVD; (*bottom*) CNTs grown atop a platelet of zirconia on Si wafer during the *in situ* XPS analysis.

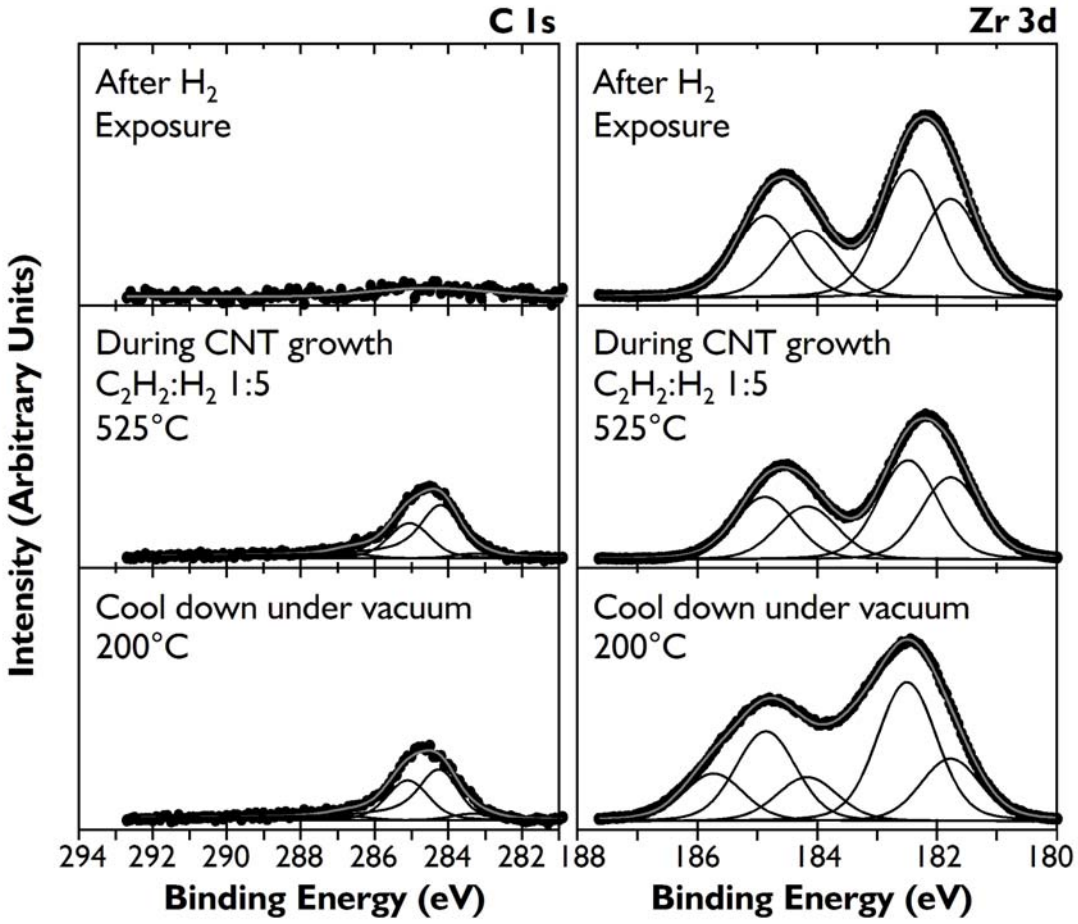

Figure 4.3 Progressive XPS snapshots of the C 1s and Zr 3d regions during growth of CNTs from zirconia on Si substrate. An appreciable carbon signal only appears upon introduction of both acetylene and hydrogen. No metallic zirconium or zirconium carbide is observed during growth.

Raman spectroscopy was performed on the Si substrates used for the *in situ* XPS growth to assess the type and quality of CNTs that resulted from the growth.[102] Radial breathing modes between 130 to 280 cm^{-1} are observed within the XPS analysis area, indicating the presence of SWNTs (Figure 4.4). For an individual nanotube on an Si/SiO_2 substrate, the diameter of the nanotube in resonance with the laser can be approximated by d_t [nm] = 233 cm^{-1}/ω_{RBM}.[103] For the spectrum shown in Figure 4.4, nanotubes of 1.67 nm, 1.18 nm, and 0.84 nm are observed. The low D-to-G ratio suggests the presence of high-quality, low-defect CNTs. Raman peaks from zirconia[104] were not readily observable relative to carbon Raman peaks where CNTs were best resolved on the substrate.

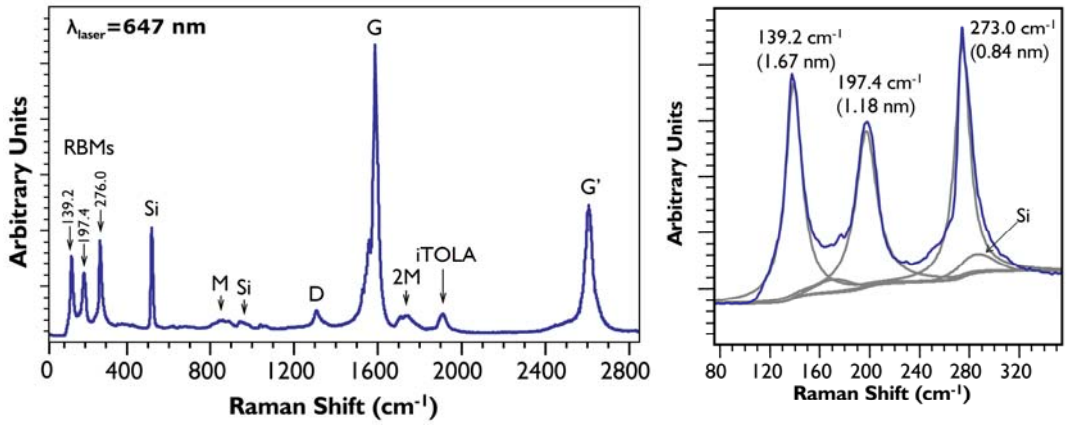

Figure 4.4 Raman spectrum from carbon nanotubes grown by CVD during *in situ* XPS analysis. The presence of radial breathing modes indicates the presence of single-wall carbon nanotubes.

CNTs grown from zirconia nanoparticles during *in situ* XPS analysis were transferred onto TEM grids (Cu with C film) to verify that the XPS measurements are in fact representative of particles at the nanoscale and that zirconia nanoparticles are the catalyst responsible for CNT growth. CNTs attached to zirconia nanoparticles are observed (Figure 4.5). To further prove that the observed particles are in fact zirconia and not zirconium metal, scanning transmission electron microscopy (STEM) and using point-localized energy-dispersive X-ray spectroscopy (EDAX) was performed to characterize their elemental composition. EDAX reveals a stoichiometry of ~30% Zr and ~70% O for these nanoparticles, verifying a stoichiometry of ZrO_2 and further validating that the *in situ* and *ex situ* XPS and XRD characterizations are representative of the nanoscale. Multiple particles attached to multiple CNTs exhibit similar stoichiometry. The ratio of oxygen to zirconium measured was consistent from particle to particle within ±5% and was not contributed by the grid or other structures on the grid as evidenced by EDAX spectra collected away from the particles of interest.

To better understand the interactions of nanoparticulate zirconia in the presence of carbon at elevated temperatures, zirconia nanoparticle-doped carbon aerogels were studied. A nanoparticle-doped carbon aerogel system offers several benefits for studying the interactions of nanoparticles of a material with carbon. First, it allows for synthesis of a bulk quantity of nanoparticles dispersed inside an amorphous carbon matrix for a wide range of nanoparticle compositions. Second, because the aerogel materials are macroscopic, three-dimensional monoliths, both bulk characterization techniques like XRD (which can be challenging to use for surface-bound particles), as well as surface analysis techniques like XPS can be used to

characterize the nanoparticles of interest. Furthermore, the materials can be pyrolyzed over a wide range of temperatures, allowing for investigation of temperature dependency on the nanoparticle-carbon interactions.

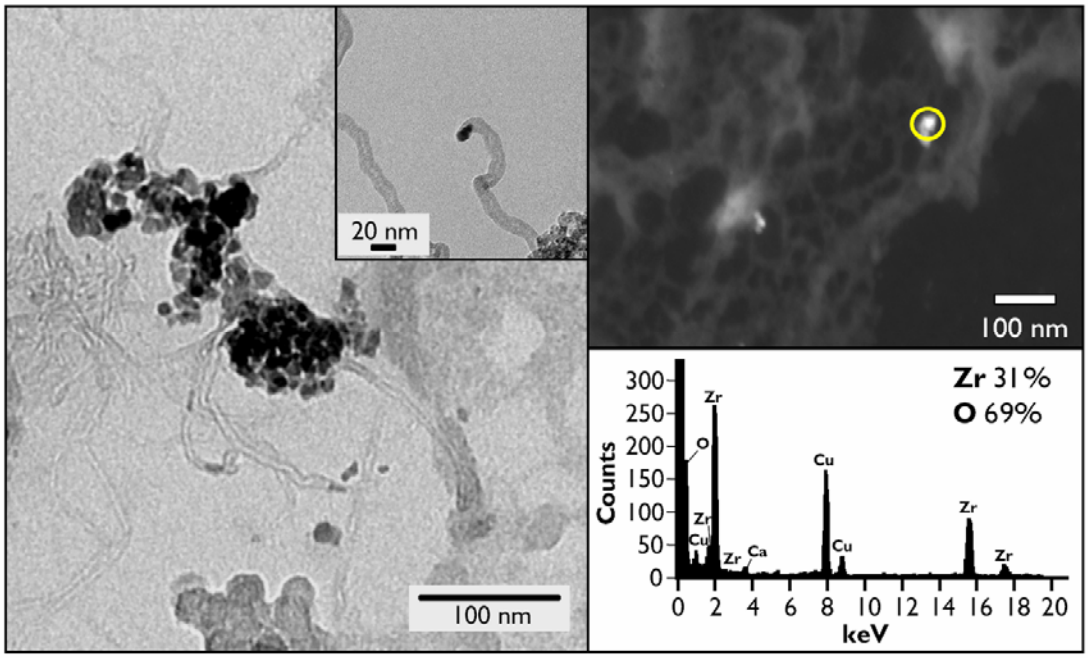

Figure 4.5 (*Left panel, main image*) TEM image of CNTs attached to zirconia catalyst nanoparticles from *in situ* XPS growth experiments (Cu with C film TEM grid); (*left panel, inset*) CNT attached to zirconia catalyst nanoparticle grown from zirconia-doped carbon aerogel; (*right, top*) scanning TEM (STEM) image of CNTs extending from zirconia nanoparticles grown during *in situ* XPS experiments; (*right, bottom*) representative point-localized EDAX spectrum of a nanoparticle (*right, top circled*) attached to CNTs from *in situ* XPS experiment, verifying a particle composition of ~ZrO_2.

Aerogels were prepared using an adapted version of the ion exchange technique used to prepare metal-doped carbon aerogels. Metal-doped carbon aerogels prepared through ion exchange[81-83] typically exhibit a "blueberry muffin" morphology in which metal-containing nanoparticles ("blueberries") are dispersed throughout a low-density mesoporous amorphous carbon framework ("muffin"). In the case of Fe-[83] and Cu-doped[81] carbon aerogels, this carbon framework is essentially the same as in undoped carbon aerogels[105] for pyrolysis temperatures up to 1050°C. During pyrolysis, the resorcinol-formaldehyde-type polymer framework of the aerogel dehydrates to afford amorphous carbon. Simultaneously, metal ions attached to the polymer framework are reduced and coarsen into a spectrum of metal-containing nanoparticles with a range of diameters and, depending on the metal, a range of crystallite phase and surface compositions. In similarly-

prepared Ni- and Co-doped carbon aerogels,[82] however, graphitic nanoribbons surrounding metal nanoparticles can be observed amongst an otherwise amorphous carbon matrix. In these materials the Ni and Co nanoparticles, which are both solvents for carbon, catalyze a solid-state transformation of the amorphous carbon into graphitic nanoribbons and other graphitic nanostructures.

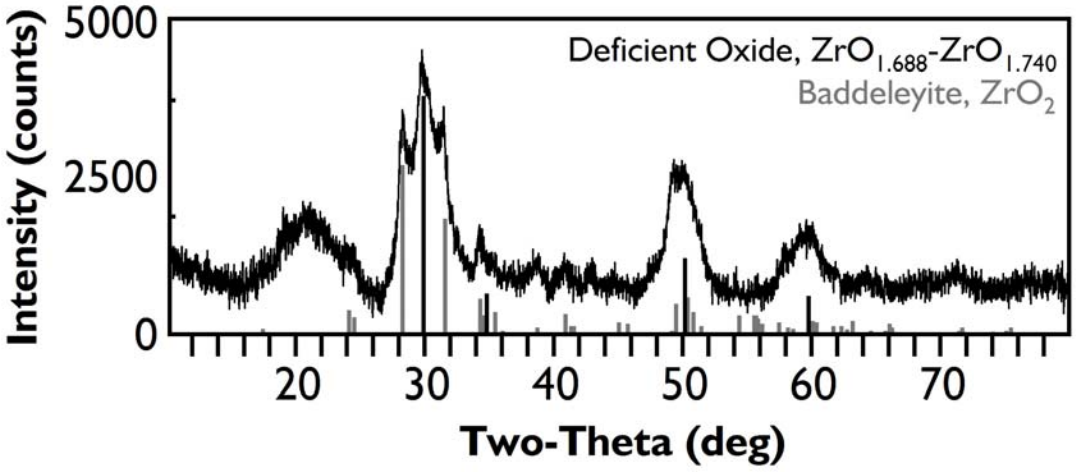

Figure 4.6 Powder XRD pattern of ZrO_2-doped carbon aerogels with possible phase matching corresponding to Baddeleyite ZrO_2 (gray lines) and an oxygen-deficient phase of zirconia (black lines). The broad peak widths indicate the presence of nanosized crystallites (~7 nm average diameter). No peaks associated with Zr or ZrC are observed. The broad peak centered about 21° 2-θ is associated with the carbon component of the aerogel and is typical of carbon aerogels.

The same ion exchange process used to prepare metal-doped carbon aerogels was used to prepare ZrO_2-doped carbon aerogels, only employing $ZrOCl_2$ as the ion exchange salt. Based on results from the Fe-doped carbon aerogel system, carbon aerogels with an amorphous carbon structure laced with metallic Zr and/or ZrC nanoparticles were initially expected. But consistent with our observations of the irreducibility of zirconyl beyond oxygen-deficient zirconia during CNT growth, carbon aerogels laced with zirconia (ZrO_2) nanoparticles resulted instead. XRD of the ZrO_2-doped carbon aerogels (Figure 4.6) shows the presence of crystallites of zirconia in these materials. The diffraction pattern was phase matched to an oxygen-deficient phase of zirconia (with stoichiometry ranging from $ZrO_{1.688}$-$ZrO_{1.740}$)[106] superimposed over monoclinic Baddeleyite zirconia (with stoichiometry ZrO_2).[107] The broad peak widths observed indicate the mean zirconia crystallite size is in the nanometer range and, using the Scherrer equation, $d = 0.9\lambda/B\cos(\theta)$, to relate peak full-width at half-maximum values to crystallite size, an average crystallite size of ~7 nm is calculated.

Ex situ XPS analysis of the exterior and interior surfaces of ZrO_2-doped carbon aerogel monoliths (Figure 4.7) shows two pairs of spin-orbit-split peaks in the Zr 3d region for samples pyrolyzed at both 800°C and 1050°C, indicating the presence of two zirconia surface chemistries. In the sample pyrolyzed at 800°C, the Zr $3d_{5/2}$ peak at 183.4 eV correlates to the binding energy for ZrO_2,[90-93] whereas the Zr $3d_{5/2}$ peak with a binding energy of 182.3 eV falls at a slightly lower binding energy than stoichiometric ZrO_2 and is likely an oxygen-deficient chemistry, ZrO_{2-x}. The lower binding energy chemistry is the dominant surface chemistry at 800°C but gives way to a higher binding energy chemistry attributed to stoichiometric ZrO_2 at 1050°C, possibly due to annealing. The lower binding energy chemistry also shifts down to 181.9 eV at 1050°C, suggesting further oxygen deficiency. This is possibly due to migration of oxygen to form stoichiometric ZrO_2. Zr metal (binding energy 178.6-179.6 eV)[92,93,96] and ZrC (binding energy 178-179 eV)[95] were not observed after 100 sweeps. The O 1s region shows the presence of several chemistries of oxygen, including two at 530 eV and at 531 eV, which are consistent with the binding energies of oxygen in ZrO_2,[91] and one at 532.8-532.9 eV, which is also seen in undoped carbon aerogels and is attributed to oxygenated surface carbon on the aerogel framework. The presence of two non-carbon aerogel oxygen chemistries and two zirconia chemistries supports the XRD pattern phase matches indicating the presence of two phases of zirconia, although there is likely a blend of substoichiometric surface oxides present in these samples. Furthermore, the low binding energy zirconia chemistries observed is consistent with the observation of an oxygen-deficient phase by XRD. The C 1s region for both ZrO_2-doped carbon aerogels and undoped carbon aerogels is essentially identical, and no peak attributable to ZrC in either the C 1s region (C 1s 282 eV) or Zr 3d region (179-181.1 eV) is observed.[94,95]

Observations regarding the surface and crystallographic composition of zirconia drawn from XRD and *ex situ* XPS of ZrO_2-doped carbon aerogels indicate that nanoparticulate ZrO_2 is not carbothermically reduced at temperatures up to 1050°C, corroborating our observations from *in situ* XPS during CVD growth of CNTs. Furthermore, it is unlikely that these oxide nanoparticles result from, for example, Zr or ZrC formed during pyrolysis that are then oxidized upon exposure to air. Other metal-doped carbon aerogels we have prepared (Cu,[108] Fe,[83] Ta,[60] Re,[60] and W[60] for example) all exhibit both metallic crystallites in their XRD patterns and detectable metallic surface chemistries in their XPS spectra long after exposure to air (months) in addition to oxide surface chemistries resulting from air exposure. Zr is less susceptible to oxidation than some of these metals, especially Fe, and so if reduced Zr was formed during pyrolysis, it

would be detectable by either or both XRD and *ex situ* XPS after exposure to air.[109,110]

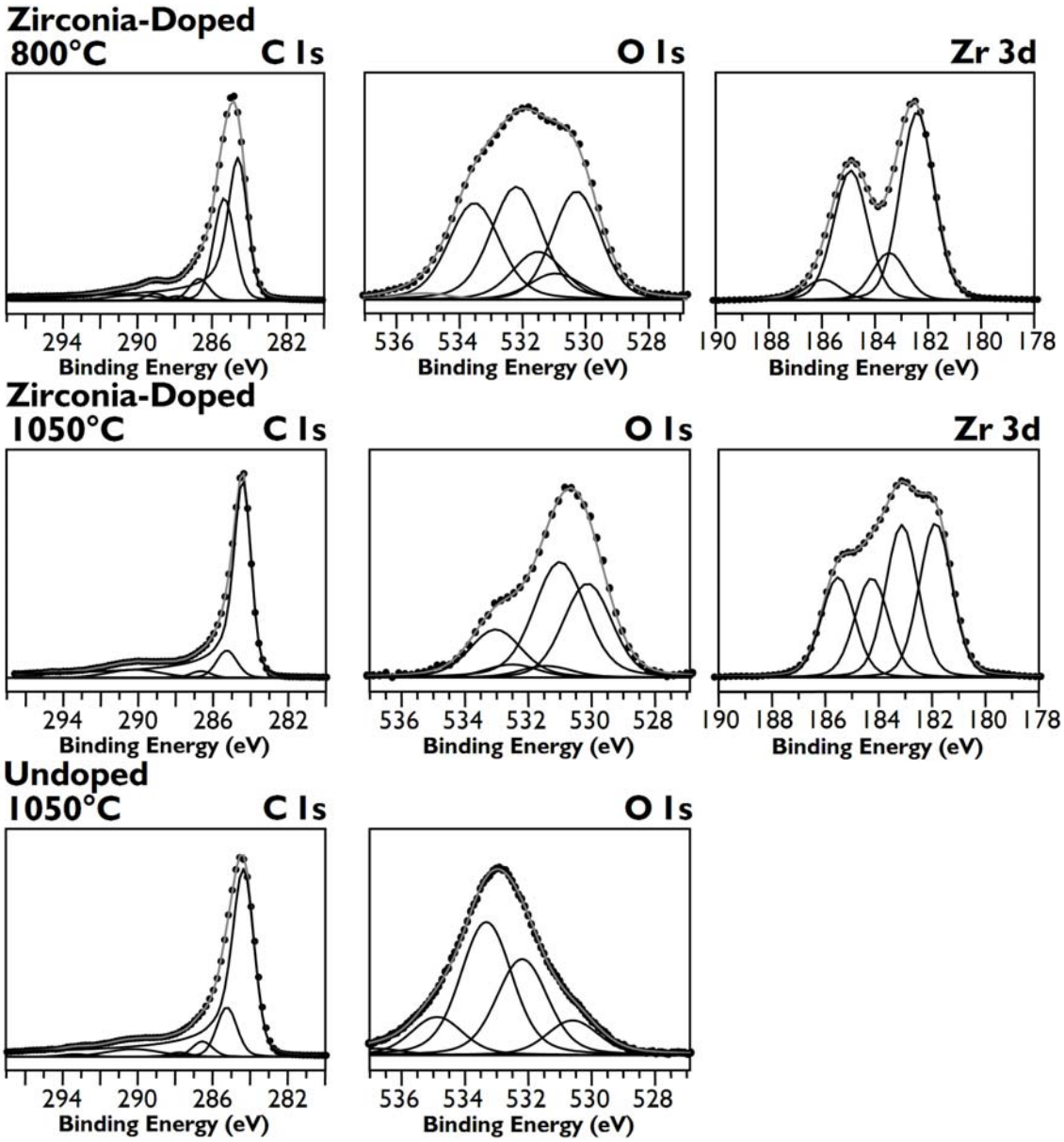

Figure 4.7 Representative XPS spectra of ZrO_2-doped carbon aerogels pyrolyzed at 800°C (*top row*) and 1050°C (*middle row*) and of undoped carbon aerogels pyrolyzed at 1050°C (*bottom row*). Two chemistries of Zr are detected in both samples pyrolyzed at 800°C and at 1050°C, both exhibiting binding energies expected for zirconia. No signals attributable to Zr or ZrC (Zr $3d_{5/2}$ binding energies of 178-180 eV) could be found. Vertical axis is signal intensity in arbitrary units.

Investigation of ZrO_2-doped carbon aerogels under TEM (Figure 4.8) revealed the presence of fullerenic cage structures encapsulating ZrO_2 nanoparticles. These types of structures are not observed in undoped carbon

aerogels. Although graphitic nanoribbons have been reported in carbon aerogels doped with Ni and Co, these metals are solvents for carbon and are also known to act as low-temperature graphitizing catalysts. ZrO_2, however, has not been reported to act as graphitizing catalyst at 800°C. Raman spectroscopy of ZrO_2-doped carbon aerogels at an excitation wavelength of 514 nm shows a broad D-band and broad G-band similar to that of undoped carbon aerogels. This suggests that the fullerenic structures in the aerogel are not representative of the entire aerogel framework but rather are localized around ZrO_2 nanoparticles in the aerogel, which only comprise ~2.9 at. % of the aerogel structure as determined by *ex situ* XPS. The average zirconia particle diameter of 7 nm calculated from the Scherrer equation is in reasonable agreement with the size of fullerenic cage structures observed by TEM (~5 nm), which encapsulate smaller zirconia nanoparticles. These observations support the conclusion that zirconia can graphitize amorphous carbon.

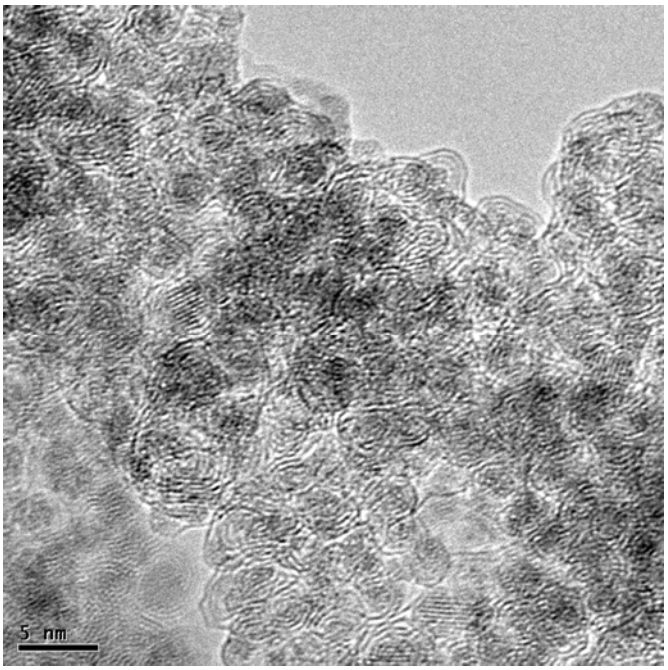

Figure 4.8 Fullerenic cage structures encasing zirconia nanoparticles in ZrO_2-doped carbon aerogel pyrolyzed at 800°C. Such structures are not observed in undoped carbon aerogels.

ZrO_2-doped carbon aerogels were then assessed for activity towards catalyzing CNT growth via thermal CVD using ethylene feedstock at 700-750°C. Tangled bundles of CNTs were observed covering the exterior surfaces of the ZrO_2-doped carbon aerogel monolith (Figure 4.9). TEM of CVD-processed ZrO_2-doped carbon aerogels verified the observed structures are in fact MWNTs (Figure 4.9, bottom). The MWNTs are found extending

from zirconia nanoparticles in the carbon aerogel skeleton under TEM. No CNTs were observed on undoped carbon aerogels after processing with the same CVD growth conditions. These observations again suggest that the zirconia particles are serving as the CNT growth catalyst. XPS analysis of ZrO_2-doped carbon aerogels post-CVD revealed no detectable change in zirconia surface chemistry due to CNT growth, again consistent with the expectation that zirconia would not be reduced by hydrogen or carbon at the CNT growth temperatures. *In situ* XPS analysis of zirconia-doped carbon aerogels during CVD growth conditions further verified the absence of any metallic zirconium or zirconium carbide. Thus it is concluded that the zirconia nanoparticles in the carbon aerogel are not reduced by the CVD growth process or from carbothermic reduction by the surrounding amorphous carbon, and serve as CNT catalysts in an oxide state. CNT yield on ZrO_2-doped carbon aerogels pyrolyzed at 1050°C was noticeably lower than aerogels pyrolyzed at 800°C. This finding suggests that the oxygen-deficient zirconia which is more prevalent in aerogels pyrolyzed at 800°C is preferable for enabling CNT growth.

Following the growth of CNTs from ZrO_2-doped carbon aerogels, CVD growth using zirconia on another carbon substrate, carbon fibers, was undertaken. Fiber tows were dip-coated with saturated $ZrOCl_2$ in 2-propanol solution, heated under H_2 to the growth temperature, and processed using CVD with ethylene as the feedstock gas as was done for the ZrO_2-doped carbon aerogels. Growth of CNTs is observed on the fibers following CVD, however with non-uniform coverage. This proof-of-concept demonstrates the possibility of using ZrO_2 as a catalyst for substrates such as carbon which react with metals at CNT growth temperatures.

As done in parts of this study, a metal oxide support of a difficult-to-reduce oxide such as Al_2O_3, SiO_2, and occasionally MgO, TiO_2, or even ZrO_2 is often used in conjunction with a (typically metal) catalyst for CVD growth of CNTs. Common examples are Fe or Co/Mo on Al_2O_3.[111-114] As highlighted earlier, while this is sometimes done to protect vulnerable substrates from unfavorable interaction with the catalyst, it is more commonly done to increase the percentage of suitably-sized catalyst particles that result in CNT formation. In addition to providing a textured surface for limiting the rate of catalyst coarsening,[28] many believe the metal oxide somehow enhances (or "promotes") the actual activity of the catalyst. Interestingly, oxygen-deficient (non-stoichiometric) alumina (AlO_x as opposed to Al_2O_3), has been shown to be the preferred phase for enhancing catalytic activity in the case of CNT growth in water-assisted growth from alumina-supported Fe.[115] Mattevi *et al.*, however, show that neither alumina nor oxygen-deficient alumina films dissociate acetylene directly,

which indicates that any enhancement in catalytic activity resulting from such oxide supports must arise from interactions with the catalyst directly.[28] Also notably, the effectiveness of oxides as heterogeneous catalysts (for example in hydrocarbon reforming) is known to be closely related to the electronic and defect properties of the oxide.[116-118] Electron transfer between catalyst and reactant(s) depends heavily on the ability of the catalyst to accept or donate excess electrons or positive charges, which dangling bonds on defective oxides can help facilitate.[117,119] Zirconia is used as a catalyst in the decomposition of nitrous oxide[120] and in the synthesis of dimethyl carbonate from methanol and carbon dioxide[121] in which Zr^{3+} and Zr^{4+} cations in the zirconia particle lattice facilitate catalysis by serving as sites for molecular absorption and allowing for temporary bonding configurations with incoming substrate molecules. Interestingly, chemisorption of various intermediate gas-phase species (i.e., oxygen and carbene) is known to occur more readily on n-type oxides.[117] As observed with the presence of oxygen-deficient zirconia by both XPS and XRD in catalysts used in this work, it is interesting to consider that defect properties may play a role in the catalytic activity of nanoparticulate zirconia. The H_2 pre-treatment in this work, while shown not to result in metallic Zr, may play a role in introducing surface defect sites onto zirconia nanoparticles that aid in enhancing catalytic activity. Additionally, as observed through *in situ* XPS, CNT growth seems to begin only upon introduction of both hydrocarbon and hydrogen, which might be due to introduction of defects by transient, localized extraction of oxygen by hydrogen. Presence of high-surface energy features (such as nanoparticles) and deposition technique are also potential variables which may affect defects. Understanding the role of defect properties of zirconia as a graphitizing catalyst and CNT growth catalyst may provide insights into the function of difficult-to-reduce oxides in their roles as catalyst supports for CNT growth.

The high melting point of bulk ZrO_2 makes it unlikely that nanoscale ZrO_2 exists in a molten state at the CVD growth temperatures used here, even after factoring in particle size effects. Additionally, given the low diffusivity of C in bulk ZrO_2, the successful growth of CNTs and graphitic nanoshells by ZrO_2 demonstrated here is suggestive of CNT growth by a surface-borne mechanism. It is hypothesized that like Fe, zirconia may catalyze reactions of organic molecules on its surface that aid in the assembly of the nanotube/nanoshell structure, however zirconia may involve different intermediates and bonding configurations than Fe and other metals. Further studies are underway to test this hypothesis.

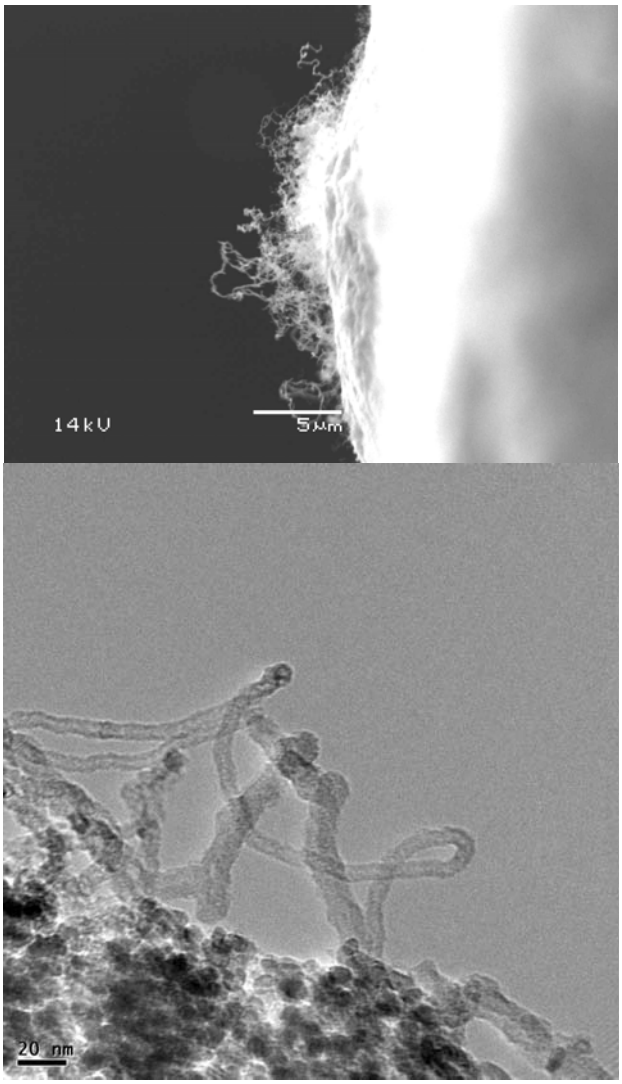

Figure 4.9 (*Top*) SEM image of multi-wall carbon nanotubes protruding from the surface of a ZrO_2-doped carbon aerogel following CVD. (*Bottom*) TEM images of MWNTs emerging from zirconia nanoparticles embedded in ZrO_2-doped carbon aerogel (mass of circular particles in lower left region); scale bar is 20 nm.

4.4. Conclusions and Next Steps

It is concluded that the oxide zirconia is a catalyst for thermal CVD growth of CNTs and can catalyze both SWNT and MWNT growth, in some cases with enough activity to create forest morphologies of CNTs. It is also concluded that nanoparticulate zirconia can catalyze transformation of amorphous carbon into a graphitic form. As seen from *in situ* XPS analysis of CNT growth from zirconia, zirconia appears to be the active CNT catalyst species and does not reduce to metallic zirconium or zirconium carbide under

the CVD growth conditions. These discoveries provide valuable perspective on the nature of CNT growth catalysts, as it appears conclusively, for the first time, that an oxide which is not reducible under CNT growth conditions can catalyze CNT growth. It is hypothesized that oxygen-deficient zirconium suboxide may be more active than stoichiometric zirconia. It is noted that ZrO_2, like Al_2O_3, SiO_2, and TiO_2, is also sometimes used as a catalyst support in heterogeneous catalysis of hydrocarbons, and hypothesize that its function in these applications may be related to the catalytic activity observed here. Furthermore, zirconia offers unique potential as a useful catalyst for substrates that are susceptible to damage by metallic CNT growth catalysts, for example, carbon substrates like carbon fibers used in composites.

It is interesting to consider fuel cells that employ yttria-stabilized zirconia (YSZ) as a solid electrolyte for understanding more about the behavior of zirconia as a catalyst. In these fuel cells, the triple-phase boundary of cathode metal, metal oxide, and hydrocarbon—not just the metal-hydrocarbon interface—serves as the catalytic center of activity for the extraction of electrons and concomitant transformation of hydrocarbons into carbon dioxide.[122] Such interfaces are also susceptible to poisoning by coking-over, which may be related to the catalytic propensity of nanoparticulate zirconia described in this study.

Initial observations of CNT growth from hafnia (HfO_2), tantala (Ta_2O_5), ceria (CeO_2), and titania (TiO_2) have also been made and efforts are underway to understand the catalytic propensity of these and other metal oxides as well.

It is important to note, however, that CNT growth with zirconia is not like growth with Fe or other metal catalysts; growth with zirconia is generally present in much lower yield and with much less uniform coverage. The necessary parameters for obtaining reliable CNT growth with zirconia are not immediately obvious based on this study. Additionally, it is not even certain that zirconia is serving as a catalyst in the chemical sense, but possibly enables CNT growth by other means. In the following chapter, efforts to better understand CNT growth from zirconia and its substantially lower activity in comparison to legacy CNT catalysts are presented.

Chapter 5

Understanding Carbon Nanotube Growth from Zirconia

In Chapter 4, nanoparticulate zirconia was identified as a non-metallic substance capable of both transforming amorphous carbon into graphitic nanoshells at elevated temperatures and facilitating growth of CNTs by thermal CVD. Using *in situ* XPS metrology during CVD growth of CNTs with zirconia, it was observed that zirconia remains in an oxidized state during the CNT growth process and in fact does not reduce to a metal nor a carbide. This demonstrated unambiguously that a stable metal oxide can in fact be used in place of legacy metallic CNT catalysts, with numerous potential advantages in doing so, such as broad substrate compatibility and new vectors of flexibility for engineering applications.

All of this suggests zirconia has great promise in applications involving CNT growth. Unfortunately, however, the yield of CNTs resulting from zirconia nanoparticles can be low (i.e., not comparable to nanoparticulate iron or similarly-active CNT catalysts). Zirconia nanoparticles can be distributed over a substrate and their presence verified by XPS, yet only a few tubes per 100 μm^2 may result and with somewhat unpredictable uniformity over the substrate surface. Still, Si substrates coated with zirconia nanoparticles exhibit a significantly greater number of CNTs than control substrates. Additionally, the *in situ* XPS analysis did not reveal the presence of any material other than zirconia and the underlying support during CNT growth. And *ex post* point-localized EDAX characterizations under TEM show zirconia nanoparticles attached to CNTs after CVD. So this begs the question, *why do some zirconia nanoparticles result in CNT growth, and others do not?*

Zirconia, as an oxide, is chemically different from metallic catalysts in several ways. First, it has an extremely high melting point and so even

factoring in size effects, nanoparticulate zirconia may be more solid-like than metal nanoparticles at similar conditions (although a molten state cannot be discounted at CVD temperatures >700°C for particles smaller than 4 nm).[123,124] Bulk diffusion of carbon through an oxide differs from metals, and surface diffusion is likely different as well. The catalytic propensity of zirconia is also different from metals such as Fe, Co, and Ni, in that while zirconia is used as a heterogeneous catalyst in some high-temperature organic reactions,[121] it does not decompose hydrocarbons into carbon or coke-over the way the aforementioned metals do.

Furthermore, it is not certain that nanoparticulate zirconia could be properly considered a "catalyst" (namely, an agent that lowers the activation energy of a reaction) since the mechanisms of CNT growth from zirconia have not been fully characterized. It could, for example, simply act as a high-surface-curvature/high-surface-energy textural support that enables incoming organic feedstock molecules to nucleate the start of a CNT by a spontaneous self-assembly process[65] which can then extend itself through a self-sustaining polymerization reaction (possibly between ethylene and alkynes[100]). In this hypothetical scenario, zirconia would not be reducing activation energy barriers in the traditional sense, or transforming something into something else, but rather serving merely as a template for CNT nucleation. As such, using the term catalyst to refer to zirconia in the context of facilitating CNT growth is, at this time, presumptuous and perhaps inaccurate. To more generally describe the role of zirconia in this process, we introduce a new term, "nanopositor", which simply means "a feature from which a nanostructure emerges" (adapted from the biological term "fibripositor", a nanostructured apparatus responsible for imparting order and alignment to collagen fibers during their excretion from a cell[125]). Additionally, the abbreviation ZrO_2 is replaced by the more general term "zirconia" as to avoid implying a stoichiometric oxygen balance in materials that may critically be substoichiometric (or possibly superstoichiometric) in this regard.

In effort to realize the potential of zirconia as a practical tool for CNT growth, a parametric study was undertaken, guided by the following hypotheses to explain its comparatively low activity:

- *Parametric shift in CVD process conditions.* The optimal process parameters for CVD growth of CNTs with zirconia differ from those used for legacy CNT catalysts since the chemical nature of zirconia differs from that of metals.
- *Reduced ability to catalyze surface reactions.* Where a metal-based catalyst may be able to accept a wide variety of organic molecules as input for

CNT growth because of its ability to catalytically decompose them on its surface, zirconia may lack this ability, thereby necessitating specially prepared "pre-digested" feedstocks. Both metals and zirconia then share the ability to assemble the CNT structure once the appropriate components are available.

- *Missing parameter.* Some undetected or unrecognized aspect of the CVD growth process that is not currently controlled or optimized enables or inhibits CNT growth with zirconia. Some conjectures regarding potential missing parameters might include excitation of nanoparticles by a specific frequency of electromagnetic radiation, the presence of defects or dopants in the nanoparticles, or the presence of a trace contaminant.

Based on these conjectures, a set of parameters of interest was identified and experiments to test the influence of these parameters on CVD growth of CNTs from zirconia were undertaken. In this chapter, these experiments and their results are described and interpreted to provide insights into the mechanism(s) underlying how zirconia works as a nanopositor in the CVD growth of CNTs. Informed by these results, preparation of effective zirconia-nanoparticle-based systems for CNT growth is discussed.

The work in this chapter was performed in substantial collaboration with Bernhard Bayer of the University of Cambridge and was performed at both MIT and Cambridge. The execution of the carbon aerogel work described at the end of this chapter was performed with the assistance of Akira Kudo of the MIT Department of Materials Science and Engineering.

5.1. Parameters of Interest for Optimizing CNT Growth With Zirconia

The initial parameters selected for this parametric study were a combination of variables typically efficacious in modulating CNT yield in CVD employing legacy CNT catalysts and the observations of oxygen deficiency and the presence of Ca^{2+} in zirconia nanoparticles attached to CNTs (see Section 4.3). The parameters selected for study are as follows:

- *Zirconia source.* Is there some undetected contamination in previously-used zirconia sources? Could engineered zirconia nanoparticles be used to attain more reliable, controllable results?
- *Nanoparticle size/monodispersity.* Are only nanoparticles within a specific size range active towards CNT growth, whereas $ZrOCl_2$ in IPA yields a wide, polydisperse distribution of particles?

- *CVD conditions.* Do chemical differences between zirconia and metal-based catalysts simply mean the optimal conditions for CVD growth of CNTs with zirconia (e.g., feedstock composition, temperature, pressure, time, etc.) are shifted relative to the conditions optimal for metal-based catalysts?
- *Concentration of nanoparticle solution.* Does too high of a concentration of zirconia nanoparticles result in sintering, thereby rendering them into larger particles incapable of facilitating CNT growth? Does too low of a concentration eliminate positive proximity effects from neighboring particles?
- *Method of dispersing nanoparticles onto a substrate.* Does the manner in which nanoparticles are introduced to a substrate cause them to agglomerate/distribute unevenly over the substrate, thereby concentrating CNT growth in specific areas?
- *Sonication.* Are the nanoparticles agglomerated together in solution in a way to result in agglomerates too large for CNT growth that could be broken up by sonication?
- *Dispersal solvent.* Do solvent-nanoparticle interactions affect the distribution/spacing of particles on the substrate? Does the solvent play an unexpected chemical role (e.g., by leaving carbon-containing organic residue on the surface)?
- *Underlying support.* Is there a promotional effect that arises from catalyst-support interactions?
- *Substrate roughness.* Does particle coarsening occur more readily on smooth substrates in a way that results in inactive zirconia deposits?
- *Presence and degree of oxygen deficiency.* Zirconia nanoparticles active towards CNT growth have been characterized as containing a substoichiometric amount of oxygen. Is oxygen-deficient zirconia more active towards CNT growth than stoichiometric zirconia (ZrO_2)? Could oxygen deficiency be controlled?
- *Presence of Ca^{2+}.* Ca^{2+} was detected in zirconia nanoparticles found attached to CNTs; is this merely a circumstantial impurity arising from the commercial production of $ZrOCl_2$ or an important contributor towards activating zirconia for CNT growth?
- *Reductive pretreatment.* Does a partial reduction of zirconia (perhaps to render it oxygen-deficient) help to activate zirconia nanoparticles?

- *Oxidative pretreatment.* Does oxygenation of zirconia enhance its activity? Are there residues that interfere with CNT growth that could be oxidized away before CVD growth with zirconia?

Methodologies for exploring these questions in a manageable way are described in the following section.

5.2. Methodology

In the methods detailed below, great care was taken to prevent contamination by metals, especially iron. Clean, dedicated plastic and glass tools and containers were used for all stages of processing. CNT growth processes were conducted with isolated, dedicated quartz process tubes not used for CVD processing for CNT growth with metal catalysts.

Work in this chapter primarily focused on monodisperse, 4-nm-diameter zirconia nanoparticles prepared by a high-temperature anhydrous sol-gel process,[126] although other zirconia sources were also surveyed.

5.2.1. Preparation of Zirconia Nanoparticle Catalysts

4-nm Zirconia Nanoparticles from High-Temperature Anhydrous Sol-Gel Process

Highly monodisperse zirconia nanoparticles ~4 nm in diameter were prepared through a high-temperature anhydrous sol-gel process according to the methods of Joo *et al.*[126] The nanoparticles used in the majority of this work were graciously prepared and supplied by Jaewon Moon of Prof. Taeghwan Hyeon's group at Seoul National University (who developed this procedure). Briefly, 20 mmol (7.8 g) of zirconium(IV) isopropoxide propanol complex ($Zr(OC_3H_7)_4 \cdot C_3H_7OH$) and 25 mmol (5.83 g) of zirconium(IV) chloride are added to 100 g of purified and degassed trioctylphosphine oxide (TOPO) at 60°C in an argon atmosphere. The temperature of the reaction mixture is then raised slowly to 340°C and held at this temperature for 2 h with vigorous stirring. The reaction mixture was then cooled to 60°C and 500 mL of dry, degassed acetone is added to precipitate zirconia nanoparticles. The precipitate is retrieved by centrifugation and washed several times with acetone to remove excess TOPO, resulting in gray-colored zirconia nanoparticles with a diameter of ~4 nm (see Figure 5.1). It is critical that during this reaction no metal objects such as a thermocouple are placed in contact with the reaction medium as the medium is highly corrosive and will leach metal elements such as Ni into the nascent nanoparticles, as found by the author of this work.

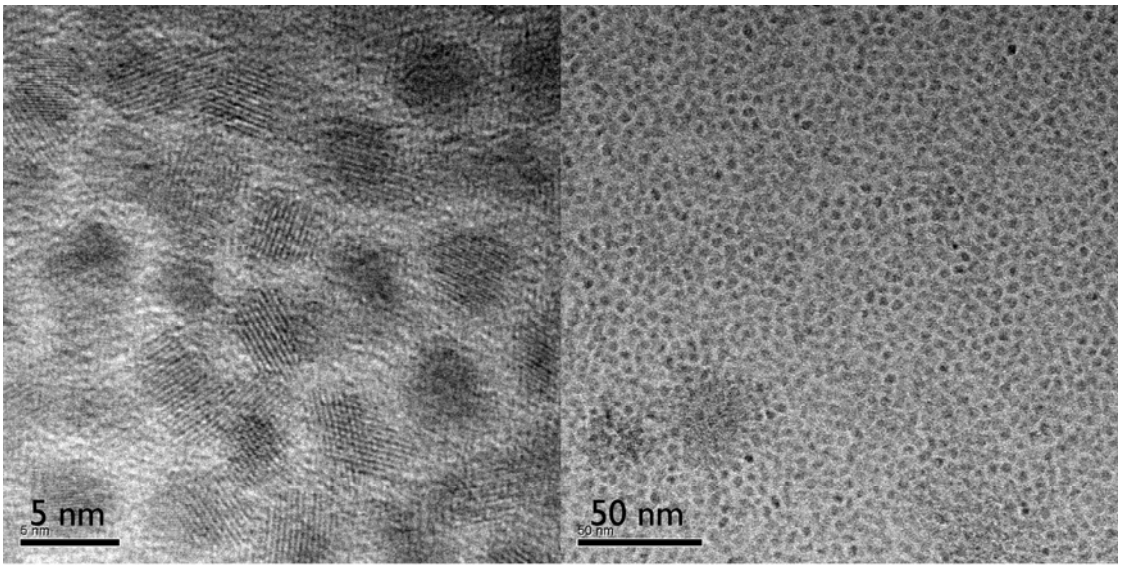

Figure 5.1 TEM images of 4-nm zirconia nanoparticles used throughout this study (nanoparticles and images courtesy Jaewon Moon, Hyeon Group, Seoul National University).

Zirconia Nanoparticles from Saturated Zirconium Oxychloride in IPA

Saturated solutions $ZrOCl_2 \cdot 8H_2O$ in 2-propanol (IPA) were prepared by adding 322 mg $ZrOCl_2 \cdot 8H_2O$ to 15.72 g (20.00 mL) 2-propanol, sonicating for ~5 min, and optionally aging for 4-5 d to facilitate further formation of nanoparticles. The supernatant from these solutions was then used for dip-coating or drop-casting zirconia nanoparticles onto Si wafers.

Micelle-Templated Zirconia Nanoparticles Using Poly(styrene)-poly(4-vinylpyridine)

Zirconia nanoparticles were prepared using a micelle-templating technique employing the amphiphilic block co-polymer poly(styrene)-poly(4-vinylpyridine) (PS-P4VP) developed by Bhavirpudi *et al.*[127] In this method, 1 g PS-P4VP (Polymer Source Inc., product number P9124-S4VP, 20-b-17.0, M_w/M_n = 1.08) was digested in 250 mL toluene at 70°C for 4-5 h with stirring. Next, a 25 mL aliquot of this was removed and used to prepare a sample solution. To this aliquot was added 0.25 mmol (120 mg) or 0.025 mmol (12 mg) of zirconium(IV) acetylacetonate ($Zr(acac)_4$, Sigma-Aldrich product number 338001, 98%). This solution was then stirred for ~12 h. $Zr(acac)_4$/PS-P4VP nanoclusters were then deposited on a substrate by drop-casting or spin-coating (1250 rpm, 1 drop, 1 min). Finally, the coated substrates were either baked in air at 550°C for 30 min or processed with an O_2 plasma for 5 min to remove the polymer shell from the nanoclusters and oxidize the metal centers to oxide nanoparticles.

Solutions of Zirconium Acetylacetonate in IPA

Solutions of zirconium(IV) acetylacetonate ($Zr(acac)_4$, Sigma-Aldrich product number 338001, 98%) in two concentrations were prepared. The first solution was prepared by adding 24 mg of $Zr(acac)_4$ into to 15.72 g (20.0 mL) 2-propanol to yield a solution with a concentration of 1.2 mg mL^{-1}. The second solution was prepared by three successive dilutions with IPA using 0.789 g (1.00 mL) aliquots of solution per dilution. This resulted in a second solution with a concentration of 0.0012 mg $Zr(acac)_4$ mL^{-1}.

Solutions of 4-nm Zirconia Nanoparticles in IPA

Zirconia nanoparticles needed to be dispersed in a solvent in order to reliably deposit onto a substrate. The mass of a 4-nm zirconia nanoparticle was estimated to be ~$2.5x10^{-19}$ g. Targeting an ideal dispersion of ~1 nm per 10 nm x 10 nm square area on a substrate, a concentration of 70 μg/20 mL vial of solvent was estimated. However, this low of a concentration did not produce good CNT growth results and was inconvenient to prepare, and so a concentration of 10 mg/20 mL vial or 0.5 mg mL^{-1} concentration was selected as a standard concentration for preparation. Successive dilutions could be made from this concentration if necessary.

The 4-nm zirconia nanoparticles used in the study are stored as a gray, clumpy solid. Using the tip of a Pasteur pipette, a clump of solid nanoparticles was carefully introduced into a polypropylene weigh boat placed on a high-precision balance. Once ~10 mg was weighed, the clump was added to a vial of 15.72 g (20.0 mL) 2-propanol and swirled until the clump had dissolved. Finally, the solution was sonicated for 3 min in an ultrasonic bath.

5.2.2. Preparation of Substrates

Preparation of Wafers

Wafer substrates used were Si wafers with 200 nm thermal oxide support or 200 nm thermal oxide with 10 nm Al_2O_3 support (deposited by e-beam evaporation on top of the wafer). Wafers were cleaved into ~5 mm x ~5 mm samples by conservatively using a diamond scribe in a way as to minimize the prospect of introducing metal contamination onto the samples. Prior to use, the diamond scribe was sonicated under 2-propanol for 3 min and then wiped dry with a new fab wipe. Wafer samples were then sonicated under 2-propanol for 3 min, rinsed with 2-propanol, and then dried with a nitrogen blowgun.

Preparation of Undoped Carbon Aerogels

Undoped carbon aerogels were used as high-surface-area amorphous carbon supports for zirconia nanoparticles and zirconia nanoparticle precursors. Carbon aerogels were prepared using an acid-catalyzed resorcinol-formaldehyde (RF) polymerization according to the methods of Mulik *et al.*[128] First, a solution of 0.337 g (3.06 mmol) resorcinol, 6.29 g (0.447 mmol) 37 wt% aqueous formaldehyde, and 11.5 mL of acetonitrile was prepared. To this was added a solution of 0.636 mL acetonitrile and 0.03 mL (0.363 mmol) 12.1 N HCl. This procedure can be scaled to prepare larger samples or many samples. The mixture was poured into 29-mm x 10 mm poly(tetrafluoroethylene) molds and allowed to gel overnight in a sealed container with an ~1-cm layer of acetonitrile in the bottom to produce an acetonitrile-rich atmosphere. Next, the pore liquor in the gels was exchanged with pure acetonitrile (1 exchange/d, 3 exchanges total, 10x volume/exchange) followed by liquid CO_2. The gels were then supercritically dried from CO_2 (T_c = 31.1°C, P_c = 72.9 atm, T_{max} = 50°C, P_{max} = 100 atm) to afford resorcinol-formaldehyde polymer aerogels. Finally, the aerogels were pyrolyzed under a flow of 200 sccm Ar at 800°C for 10.5 h, affording carbon aerogels with both meso- and macroporous character (primarily containing pores ranging from 2-25 nm with larger micron-sized pores throughout).

Drop-Casting

Zirconia nanoparticle solutions were frequently drop-cast onto substrates. In this technique, a single drop of nanoparticle solution was placed onto a substrate with a Pasteur pipette. Clamping the wafer with a pair of plastic (not metal) tweezers, the sample could then be dried with a nitrogen gun or alternatively the sample could be allowed to dry in air, in which case a glass dish was placed over the sample as to avoid accumulation of air-borne dust and debris on the substrate.

5.2.3. Equipment and Processes for CVD Growth of CNTs

Several CVD processes were used over the course of this study, and in some cases CVD process was a variable of focus. For ease of discussion, the CVD processes used are assigned process names used throughout this chapter. Table 5.1 summarizes the CVD processes used and assigns them process names.

Process Name	Equipment	Press-ure	Flush/ Pump	Ramp	Soak	Growth	Cool Down
1″-C_2H_4-#	1″ CVD Furnace, MIT	Atm.	100 sccm He or Ar, 2 min	400 sccm H_2, 100 sccm He or Ar to 750°C or #°C	0-10 min	15 min, 100 sccm C_2H_4, 400 sccm H_2, 100 sccm He or Ar	200 sccm He or Ar to room temp
2″-C_2H_4-#(#)	2″ CVD Furnace, MIT	Atm.	400 sccm He, 2 min	1600 sccm H_2, 400 sccm He to 680°C (760°C) or #°C (#+80°C)	0-10 min	15 min, 400 sccm C_2H_4, 1600 sccm H_2, 400 sccm He	400 sccm He to room temp
C_2H_2-750	2″ CVD Furnace, Cambridge	Atm.	1000 sccm Ar, 3 min	1000 sccm Ar, 3 min to 750°C at 20°C min^{-1}, then 5 min 6000 sccm Ar	3 min, 200 sccm Ar, 500 sccm H_2	30 min, 10 sccm C_2H_2, 500 sccm H_2, 200 sccm Ar, then 5 min 6000 sccm Ar	400 sccm Ar to room temp
CH_4-900	2″ CVD Furnace, Cambridge	Atm.	1000 sccm Ar, 3 min	1000 sccm Ar to 900°C at 20°C min^{-1}	10 min, 200 sccm H_2	15 min, 100 sccm H_2, 500 sccm CH_4, then 5 min 4000 sccm Ar	400 sccm Ar to room temp
LP-C_2H_2	LP-CVD System, Cambridge	3-5x10^{-1} mbar	3x10^{-6} mbar	4.5x10^{-1} mbar H_2 to 800°C (635°C)	10 min	30 min, 0.5 x10^{-1} mbar C_2H_2, 4.5x10^{-1} mbar H_2	Gases off to room temp
LP-C_2H_2-NH_3	LP-CVD System, Cambridge	3-6x10^{-1} mbar	1x10^{-6} mbar	5.5x10^{-1} mbar NH_3 to 800°C (650°C)	10 min	30 min, 0.5 x10^{-1} mbar C_2H_2, 5.5x10^{-1} mbar H_2	Gases off to room temp

= Set point temperature, (#) = actual process temperature.

Table 5.1 CVD process names and associated CVD conditions used in the work presented in this chapter.

5.2.4. Characterization

Samples in this study were primarily analyzed by scanning electron microscopy (SEM) and *ex situ* X-ray photoelectron spectroscopy (XPS). SEM was performed with a JEOL 6700 microscope and an FEI Philips XL30 sFEG microscope operating at 5 kV or 2 kV. *Ex situ* XPS spectra were obtained on an AXIS Ultra DLD Spectrometer (Kratos Analytical Ltd, UK) using Al K-alpha radiation (energy = 1486.6 eV) in a chamber with a base pressure of 5 × 10^{-9} torr. Sample substrates were directly mounted on the sample holder with carbon tape. All measurements were performed using an X-ray power of 150

W (15 kV and 10 mA), a pass energy of 10 eV, and an analysis area of 750 μm × 350 μm. A charge neutralizer was not used. Charge correction was generally not performed as little to no charging effect was observed, but calibrated to a C peak of 285.0 eV when necessary.

5.2.5. Assessing Results and Promise

The primary metric of interest for assessing samples was the presence of CNTs that appear unlikely to have grown from a non-zirconia nanopositor. This was assessed by differential comparison with control samples (with no zirconia) processed under the same conditions as the variable sample. SEM served as the primary method for assessing the presence of CNTs on samples. Control samples typically exhibited some CNT growth, usually on the order 0-10 findable bundles containing less than about 10 CNTs each over the surface of a 5 mm x 5 mm chip, as well as occasional bundles of CNTs on cleaved wafer surfaces (see Figure 5.2). These types of bundles are attributed primarily to dust/debris from the atmosphere, vials, or in some cases (particularly on edges) possibly catalytically-active silica. A variable sample was deemed unpromising if its CNT growth was comparable to the control (see the Assessment Protocol below). Notably, the majority of samples surveyed exhibited little or no CNT growth, however the samples that did exhibit CNT growth, while not comparable to Fe-based catalysts for example, were distinguishable from controls repeatably.

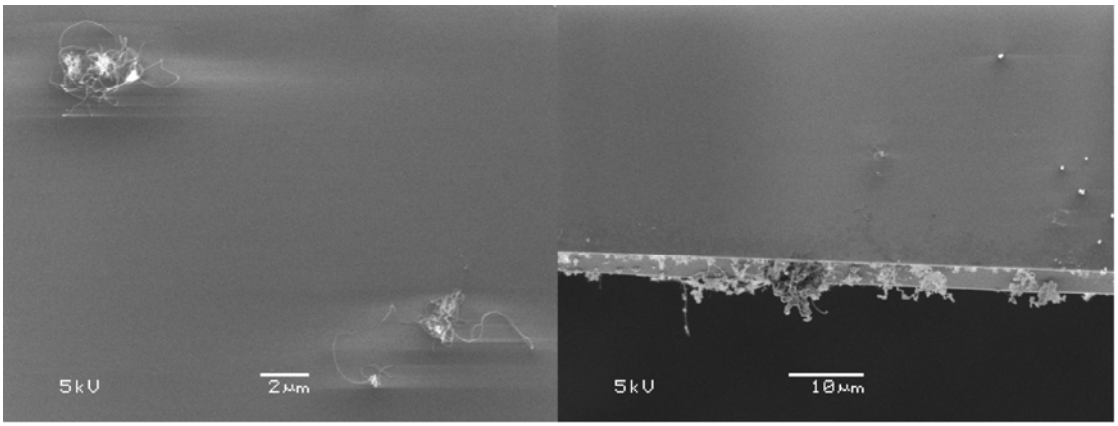

Figure 5.2 CNT growth typically found on control wafers upon which no catalyst or nanopositor nanoparticles have been intentionally added: *(left image)* typical "debris bundles" found away from edges; *(right image)* thin- and thick-CNT bundles found at the cleaved edges of the wafer, possibly arising from nanoparticulate silica.

Second, the approximate yield of CNTs, i.e., the quantity of CNTs spread over the area of a wafer, was used to assess if the parameters surveyed with

that sample were promising and merited further study or iteration. Because few samples exhibited uniformly-distributed CNT growth across the wafer, samples with bush-like growth or other features characteristic of CNTs grown from catalysts know to be highly active on oxide supports were analyzed in greater depth due to the possible presence of contamination. Lastly, the presence of other features such as debris, craters, films, nanostructures, and microparticles was noted.

Since the study involved preparing, processing, and analyzing nearly 200 samples, a rubric for assessing results and gauging promise for particular parametric vectors *en masse* had to be devised. This was complicated by the fact that the study required cataloging large arrays of null results and results that were only incrementally better than control samples. To accommodate these challenges, the following Assessment Protocol was used:

- SEM the sample.
  - Scan regions along the sample border within a range of 200 μm from the nearest edge.
  - Look for clusters of growth and study them.
  - Look for variations in texture and/or contrast and study them.
  - Check the center of the wafer.
- If the types of CNT structures and concentration of CNT bundles over the sample is comparable to the control sample, the sample is assigned a grade of "0". Images do not need to be recorded.
- If the number of CNT structures is higher than the control but the types of CNT structures are similar, the sample is assigned a grade of "0.5". Images do not need to be recorded.
- If the number of CNT structures is noticeably higher than the control and one or more regions containing a plurality of CNTs spread over an area of ~25 μm^2 or greater not originating from a single point of origin or observable particle is observed, the sample is assigned a grade of "1" or "1.5", depending on whether few or many such patches are found. Images of regions with growth and regions representative of most of the sample should be recorded. Fewer CNTs are expected from low-pressure, low-temperature, and CH_4 CVD processes but should still stand up against a differential comparison with a control. Further study is not merited, but parameter space around the parameters surveyed with the sample should be surveyed.
- If regions containing a plurality of short (<10 μm) CNTs spread over areas of ~100 μm^2 or greater not originating from a single point of

origin or observable particle are observed frequently over the entire sample, the sample is assigned a grade of "2". Images of regions with growth and regions representative of most of the sample should be recorded. Further characterization of the sample should be performed to verify the absence of contamination. If no contamination is detected, the process should be repeated and the associated parameter space iterated.

- If bush-like CNT bundles comprised of closely-spaced CNTs and/or long (>10 μm) CNTs are present regularly over the wafer, but the majority of the wafer is bare, the sample is assigned a grade of "3" and is handled like samples of grade "2".
- If CNT growth is present extensively and nearly uniformly over the entire surface of the wafer, the sample is assigned a grade of "4" and handled like samples of grade "2".
- If forest-like alignment is observed routinely over the wafer, the sample is assigned a grade of "5" and is handled like samples of grade "2".

5.3. Results of Parametric Study

In this section, the results of the parametric study are presented as a sequence of substudies that were undertaken to evaluate the various hypotheses outlined in Section 5.1. The section headings in this section represent the parameters of interest for that particular substudy.

5.3.1. Precursor Solution Concentration and Ethylene CVD Temperature

Initially, a solution of 10 mg of engineered 4-nm zirconia nanoparticles was dispersed in 20.0 mL (15.72 g) IPA and sonicated for 3 min. This formulation was chosen as a suitable starting point based on methods derived in the work described in Chapter 4 and relied on the smallest reliably measured quantity of the nanoparticle-containing solid that could be dispersed in a scintillation vial full of IPA. Samples were prepared by drop casting 1-2 drops of nanoparticle solution onto wafers coated with a 10-nm alumina support and drying the drops under a gentle stream of N_2 with a hand-operated blowgun. A CVD process employing ethylene at a process temperature of 750°C was used based on optimal process conditions also found during the course of work described in Chapter 4. To ascertain what the optimal concentration would be for dispersing zirconia onto wafer substrates and what the optimal CVD temperature for basing other studies on

would be, solutions of 4-nm zirconia in IPA of varying concentrations were prepared and surveyed against CVD processes at various temperatures (see Table 5.2).

System	CVD Process	CVD Temp. Set Point[a]	4-nm ZrO_2 in IPA 0.5 mg mL^{-1}	4-nm ZrO_2 in IPA 0.05 mg mL^{-1}	4-nm ZrO_2 in IPA 0.005 mg mL^{-1}	4-nm ZrO_2 in IPA 0.0005 mg mL^{-1}
1″ CVD System	1″-C_2H_4	720°C	0	0	0	0
		750°C	1	0.5	0	0
		780°C	1	0	0	0
2″ CVD System	2″-C_2H_4	680°C (760°C)	1	0	0	0
		730°C (810°C)	0	0	0	0

[a]Temperature set points in the 2″ CVD system underestimate the actual process temperature by approximately 80°C; adjusted values shown in parentheses.

Table 5.2 Parameter matrix for solution concentration versus CVD temperature with grades indicating the level of CNT growth observed for each set of conditions.

Despite initial calculations suggesting that a concentration of 0.5 mg mL^{-1} was several orders of magnitude higher than the concentration of nanoparticles used in solutions for dispersing legacy CNT catalysts, reducing the concentration of 4-nm zirconia in IPA below this level did not yield substantial CNT growth beyond control samples for any CVD condition surveyed. This said, samples processed at CVD temperatures between 750-780°C did routinely show enhanced CNT growth beyond the control (see Figure 5.3 and Figure 5.4). Under SEM at 5kV or 2kV and moderate brightness and contrast settings, samples typically presented a dual-contrasted film over the surface with gray-contrasted and dark-contrasted regions. Periodic white-contrasted small particles (nm-scale) could be found dotting the surface of the wafer as well. Patches of CNTs (as opposed to small, isolated bundles emerging from a single point of origin) were most commonly found in dark-contrasted regions of the surface, which tended to border wafer edges but were also found in the middle of wafers and were usually present as relatively wide (~200 μm) patches. These darker-contrasted areas were also often found as features of larger patterns where signs of solvent evaporation were evident. It is hypothesized these darker regions are artifacts created by evaporation of the dispersal solvent (in this substudy, IPA) since they seem to be found in areas where the solvent would be expected to evaporate last, namely, the border of the sample, isolated microdroplets, etc. It is further hypothesized that these regions have a

different particle density than the gray-contrasted regions or possibly contain carbonaceous or organic residue left by the solvent.

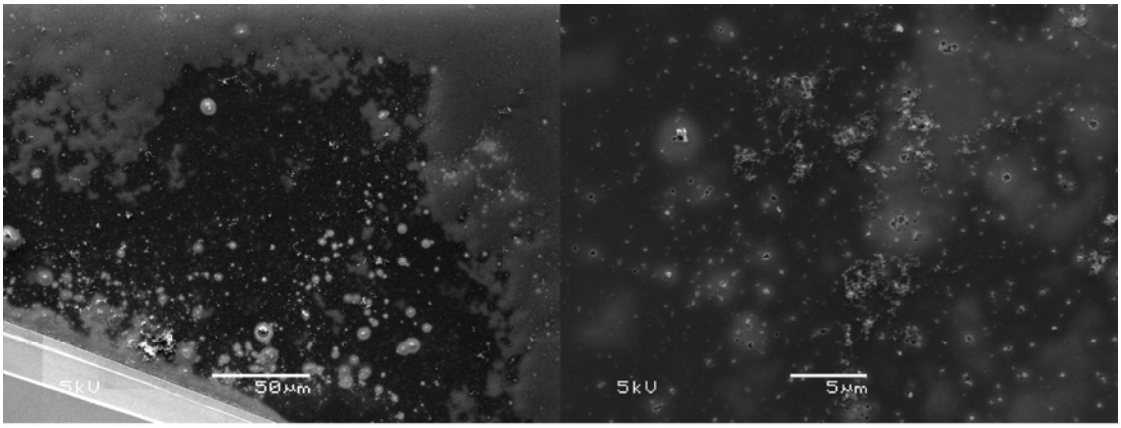

Figure 5.3 Examples of enhanced CNT growth beyond what is observed on control samples (grade 1) facilitated by 4-nm zirconia nanoparticles: *(left)* region containing growth; *(right)* detail of CNT growth within this region.

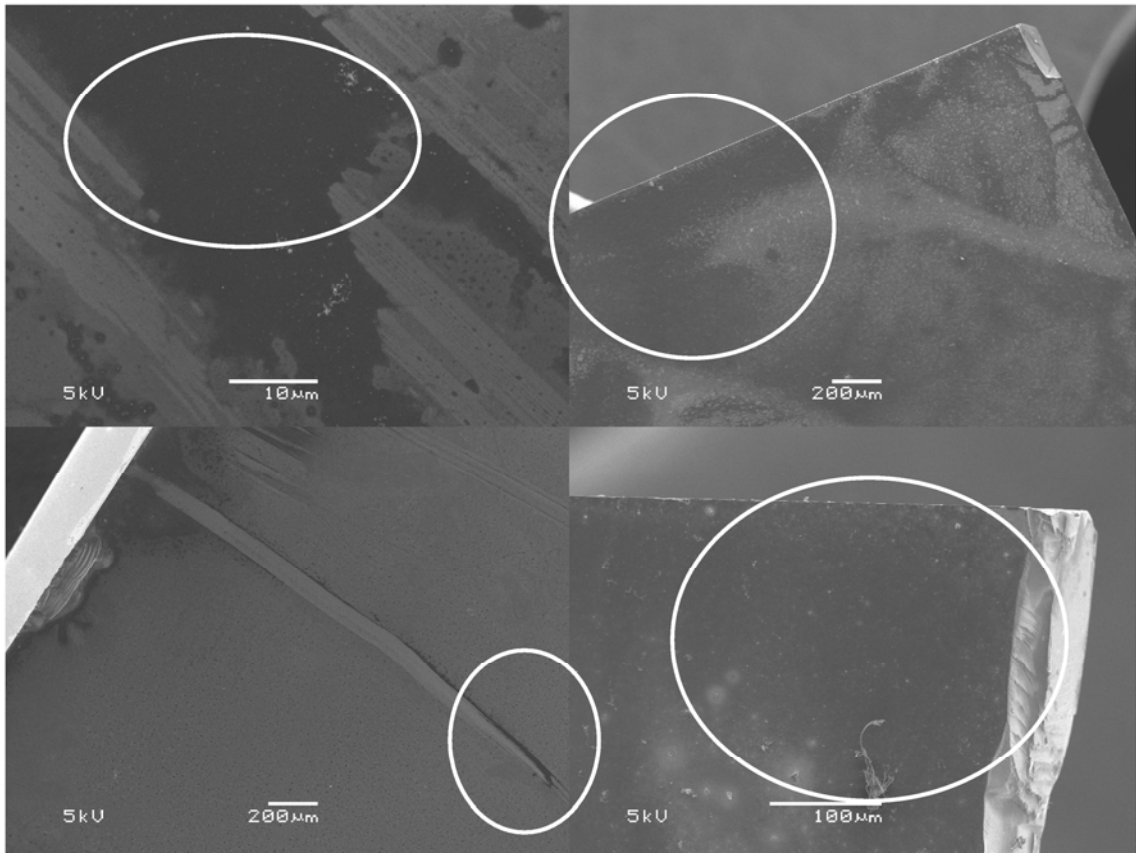

Figure 5.4 Regions on a wafer covered with 4-nm zirconia nanoparticles that exhibit CNT growth (marked with ellipses) following CVD processing with 2″-C_2H_4-680(760) with a grade of 1.

Samples prepared with 5 mg mL^{-1} concentration of nanoparticles in IPA (10x the highest concentration shown in Table 5.2) resulted in virtually no CNT growth anywhere on the wafer and instead only a thick, light-gray-contrasted film (assumedly sintered zirconia nanoparticles) over the wafer surface. The dark regions where CNT growth is typically observed were not present. This result suggests that below 0.05 mg mL^{-1} there are too few nanoparticles present for widespread CNT growth, or that the activity of the nanoparticles is so low that a large concentration is needed before CNT growth becomes noticeable. If too high of a concentration is used, sintering occurs, destroying the nanoparticulate nature of the zirconia. Thus, a concentration of 0.5 mg mL^{-1} and a CVD temperature of ~750°C employing ethylene (processes 1"-C_2H_4-750 and 2"-C_2H_4-680(760)) were found to be the conditions that resulted in the highest CNT yield, which notably was not high comparative to legacy CNT catalysts (see Figure 5.4). Additionally, thick films resulting from high concentration (5 mg mL^{-1}) solutions indicated that the zirconia nanoparticles will undergo sintering upon CVD processing, suggesting that deposition of a sparser array of nanoparticles may be required to achieve enhanced CNT yields.

5.3.2. Catalyst Solution Deposition Method and Precursor Solution Concentration

Following from the results presented in Section 5.3.1, questions arose surrounding the nature of the dark-contrasted regions where CNT growth on samples coated with 4-nm zirconia was typically found. Towards this, a series of experiments surrounding methods of depositing the zirconia solution onto wafers was undertaken.

In this substudy, solutions of 4-nm zirconia in IPA of varying concentrations were used as the zirconia source. The following deposition methods were surveyed: drop-casting followed by unassisted air drying, drop-casting followed by N_2 blowgun-assisted drying, dip-coating, spin-coating (5000 rpm, 60 s) with 1 drop from a Pasteur pipette, and spin-coating (5000 rpm, 60 s) with 20 drops from a Pasteur pipette. Drop-casting and dip-coating were evaluated against the following solution concentrations: 0.5 mg/mL, 0.05 mg/mL, 0.005 mg/mL, and 0.0005 mg/mL on both silica and alumina supports. Spin-coating was evaluated for 0.5 mg/mL concentrations only on both silica and alumina supports. Drop-cast and dip-coated samples were processed using CVD process 2"-C_2H_4-680(760) and spin-coated samples were processed using CVD processes C_2H_2-750, CH_4-900, and LP-C_2H_2.

Figure 5.5 shows SEM images from uncoated control samples and samples coated with 4-nm zirconia in IPA solution by different methods following

CVD processing with process 2"-C_2H_4. Both the dip-coated and drop-cast samples result in CNTs, however the drop-cast samples gave higher yields (grade of 1-1.5) than the dip-coated samples (grade of 0.5-1) regardless of CVD process or support. Controls did not exhibit CNT growth beyond the "background level" typically observed.

Figure 5.6 compares SEM images of samples prepared by drop-casting with samples prepared by spin-coating on both silica and alumina supports and grown with C_2H_2-750 and CH_4-900. Spin-coated samples presented an array of dark-contrasted spots ~100-300 nm in diameter separated by about 1 μm and containing a white-contrasted dot in the middle. Both samples spin-coated using 20 drops of solution and 1 drop of solution presented the same surface and similar spot-feature densities. Growth from spin-coated samples was consistently poor or non-existent (grades of 0) except when processed with CH_4-900 (grades of 1).

No substantial difference was observed between N_2-assisted drying and air-drying, although N_2-assisted drying seemed to provide incrementally more dark regions over samples and thus an incrementally higher yield of CNT growth. More interestingly, however, was the observation of Marangoni patterns[129,130] over samples that were dried with N_2 (see Figure 5.7 and Figure 5.8). Marangoni patterns arise as a droplet or film of liquid evaporates from a surface. As the film recedes, interfacial energies change and instabilities in the drying film arise. This results in the formation of various types of residue patterns on the substrate surface including rings and Marangoni fingers ("coffee-stain effect") upon evaporation of the film. In this case, the Marangoni features appeared as dark-contrasted regions under SEM and contained appreciable CNT growth. Various attempts at reproducing this result were made and in fact engineered Marangoni patterns were obtained, however the unusual high-yield growth in Marangoni fingers was not replicable. As mentioned, however, CNT growth on N_2-dried samples was still observed in dark-contrasted regions of which there were incrementally more than without N_2-assisted drying.

In summary, this substudy provided interesting clues regarding the nature of the dark-contrasted regions observed under SEM where CNT growth tends to be found (and that it is likely organic residue left over from evaporation of solvent), demonstrated that drop-casting was the most certain method for ensuring CNT growth for each CVD process, showed that spin-casting with more than 1 drop of solution is unnecessary, and suggested that CVD with spin-cast samples does not result in CNTs unless using process CH_4-900. However, drying method (and the density of particles distributed from it) is not a major factor contributing to the limited yield of CNTs observed with zirconia.

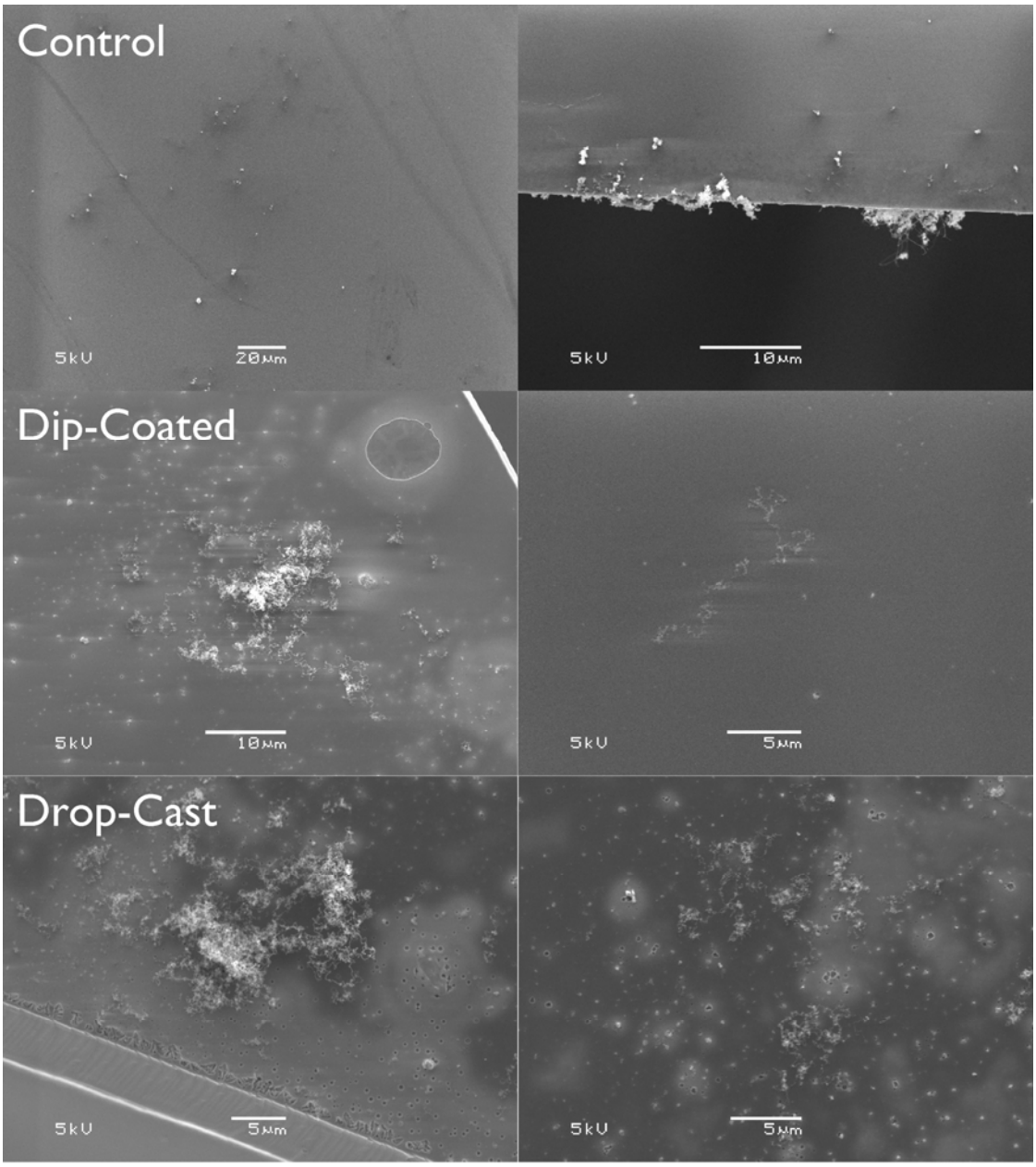

Figure 5.5 SEM images of control wafers *(top)* and wafers coated with 4-nm zirconia in IPA catalyst solutions deposited by dip-coating *(middle)* and drop-casting *(bottom)* following CVD process 2″-C_2H_4-680(760).

5.3.3. Age of Catalyst Solution and Sonication Prior to Use

One potential concern in using solutions of disperse nanostructures is that over time the particles may aggregate. In the case of CNT growth, aggregated particles can sinter into larger particles and become too large to facilitate growth. Sonicating is a way to help break up nanoparticle aggregates and is

often used both to prepare nanoparticle solutions and to prevent nanoparticles in them from aggregating over time.

In this substudy, the effects of nanoparticle solution age and sonication time immediately prior to deposition were surveyed. The zirconia sources were 4-nm zirconia dispersed in IPA in a concentration of 0.5 mg mL^{-1} and saturated $ZrOCl_2 \cdot 8H_2O$ in IPA. Si wafers with alumina support were used. Freshly-prepared solutions and solutions aged for 12 days, 5 days, 3 days were sonicated for 0 min, 3 min, and 18 min and deposited on the wafers. Samples were subsequently processed with CVD process 1"-C_2H_4 or 2"-C_2H_4.

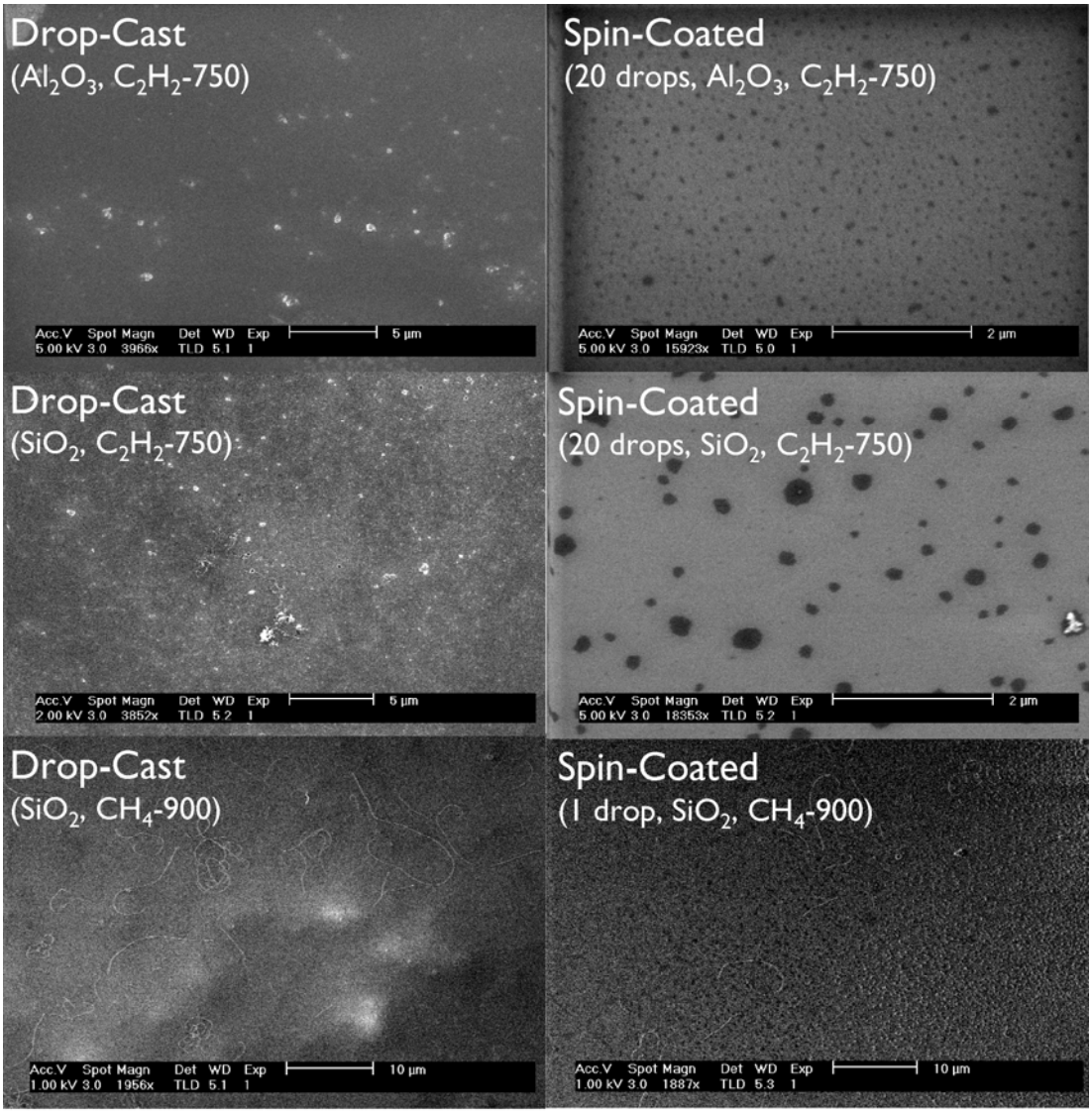

Figure 5.6 SEM images comparing influence of drop-casting versus spin-coating on alumina and silica supports for CVD processes C_2H_2-750 and CH_4-900; CNTs are visible on all drop-cast samples (more so on SiO_2 than Al_2O_3) and on spin-coated samples with SiO_2 supports processed with CH_4-900.

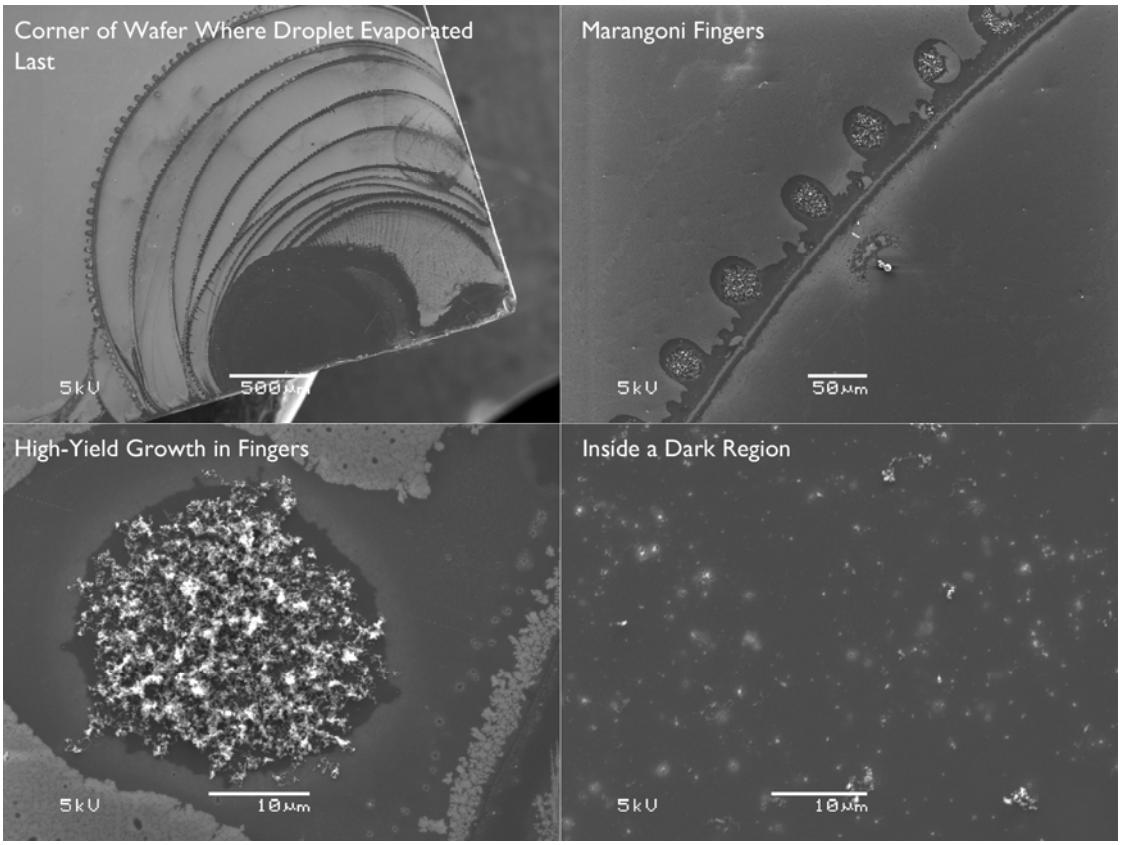

Figure 5.7 SEM of CNTs clusters grown within Marangoni fingers resulting from N_2-assisted drying of 4-nm zirconia dispersed in IPA drop-cast onto a Si wafer with alumina support and processed with 2″-C_2H_4-680(760); CNTs are present in dark-contrasted regions outside of the Marangoni pattern as well.

No substantial differences between aged and/or sonicated samples were observed for 4-nm zirconia particle solutions. The yield observed from oxychloride solutions tended to improve (from grades of 0.5-1 to 1-1.5) with solutions 5 days or older. It is hypothesized that this is because of the formation of nanoparticles through a sol-gel mechanism over the course of several days (from hydrolysis and subsequent polycondensation of $ZrOCl_2$).

5.3.4. Nanoparticle Dispersal Solvent

Concerns about nanoparticle agglomeration in solution and the potential role of solvent residues on a wafer surface raised the question of whether or not changing the dispersal solvent would result in a change in CNT yield. In this substudy, solutions of 4-nm zirconia were prepared with IPA (control), acetone (alternate polar organic), pentane (volatile non-polar organic), toluene (less volatile non-polar organic), and water. Concentrations of 0.5 mg per 20.0 mL solvent were used. Wafers were Si with alumina support. Drop-casting

was used as the deposition method. CVD was performed using processes 1″-C_2H_4 and 2″-C_2H_4. Additionally, to serve as a solvent-free comparison, a macroscopic amount (a few mg) of zirconia nanoparticles were pressed onto a wafer and CVD processed.

No improvement in CNT yield was observed from any of the samples. IPA followed by pentane (see Figure 5.9) gave the highest yields with grades of 1 and 0.5, respectively. Solids from the solvent-free sample survived CVD processing but presented no CNTs; instead, a sintered mass was observed. This substantiated the hypothesis that more concentrated solutions do result in sintering of the nanoparticles.

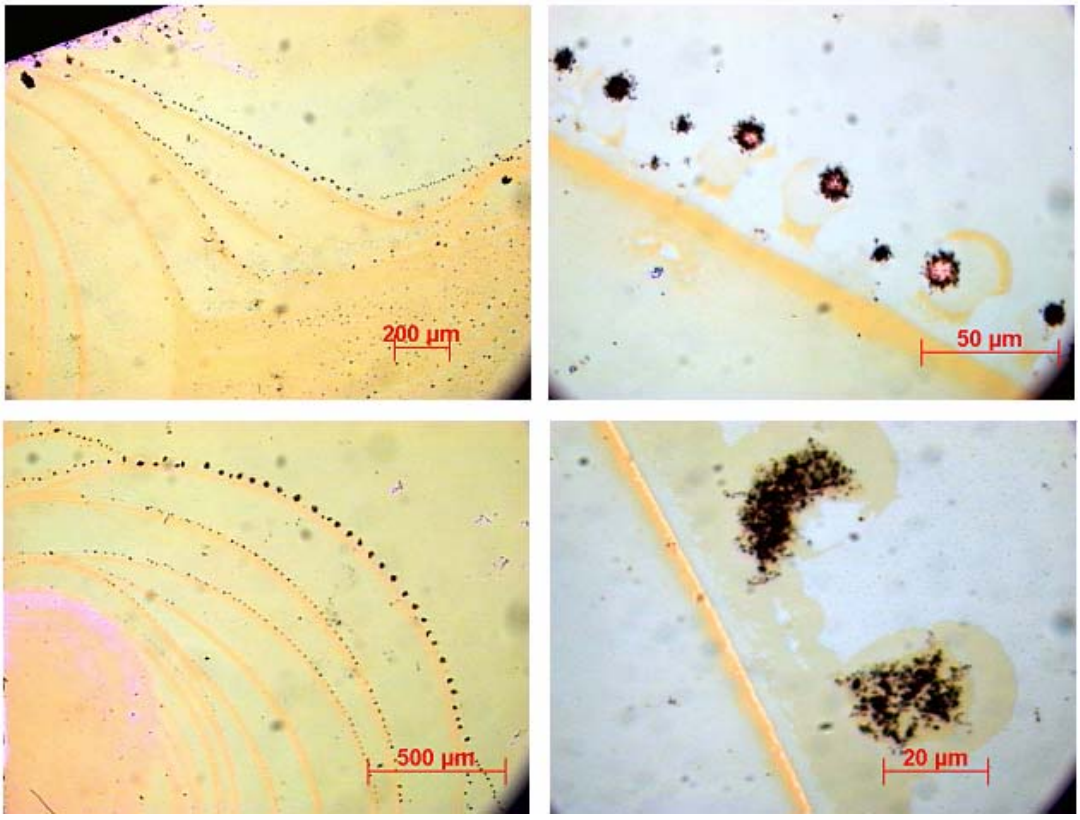

Figure 5.8 Optical microscopy of CNT clusters grown within Marangoni fingers resulting from N_2-assisted drying of 4-nm zirconia dispersed in IPA drop-cast onto a Si wafer with alumina support and processed with 2″-C_2H_4-680(760).

5.3.5. Inclusion of Ca^{2+}, Side of Wafer Coated, and Addition of C_2H_4/H_2 Flow on Ramp-Up to Set Point

No set of conditions evaluated up to this point was found to result in a major improvement in CNT yield than achieved by drop-casting a solution of 0.5 mg mL^{-1} 4-nm zirconia nanoparticle in IPA onto a wafer and using

ethylene-based CVD. Previous experiments and the broader parametric study do, however, provide some clues that are worth extrapolating upon:

- CNT growth from zirconia on wafers is repeatably better than without zirconia
- CNT growth from zirconia seems to occur in regions correlating with the presence of organic residue deposits on the surface
- Zirconia nanoparticles attached to CNTs were observed to contain ~2 at% Ca (Chapter 4)

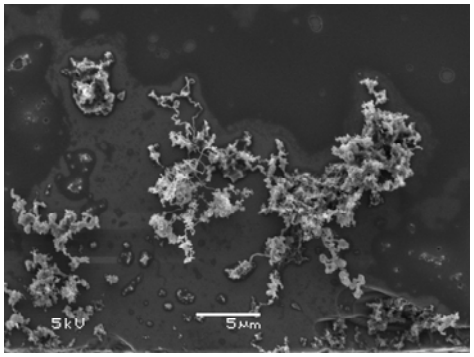

Figure 5.9 Region of CNT growth from sample coated with zirconia deposited from pentane; most of the wafer is bare, however.

In this substudy, a parameter matrix was established to exploit these observations towards dramatically improving growth. First, $CaCl_2$ was added into solutions of 4-nm zirconia in IPA in an amount equivalent to 2 at% of the dispersed zirconia. This was based on a hypothesis that the presence of Ca observed in zirconia nanoparticles attached to CNTs (Chapter 4) was more than circumstantial but rather functional, and that by adding Ca^{2+} to an engineered zirconia nanoparticle dispersion, Ca could be uptaken into the nanoparticles on a wafer surface by sintering action consequently enhancing activity of the nanoparticles for facilitating CNT growth. Second, depositing the zirconia on the rough back side of a wafer was evaluated as way of providing a rough textural support to stifle particle coarsening. Third, the addition of ethylene during ramp-up to the growth temperature was evaluated with the dual intents of nucleating CNTs (or their protostructures) before the particles could sinter extensively while simultaneously providing a source of organic residue.

Solutions of 4-nm zirconia in IPA (0.5 mg mL^{-1}) were prepared with 0.18 mg anhydrous $CaCl_2$ added. Control solutions were the same but did not contain $CaCl_2$. These solutions were drop-cast onto the smooth top of the wafer with alumina support or the rough, unpolished bottom (no alumina support). Samples were processed with 1”-C_2H_4-750 with 400 sccm H_2 and

100 sccm He flowing on ramp-up to the growth temperature or alternatively with 400 sccm H_2, 100 sccm He, and 100 sccm C_2H_4.

No clear effect was observed from the inclusion of Ca. Similarly growths on the backsides of wafers had no advantage, as the roughness of the surface as observed by SEM was not at a length scale useful for inhibiting particle coarsening. Fumed silica, fumed alumina, nanostructured magnesium oxide, or an aerogel material would be alternatives to consider for future work. CVD growth with and without C_2H_4 during ramp-up both gave CNT yields with a grade of 1 but again were limited to dark-contrasted regions of wafers and so the C_2H_4 on ramp-up did not substantially influence CNT growth.

Results from this substudy eliminated additional variables from the parametric study. The next parameters of interest were nanoparticle-based parameters, specifically other zirconia nanoparticle sources and pretreatments, followed by alternative CVD processes.

5.3.6. CVD Process and Support Oxide

In the following sections, additional CVD processes were introduced into the various parametric substudies undertaken with a twofold intent: one, to ascertain if zirconia would be more active under a different set of CVD parameters than those based on legacy CNT catalysts (other than ethylene-based CVD processes such as 1"-C_2H_4-750 and 2"-C_2H_4-680(760)); and two, to migrate towards a viable zirconia-based CNT growth procedure that could be used at BESSY for *in situ* XPS analysis during CNT growth, which needs to be acetylene-based and performed under vacuum.

A baseline for CNT growth performed with acetylene at atmospheric pressure (process C_2H_2-750), methane at atmospheric pressure (process CH_4-900), and acetylene at reduced pressure (process LP-C_2H_4) for two supports (alumina and silica) and two deposition methods (drop-casting and spin-coating) is presented in Table 5.3. The zirconia source was a solution of 0.5 mg mL^{-1} 4-nm zirconia nanoparticles dispersed in IPA. Drop-casting and spin-coating (5000 rpm, 1 drop, 1 min) were used to deposit the zirconia on wafers.

CVD growth was present in higher yield with atmospheric pressure C_2H_2- and C_2H_4-based processes than for the LP-CVD process or CH_4 process. However, CVD with CH_4-900 on zirconia-coated wafers does consistently result in CNTs where no growth or near no growth is observed on control samples processed under similar conditions.

Silica support seemed to be better than alumina for CNT growth at these different conditions, and so in consideration of this and that Si wafers with silica supports were more readily available, silica was used for further studies.

Substrate Support Oxide, Deposition Method	C_2H_2-750	CH_4-900	LP-C_2H_2
Drop-Cast 4-nm Zirconia on Alumina Support	0.5	0	0
Drop-Cast 4-nm Zirconia on Silica Support	1	1	0
Spin-Coated 4-nm Zirconia on Alumina Support	0	-	-
Spin-Coated 4-nm Zirconia on Silica Support	0.5	1	-

Table 5.3 Parameter matrix for support type and deposition method versus CVD process with grades indicating the level of CNT growth observed for each set of conditions.

5.3.7. Other Zirconia Nanoparticle Sources

Although the 4-nm zirconia nanoparticles used throughout this study were a substantial improvement towards monodisperse nanoparticles with predictable behavior in comparison with saturated $ZrOCl_2$ in IPA solutions, it was hypothesized that if CNT growth from zirconia only proceeds via a surface-mediated reaction, even 4 nm may be too large for reliable, high-yield growth of CNTs. Additionally, the ability to control (remove) the presence of phosphorus (from attached ligands) and to controllably introduce defects was desired. Towards these goals, three new methods for producing zirconia nanoparticles were devised and evaluated:

- Micelle-templating employing the block co-polymer poly(styrene)-poly(vinyl-4-pyridine) (PS-P4VP)[127] and $ZrOCl_2$
- Micelle-templating employing the block co-polymer PS-P4VP[127] and zirconium(IV) acetylacetonate ($Zr(acac)_4$)
- Dilute solutions of $Zr(acac)_4$ in IPA

5.3.7.1. Micelle Templating with Poly(styrene)-poly(vinyl-4-pyridine) (PS-P4VP)

The micelle templating technique used was adapted from the work of Bhaviripudi *et al.*[127] Procedural details are described in more detail in Section 5.2.1. Briefly, PS-P4VP is dissolved in anhydrous toluene. To this solution, a small quantity of a water-soluble metal salt is added. The lone pairs of electrons on the nitrogens in the pyridine side groups of the P4VP blocks then donate electron density into vacant orbitals of the metal ion

centers, while the phenyl side groups in the PS blocks are repelled outward and intermingle with the surrounding toluene. This results in the formation of nanoclusters of the metal salt encased by PS-P4VP. These nanoclusters can then be deposited onto a substrate by drop-casting or spin-coating. Finally, the polymer is baked off or preferably ashed off with an O_2 plasma, leaving behind small (<2 nm) domains of metal oxide on the substrate. For adaptation to the synthesis of zirconia nanoparticles, $ZrOCl_2 \cdot 8H_2O$ was initially used. XPS of wafers upon which this solution was deposited, however, revealed no zirconium of any sort to be present over the wafer surface (and consistently, CVD growth with wafer samples prepared with these solutions yielded no CNTs). Apparently, $ZrOCl_2$ does not offer any accessible orbitals into which pyridine side groups on the templating polymer can donate electron density. Alternatively, since the octahydrate was used, the water contained within the oxychloride crystal lattice may be liberated and hydrate the PS-P4VP much more readily than the P4VP blocks can interact with the oxychloride. Following this result, zirconium(IV) acetylacetonate ($Zr(acac)_4$) was used instead of $ZrOCl_2$ and found to yield uniformly-distributed rod- and web-like nanostructures over the surface of wafer samples. It seems that $Zr(acac)_4$/PS-P4VP micelles preferentially result in elongated nanostructures rather than round nanoparticles. Two concentrations of $Zr(acac)_4$ in PS-P4VP/toluene were explored based on concentration values used in the report of Bhaviripudi *et al.*: 0.25 mmol and 0.025 mmol $Zr(acac)_4$ per 250 mL PS-P4VP/toluene solution. These solutions were drop-cast and spin-coated at 1250 rpm onto Si wafers with silica support. The wafers were subsequently baked in air at 550°C for 30 min. Finally, the samples were processed by CVD processes CH_4-900 and LP-C_2H_2.

5.3.7.2. Dilute Solutions of Zirconium(IV) Acetylacetonate in 2-Propanol

$Zr(acac)_4$ is used as an organometallic precursor for deposition of Zr metal. As such, it was hypothesized the dilute solutions of this precursor could be applied to a wafer surface and then oxidized in air to yield zirconia nanoparticles.

Solutions containing 0.12 mg/mL and 0.12 μg/mL of $Zr(acac)_4$ in IPA were prepared and drop-cast onto Si wafers with silica support. The wafer samples were then baked in air at 550°C for 30 min and processed by CVD processes CH_4-900 and LP-C_2H_2.

5.3.7.3. CNT Growth Results

CNT growth was observed for wafers coated with both concentrations of $Zr(acac)_4$/PS-P4VP nanoparticles with both LP-C_2H_2 and CH_4-900. Again a plurality of non-CNT nanostructures is observable by SEM and in greater density with samples prepared with the higher concentration of $Zr(acac)_4$/PS-P4VP. This said, further characterization of the observed nanostructures (e.g., by TEM) is warranted to verify their nature and composition. CVD processing with CH_4-900 yielded substantially better (grade of 1.5) CNT growth over control samples (Figure 5.10). Solutions of $Zr(acac)_4$ in IPA did not yield substantial CNT growth over the controls, instead resulting in an array of assumedly zirconia-based micro- and nanostructures over the surface (Figure 5.11).

In conclusion, the $Zr(acac)_4$/PS-4VP approach looks promising and provides validation of CNT growth from a third source of zirconia (the other two being $ZrOCl_2$-derived nanoparticles and $ZrCl_4/Zr(OC_3H_7)_4$-derived nanoparticles, i.e., the 4-nm zirconia nanoparticles used in this work). XPS analysis of wafers coated with these solutions verifies the presence of zirconia and the absence of metallic contamination or other unexpected elements. Further investigation of this nanoparticle approach is merited.

5.3.8. Nanoparticle Pretreatments

In this section, three types of pretreatments were surveyed to assess if CNT growth with zirconia nanoparticles can be markedly enhanced through a broad-spectrum chemical modification of the nanoparticle surfaces. These included approaches to remove surface ligands from the 4-nm zirconia nanoparticle source by baking in air and with O_2 plasma, H_2-plasma treatments intended to invoke oxygen deficiency into zirconia nanoparticles, and Ar-plasma treatments intended to reduce the average size of zirconia nanoparticles and/or nanoparticle clusters.

5.3.8.1. Oxygen Plasma Pretreatment and Baking in Air to Remove Surface Ligands from Nanoparticles

To inform development of a best practice in preparing the 4-nm zirconia nanoparticles for CVD, one set of parameters investigated included methods intended to oxidatively remove trioctylphosphine ligands from the exterior surfaces of the 4-nm zirconia nanoparticles in advance of CVD processing. Two methods were surveyed: oxygen plasma pretreatment and baking in air. The zirconia source was 0.5 mg mL^{-1} solutions of 4-nm zirconia in IPA. Drop-casting and spin-coating (5000 rpm, 1 drop of solution, 1 min) were used as

deposition methods. Substrates were Si wafers with silica supports. Oxygen plasma was generated using a Philips RIE ET PlasmaFab 340 system. The system was pumped down to a pressure of 150 mtorr at which point a flow of 50-60 sccm of O_2 was introduced and the pressure was stabilized at ~35 mtorr. A power of 100 W was used. Oxygen plasma times of 2 min and 10 min were used.

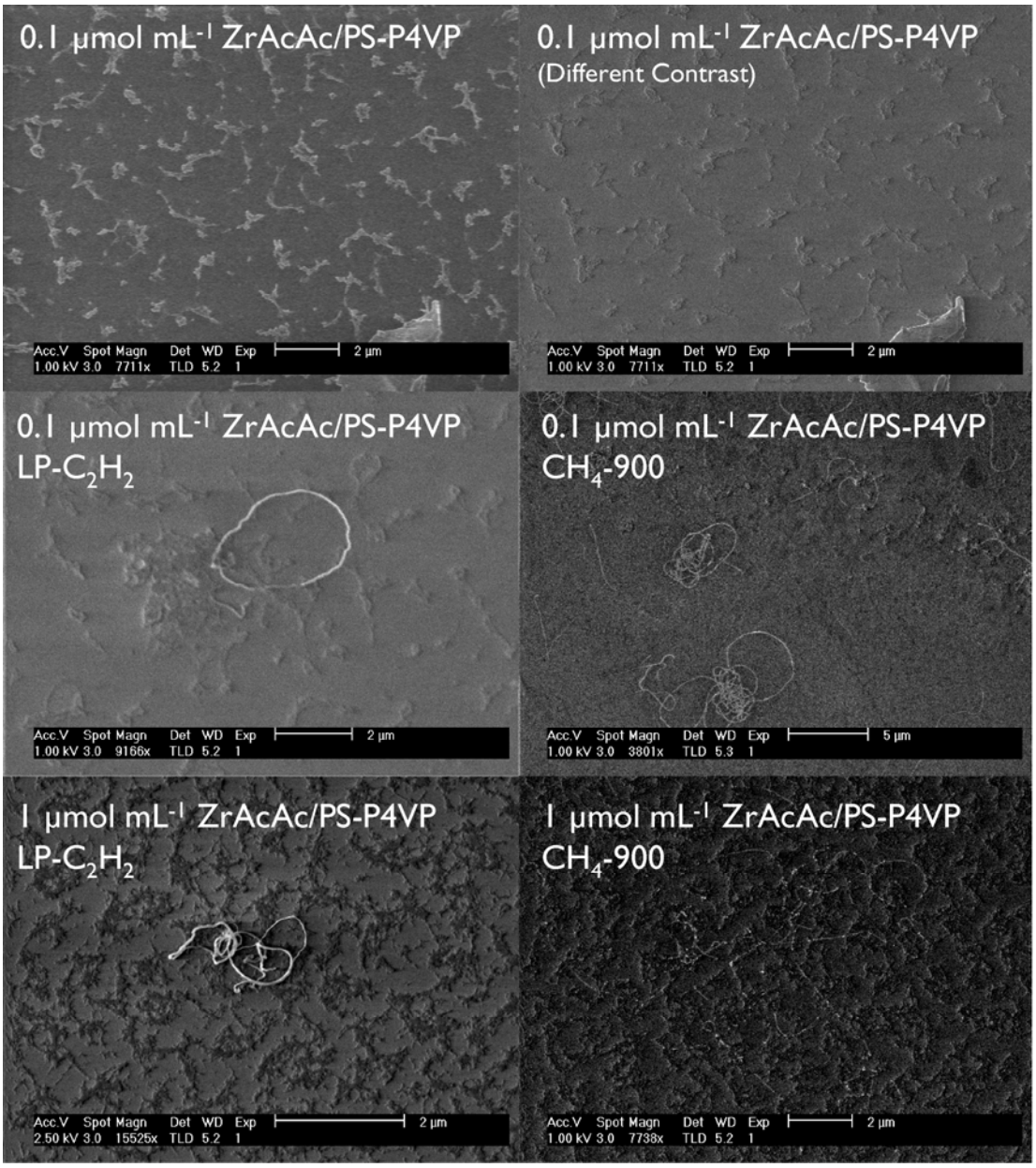

Figure 5.10 SEM images of zirconia nanoparticles from $Zr(acac)_4$/PS-P4VP showing structures that, at first glance, are similar in appearance to CNTs *(top left)*, however when viewed in a different contrast are found instead to be oxide nanostructures *(top right)*; CNTs resulting from LP-C_2H_2 *(left column, middle and bottom panels)* and CH_4-900 *(right column, middle and bottom panels)*.

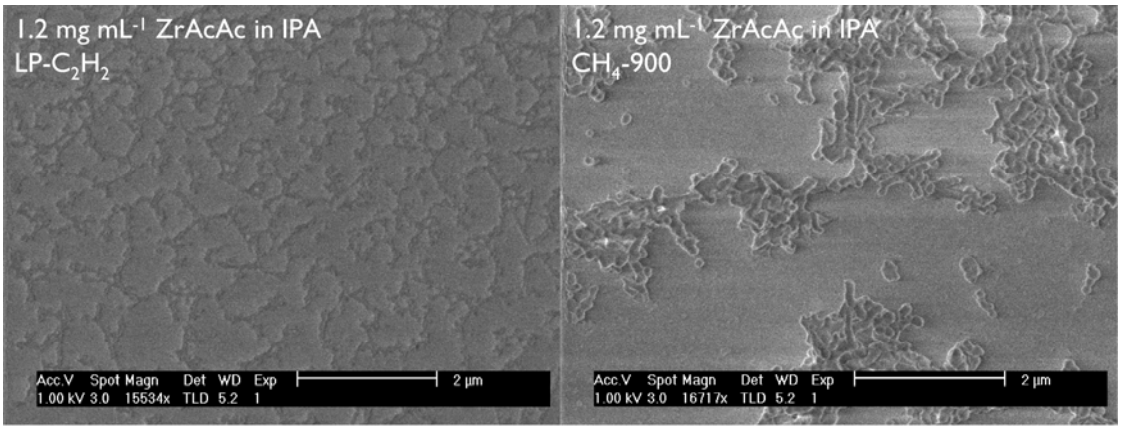

Figure 5.11 Micro- and nanostructures resulting from CVD processing of wafers coated with solutions of $Zr(acac)_4$ in IPA; little CNT growth is observed with this approach (grades of 0-0.5).

Zirconia Nanoparticle Source[a]	LP-C_2H_2	CH_4-900
1 µmol mL^{-1} $Zr(acac)_4$/PS-P4VP	1	1.5
0.1 µmol mL^{-1} $Zr(acac)_4$/PS-P4VP	0.5	0.5
1.2 mg mL^{-1} $Zr(acac)_4$ in IPA	0	0.5
1.2 µg mL^{-1} $Zr(acac)_4$ in IPA	0	0

[a]Drop-cast onto Si wafers with SiO_2 support and baked in air (in a class 10k clean room) at 550°C for 30 min.

Table 5.4 Parameter matrix for new nanoparticle sources surveyed versus CVD process with grades indicating the level of CNT growth observed for each set of conditions.

Subsequent CVD processing of baked and O_2-plasma-treated samples with C_2H_2-750 resulted in sintered zirconia films in the case of baking and spiky webs of zirconia nanostructures over wafer surfaces in the case of O_2 plasma The thickness of the features became finer (from 50-100 nm to 10-50 nm) with plasma treatment time. Virtually no CNT growth was observed (a grade of 0). SEM reveals many regions with structures that look like CNTs, however upon further investigation these structures are verified not to be CNTs.

Thus it was concluded that O_2 pretreatments serve to anneal and sinter zirconia nanoparticles on the surface and should be avoided. This said, O_2 plasma treatment may an interesting synthetic pathway for producing porous, nanostructured zirconia or other oxide scaffolds.

5.3.8.2. Hydrogen Plasma Pretreatment to Install Oxygen Deficiency

Following from observations of oxygen deficiency in zirconia nanoparticles investigated in Chapter 4 as observed by XPS and XRD of zirconia-doped carbon aerogels, methods for rendering 4-nm zirconia nanoparticles into a phase with a substoichiometric quantity of oxygen were investigated. Hydrogen plasma treatment was one method considered and is explored here.

In this substudy, 4-nm zirconia in IPA (0.5 mg mL^{-1}) was deposited onto silicon wafers with alumina or silica supports by drop-casting. These samples were then treated with hydrogen plasma and subsequently CVD processed.

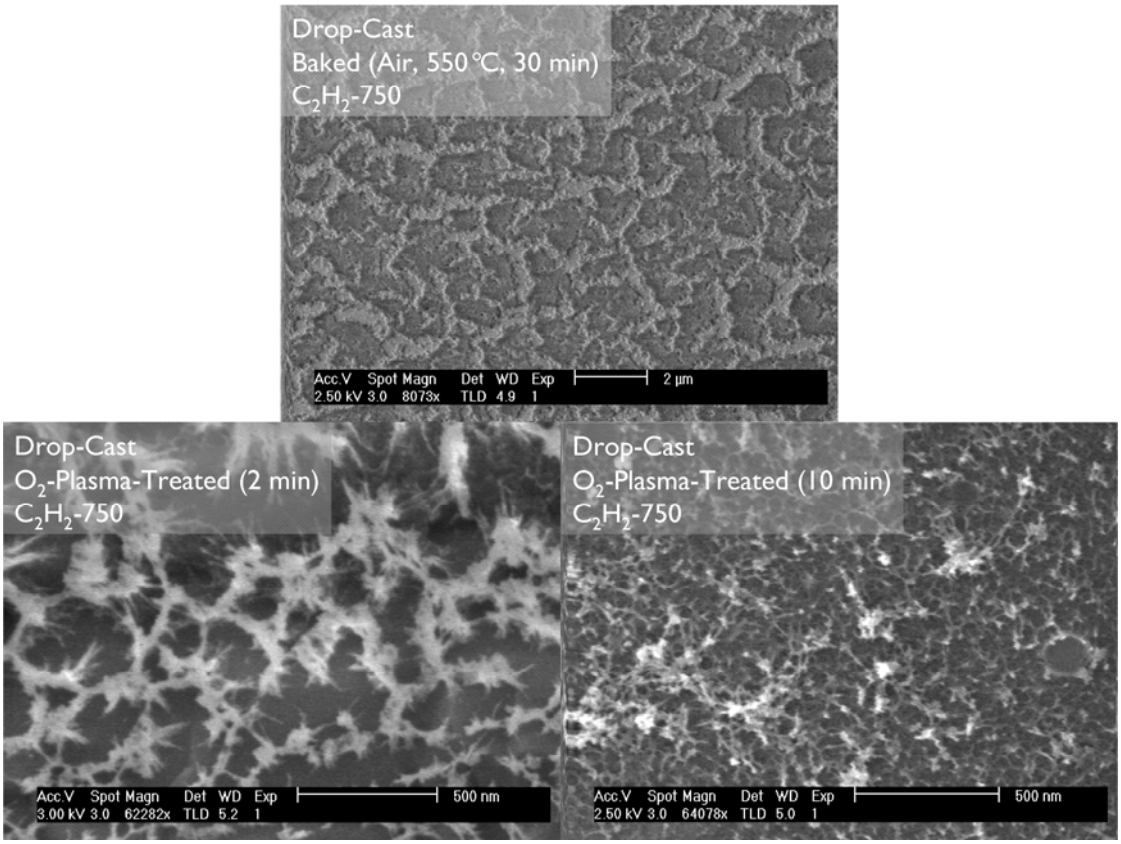

Figure 5.12 Oxide formations observed after CVD processing of wafers coated with 4-nm zirconia nanoparticles pretreated by baking in air at 550°C for 30 min *(top)*, with O_2-plasma treatment for 2 min *(bottom left)*, and O_2-plasma treatment for 20 min *(bottom right)*; in some cases webs of oxide nanostructures confusingly similar in appearance to webs of CNTs were observed (such as the structures shown in the bottom right panel).

The first attempt at preparing H_2-plasma-treated zirconia nanoparticles was performed using a Harrick Scientific PDC-32G RF plasma cleaner

connected to a gas tank containing 10% H_2 in Ar. Samples were processed with this system for 5 min on a medium power setting at a pressure of ~250 mtorr. Following plasma treatment, the samples were analyzed for surface chemistry by XPS, initially to characterize the oxidation state of Zr, but instead revealing the presence of F and N where none had been present before (Figure 5.13). Untreated samples presented only one chemistry of zirconia with a Zr $3d_{3/2}$ peak at 183.8 eV (FWHM=1.17 eV). This chemistry shifted to 184.0 after H_2 plasma treatment and was joined by a second, higher-binding-energy chemistry with a Zr $3d_{3/2}$ peak falling at 184.5 eV. Clearly, the zirconia was further oxidized by this process. Likely, the H_2 plasma reacted with a fluoropolymer coating on an RF coil in the plasma cleaner and fluorinated some of the zirconia nanoparticles on the sample surfaces. A similar phenomenon may have occurred with N as well. The magnitude C 1s peak also reduced following plasma treatment, suggesting C was oxidized into volatile products. Notably, P (from trioctylphosphine ligands on the surface of the nanoparticles leftover from synthesis) remains following this treatment. It is hypothesized that this P may play a role in the activity of these nanoparticles. Subsequent CVD growth via process 2"-C_2H_4 with the fluorinated substrates showed no growth whatsoever. This could be attributable to the presence of new elemental contaminants, the fluoridation of the nanoparticles, and/or loss of beneficial organic residue.

Hydrogen plasma treatment was attempted again using a Plasmalab remote plasma CVD (RP-CVD) system designed for this type of process. A matrix of samples were prepared and processed with this system. Zirconia sources included saturated $ZrOCl_2$ in IPA and 4-nm zirconia in IPA (0.5 mg mL^{-1}). Substrates were all Si with silica supports. Deposition methods used were drop-casting and spin-coating (5000 rpm, 1 drop, 1 min). Samples were first placed in the RP-CVD. The system was then evacuated to a pressure of $<10^{-4}$ mbar. Next, a flow of 50 sccm of hydrogen was introduced into the chamber and the pressure was stabilized to 0.38 mbar. A power of 20 W at 0.84 kV was used and the plasma was sustained for 5 min. H_2-plasma-treated samples were then CVD processed with CH_4-900. None of the samples surveyed exhibited substantial CNT growth. However, samples prepared with 4-nm zirconia by drop-casting and which were baked at 550°C in air for 30 min prior to H_2 plasma treatment showed improved growth over control substrates for both processes C_2H_2-750 and CH_4-900. These results may be due to contamination introduced from the H_2 plasma chamber or the baking process and would require further investigation to substantiate.

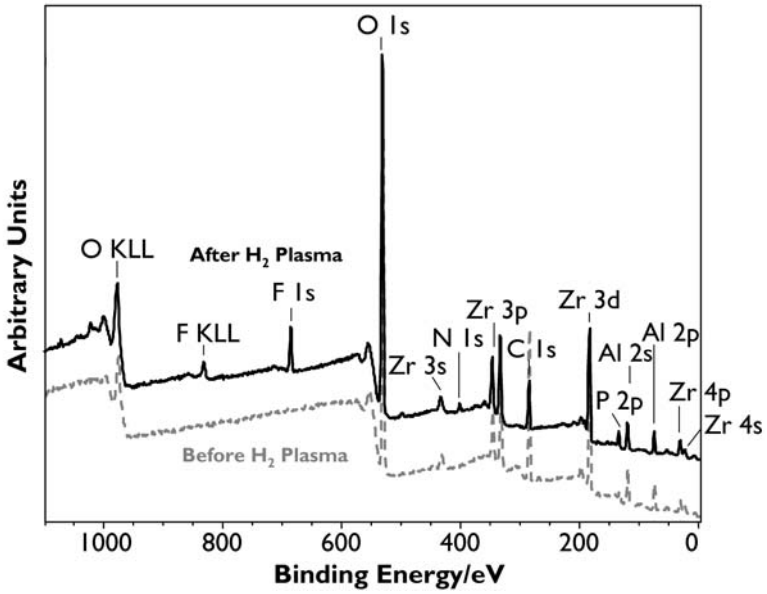

Figure 5.13 XPS spectra of alumina-supported zirconia nanoparticles before *(gray line)* and after *(black line)* exposure to H_2 plasma treatment showing the emergence of F and N following plasma treatment, likely due to a material incompatibility between parts in the plasma cleaner and H_2 plasma.

It was concluded that chemical surface analysis would be required to verify if the plasma treatment was effective in changing the oxidation state of the zirconia nanoparticles in order to proceed effectively and that optimizing the H_2 plasma process may be required to achieve the desired results. XPS was not available within the remaining timeframe of the study; as a result, further work with H_2 plasma treatments was not pursued for the remainder of the parametric study. This is, however, a region of parameter space that merits future work but will require access to both a proper H_2 plasma system and XPS.

5.3.8.3. Argon Plasma Pretreatment to Reduce Nanoparticle Size

Provided observations of sintering under certain conditions, it was hypothesized that the nanoparticles were likely sintering to at least some extent under conditions where overt sintering was not otherwise observed. To test this, an Ar plasma pretreatment was envisioned as a way of "milling down" zirconia nanoparticles on a surface, breaking up agglomerated particle clusters deposited from solution, and possibly even installing oxygen deficiency into particles.

A substudy was conducted surveying the effect of argon plasma treatment on CNT growth with samples prepared from multiple catalyst sources and deposition techniques. Zirconia sources included saturated $ZrOCl_2$ in IPA

and 4-nm zirconia in IPA (0.5 mg mL^{-1}). Substrates were all Si with silica supports. Deposition methods used were drop-casting and spin-coating (5000 rpm, 1 drop, 1 min). Some samples were optionally baked in air at 550°C prior to plasma treatment. Samples designated for processing by Ar plasma treatment were processed using a Plasmalab remote plasma CVD (RP-CVD) system. First, the samples were placed in the RP-CVD. Next, the system was evacuated to a pressure of $<10^{-4}$ mbar. A flow of 15 sccm of argon was then introduced into the chamber and the pressure was stabilized to 0.35 mbar. A power of 10 W at 0.5 kV was used and the plasma was sustained for 5 min.

Table 5.5 shows grades assigned based on CNT growth observed for various combinations of catalyst sources and CVD processes surveyed. Samples with baked, Ar-plasma-treated, 4-nm zirconia displayed a much higher yield (grade 2.5) than other samples in the parametric study. However, surface craters and debris arranged in a way suggestive of an impact event were also visible. Additionally, electric arc discharges grounding on both sample wafers and vacuum chamber walls had been witnessed during the plasma process. As a result, it was hypothesized that these samples had been contaminated with metallic materials deposited due to sputtering of the metallic vacuum chamber. Accordingly, control samples exhibited similar levels of CNT growth as variable samples.

Nanoparticle Deposition Method, Processing	**Saturated $ZrOCl_2$ in IPA**		**4-nm Zirconia**	
CVD Process	**C_2H_2-750**	**CH_4-900**	**C_2H_2-750**	**CH_4-900**
Drop-Cast	0.5	0	1	1
Drop-Cast, Ar Plasma*	-	0	0.5	0.5
Drop-Cast, Baked, Ar Plasma*	1	-	1	2.5

*The Ar plasma was found to introduce metallic contamination due to sputtering of the surrounding vacuum chamber walls. Accordingly, control samples not coated with zirconia exhibited grades of 1-2 for growth as well. Grades for Ar plasma-treated samples should be considered within this context.

Table 5.5 Parameter matrix surveying effects of Ar plasma pretreatment on two nanoparticle sources versus CVD process with grades indicating the level of CNT growth observed for each set of conditions.

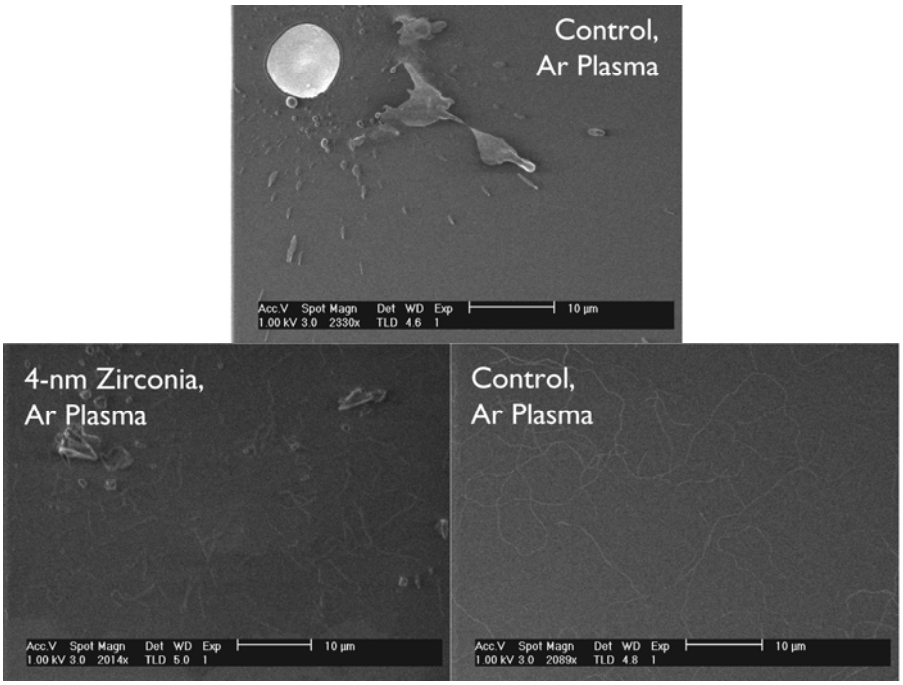

Figure 5.14 SEM images of samples processed by Ar sputtering: *(top)* impact debris and cratering found on control sample; *(bottom left)* CNTs in good yield over surface of wafers coated with 4-nm zirconia; *(bottom right)* similar CNT yield found on control samples, suggesting the presence of contamination.

Based on these findings, Ar plasma treatments were not pursued for the remainder of the parametric study, although with the proper equipment and process refinement may be an area of interest for future study.

5.3.9. Parametric Study Conclusions

The parametric study provided an increased level of confidence that zirconia nanoparticles do catalyze CNT growth and provided clarity regarding what types of CNT morphologies with zirconia are repeatably obtainable on oxide supports and under what circumstances. Three different zirconia sources were validated as effective for CVD growth of CNTs (nanoparticles from saturated $ZrOCl_2 \cdot 8H_2O$ in IPA, 4-nm zirconia from high-temperature sol-gel, and PS-P4VP-templated zirconia from $Zr(acac)_4$). Most importantly, a large amount of the parameter space that has been effective for optimizing CNT growth from legacy CNT catalysts has not yielded any substantial improvement in yield over what has been consistently observed. Based on this study, zirconia nanoparticles do not seem to be highly active towards CNT growth on oxide supports. Outstanding opportunities for future parametric study include more highly controlled H_2 and Ar plasma treatments, variation of particle diameter, and investigations regarding the

role of Ca, P, and other potential dopants included in zirconia nanoparticles. Some indications of enhanced growth in the presence of organic residue have also been observed and merit a more controlled study as well.

In summary, the parametric study did not reveal a clear, positive trajectory towards mastering growth with zirconia nanopositors. Rather, it served to demote the probability of a large area of parameter space as having reasonable potential to resolve the core problems of yield and predictability. That is, the answers to the problems underlying practical use of zirconia for CNT growth lie somewhere else. With this in mind, the following section presents a discussion of where else these answers may lie and next steps that could be taken in pursuit of them.

5.4. Deductions

Over 200 parametric conditions (not all of which were described in depth in the previous section) were analyzed over the course of the parametric study reported in Section 5.3 in an effort to improve CNT yield with zirconia, yet none of these conditions stand out as being an obvious path forward. However, a differential analysis between conditions that do give rise to CNT growth with zirconia but not on control samples and conditions that do not give rise to CNT growth with zirconia has provided some insight.

Following the parametric study, four hypotheses remain:

- *Outstanding missing parameter.* Some unrecognized parameter is required to get CNTs to grow from zirconia nanoparticles.
- *Something is wrong with most of the nanoparticles surveyed.* Problems could include nanoparticle size, composition, agglomeration, shape, and other factors.
- *Something is wrong with the supports surveyed.* Zirconia may only be active towards CNT growth on certain supports, just as many other heterogeneous catalysts are only active towards their respective applications on certain supports. Oxide supports may not provide the necessary functions required for activating zirconia nanopositors.
- *Zirconia is not a catalyst/nanopositor for CVD growth of CNTs.* This seems unlikely given the extensive *in situ* and *ex situ* characterization performed in Chapter 4 and the consistent enhanced, albeit low-yield, CNT growth observed on substrates coated with zirconia nanoparticles over control substrates. However, it is possible that very trace levels of metallic contamination, when in the presence of zirconia (in which zirconia nanoparticles act as a solid-acid support), result in CNT

growth but such contamination is undetectable by the characterization methods used.

In the following sections, experiments designed to probe the likelihood of each of these hypotheses being true are described.

5.4.1. Possible "Missing Parameters": Ultraviolet Radiation, Alkynes

Zirconia and its Group-4 analog titania are known as highly efficient photocatalysts for various organic reactions.[121,131,132] In photocatalysis, a photon tuned to the bandgap of the catalyst material stimulates an exciton (electron-hole pair) to form on the catalyst surface. These can then enable chemical reactions that would otherwise not occur, or not occur as quickly, without such photonic surface excitation. It is intriguing to consider whether ultraviolet radiation plays a role in mediating the activity of zirconia nanoparticles for CNT growth and whether it could be used to enhance their activity. In engineering of photocatalysts, the photocatalyst particles are often doped with other elements including metal ions such as Sn[133] and non-metals such as N[134] to enhance the activity of the oxide towards photocatalytic reactions. Furthermore, the non-metallic nanopositors that have been demonstrated to be successful at facilitating CNT growth (ZrO_2,[55] Al_2O_3,[75] SiO_2,[77,78,135] and most recently nanodiamond[65] are all wide bandgap semiconductors with absorption in the ultraviolet range. This absorption can be red-shifted by the inclusion of dopants, which introduces states into the bandgap and allows for stimulation by longer wavelength photons. Indeed, doping is frequently used in the engineering of novel photocatalysts in order to shift the wavelength(s) required for activation of the catalyst from the ultraviolet into the visible range.[131,134,136-138] Photocatalysis is a unique capability zirconia boasts over metallic CNT catalysts. Exploration of a possible role of or opportunity for incorporating photocatalytic behavior in CNT growth from zirconia is a fascinating prospect and merits further exploration.

Zirconia also differs from metallic catalysts in capability to decompose hydrocarbons. The activity of refractory metal oxides towards decomposition of hydrocarbons is substantially lower than that of metallic catalysts. As has been discussed previously, zirconia may require different gas-phase precursors than metallic catalysts in order to facilitate CNT growth. Plata *et al.* have demonstrated that the concentration of specific alkynes is proportional to the growth rate of CNT forests catalyzed by Fe/Al_2O_3 catalysts.[97,100,101] It is hypothesized that some of these specialty alkynes may enhance the growth of CNTs with zirconia by serving as a more suitable precursor absent

the ability to decompose suboptimal hydrocarbons. Furthermore, the methods demonstrated by Plata *et al.* may be useful in elucidating feedstock molecules whose concentrations are proportional to CNT growth rates from zirconia (provided a reliable, high-yield CNT growth process with zirconia). The prospects of ultraviolet-excitation and engineered feedstocks could be synergistically combined to perhaps enable very active CNT growth from zirconia (Figure 5.15). Towards these prospects, a special CVD system has been engineered and is described in Chapter 6.

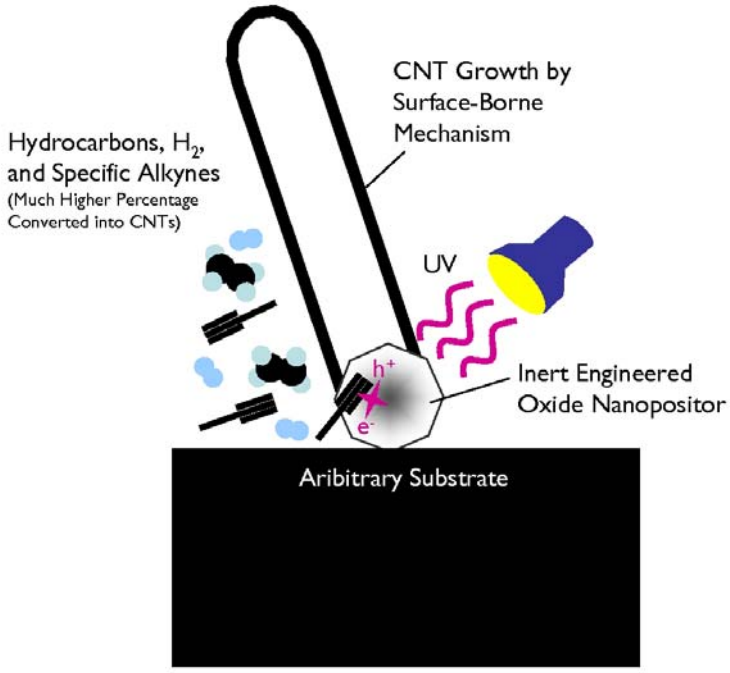

Figure 5.15 Illustration of ultraviolet excitation and engineered feedstocks enabling CNT growth from an oxide nanopositor, such as a zirconia nanoparticle, on an arbitrary substrate.

5.4.2. Preparation of Oxygen-Deficient Zirconia

Oxygen deficiency in zirconia nanoparticles remains an important aspect of CNT growth from zirconia to be fully characterized and investigated in a controlled way. It is also an appealing explanation for non-uniform CNT growth as it would like present itself as a spectrum of stoichiometries among a population of nanoparticles, possibly rendering only some nanoparticles active towards CNT growth.

Ar-ion sputtering, a technique used in XPS systems to depth profile chemical composition through a surface, is known to selectively sputter oxygen away from refractory oxides such as Ta_2O_5.[139] We have observed

that oxygen-deficient zirconia nanoparticles are stable in air and retain their substoichiometry upon exposure to air. It was hypothesized that Ar-ion sputtering in an XPS system could be used to install oxygen deficiency into zirconia on a substrate. This would simultaneously enable monitoring of the chemical state of Zr between sputtering cycles and thus enable tailoring the stoichiometry of zirconia nanoparticles.

A proof-of-concept demonstration was performed. Zirconia-coated Si wafers with silica supports were prepared by sputtering ~1 nm Zr metal onto the wafer, which subsequently oxidizes upon exposure to air. The zirconia-coated wafers were placed in an XPS (Kratos Analytical Axis Ultra DLD) and analyzed for chemical composition. Only signals attributable to zirconia and not zirconium were observed. Next, Ar-ion sputtering was initiated in 30-s cycles for a total of 150 s (Figure 5.16). After only 30 s of Ar-ion sputtering, a second chemistry of oxygen appears at a lower binding energy than the first chemistry, causing the valley between the spin-orbit-split pair of peaks to rise with each sputter cycle. Zr metal also emerges after 90 s of sputtering. Thus it appears it is possible to install oxygen deficiency into zirconia by argon-ion sputtering, however not all of the zirconia will be rendered into this phase before metallic Zr also starts to appear.

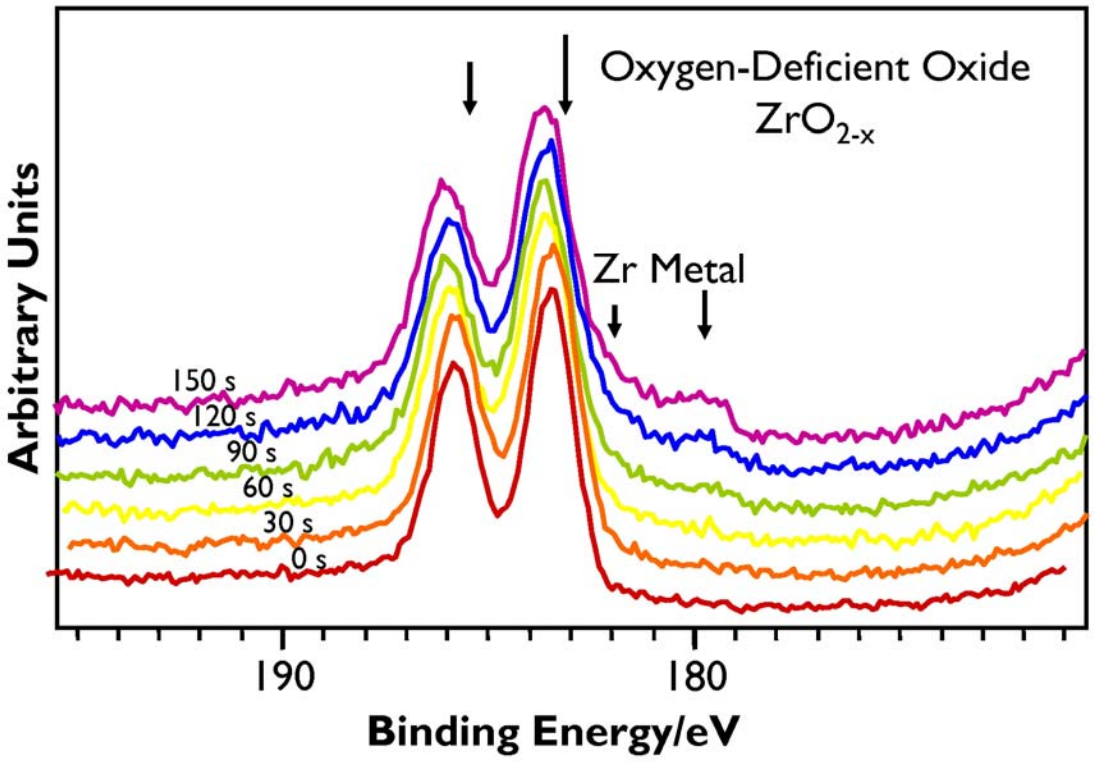

Figure 5.16 XPS spectra of Zr 3d region of 1-nm zirconia thin film after sputtering with Ar-ion gun for 30 s, 60 s, 90 s, 120 s, and 150 s; an oxygen-deficient phase is already present after 30 s of sputtering and Zr metal begins to emerge after 90 s.

Subsequent CVD processing of this sample by process 1″-C_2H_4 did not result in any CNT growth, however this is likely a morphology problem as the zirconia on the substrate was present as a continuous thin film, not as discrete nanoparticles. As such, this experiment merits repeating with engineered zirconia nanoparticles such as the 4-nm zirconia nanoparticles used throughout this parametric study.

5.4.3. Carbon Aerogels as an Alternative to Oxide Supports

A major likely factor limiting the yield obtained from CVD growth of CNTs on zirconia-doped carbon aerogels is the polydispersity of particle sizes (and possibly stoichiometry) present throughout the aerogels. This polydispersity is a natural consequence of the ion-exchange/pyrolysis technique used to grow zirconia nanoparticles within the aerogel. Despite this, CNT yields with zirconia-doped carbon aerogels were found to be consistently better than with zirconia nanoparticles deposited on Si wafers with oxide supports. This gave rise to the hypothesis that perhaps a high-surface-area carbon support was more appropriate for zirconia than a flat oxide support.

To test this hypothesis, carbon aerogels were doped with saturated $ZrOCl_2 \cdot 8H_2O$/IPA solutions or 0.5 mg mL^{-1} engineered 4-nm zirconia/IPA solutions instead of growing zirconia nanoparticles inside the aerogel (as was done in Chapter 4). This decouples production of the aerogel support from production of zirconia nanoparticles, thereby enabling greater control over each of these components.

Methods

Carbon aerogels were prepared from resorcinol-formaldehyde (RF) precursors prepared via an acid-catalyzed reaction according to the methods of Mulik *et al.*[128] (see Section 5.2.2). Aerogel monoliths (~17 mm x 7 mm discs pre-pyrolysis, about half this size post-pyrolysis) were broken into smaller fragments and loaded with zirconia nanoparticle solutions. Zirconia nanoparticle solutions were added to both unpyrolyzed RF aerogels (which were subsequently pyrolyzed) and already-pyrolyzed carbon aerogels (see Table 5.6). This provides samples in which nanoparticles were pyrolyzed with the aerogel and wrapped with carbon aerogel support as well as samples in which nanoparticles were simply added upon a carbon aerogel support.

Zirconia-loaded carbon aerogels and controls were subsequently CVD processed with 1″-C_2H_4. Each variable sample was pyrolyzed with an unloaded control and CVD processed with an unloaded control. Pyrolysis and CVD growth were performed in the same quartz tube and baked in air at 750°C for 20 min between runs. SEM imaging was used to assess the presence

of CNTs over the aerogels. SEM images of variable samples were compared with SEM images of control samples to assess the presence of any contamination.

Zirconia Source	Added Before Pyrolysis	Added After Pyrolysis
Saturated $ZrOCl_2$ $8H_2O$ in IPA	bp-CA-OC-##	ap-CA-OC-##
1% of Saturation Concentration $ZrOCl_2$ $8H_2O$ in IPA	bp-CA-OC1%-##	ap-CA-OC1%-##
0.5 mg mL^{-1} 4-nm Zirconia in IPA	bp-CA-ZNp-##	ap-CA-ZNp-##
None	CA-## or "control"	
## = Hours pyrolyzed under Ar		

Table 5.6 Sample code chart for zirconia-loaded carbon aerogel samples.

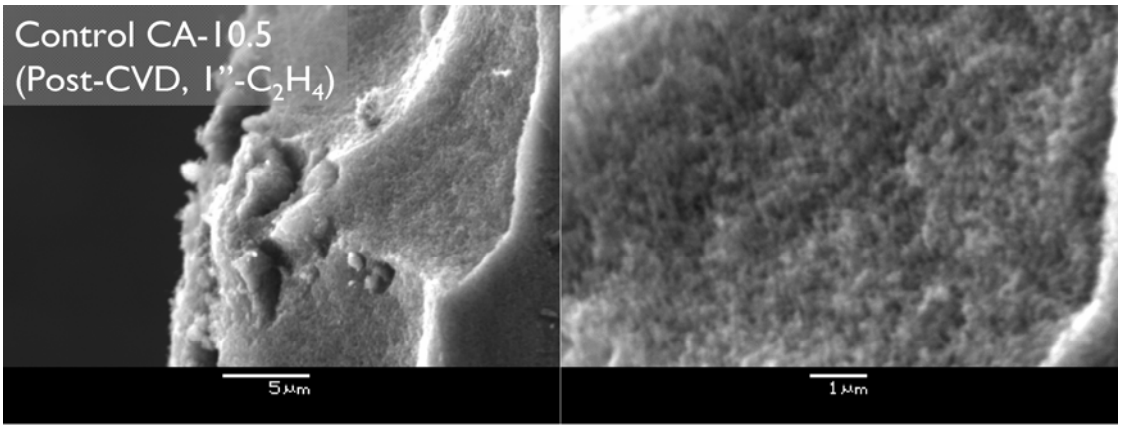

Figure 5.17 SEM images of control sample (CA-10.5) following CVD processing with 1"-C_2H_4: *(left)* overview, *(right)* detail showing typical textured surface of a carbon aerogel.

5.4.4. Results

The results of this study were surprising. CNT growth was observed in high yield (grade 3) over many surfaces of zirconia-loaded carbon aerogels, but not on controls. Samples loaded with 4-nm zirconia both before and after pyrolysis grew CNTs. Samples loaded with oxychloride solution only gave CNTs when loaded before pyrolysis. Oxychloride-loaded samples instead present a cracked, oxide film only. A range in CNT diameters is observed on each sample, with larger bundles tending to be found near sharp edges of the monolith. Sample bp-CA-OC-10.5 gave arrays of very fine, long CNTs, possible because of the presence of very small zirconia nanoparticles resulting

from slow carbothermic reduction of the oxychloride salt during the 10.5-h pyrolysis process. Controls in comparison presented only a few random bundles (grade 0) consistent with growth observed on previous control substrates.

The more pronounced CNT growth found at sharp edges may be due to capillary effects during nanoparticle loading which concentrate nanoparticles in these regions. Additionally, the pore structure of the acid-catalyzed carbon aerogels varies from mesoporous near the top and bottom surfaces of the original disc monolith to more macroporous (micron-diameter porosity) in the bulk interior of the monolith. CNT growth is most pronounced in mesoporous regions. This suggests that higher surface area (and perhaps surface energy) within the support may somehow be advantageous.

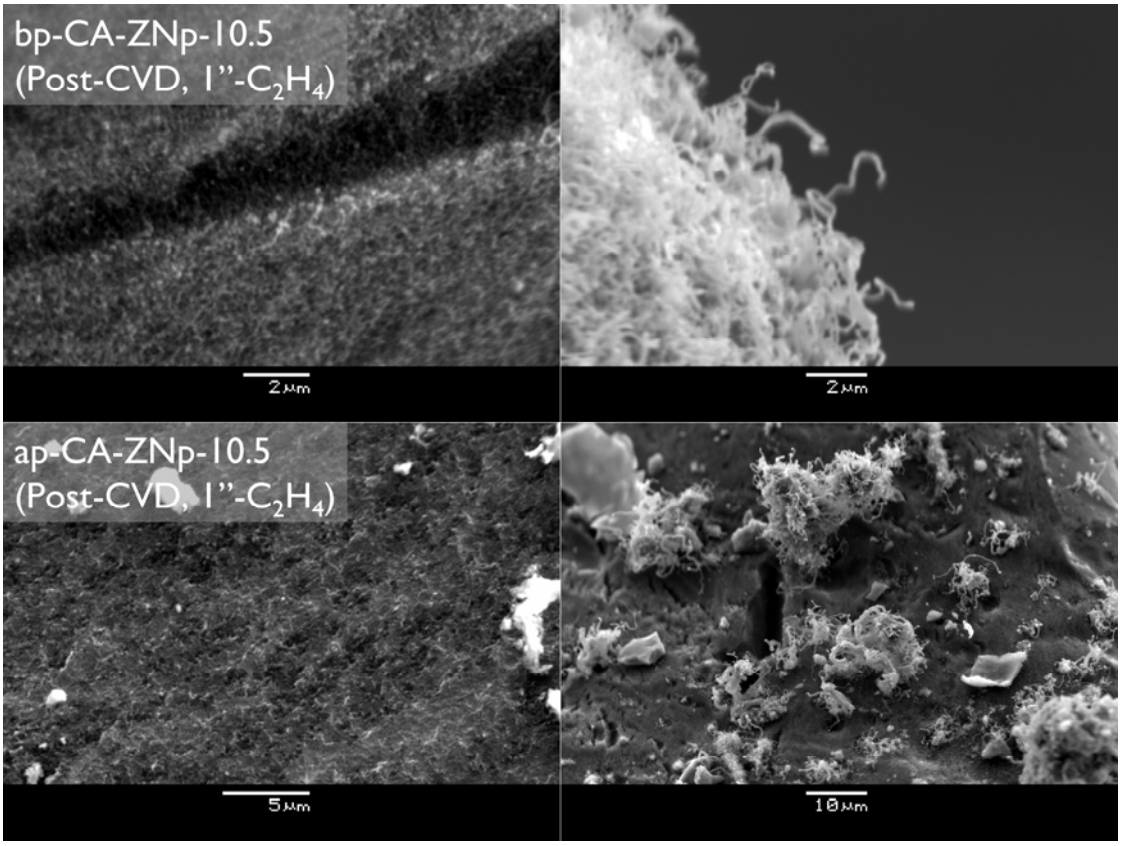

Figure 5.18 Growth of CNTs on carbon aerogels loaded with 4-nm zirconia nanoparticles before pyrolysis *(top)* and after pyrolysis *(bottom)*.

5.4.5. Conclusions and Future Work

It appears that multiple zirconia nanoparticle sources become active for CNT growth when placed on carbon aerogel supports. In the context of the observations made in Chapter 4, it is hypothesized that zirconia, when in

direct contact with amorphous carbon at elevated temperatures, forms a nanoonion around itself which becomes a suitable protostructure for a subsequent CNT polymerization process to occur. The average diameter and length of CNTs appears coupled to the stage at which the zirconia was loaded onto the aerogel sample (pre- or post-pyrolysis). The larger CNT diameters observed in samples loaded with zirconia pre-pyrolysis is hypothesized to arise either from particle coarsening caused by longer exposure to high temperatures or perhaps due to increased size of a surrounding nanoonion shell which in turn gives rise to a larger diameter CNT.

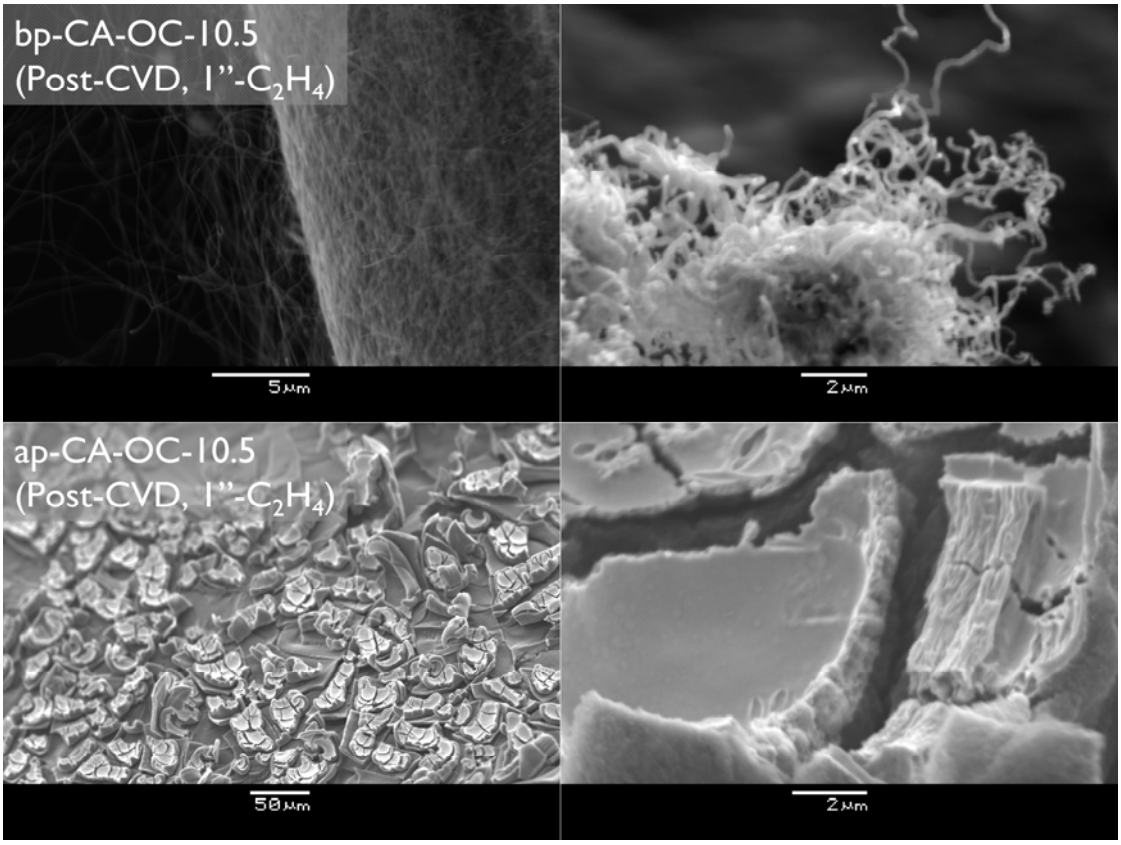

Figure 5.19 Carbon aerogels loaded with zirconia from saturated $ZrOCl_2$/IPA solutions before pyrolysis *(top)* and after pyrolysis *(bottom)*; samples loaded before pyrolysis result in fields of CNTs over the sample surface after CVD with 1"-C_2H_4, whereas samples loaded after pyrolysis only show a thick, cracked zirconia film.

This study is newly underway and the results described herein are considered preliminary. A study in which each sample type is pyrolyzed in its own, dedicated quartz tube and CVD processed in a separate, dedicated quartz tube should be undertaken to ensure cross-contamination is not occurring among samples. Carbon aerogels of varying densities and surface areas should be analyzed to understand relationships between these

properties and propensity for activating zirconia nanoparticles. Other sources of high-surface-area amorphous carbon should be considered. Other zirconia sources, such as zirconia from $Zr(acac)_4$/PS-P4VP, should be surveyed. Surface analysis with XPS should be performed to verify contamination is not present. A more rigorous elemental analysis method such as ICP should be considered. *In situ* metrology such as XPS at BESSY or HR-TEM should be performed on samples with high repeatability that have passed other screening tests for contamination in order to observe the growth mechanism directly.

In conclusion, the carbon aerogel support approach looks like the most promising path forward for understanding and mastering growth of CNTs with zirconia.

5.5. A Possible Missing Condition: Presence of Solid-State Carbon

Based on the experiments described in the previous section, it appears that zirconia, including monodisperse engineered zirconia nanoparticles, becomes active when supported by a high-surface-area solid form of carbon (i.e., a carbon aerogel). It is hypothesized, based on the observation that a zirconia nanoparticle catalyzes solid-state transformation of amorphous carbon into graphitic nanoshells around itself when heated, that not only *can* zirconia do this, but that it *must* do this before a CNT can be grown by CVD. It seems that a graphitic nanoshell needs to form (or be formed) around a zirconia nanoparticle before it can be used CNT growth.

The chronology here is interesting: the first successful growths of CNTs from zirconia were performed on zirconia-doped carbon aerogels (as described in Chapter 4). Subsequent generally unsuccessful efforts to reduce CNT growth from zirconia to practice on silicon wafers were founded on a *critical bad assumption*—that the first identification of CNT growth from zirconia being on carbon aerogels was *circumstantial*. Rather, the carbon aerogel provides an already near-optimal configuration for CNT growth for zirconia that made observation of its activity for CNT growth believable at all. Had zirconia been studied for its propensity to facilitate CNT growth on wafers first, it would have almost certainly been written off as inactive (as some have done before[140]) or simply presenting growth due to elevated levels of contamination. Just as H_2 pretreatments were found to "activate" Fe- and other metal-based catalysts used in typical CVD growth of CNTs (to reduce them from an oxidized state), a "solid-state carbon pretreatment" seems to be necessary to "activate" zirconia-based nanopositors. This would substantiate the initial hypothesis that zirconia lacks or is deficient in an

ability possessed by metal-based catalysts—namely, the ability of nucleating the protostructure of CNTs from gas-phase precursors alone.

This mechanism could be validated by direct observations made by *in situ* TEM during CVD growth of CNTs from zirconia encased in nanoshells (or "ZEN"). Furthermore, ZEN precursors could be manufactured by wrapping zirconia nanoparticles with pyrolyzable polymers or passivating zirconia nanoparticles with pyrolyzable ligands. The ZEN precursors could then be placed on an arbitrary support, not just amorphous carbon, and simply heated under inert atmosphere to produce ZEN nanopositors suitable for CNT growth. Essentially, the ZEN precursor would include its own carbon "support". These experiments as well as an upcoming demonstration employing micropatterned arrays of high-surface-area amorphous carbon on a silicon wafer to produce controlled patterning of CNT growth from zirconia nanoparticles is planned.

Speculating as to understand the origins of the best conditions deduced in the parametric study, an argument based on the presence of organic residues serving as a precursor to amorphous carbon could be made. The repeatable correlations between CNT growth in dark-contrasted regions, presence of dark-contrasted regions near features attributable to solvent evaporation, and the tendency to obtain the highest yield with IPA as a nanoparticle dispersion solvent all support a residual carbon-from-solvent argument. IPA, a hydroxylic organic, tends to adsorb onto oxides (such as a silica or alumina support, or possibly even zirconia nanoparticles) by hydrogen bonding. As the solvent film evaporates from the substrate, instabilities arising from changing interfacial energies evolve. As the solvent film recedes into a droplet and/or substrate edges, these interfacial energies become quite high and the residue left behind from such small film domains will be different from residue left from the wider receding front. Upon heating, the adsorbed solvent decomposes and, perhaps in intimate contact with small zirconia nanoparticles, serves to facilitate nanoonion formation around the zirconia nanoparticles which can then serve as suitable nucleating points for CNTs upon introduction of the CVD gases. Similarly, the PS-P4VP-templated nanoparticles, a different zirconia source, are coated with an aromatic polymer shell prior to CVD. Since baking was used in their preparation rather than oxygen plasma, for the process used this polymer shell may aromatize into a substantially carbonaceous material around the zirconia which can then graphitize into a precursor nanoonion. Further surface analysis work and TEM would need to be performed to substantiate this hypothesis and is recommend for future work.

5.6. Conclusions

Sufficient conditions for enabling CNT growth from zirconia have remained elusive since the initial discovery that CNT growth from zirconia was even possible, but have recently begun to come to light. The role of the underlying support shows likelihood of serving a crucial role in zirconia-based growth of CNTs. The roles of oxygen deficiency and dopants have not yet been conclusively ascertained and remain as outstanding parameter space of great interest for future work. Similarly, it is possible that with specially-engineered CVD gas blends, such as those identified by Plata *et al.*[100] that employ specialty alkynes, that CNT growth without a solid-state carbon pretreatment may be possible. Additionally, while not believed to be an "undetected parameter" in this work, the unique capability of oxides such as zirconia to serve as photocatalysts invites the intriguing possibility of photocatalytically-enhanced growth of CNTs from oxides.

In order to explore this expanded parameter space, a new CVD system that can facilitate multiple new gas vectors (such as specialty alkynes), allows introduction of ultraviolet light during CVD, and decouples substrate temperature from gas-phase processes is required. In the following chapter, the design and construction of such a system is presented.

Chapter 6

Development of a CVD System for Carbon Nanotube Growth Optimization

The unique challenges and opportunities posed by oxide nanopositors for enabling new applications for CNT growth requires expanded capability, contamination control, and modularity over legacy CVD systems used for CNT research. In this chapter, a new, modular system for CNT growth designed to expand the currently accessible parameter space attainable for CNT growth, reduce process irregularities, and incorporate *in situ* metrology during CNT growth is presented.

6.1. Parameter Space of Interest and Associated Challenges

As discussed in Chapter 5, several opportunities for improving growth of CNTs from zirconia (and possibly other nanopositors) have been identified. Use of specialty alkynes, introduction of ultraviolet light, and engineering oxygen deficiency (e.g., by Ar^+-ion sputtering) are all of great interest but difficult to explore without dedicated equipment. Demanding surface analysis needs and complications to differential experiments from contamination are major concerns. Promising approaches for low-temperature growth of CNTs on carbon fibers and other substrates (as described in the following chapters) leverage new CVD processes and feedstock blends. Growth of >1-mm tall CNT forests for applications such as

polymer nanocomposite research require improved reliability.[141,142] Thus, the following are desirable features for consideration in designing a system specialized for performing research in these and other emerging areas:

- Capable of delivering a wide range of novel feedstocks including specialty alkynes, liquid vapors, and carbon dioxide[46,100,114,143,144]
- Expandability, modularity, and configurability
- Decoupling of thermal processing of gas feedstock from thermal processing of substrates[145] (these are separate and unrelated optimization problems)
- Elimination of fenestrations for moisture perfusion
- Ability to incorporate *in situ* metrology for temperature monitoring and possibly Raman and/or IR spectroscopy
- Ability to quantitatively eliminate organic residues and contamination from the growth chamber
- Ability to introduce various forms of electromagnetic radiation, particularly ultraviolet light, into the growth process
- Automation of processing and reliable process feedback and control
- Control over process pressure

A system that incorporates these features was designed and constructed and is now in service growing CNTs. A description of the system architecture follows.

6.2. System Overview

In this section, the design considerations and implementation of the new CVD system is presented. The system is called "MANGO-TANGO", a loose acronym for "Mass flow controller Array for Nanostructure Growth Optimization" (a control box that manages gas flow and processing) and "Table-top Apparatus for Nanostructure Growth Optimization" (a quartz-body cold-wall reaction chamber), hyphenated to reflect the coupling of these two modules into one system (i.e., MANGO connects to TANGO). As such, the term "MANGO" used herein refers to the mass flow control boxes used in the CVD system and the term "TANGO" to the system's all-quartz-body reaction chamber.

6.2.1. Motivation and Design Philosophy

Design and construction of this system served multiple roles. First, it served to fill unmet research needs specifically required for research investigating CNT growth from oxides and other non-legacy nanopositors. Second, it served to provide a set of scalable, easily-manufactured/procured CVD tools (e.g., for mass flow control, liquid reagent bubblers, improved CNT growth reliability, etc.) for future research needs. Third, it served to provide a versatile platform for new research ideas where unorthodox concepts could be tried quickly and easily and ad hoc hardware could be connected without major hardware setbacks or complications.

In implementing these goals, a philosophy was embraced incorporating reductionist design (consolidate functions and reduce number of disparate parts), replicability (make it easy to copy and make more), tectonic construction (make it understandable by how it is built), and product longevity considerations (make it useful for future users with unknown research needs).

6.2.2. System Concept

The general concept behind the system is a versatile array of mass flow controllers connected in-line with a preheater that feeds into an all-quartz cold-wall reactor which may be optionally fit inside an ultraviolet photochemical reactor (Figure 6.1).

6.2.3. Special Features

The following include some of the special design aspects of the MANGO-TANGO system:

- Simultaneous delivery of up to 12 unique gases including liquid feedstocks (see Table 6.1)
- Solenoid-valve-controlled dual-manifold gas delivery system enables simultaneous hydrocarbon cracking ("preheating") of some gases and direct injection of others without hardware reconfiguration—for example, a cracked blend of C_2H_4/H_2 could be doped with propyne (which should be used directly) prior to delivering to feedstock blend growth substrate
- Virtually polymer-free design eliminates unpredictable process variations from oxygen and moisture perfusion—the only wetted polymers are Viton® and Teflon® o-rings (in the MFCs and at ultratorr

fittings) and a thin film of Dow-Corning® silicone high-vacuum grease sealing the top and bottom of the TANGO reactor

- Cold-wall design decouples substrate and gas conditioning
- Externalized sample heater heats substrates through a quartz tunnel, eliminating the potential for off-gassing or adsorption and re-release of contaminants from the substrate heater
- All-fused-quartz reactor enables introduction of ultraviolet radiation from multiple angles
- Flat optical access window facilitates real-time point-localized (3-mm resolution) temperature readings via a fiber optic infrared pyrometer, expandability for *in situ* Raman and infrared spectroscopy
- Designed for operation from 10^{-3} torr to over-atmosphere

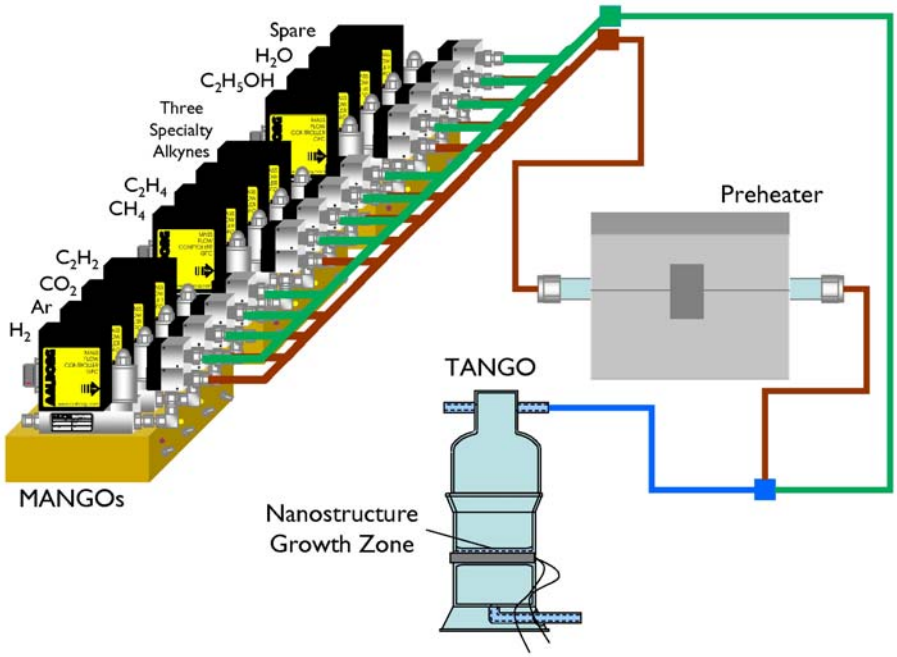

Figure 6.1 CVD system concept featuring dual-manifold gas flow management system, preheater, and all-quartz-body reactor.

6.2.4. Modular Mass Flow Controller Array Control Box ("MANGO")

The MANGO module serves to provide four vectors of gases by computer-controlled mass flow controllers (Aalborg Instrument and Controls, model GFC17S-VADN4-C0A, stainless steel body, 24 VDC, 1/4" compression

connection, 0-5 VDC input and output), each of which is independently divertible to the hot-wall preheater (Lindberg/Blue M MiniMite, T_{max}=1100°C) or to the cold-wall reaction chamber (TANGO, T_{max}=850°C) through a manifold comprised of two solenoid valves (Spartan Scientific, series 3900, fluoroelastomer o-ring, 1/8" NPT openings, see Figure 6.2). The housing for the module is a custom on-demand-manufactured hinged aluminum chassis (Figure 6.3). Dimensions for the chassis are provided in Figure 6.4 and Figure 6.5. The chassis houses:

- A 24 VDC/5 VDC (5.0 A/25 A) switching power supply
- Two LED driver circuit boards, each controlling two LEDs (Figure 6.6)
- Two panel-mount LED boards, each with two LEDs to visually communicate gas flow state by LED (off = disabled, red = idle, yellow = preheater manifold on, purple = reactor manifold on, white = both manifolds on) *(bottom)*. (Figure 6.6)
- Two lid-mounting combination data acquisition (DAQ)/switchboards that interface with mass flow controllers through DB-15 female connectors mounted in the lid, each board capable of addressing two mass flow controllers (Figure 6.6 and Figure 6.7)
- Two lid-mounting solid state relay boards that interface with the solenoid valves with four-pin female receptacle, each capable of addressing four solenoid valves (one per each manifold per mass flow controller) (Figure 6.6 and Figure 6.7)
- A central 5.0-A ten-port USB hub
- Four "gas enable" toggle switches
- Four micro-OLED screens, each with its own RS-232 to USB converter, plugged into the USB hub
- An IEC power entry module with breaker and illuminated power rocker
- A standard USB type B female data entry module
- An IEC power exit module
- A standard USB type B male data exit module

A photograph showing the interior component layout of a MANGO control box is shown in Figure 6.8. The MANGOs pass USB data connections to each other through a USB exit module on the right side of the box (Figure 6.9) via their internal 5.0-A USB hubs (powered by the box internal power supply), and 120-VAC power via an IEC power exit module (Figure 6.9).

Daisychaining is as simple as turning both the host and guest boxes on and sliding together. The daisychained MANGOs are then controlled by a computer through the DAQs. Once daisychained, the solenoid valves can be manifolded. To eliminate the possibility of moisture of oxygen perfusing into the system and causing unpredictable results, no polymer tubing is used in connecting the MANGOs to gas cylinders or to each other—only stainless steel tubing and flex bellows are used. Additionally, since the system uses acetylene and other alkynes, no brass or copper fittings are used anywhere in the system as to minimize risk of formation of explosive copper acetylide complex resulting from reaction of copper with acetylene. Currently, three MANGOs have been manufactured and provide 12 vectors of gases (Table 6.1) when daisychained together. A list of components used in the MANGO system is provided in Appendix B.

Calibration Gas	Flow Range	O-Ring	Intended Gas
	MANGO-1		
Hydrogen	0-1000 sccm	Viton	Hydrogen
Argon	0-1000 sccm	Viton	Argon
Carbon Dioxide	0-200 sccm	Teflon	Carbon Dioxide
Acetylene	0-200 sccm	Viton	10% Acetylene in Argon (Acetone-Free)
	MANGO-2		
Methane	0-1000 sccm	Viton	Methane
Ethylene	0-500 sccm	Viton	Ethylene
Argon	0-20 sccm	Viton	Vinyl Acetylene
Argon	0-50 sccm	Viton	1-Propyne
	MANGO-3		
Argon	0-200 sccm	Viton	Water Vapor in Argon (Bubbler)
Argon	0-50 sccm	Teflon	Ethanol Vapor in Argon (Bubbler)
Argon	0-50 sccm	Teflon	Spare
Argon	0-20 sccm	Viton	1,3-Butadiyne

Table 6.1 List of gas calibrations, flow ranges, o-ring type, and intended gases for mass flow controllers on the three MANGOs.

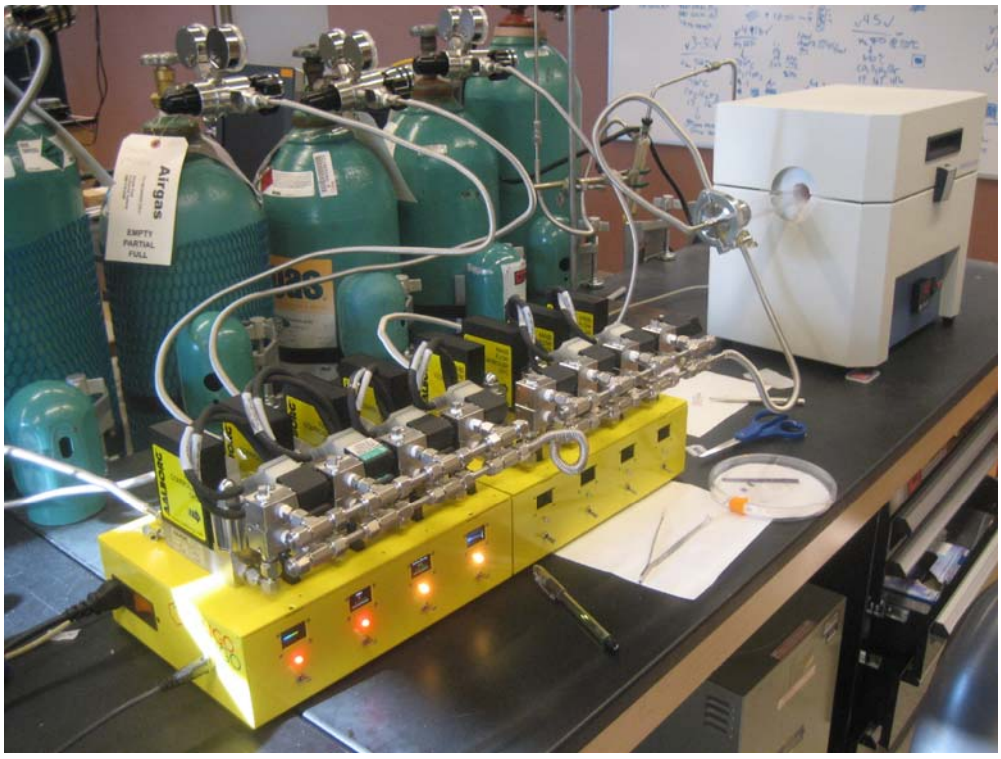

Figure 6.2 Two daisychained MANGOs with dual-manifold gas delivery system connected inline with the preheater module.

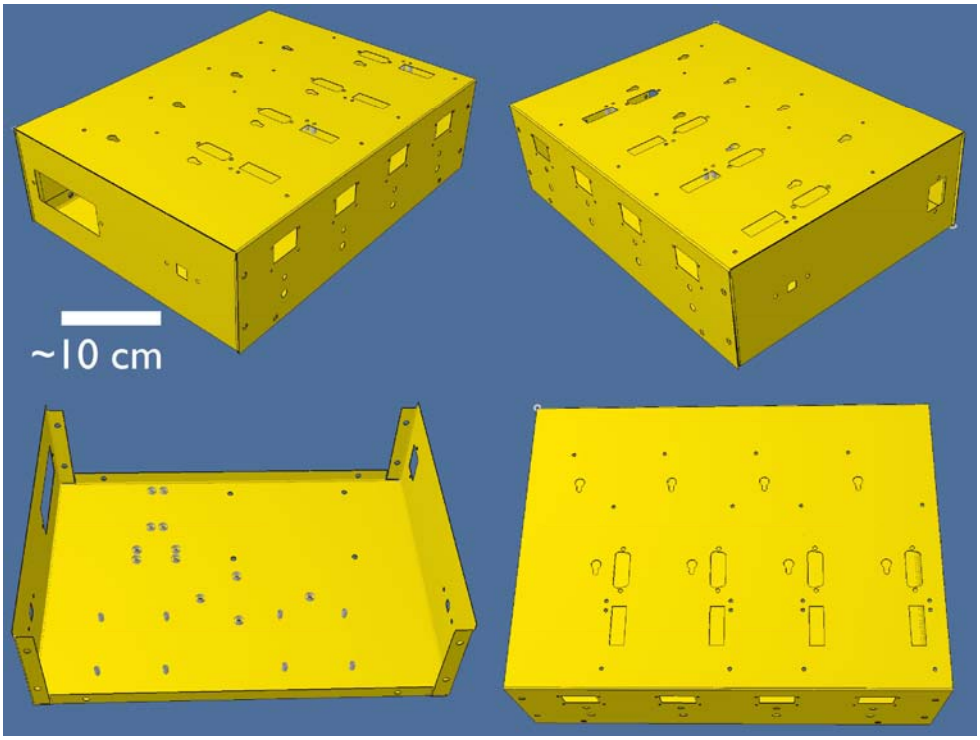

Figure 6.3 Renderings of on-demand-manufactured hinged aluminum chassis for MANGO.

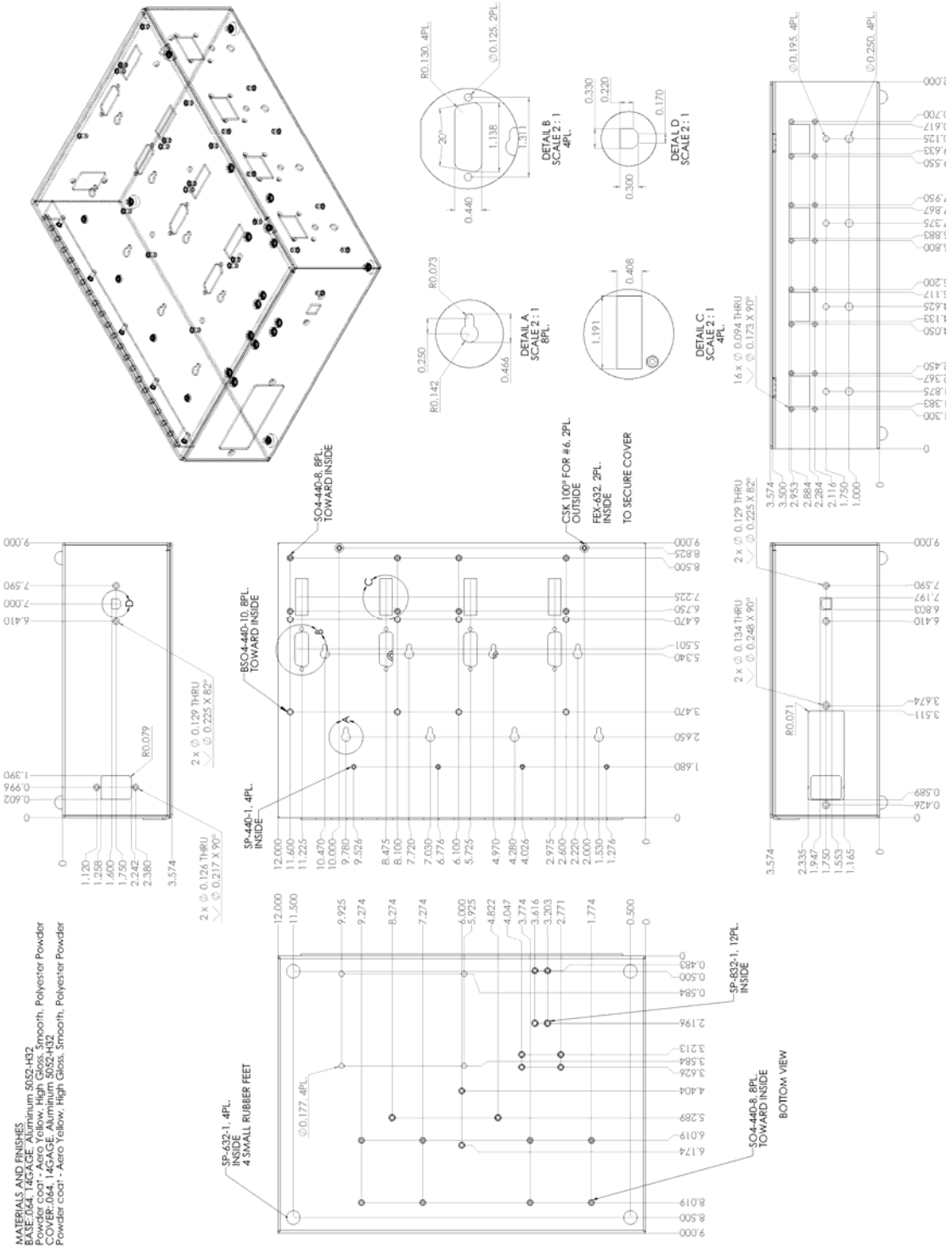

Figure 6.4 Dimensions and positions of standoffs for MANGO chassis (dimensions are in mm).

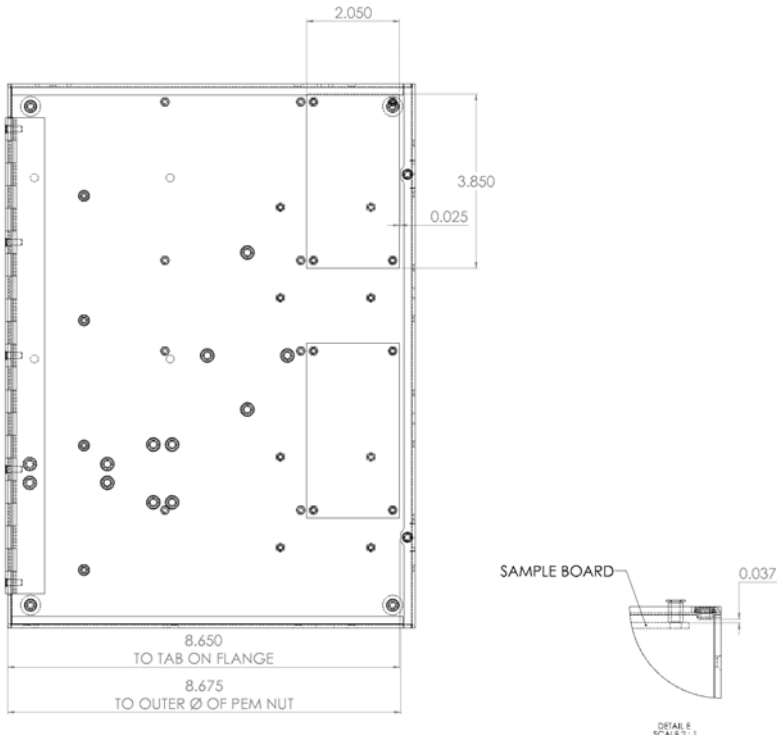

Figure 6.5 Dimensions and specifications for relay board lid mounting for MANGO (dimensions are in mm).

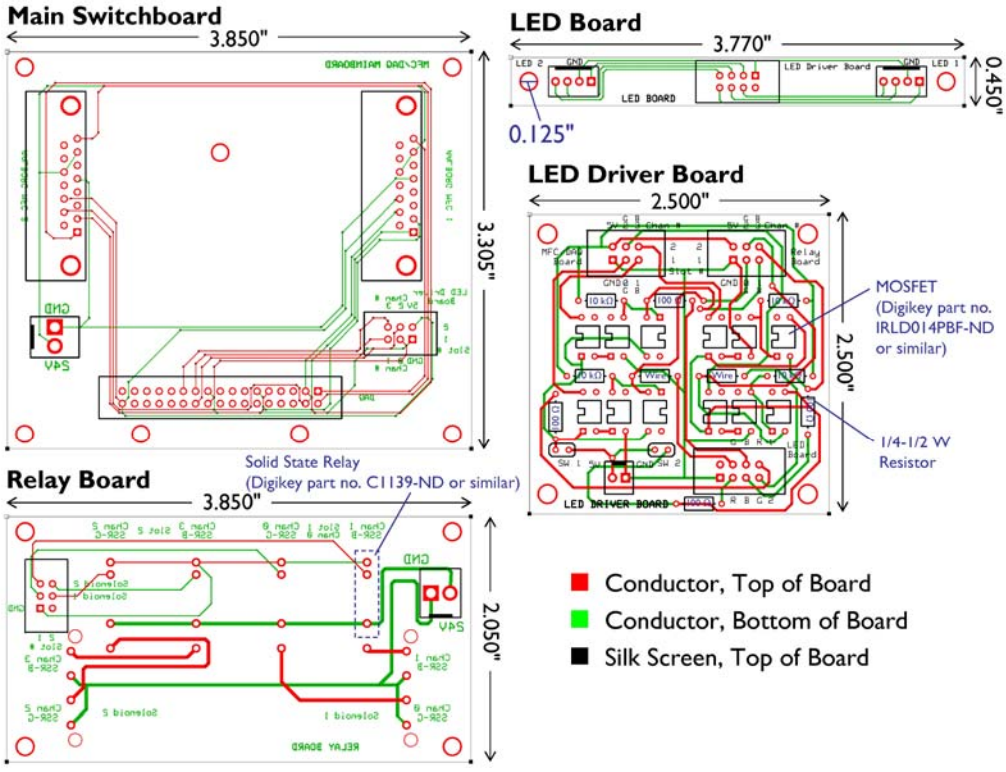

Figure 6.6 Circuit board layouts and dimensions for MANGO.

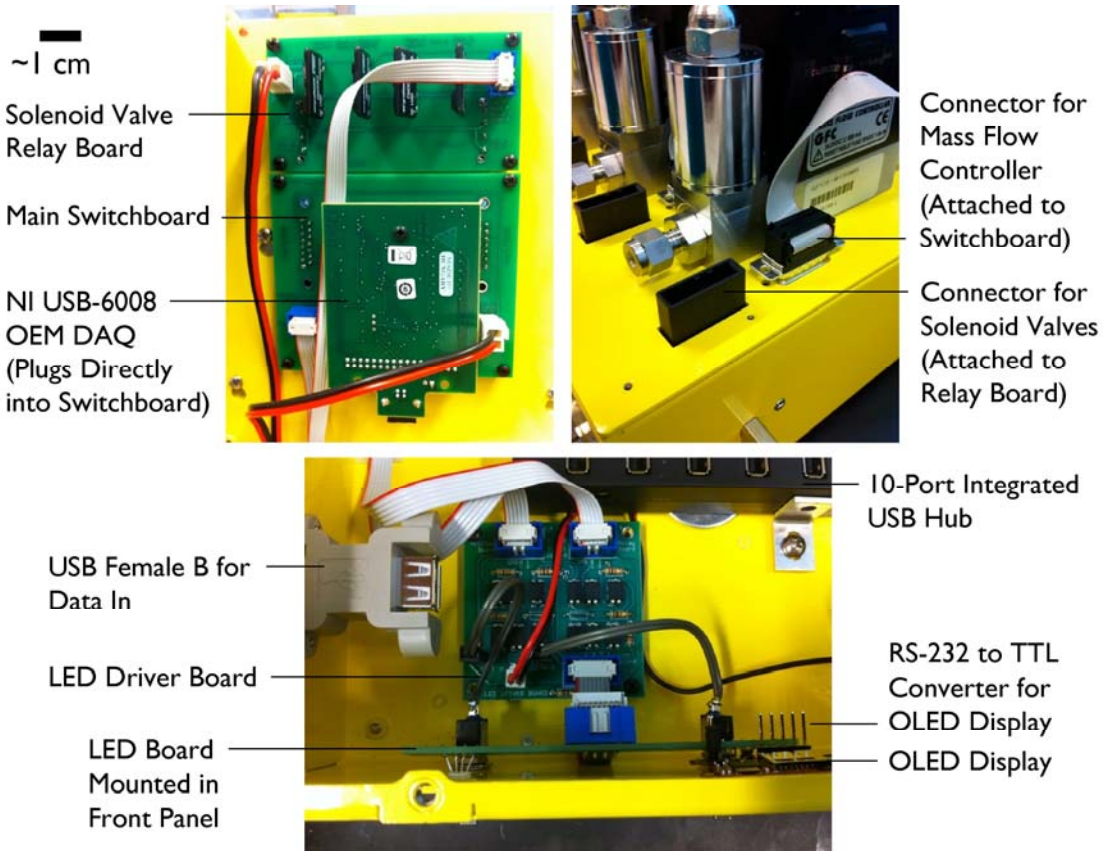

Figure 6.7 Detail of lid-mounted circuit board hosting data acquisition and switchboarding *(top left)* with integrated physical connectors for analog mass flow controllers *(top right);* detail of panel-mounted LED board and LED/toggle switch driver board *(bottom)*.

6.2.5. All-Quartz Table-Top Apparatus with Optical Access for Cold-Wall CVD ("TANGO")

An all-quartz cold-wall reactor (fused quartz 124, see Figure 6.10 and Figure 6.11) was designed to decouple feedstock processing temperature from substrate processing temperature and to facilitate introduction of ultraviolet light for photocatalytic CVD (PCVD) with oxide nanoparticles. The reactor was fabricated by G. Finkenbeiner Glassworks, Waltham, MA.

The reactor separates into a top and a bottom part that join via a ground-glass-type flange. A seal is made by applying silicone high-vacuum grease to this joint. A unique quartz tunnel penetrates the bottom of the reactor (Figure 6.12) so that a substrate heater may be inserted such that a substrate inside the reactor can be heated through the wall of the tunnel without the heater contacting the CVD atmosphere. A 2" heat pad (Micropyretics Heaters International, model HeatPad® 2", 100-120 W, >10 VAC) can be inserted into

this reactor and enables silicon wafer substrate temperatures upwards of 850°C as measured by a two-color pyrometer (Figure 6.13, described below). A higher power $MoSi_2$ element (up to 450 W) may be used if higher substrate temperatures are needed (e.g., if the pyrometer overestimates the actual substrate temperature). The top of the reactor has two 1/4" diameter connection ports; one for gas intake and one for a pop-safety valve. A flat optical access window is located at the very top of the reactor, through which the two-color pyrometer can look at the substrate. On the bottom of the bottom part is another 1/4" connection port for exhaust. Finally, if TANGO becomes contaminated or needs to be cleaned for an analytical study, it can be placed in a base bath and/or acid bath to remove contaminants or baked in an oven at high temperatures.

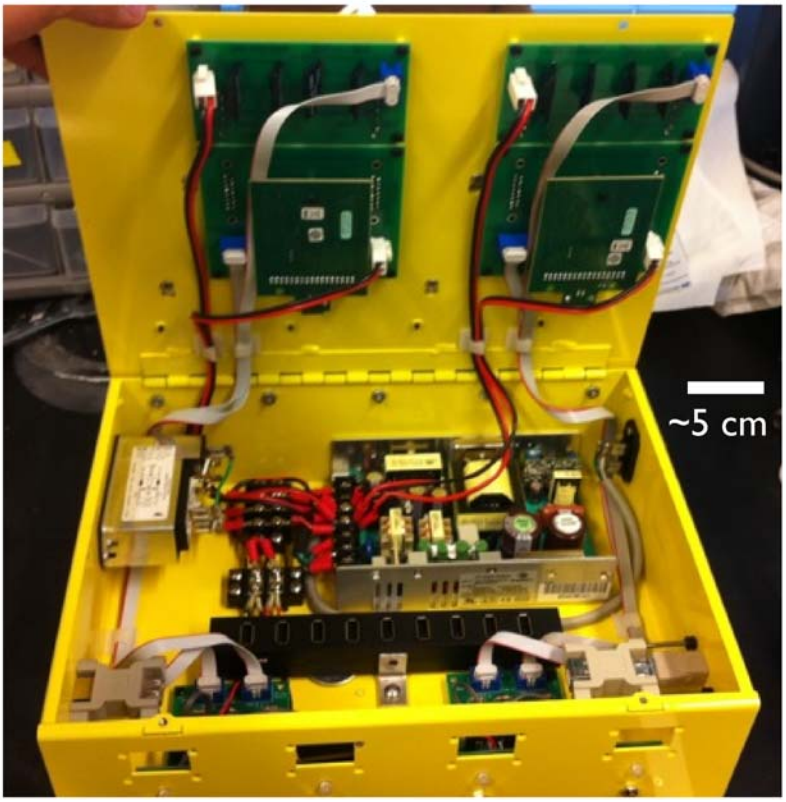

Figure 6.8 Interior layout of circuit boards, power supply, USB hub, and power/data entry modules.

6.2.6. Power Electronics and Feedback Control

Substrate temperature is measured in real time via a two-color pyrometer (Omega IR2P-300-53-C24, manufactured by Newport Electronics, Santa Ana, CA) with a quartz-fiber-optic sensor that enables 3-mm spot resolution at a distance of 225 mm from the target substrate through the optical access port

in the top of TANGO. The temperature controller for the pyrometer then communicates directly with the computer, which automates the temperature controller set point as well as the mass flow controllers and valves. The temperature controller sends a 4-20 mA proportional signal to a phase-angle-fired silicon controlled rectifier controller (MHI, model 9001). This throttles AC power to a transformer, which can be a 100-W 10 VAC transformer if the heat pad is used or a much larger 1600 W transformer (Figure 6.14) if a high-power $MoSi_2$ heating element is needed.

Figure 6.9 Near-complete MANGO control box: *(top left)* front of box showing gas enable switches, gas state LED, and OLED status update screens; *(top right)* back of box showing welded hinge; *(lower left)* power entry module and data entry module (standard USB type B female); *(lower right)* data exit and power exit modules for daisychaining.

6.3. Implementation

Implementation of the MANGO-TANGO CVD system is planned in two phases. In Phase 1, the system is configured with the preheater serving as hot-wall reactor for CVD reactions. Only two MANGOs are daisychained in this configuration. The system is calibrated with known CVD processes and

initial experiments with zirconia and low-temperature CVD are performed in anticipation of more advanced CVD processes to be performed in Phase 2.

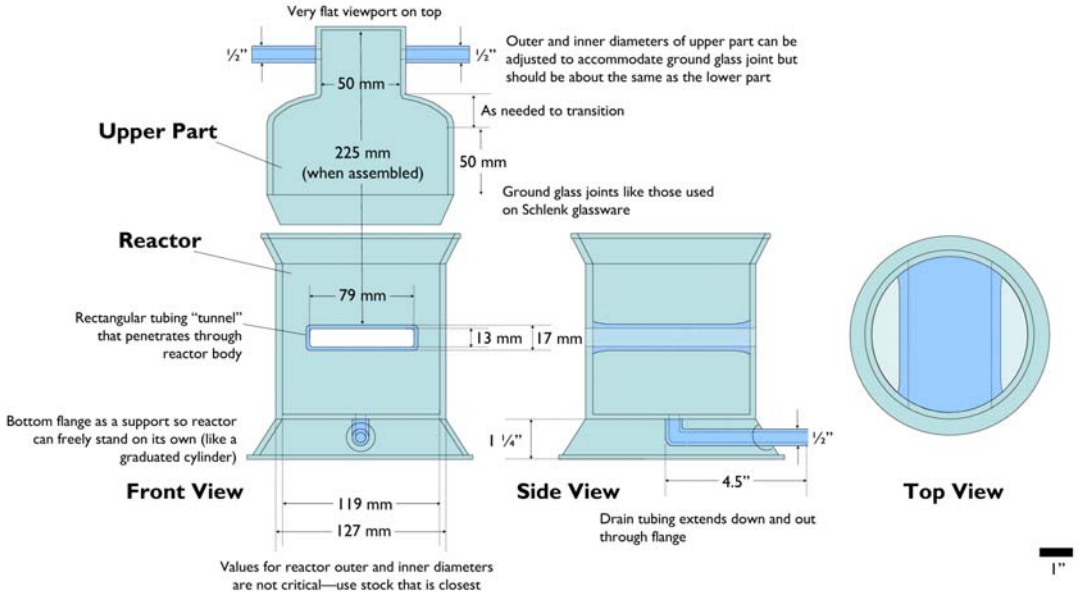

Figure 6.10 Dimensions of TANGO reactor (English units are presented where components are typically sized in English units for convenience).

Figure 6.11 Two-piece all-quartz TANGO reactor with substrate heater tunnel.

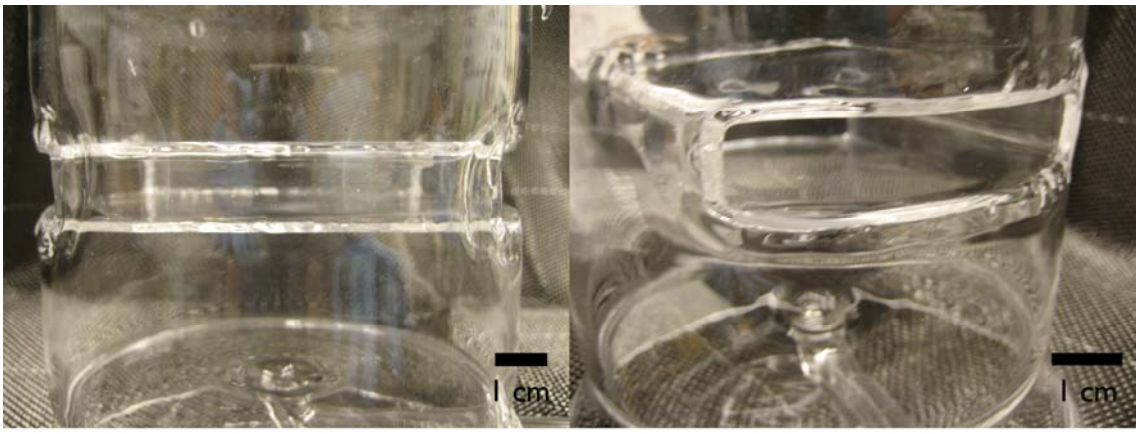

Figure 6.12 Detail of quartz tunnel for substrate heater in TANGO reactor bottom: (*left*) side view of substrate heater tunnel; (*right*) angled view of substrate heater tunnel showing its penetration through the reactor body.

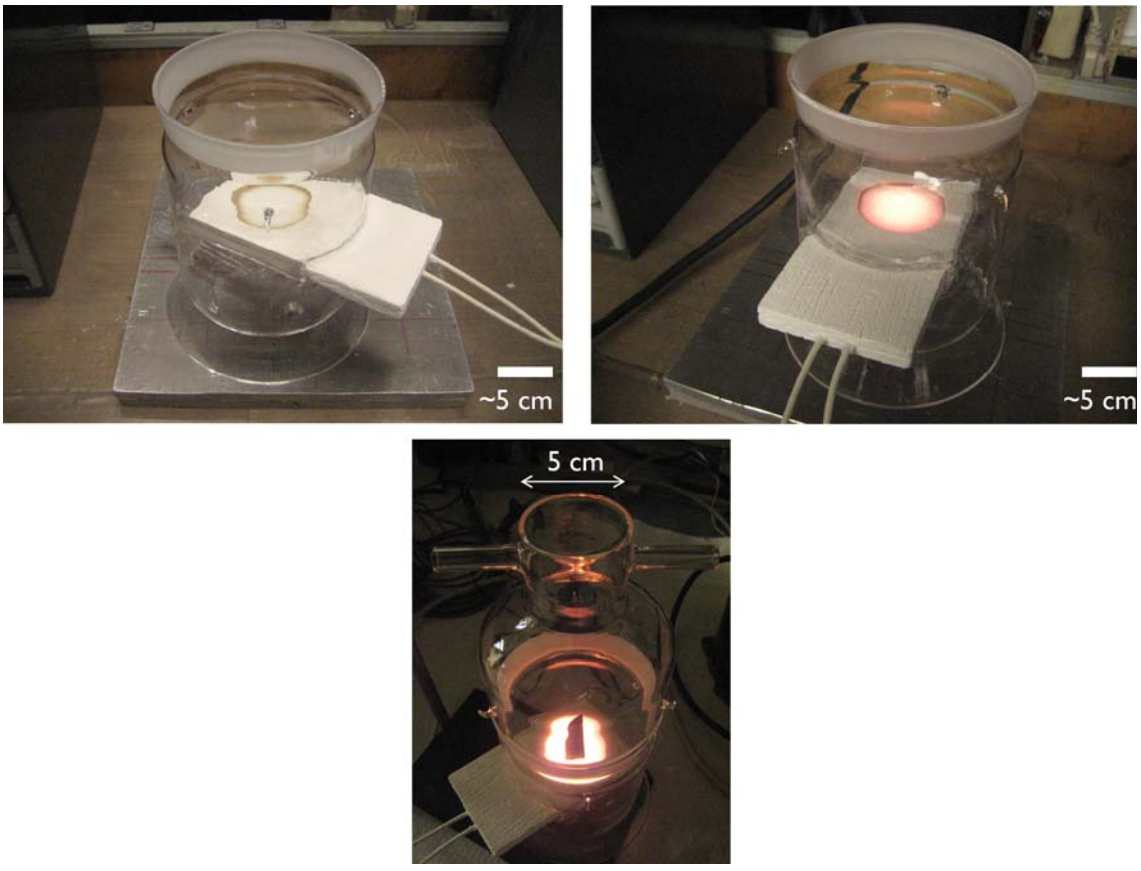

Figure 6.13 TANGO reactor with heat pad installed and operating at ~850°C (top optical access window remains at ~30°C).

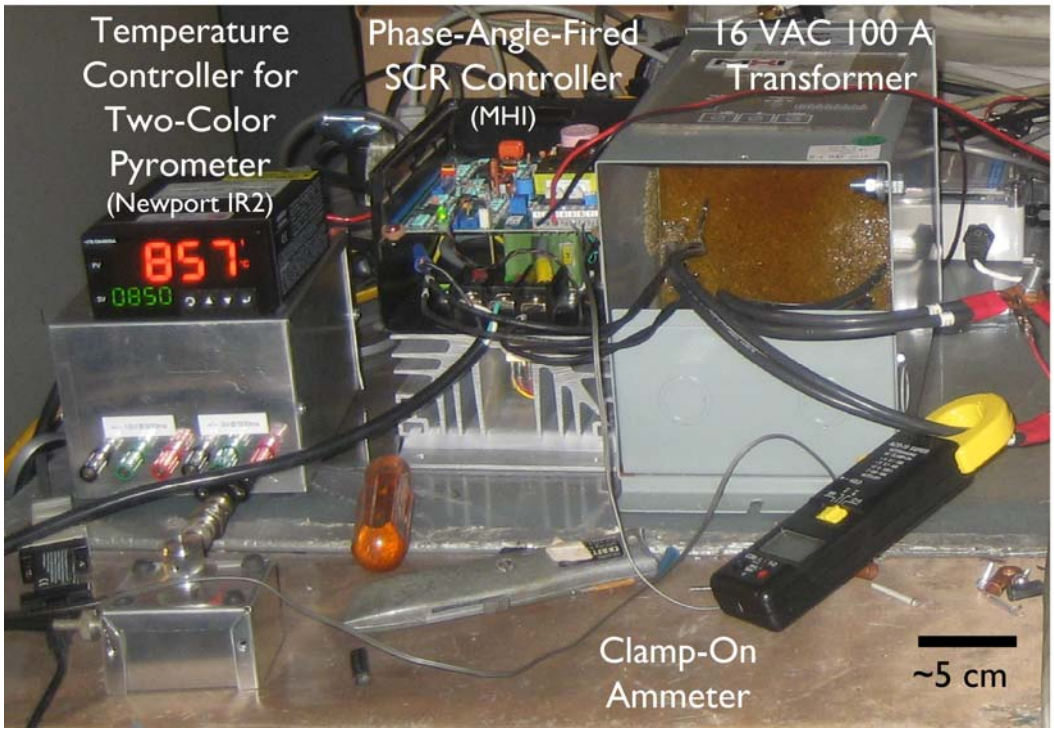

Figure 6.14 Power electronics configuration for controlling substrate heater; a 1.6 kW transformer is shown here for controlling high power-density $MoSi_2$ elements, however a smaller 100 W transformer may be used for the heat pad.

6.3.1. Phase 1: Hot-Wall Configuration and Testing

A CVD study was conducted to test system functions and to examine a recently reported low-temperature CVD process employing CO_2 and C_2H_2,[46] which were not previously available with other CVD systems in our laboratory. In this study, the optimal growth temperature for CVD growth of CNTs employing CO_2 and C_2H_2 in a 1:1 molar ratio was determined through a parametric study. Substrates were silicon wafers with a 10-nm Al_2O_3 support on 200 nm SiO_2 upon which 1 nm Fe had been e-beam evaporated. The system was configured with two daisychained MANGOs and with the preheater serving as a 1" electric clamshell furnace.

All gases used were ultrahigh purity grade (Airgas, >99.999%). In a typical process, a 0.5 cm x 0.5 cm wafer was placed in a fused quartz process tube (25 mm OD, 22 mm ID, 76 cm length) inside the furnace and positioned at 75% of the length of the quartz tube. The tube was flushed with 200 sccm Ar for 2 min prior to heating. Next, a flow of 400 sccm H_2 and 100 sccm Ar was introduced into the reactor. The substrate was then heated to the set point temperature (here, increments of 20°C between 680-820°C). Once reaching the set point, the Ar and H_2 were turned off and a flow of 167 sccm

10% C_2H_2 in Ar (acetone-free) and 17 sccm CO_2 were added. After 15 min, the C_2H_2 and CO_2 were turned off and the system was cooled under a flow of 200 sccm Ar to room temperature.

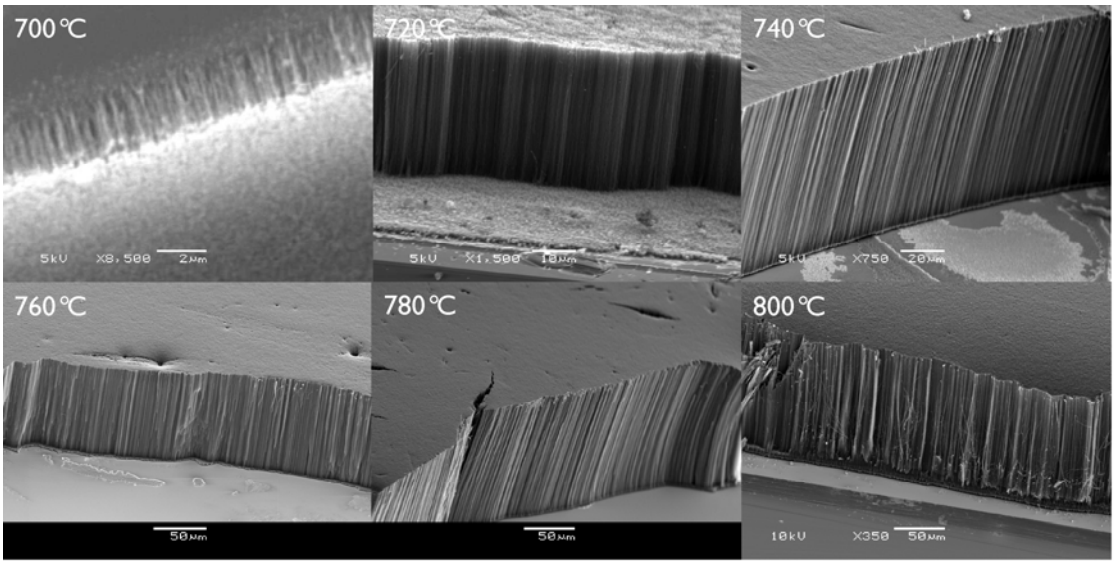

Figure 6.15 CNT forests grown with CO_2/C_2H_2 at temperatures ranging from 700°C to 800°C using the MANGO-TANGO system in hot-wall configuration (i.e., with the preheater serving as the growth reactor).

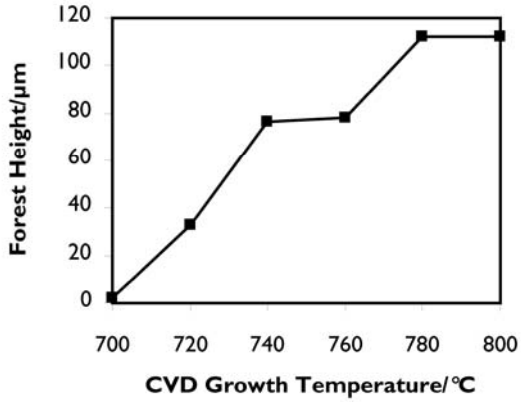

Figure 6.16 CNT forest height versus growth temperature used with CO_2/C_2H_2 CVD process; the optimal growth condition (factoring in forest quality) was found to be 760°C.

SEM images of forests grown with the CO_2/C_2H_2 process over the range 700°C to 800°C are shown in Figure 6.15 and a summary of forest height versus growth temperature is shown in Figure 6.16. The forests obtained were generally consistent in appearance and height with CNT forests observed by Magrez *et al.*[46] A flat, black mat of CNTs was achieved at 680°C. Appreciable forest growth was observed at temperatures of 720°C and

higher. For temperatures of 780°C and higher, however, the top of the CNT forest appeared dark gray and the forest became brittle. It is hypothesized that the CO_2 is corrosive to the CNT forests at these temperatures and is damaging them, creating defects that give rise to the dark gray color. Thus it was deduced that 760°C was the optimal temperature for maximizing CNT forest height but not compromising material quality with this process. Notably, Magrez *et al.* report 680°C to be the optimal growth temperature for Fe/Al_2O_3 catalysts.[46] As a result, this study provided a critical calibration point for their work, as a low-temperature CVD process for growth of CNTs from Fe catalysts on carbon was reported by them and of great interest for application on carbon fibers, but was reported as being performed at 400°C. Based on this calibration study, we calibrated their low-temperature result to be optimal at 480°C in our system. Indeed, this proved to be correct and is described in greater detail in Section 7.3.2.

6.3.2. Phase 2: Cold-Wall Configuration and Integration of Ultraviolet Radiation Source

In Phase 2, all three MANGOs will be daisychained and TANGO will be put into service. A calibration study using C_2H_4/H_2 CVD on Fe/alumina catalyst will be performed with TANGO to provide reference temperature calibration curves and to understand how hot-wall CVD processes translate to the cold-wall configuration. Following calibration, ultraviolet CVD will be attempted with zirconia and other nanoparticles.

6.4. Conclusions and Recommendations

A new CVD system that provides an extended array of gases, decouples gas processing temperatures and substrate processing temperatures, and incorporates ultraviolet irradiation has been developed. The core elements of the system have all been produced and tested. A system-level integration and calibration is now required in anticipation of advanced experiments with oxide nanopositors and photocatalytic CVD.

It is recommended that a vacuum module be developed and deployed on this system to enable process optimization for *in situ* XPS studies at the BESSY facility and to further expand the parameter space accessible with this system. Multiple TANGOs and alternative reaction chambers could be explored as well, making use of the modular design of the system. A wider diameter TANGO, for example, could enable larger-area growth on substrates such as Si wafers, ceramics, and carbon/carbon composites. A relay box to control automation of a vacuum pump, pressure control valves, a pressure sensor, the

ultraviolet reactor, and other system components is recommended and could be designed to daisychain with the MANGO arrays. Lastly, *in situ* spectroscopy should be pursued, as this system enables practical monitoring of CNT growth as growth happens, made possible by the all-quartz reactor and optical access window.

Chapter 7

Development of Coatings for Facilitating Carbon Nanotube Growth on Carbon Fibers

As discussed in previous chapters, carbon fibers present a challenging surface upon which to grow CNTs. Aspects including poor wettability, coupling of the fiber's mechanical properties to its surface morphology, and a lack of ability to facilitate formation of aligned CNT arrays necessitate technological intervention be taken to modify the fiber surface to produce fuzzy carbon fibers that meet the application requirements of hierarchical nanoengineered composite architectures.

This chapter describes efforts undertaken to develop conformal coatings for application on carbon fibers with the goal of facilitating various aspects of CNT growth not natively supported by as-manufactured carbon fibers. These efforts include development of:

- *Alumina barrier coatings* to facilitate growth of highly-aligned CNT arrays on carbon fibers and eliminate potentially deleterious catalyst-fiber interactions,
- *Polymer coatings* for non-covalently enhancing the wettability of the carbon fiber surface, and
- *Iron-loaded polymer coatings* for enabling low-temperature (sub 500°C) growth of CNTs.

7.1. Functional Coatings for CNT Growth on Carbon Fibers: Objectives and Approaches

As demonstrated previously by numerous publications,[19,20,35,37-40,44,46,146,147] growth of CNTs on carbon fibers can be achieved via several techniques, to date most commonly employing some method involving loading of catalyst or catalyst precursor directly onto the fiber surface. These include application of aqueous catalyst ions via incipient wetness techniques (e.g., dip-coating),[19,20,35,38,44] *in situ* deposition of Fe nanoparticles during CVD growth of CNTs via vapor-phase decomposition of organometallic iron complexes (such as a process that employs xylene/ferrocene),[21,37,40] and e-beam evaporation of Fe metal onto the fiber surface.[45] In each of these approaches lie substantial process disadvantages, however. Incipient wetness techniques require a wettable surface in order to attach ions to the fiber surface, necessitating aggressive surface oxygenation of the carbon fiber through, for example, acid or electrochemical etching. Such processing in turn alters the fiber surface morphology and consequently can reduce the fiber's ability to transmit tensile load. Additionally, each of the aforementioned catalyst application approaches result in direct contact between catalyst and fiber thereby providing a configuration in which (detrimental) high-temperature interactions such as carbide formation or catalytic restructuring of the fiber surface can occur. Furthermore, in each case the resulting CNT array morphology is unaligned ("scraggly"), where aligned CNT morphologies would be more advantageous for nanoengineered composite architectures. In the case of aligned CNT growth from Fe on alumina supports, CNT alignment is enabled by the presence of a plurality of small, active Fe catalyst nanoparticles distributed in a high density over the alumina surface.[70] This surface serves as both a textural support and a solid-state electrophile, which is believed to increase the proportion of particles that are active towards CNT growth. The smooth, graphitic surface of a carbon fiber provides neither of these features, thereby tending CNT growth from catalysts placed directly on its surface towards unaligned morphologies.

Coatings can be used to provide an alternative textural and/or chemical surface over the geometry of a fiber without disrupting the chemistry or microstructure of the fiber. For composites applications, the following missing functionalities were identified as targets for coatings design parameters:

- Promotes CNT alignment
- Prevents catalyst nanoparticles from interacting with the fiber surface

- Improves wettability towards ions and depositions mediated by polar intermediates
- Reduces temperature required for CNT growth

Simultaneously, in order to circumvent problems encountered in previous approaches and to maximize the potential for enabling aerospace-scale composite specimens (including laboratory-scale composite coupons for mechanical standards testing) and future large-scale industrial manufacture, the following guidelines were placed on the coating design process:

- Should avoid chemical modification of the carbon fiber surface
- Must not jeopardize the tensile properties of the carbon fiber outright or upon thermal/thermochemical processing (e.g., CVD growth of CNTs)
- Must be potentially scalable to a large-scale continuous process
- Must be extensible to both fiber tows and weaves

With these objectives and guidelines in mind, it was decided that coating efforts would be focused on unsized (i.e., never-sized) intermediate-modulus (high-tensile-strength) carbon fiber tows obtained from industrial supplier TohoTenax (fiber HTR-40) and another major aerospace-grade carbon fiber manufacturer (fiber AS4). Use of unsized fibers avoids potential chemical changes and/or damage arising from thermally or chemically desizing commercially-available fiber tows. It should be noted that unsized fibers are not normally commercially available as sizing is needed to prevent abrasion and tangling of fiber tows during winding and handling and to protect the quiescently engineered oxygenated surface chemistry of the carbon fiber (installed during manufacture to improve bondability of the fiber with matrix resins) from changing over time. This said, sizings as they are known today may prove to be unnecessary in composites prepared with fuzzy carbon fibers, as CNT-cushioned fibers would not self-abrade the way native carbon fibers do and CNT arrays may eliminate the need for an oxygenated surface chemistry by serving as an "active sizing" that facilitates bonding with resins via capillarity-driven wetting.[47] As such, the fibers used in this work, obtained specially through industrial liaisons, were spooled from their respective production lines prior to the surface oxygenation and sizing steps typically performed in their manufacture.

Lastly, following from the design guidelines listed above, the following techniques were avoided in the coatings development process:

- Acid, base, or electrochemical etching of fibers, not including acidic or alkaline processing steps that are non-etching in nature—damages fiber surface
- Vapor-borne catalyst deposition during CVD—hazardous and chemically aggressive, occurs >800°C
- E-beam evaporation—expensive and difficult to scale

To meet the objectives of promoting CNT alignment and preventing catalyst-fiber interactions, a conformal alumina barrier coating was selected as a desirable coating target. Towards this target (Section 7.2), the processing techniques of sol-gel deposition (Section 7.2.1), electrodeposition (Section 7.2.2), and chemical vapor deposition (Section 7.2.3) were explored. To meet the objective of enhancing wettability without chemically modifying the fiber surface, non-covalent functionalization via polymer deposition was explored (Section 7.3). Finally, to meet the objective of enabling lower CNT growth temperatures, a low-temperature CVD process was identified and a coating technology to facilitate this process was developed (Section 7.3.2). Low-temperature (<500°C) CVD growth of CNTs was recently described by Magrez *et al.* employing oxidative dehydrogenation of acetylene with carbon dioxide over Fe-containing catalysts.[46] This process has been reported to be effective over a range of 400°C to 800°C, depending on the composition of the substrate supporting the nanoparticle catalyst. Conveniently, the lowest-temperature growths reported were observed with Fe-based catalysts on carbon supports. As such, polymer-based coatings that simultaneously facilitate wetting of the carbon fiber surface by iron ions and can be subsequently pyrolyzed to provide a sacrificial carbon support were explored.

7.2. Alumina Barrier Coating Development

Alumina is widely used as a support for Fe catalysts in the growth of aligned CNT arrays.[47,70,115,143,148] Alumina serves as both a textural support to stifle particle coarsening of Fe catalyst nanoparticles to maintain a closely-spaced population of small nanoparticles to facilitate growth of the high areal density of CNTs needed for an alignment event as well as a solid-state acid (electrophile), believed to enhance catalytic activity at the feedstock-nanoparticle-support interface.[70,115] Aligned CNTs, to the best of our knowledge, had not yet been demonstrated with carbon-supported catalysts. In the case of carbon fibers, an alumina coating would not only serve to add this functionality to the fiber surface, but also to serve as a barrier to prevent Fe catalyst nanoparticles from chemically interacting with the fiber surface,

for example, by making carbides or dissolving carbon from the surface upon heating.

Here, sol-gel-, electrodeposition-, and CVD-based processes for depositing alumina (and to a lesser extent, silica) coatings onto carbon fibers are explored and characterized for their efficacy in facilitating aligned CNT growth.

7.2.1. Sol-Gel Deposition of Alumina

Sol-gel processing is a method for producing materials using solution-based chemistry at ambient or near-ambient conditions.[149] The term refers to a process in which solid nanoparticles dispersed in a liquid (i.e., a sol) agglomerate together to form a continuous three-dimensional network that extends throughout the liquid (i.e., a gel).

Most sol-gel processes begin with a solution containing reactive monomers appropriate for producing the target material (e.g., an organometallic such as an alkoxide, one ore more polymerizable organics, etc.). The monomers in this solution are then chemically, thermally, or photolytically invoked to undergo polymerization. The result of this polymerization event is the formation of a plurality of nanostructured particles throughout the liquid. Alternatively, nanostructured particles can be manufactured by another process and then dispersed in a liquid to create a sol. The nanostructures in the solution are then further invoked to agglomerate through sustention of the polymerization event (if applicable), introduction of a chemical, thermal, or photolytic stimulus, and/or allowing mutual attractive forces among the nanostructures to cause the nanostructures to adsorb and/or bond to each other. As nanostructures continue to agglomerate together, the viscosity of the solution increases until reaching infinity, at which point a porous, three-dimensional network of interconnected nanostructures spans the volume of the liquid medium; this sol-gel transition is the gel point, the product of which is a gel material. Further maturation of the gel network generally continues after the gel point is reached, as reactive materials are still present throughout the pore liquor (the volume of liquid within the pore network).

After an optional, controlled aging process to allow the gel network to fully develop, the pore liquor may be diffusively exchanged with a (or a series of) pure solvent(s) to purify the gel network. If the target material is a solid, the pore liquor must next be removed to isolate the solid component of the gel. The gel network is both nanostructured and substantially nanoporous and presents a high-surface-area chemical functionality over its sponge-like skeleton. If the pore liquor is removed evaporatively, capillary stresses will evolve at the solid-liquid interface as the liquid-vapor interface penetrates

into the pore network (i.e., the liquid leaves the gel network). If the modulus of the gel network cannot resist the capillary stresses that result from this phenomenon, the gel network will collapse in on itself and densify into a solid with substantially less porosity than the starting gel. If the surface chemistry of the solid network is self-interactive (such as a hydroxylated surface), the gel network will stick to and possibly chemically bond to itself; this results in irreversible collapse of the gel network. Alternatively, if the surface chemistry is substantially non-interactive (such as a trimethylsilylated surface) or has been chemically passivated prior to drying (for example, by reacting surface hydroxyl groups with trimethylchlorosilane), the gel network can recover the majority of its original volume through a process know as spring back. Instead of evaporatively drying the gel network, the gel can be lyophilized by supercritical or freeze drying. In supercritical drying, the liquid in the pore network is heated and pressurized above its critical point, where its surface tension becomes zero thereby losing its ability to exert capillary stress. At these conditions, the supercritical fluid in the pore network can be removed through quasi-isothermal depressurization without causing collapse of the gel network. In freeze drying, the pore liquor is frozen and subsequently sublimed to leave behind the solid component of the gel network. Regardless of how the material is processed, if the resulting material exhibits <50% porosity, the product is called a xerogel ("xero" from the Greek for "dry" and "gel" from the Greek for "frozen"). If the product is open-celled, primarily mesoporous (i.e., primarily exhibits pores ranging from 2-50 nm across), and exhibits no less than 50% porosity, the material is called an aerogel.[150]

Following drying, the xerogel or aerogel may be further processed. The material may be thermally treated to reduce residual porosity from the material, sinter constituent particles, and/or invoke a solid-state phase change of the material. In the case of aerogels, the materials may be thermally processed to produce a secondary aerogel (such as pyrolyzing an organic polymeric aerogel to produce a carbon aerogel) or chemically processed to change its surface chemistry (for example, to render a hydroxylated surface hydrophobic).

Sol-gel has the advantages of enabling deposition of a wide variety of materials in coating or monolithic form. Historically, sol-gel processing focused on the production of ceramic materials, which otherwise require tremendous energy and high temperatures to produce, and specifically metal, metalloid, and mixed-matrix oxides. Sol-gel processing poses a number of challenges that should be taken into consideration in the development of a coating, however. Sol-gel-derived materials, borne from liquid-based solutions, frequently undergo substantial mass loss during drying which

results in contraction of the material due to capillary stresses (as described previously). When a sol-gel-derived material shares an interface with a stiffer material (such as a carbon fiber) as it is dried, it may undergo severe cracking and leave bare the underlying substrate where volume loss results in recession of the material from the substrate. This is a potential disadvantage in considering production of sol-gel-derived alumina coatings for carbon fibers. This said and as mentioned, defective (non-stoichiometric), rough alumina has been found to be more effective in facilitating CNT growth than crystalline alumina.[115,151] Sol-gel-derived alumina coatings are both stoichiometrically imperfect, usually presenting hydroxyl-terminated surfaces as-deposited, and generally exhibit high surface areas, arising from their highly porous precursors. These features, in addition to ambient-temperature processing and solution-based deposition, make sol-gel a highly appealing approach to depositing alumina coatings on carbon fibers.

In the 1970's, Yoldas demonstrated production of transparent sol-gel-derived alumina materials via controlled hydrolysis of aluminum alkoxides such as aluminum tri-*sec*-butoxide (ATSB).[152] In this approach, ATSB, a highly viscous, readily-hydrolyzed liquid, is dissolved in an alcohol and hydrolyzed with water. Acid is then added and heating is applied to solubilize the resulting precipitate, which subsequently undergoes gelation. Due to the easily-hydrolyzable nature of ATSB, however, it is reasonably challenging to obtain reproducibility from this process. Recently, Tillotson, Gash, Baumann, and coworkers at Lawrence Livermore National Laboratory rediscovered and refined a versatile method for preparing a wide variety of metal oxide gels including alumina employing epoxide-assisted gelation of metal salts.[153,154] In this process, an anhydrous or hydrated metal salt such as a chloride or nitrate are dissolved in one of many solvent systems, most commonly water and/or an alcohol. An epoxide (oxirane) such as propylene oxide or epichlorohydrin is then introduced, resulting in a gradual rise in solution pH. The metal salt is then slowly hydroxylated and undergoes water condensation reactions with neighboring metal centers, giving rise to metal-oxygen-metal bridges. As this polymerization process proceeds, a hydroxyl-terminated metal-oxide gel forms. Not only is the epoxide-assisted method more reliable than alkoxide-based methods for metals and metalloids with easily-hydrolyzed alkoxides, but the resulting materials are often much more homogeneous, transparent, and can be tailored more effectively.

Another set of approaches for preparing sol-gel coatings involves producing a sol, depositing the sol onto a substrate, and then thermally sintering the sol to produce a contiguous film.[155,156] These "baked-on" approaches typically result in denser (less porous) materials, however are less

likely to undergo volume contraction, as the starting materials do not have an appreciable pore network that collapses upon drying. Furthermore, coating thickness can be controlled through multiple depositions and adjusting solution concentration.

In this section, methods for depositing alumina over a fiber from epoxide-assisted sols and gels (Section 7.2.1.1) and alkoxide-based sols and gels (Section 7.2.1.2) are explored. Silica coatings produced through alkoxide-based gelation are also considered as an alternative to alumina and are explored in Section 7.2.1.3.

7.2.1.1. Alumina Coatings from Alkoxide-Free Epoxide-Assisted Sol-Gel Processes

Epoxide-assisted gelation of metal salts is to date the most versatile approach for preparing metal oxides via sol-gel processing. Historically, metal and metalloid alkoxides have been employed as monomeric precursors for preparing oxide gels, aerogels, glasses, and ceramics. For silica this approach works well, however for most other oxides (such as alumina, iron oxide, and most other transition metal oxides), the available alkoxide precursors are too easily hydrolyzed to yield monolithic, well-controlled materials and are also often very expensive or not readily available commercially. Aluminum alkoxides can be used to prepare monolithic and even transparent gels and glasses,[152,157] but are difficult to work with and make scaling to an atmosphere-friendly process challenging.

Alternatively, epoxide-assisted gelation of an aluminum(III) salt in water- or water/alcohol-based solutions can be performed more easily and with better reproducibility than with alkoxides, resulting in higher quality products at a lower cost. Baumann *et al.* demonstrated a method for preparing high-surface-area alumina gels using $AlCl_3 \cdot 6H_2O$ with propylene oxide (methyloxirane) in water or 50/50 vol % water/ethanol mixture.[154] This method is explored here for its utility in facilitating aligned CNT growth on carbon fibers.

As described below, however, the propylene-oxide-assisted method results in alumina gels that undergo substantial volume loss due to syneresis (the process by which liquid is expelled from a gel as the gel network strengthens and consolidates). It was determined experimentally that this could be mitigated by replacing propylene oxide with another epoxide, namely epichlorohydrin (chloromethyloxirane). A new formulation incorporating this epoxide was developed and explored here.

Materials

Aluminum chloride hexahydrate ($AlCl_3 \cdot 6H_2O$, Sigma-Aldrich product number 237078, 99%), aluminum nitrate nonahydrate ($Al(NO_3)_3 \cdot 9H_2O$, Sigma-Aldrich product number 237973, ≥98%), (±)-propylene oxide (C_3H_5O, Sigma-Aldrich product number 110205, 99%, or 82320, ≥99.5%), anhydrous absolute ethanol (C_2H_5OH, Pharmco-Aaper product number 111000200, ACS/USP grade), 2-propanol (isopropanol, Mallinckdrodt Chemicals product number 3032-16, ACS grade), (±)-epichlorohydrin (C_3H_5OCl, Sigma-Aldrich product number 240699, ≥99%), and analytical reagent grade deionized water (Ricca Chemical Company product number 9150-1) were used as received. All reagents were measured by weight instead of volume to ensure reproducible results.

Sol-Gel Deposition of Alumina via Propylene-Oxide-Assisted Gelation

Various propylene-oxide-based formulations were developed to control gel time in order to better control processing. In the best process, 2.96 g $AlCl_3 \cdot 6H_2O$ was dissolved in a mixture of 20.0 g (20.0 mL) deionized water and 20.0 g (25.4 mL) 2-propanol. The mixture was stirred until the salt had fully dissolved. Next, 7.86 g (9.5 mL) propylene oxide was added slowly into the solution via syringe with stirring. The solution was then stirred another 5 min and allowed to solify. Gel time was ~4 h. Alternatively, a solution of 10.0 g (10.0 mL) deionized water and 7.89 g (10.0 mL) absolute ethanol could be used. In this case the gel time was reduced to ~1 h 40 min. Gel time could be further adjusted for either of these processes by increasing the amount of solvent used, however this also results in an increase in porosity.

Sol-Gel Deposition of Alumina via Epichlorohydrin-Assisted Gelation

A solution of 15.78 g (20.0 mL) ethanol and 4.52 g (4.52 mL) H_2O was prepared. To this solution was added 2.96 g $AlCl_3 \cdot 6H_2O$ with stirring. With this solution placed on a balance, 12.52 g (10.58 mL) epichlorohydrin was added slowly by a syringe with an 18-gage needle (at a rate of a few drops per second). The solution was then stirred for another 5 min. Gel time is approximately 120 min. The density of the gel could be lowered by adding more ethanol. At least the amount of water specified here is required to dissolve all of the $AlCl_3$, however if water is added until the solution is >30-40% water by volume, the epichlorohydrin will separate into a second phase and no gelation will occur. Similarly, when using barely enough ethanol to get the solution into a single phase, the solution may spontaneously become hazy and epichlorohydrin may separate out due to evaporation of the ethanol.

Application of Alumina Sol- and Gel-Based Coatings onto Carbon Fibers

Unsized (i.e., never-sized), never-surface-treated carbon fiber tow (TohoTenax product number HTR40 N00 24k 1550tex) was used for substrates. (*Note:* This product was obtained through industrial liaisons and is not available commercially. The equivalent commercial version, HTA40 F22 24k 1550tex, is surface-treated and sized.) Carbon fiber tows (~10 cm long) were cut and taped at one end with masking tape (3M 2600) for ease of handling. Tows were soaked in freshly-mixed alumina sol and removed at fixed time intervals: for 45-min gel times, samples were removed at 15 min, 30 min, and right at gelation; for 4-h gel times, samples were removed at 1 h, 2 h, and right before gelation; for 120-min gel times, samples were removed at 30 min, 1 h, and right at gelation. Next, a screw-top Erlenmeyer flask containing just enough of 2-propanol or ethanol (the same solvent used in the sol-gel process) is used to provide a pool ~1-cm deep at the bottom. Samples were then taped to the top of the screw-top cap for the flask and screwed into place. This provided a solvent-saturated atmosphere to allow sol coating on the fibers to gel without drying out. Once the gel point had been reached, samples were optionally soaked under 2-propoanol or ethanol, respectively. This ensures excess water and leftover reactive materials are removed from the pore network as to minimize syneresis of the gel coating. Finally, the alumina-gel-coated fibers were optionally hung and allowed to dry in air.

Application of Catalyst to Alumina Coatings and Subsequent CVD Growth of CNTs

Alumina-coated fibers were then dip-coated with 0.050 M $Fe(NO_3)_3 \cdot 9H_2O$ in 2-propanol (Fe^{3+}/IPA). Some alumina-coated fibers were dip-coated before the coating was dry, others were dip-coated after it was dry. After dip-coated with catalyst solution, fibers were hung and allowed to air dry. Once the tow was dry and ready for further processing, the taped end was cut off.

To determine the efficacy of the alumina coating for growing CNTs, the tow was CVD processed for CNT growth. CVD growth of CNTs was performed in a fused quartz tube (54-mm outer diameter, 50-mm inner diameter, 137-cm length) heated by a three-zone split-hinge tube furnace (Lindberg/Blue M model HT55667C, 30-cm heated zone lengths). (*Note:* Due to the distance between thermocouples in this furnace and how a 54-mm process tube sits in this furnace, reported temperatures may underestimate actual process temperatures by ~80°C as determined by calibrations performed with *in situ* thermocouple measurements. Throughout this thesis, set points for this furnace will be cited in methods and processes and the actual calibrated temperature will be used for data processing and analysis.) In a typical process, specimens were placed in a fused quartz process tube at the center of the third zone. The tube was then flushed with a flow of 2070

sccm He for 10 min to displace oxygen from the tube. Next, He was turned off and a flow of 1040 sccm H_2 gas (Airgas, ultrahigh purity grade, >99.999%) was introduced. The sample was then heated to 650°C under H_2 gas over the course of ~8 min to reduce iron oxide nanoparticles on the specimen to catalytically-active iron. The sample remained at these conditions for an additional 7 min to further reduce remaining iron oxide nanoparticles. A flow of 316 sccm ethylene (Airgas, ultrahigh purity grade, >99.999%) was then added for 5 min to facilitate CNT growth. Lastly, H_2 and C_2H_4 were turned off and the sample was allowed to cool to room temperature under a flow of 2070 sccm He.

Results

Carbon fibers were coated with alumina gel produced by reaction of aluminum(III) chloride with propylene oxide. The gel coating was then evaporatively dried in air, coated with Fe^{3+}/IPA, and CVD processed for CNT growth. A high yield of bundles of aligned CNTs is observed over the surface of the fibers (Figure 7.1). The bundles are present as worm- and shell-shaped formations, each one a microscopic CNT forest. This growth result is very close to the ideal architecture for composites applications. Unfortunately, such bundles are only observed where alumina is present on a fiber. SEM imaging of the coating shows the alumina loses a substantial amount of volume on drying, leaving chunks of alumina clinging to the fibers and leaving most of the surface area in the tow bare. Gel monoliths prepared with this same sol-gel process were measured to lose ~50% of their volume after syneresis and 90% of that remaining volume upon drying, totaling ~90-95% of the volume of the original gel coating.

In effort to mitigate volume loss, alternative formulations were explored. Both aluminum(III) nitrate and aluminum(III) chloride yielded similar volume loss due to syneresis, suggesting it is the solvent or epoxide that controls syneresis. Changing the solvent from 50/50 vol % water/ethanol to 100% ethanol resulted in better volume retention after gelation, but extended the gel time to 8-12 h. Additionally, the effectiveness of propylene oxide degraded soon after first use of the reagent due to hydrolysis from the atmosphere making reproducibility a problem. An alternative formulation based on epichlorohydrin was then developed and addressed both volume loss (10-20% following syneresis, arrestable by placing the gel in ethanol as soon as it is formed) and irreproducibility arising from hydrolysis of propylene oxide, as epichlorohydrin is much less reactive to atmospheric moisture, without dramatically extending gel time (~120 min). Like the propylene oxide formulations, however, epichlorohydrin formulations still resulted in coating volume loss and adhered only by mechanically

encompassing a fiber or groups of fibers as with propylene oxide formulations. To avoid volume loss due to evaporative drying, fibers were soaked in sol until 5 min prior the gel point in order to coat them with a non-interconnected particle-rich film. The fibers were then annealed in air at 200°C for 10 min followed by 30 min at 900°C under He. The result of this process was the formation of sparse, poorly-adhered alumina films that easily delaminate upon handling the tow upon which it was deposited (see Figure 7.3). Simply put, the highly porous precursor does not provide enough starting material for a contiguous film to form upon annealing.

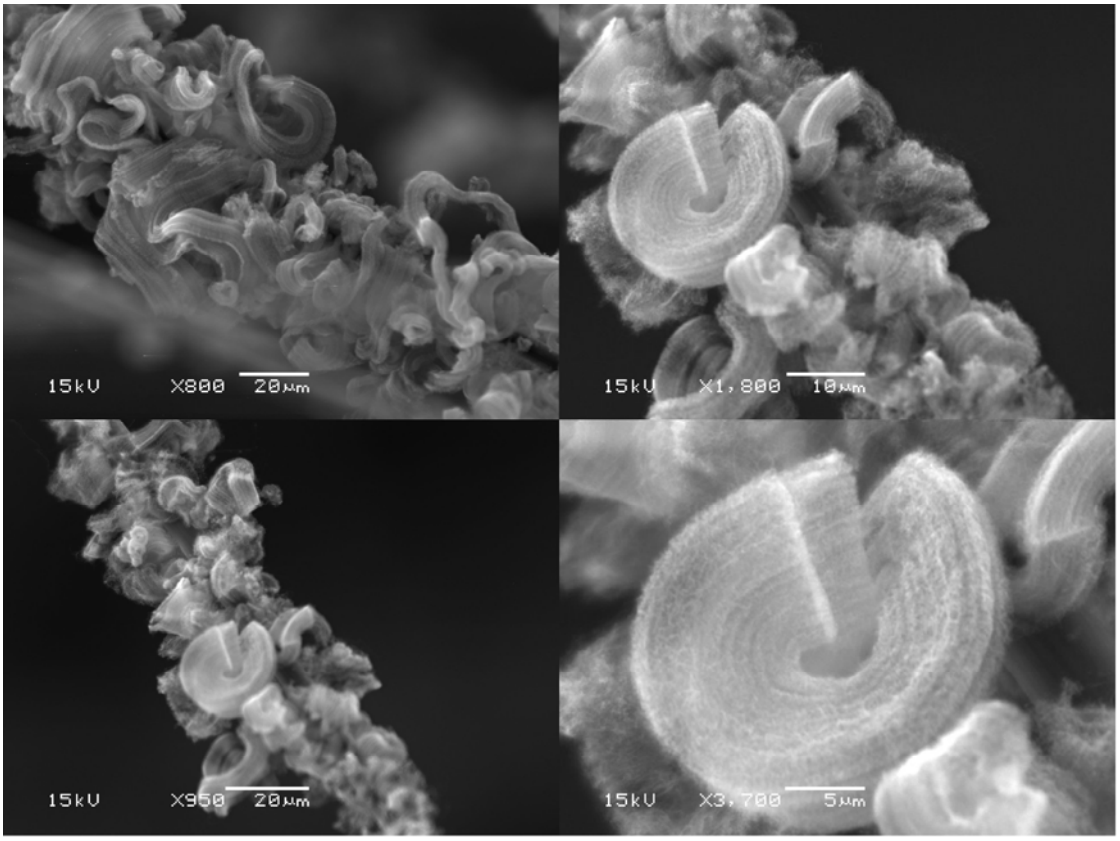

Figure 7.1 Worm- and shell-shaped bundles of aligned CNTs grown directly on carbon fibers coated with alumina deposited by sol-gel employing propylene oxide and aluminum(III) chloride.

Conclusions

The high surface area and hydroxylated surface provided by alumina gels produced by sol-gel with propylene oxide and aluminum(III) chloride provides the right chemistry for facilitating aligned CNT growth, however poor adhesion of the coating and severe volume loss complicate their practical utility. Multiple depositions could be used to build up a contiguous film, however this is quite time consuming. Alternatively, multiple coatings

with sol followed by low-temperature annealing may accomplish the same result yet require less time. These processes, however, serve as useful proofs-of-concept for growing CNTs on carbon fibers and could be practical if a method for improving coating and coverage were available. A technology for doing so is described in Section 7.3.1

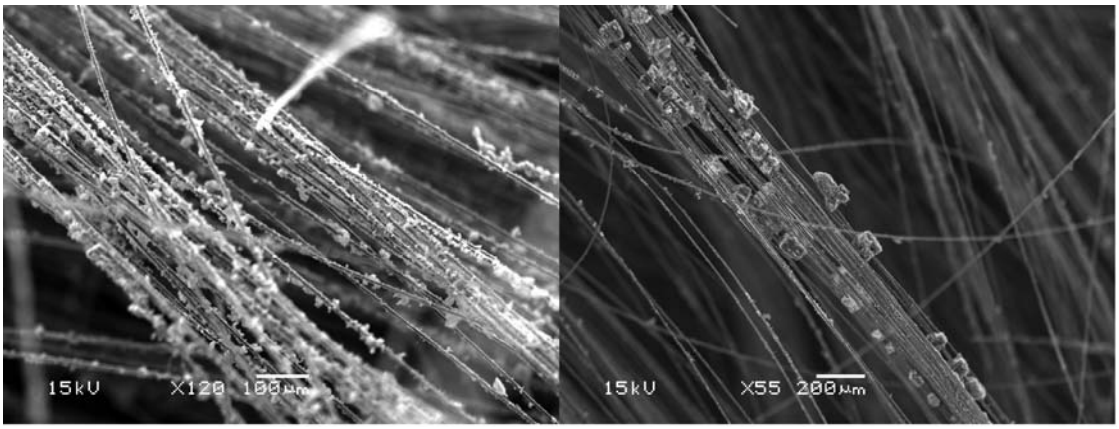

Figure 7.2 Overview of morphology of alumina coating derived from sol-gel employing propylene oxide and aluminum(III) chloride, exhibiting substantial cracking and exposed fibers surfaces.

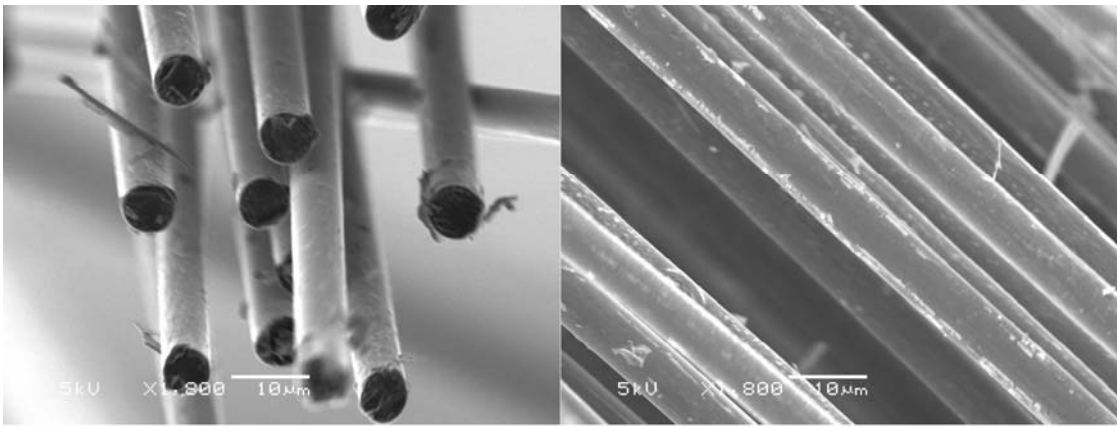

Figure 7.3 Survey of carbon fibers coated with alumina sol prepared by sol-gel employing propylene oxide and aluminum(III) chloride after oxidation at 200°C and subsequent annealing under inert atmosphere at 900°C; film coverage is not extensive and the film readily peels off.

7.2.1.2. Alkoxide-Derived Alumina Coatings

In consideration of the difficulties with mass/volume loss encountered with gel-based sol-gel depositions, methods for depositing denser coatings used for wear- and thermal-resistant applications, for example, were evaluated next.[155] In these approaches, methods of passivating alumina

nanoparticles in the sol are employed to prepare a concentrated, viscous solution that can be used to uniformly coat a substrate without gelation, which as observed encases fibers into bundles and holds them together with caked-on chunks of alumina as opposed to resulting in a uniform, conformal coating.

Methods and Materials

Aluminum tri-*sec*-butoxide (ATSB, Sigma-Aldrich product number 201073, 97%), 2-methoxyethanol (MeOEtOH, Sigma-Aldrich product number 185469, ≥99.0%), acetylacetone (acac, Sigma-Aldrich product number 10916, ≥99.5%) nitric acid (Sigma-Aldrich product number 438073, ACS grade), and analytical reagent grade deionized water (Ricca Chemical Company product number 9150-1) were used as received. Carbon fiber substrates, catalyst deposition, and CVD processing for CNT growth are the same as described previously.

Deposition of Alumina from Cyclic Baking of ATSB-Derived Sol

A solution of 50 mL MeOEtOH, 1.25 mL ATSB, and 0.5 mL acac was prepared. Next, carbon fiber substrates were rinsed with acetone followed by 2-propanol and baked dry on a hot plated at 80°C. The carbon fibers were then soaked in the alkoxide solution and baked in air at 200°C. The process was repeated 3-6 times to build up a thicker (up to ~1 μm) alumina coating.

Deposition of Alumina from 2-Methoxyethanol-Passivated ATSB -Derived Sol

To a beaker was added 2.07 g ATSB. The beaker was then heated on a hot plate to 80°C, at which point 14.61 g H_2O was added with stirring. A cloudy suspension resulted. To this mixture was added ~1 mL MeOEtOH and ~1 mL of concentrated HNO_3. The suspension became clearer and remained monophasic. Carbon fibers were then dip-coated into this suspension at 80°C.

Results

SEM images of alumina coatings produced by cyclic baking of ATSB-derived sols onto carbon fibers are shown in Figure 7.4. In this method, sol nanoparticles are applied and calcined directly on the carbon fiber surface. A film is then built up through multiple successive coatings. Cracking, peeling, and exposed fiber surfaces are again observed on carbon fibers coated with this process, however a noticeably thicker film is present (~500 nm) and is sufficiently self supporting that, despite the apparent poor adhesion between coating and fiber, the coating "clamps" onto the fibers. After subsequent loading with catalyst precursor by dip-coating in Fe^{3+}/IPA and CVD processing for CNT growth, CNTs are observed over fiber surfaces in a density higher than uncoated control fibers, however present as unaligned

mats and not uniformly over the fiber surface. These observations suggest that the denser alumina coating resulting from this process does not possess an appropriate surface chemistry and/or texture to promote CNT alignment, in addition to sharing the disadvantages of the other sol-gel processes surveyed.

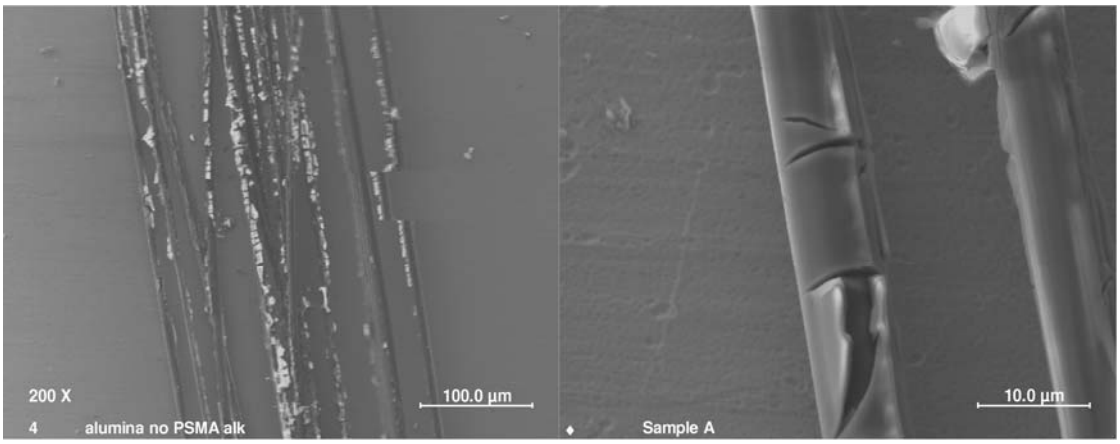

Figure 7.4 Overview and detail of alumina coating produced by sol-gel employing baking on ATSB-derived sols, showing extensive cracking and peeling away from the carbon fibers.

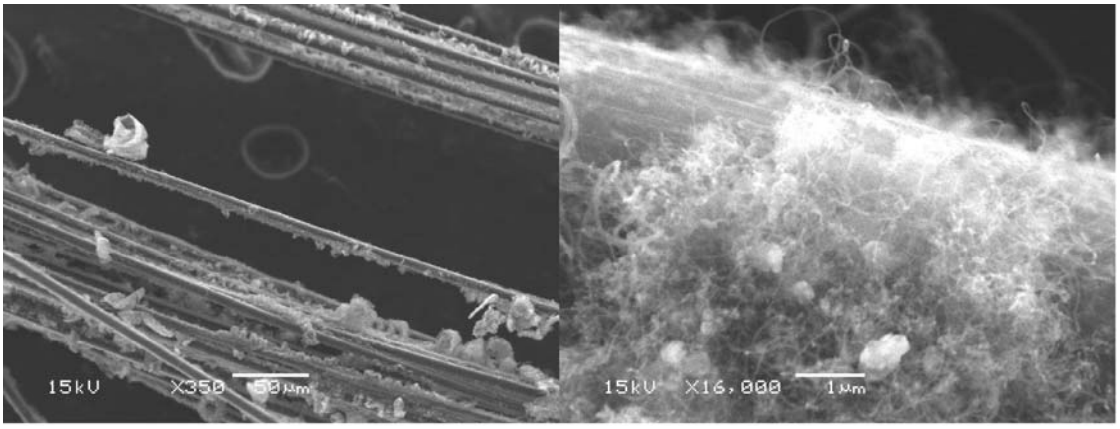

Figure 7.5 Overview and detail of CNT growth on carbon fibers coated with alumina produced by sol-gel employing baking on ATSB-derived sols showing unaligned growth and non-uniform coverage.

Carbon fibers coated with sols derived from ATSB/MeOEtOH are shown in Figure 7.6. In this process, the alkoxide ATSB is hydrolyzed in the presence of MeOEtOH which serves not only as a solvent but as a surface passivating agent that esterifies with surface aluminol groups on sol nanoparticles through a temperature- and/or pH-activated water condensation reaction. Carbon fibers exhibit more (but not complete) film coverage than the other

processes surveyed, but the film exhibits extremely poor adhesion and readily delaminates.

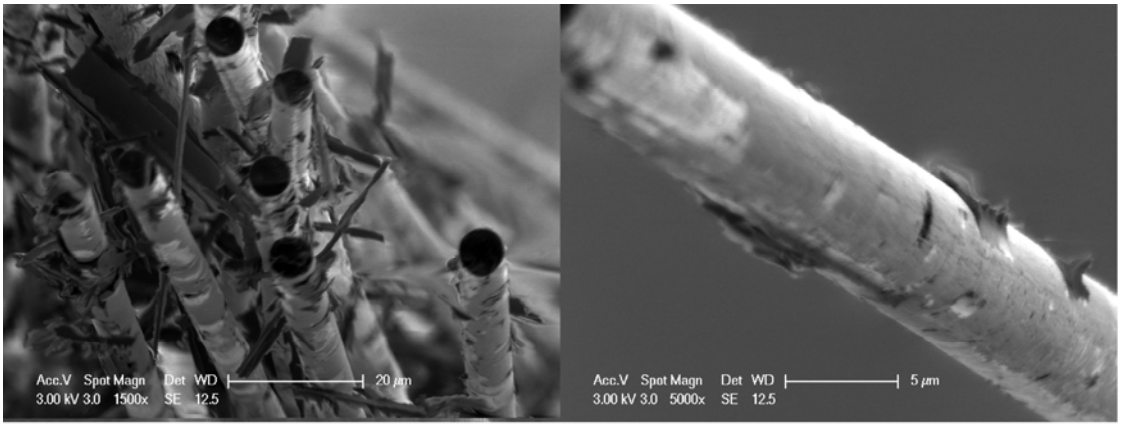

Figure 7.6 Overview of alumina coating prepared by dip-coating carbon fibers into sol derived from ATSB/MeOEtOH showing appreciable coverage but severe delamination of the coating off the carbon fibers.

7.2.1.3. Alkoxide-Derived Silica Coatings

Sol-gel processes for producing silica materials are well-established and quite versatile in terms of enabling production of high-density, high-quality materials, being able to tune gel times, and controlling surface chemistry. If silica could be used in place of alumina, a great deal of process simplification is to be had. Here, a rapid gelation process is developed and evaluated as a means for coating carbon fibers with a porous gel coating in less than one minute. The resulting silica coating is then investigated for its ability to adhere to carbon fibers and promote aligned CNT growth.

Methods and Materials

A rapid gelation technique employing a silicon alkoxide was used to form a high-quality gel coating over carbon fibers in less than one minute. Tetramethoxysilane (TMOS, Sigma-Aldrich product number 218472, 98%), sodium fluoride (NaF, Sigma-Aldrich product number 201154, ACS grade), anhydrous absolute ethanol (Pharmco-Aaper product number 111000200, 200-proof), analytical reagent grade deionized water (Ricca Chemical Company product number 9150-1) were used. A solution containing 5.17 g TMOS and 3.97 g ethanol and a second solution containing 2.00 g $NaOH_{(aq)}$ stock solution (19.1 mg/mL), 2.00 g $NaF_{(aq)}$ stock solution (1 mg/mL), and 2.36 g ethanol were prepared. The salt solution was then added to the alkoxide solution and swirled vigorously. Gel time is ~17 sec. Fibers were coated by quickly

dipcoating within this time period or alternatively by pouring the gelling sol over a tow placed on aluminum foil.

Following application of the gel coating, the gel-coated tow was soaked in ethanol for 1-4 h to remove unreacted materials from the pore network. The tow was then air-dried, dip-coated with Fe^{3+}/IPA, and CVD processed for CNT growth as described in the previous sections.

Results

Unsized carbon fibers were dip-coated with a rapidly-gelling sol. Within 15-20 sec, the sol gelled. The tows were then dried, coated with catalyst, and CVD processed for CNT growth. Figure 7.7 shows SEM images of carbon fibers coated with sol-gel-derived silica before (left) and after (right) CNT growth. No substantial improvement over alumina-based coatings in deposition coverage is observed. High-yield CNT growth is facilitated by the silica domains on the fibers, but unlike similarly porous alumina sol-gel coatings, no alignment is observed. This is probably due to chemistry differences between silica and alumina in their role as electrophiles that promote a catalytically active feedstock-support-catalyst interface.

Although the process advantage of a rapid gel time is desirable, alumina remains as the coating material of interest for facilitating CNT growth on carbon fibers because of its ability to promote CNT alignment.

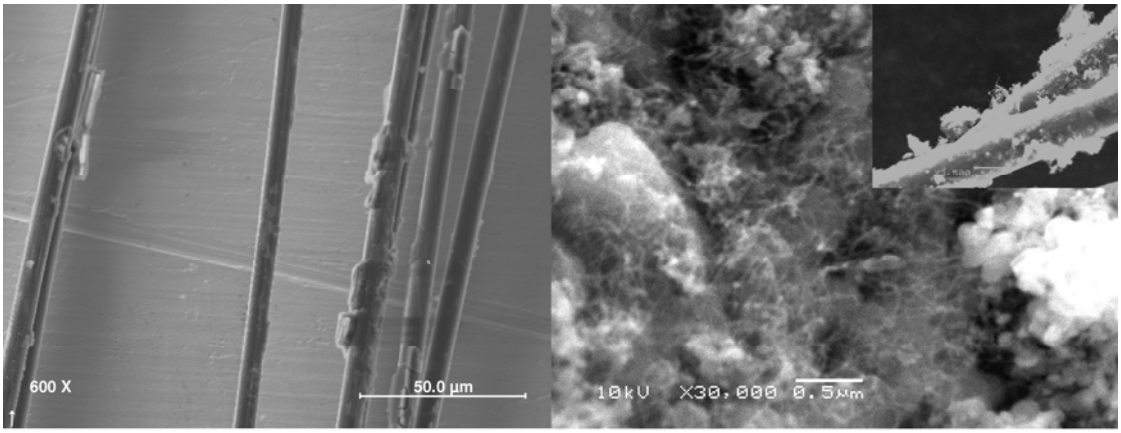

Figure 7.7 SEM images of sol-gel-derived silica coating on carbon fibers with sporadic coverage *(left)*, unaligned CNTs grown on a silica deposit on a carbon fiber *(right)*, and representative fibers presenting non-uniform silica/CNT coverage over carbon fibers *(inset)*.

7.2.1.4. Conclusions and Recommendations

The themes underlying all of the sol-gel processes surveyed include:

- Substantial mass and consequently volume loss upon drying of the coating
- Poor adhesion of the coating to the underlying carbon fiber
- Cracking of the film
- Incomplete coverage of the fiber

The propylene oxide method surveyed struggles with the most severe mass loss of any of the sol-gel processes surveyed, although provided the most optimal surface chemistry and/or texture. If coverage of this method could be improved, this would be a suitable and straightforward approach for growing aligned CNTs on carbon fibers. The related epichlorohydrin formulation described here likewise is expected to be a good candidate for growing aligned CNTs, provided coverage can be improved, as materials produced with this method have similar pore and surface properties to materials produced through the propylene oxide method.

Application and calcination of alumina coatings from viscous sols is a reasonable approach for improving coverage but like the gel-based coatings approach, adhesion needs to be improved. Additionally, a chemical modification (e.g., etching) of the alumina surface after deposition could be implemented to render it more favorable for aligned CNT growth.

Many other sol-gel processes could be explored with a high probability of success, however maintaining a hydroxylated surface, maintaining porosity, and minimizing/compensating for volume loss remain as challenges. With respect to this final point, since sol-gel inherently results in mass loss, refining sol-gel formulations is not a recommended strategy for reducing volume and associated consequences. Rather, methods of modifying the chemistry of the carbon fiber surface (in a way that adheres to the design guidelines set forth in Section 7.1) is a more promising approach as adhesion, coverage, and cracking can all be addressed if alumina sol particles can adsorb readily onto the carbon fiber surface. Sol-gel as employed in this section is ionically-mediated (i.e., involves polar intermediates), which means hydrophobic surfaces such as those presented by an unsized carbon fiber are ill-suited to facilitate adhesion of sol-gel-derived coatings.

In Section 7.3, a method for improving adhesion of the sol-gel-based coatings described in this section is explored.

7.2.2. Electrodeposition of Al

Electrodeposition is a technique for depositing a substance (such as a metal) from liquid-based solutions onto an electrically-conductive substrate at ambient or near-ambient conditions via the assistance of an electric current.

Electrodeposition is a potentially appealing alternative to sol-gel processing as it does not involve mass loss following deposition which, in sol-gel-deposited materials, can give rise to residual stresses and cracking due to material consolidation. Conveniently, carbon fibers, being highly graphitic, are electrically conductive and therefore viable candidates for electrodeposition targets. It was hypothesized that a conformal aluminum metal coating could be deposited over carbon fibers and subsequently oxidized to produce an alumina barrier coating. As a result, electrodeposition was explored as a possible approach for producing conformal, crack-free alumina barrier coatings on carbon fibers.

Electrodeposition of many metals, such as Cu and Ni, is a straightforward electrochemical process performed routinely in industry and performed easily in a laboratory setting. In a basic process, a working electrode of a source metal (e.g., a clean Cu wire), a water-based electrolyte containing aqueous ions of the source metal (e.g., aqueous Cu^{2+} from copper(II) sulfate), and a conductive target electrode upon which to deposit (e.g., a metal spoon) are provided. An electric current is then applied across the two electrodes at or above the potential required to reduce the aqueous metals ions in the electrolyte to their zero-valent metallic form. Upon doing so, the target electrode, which serves as the source of electrons for reduction of the aqueous metal ions, is conformally coated with the source metal. The working electrode is likewise oxidized and replenishes metal ions lost to the target electrode into the electrolyte. Various additives may be included in the electrolyte and pulsing of the applied current varied to direct the evolution of the grain structure and morphology of the deposited metal. While straightforward water-based electrodeposition can be easily performed for many elements, elements with reduction potentials falling outside of the electrochemical window of water (i.e., the voltage above which water decomposes) cannot be electrodeposited from water, thus necessitating the use of more exotic electrolyte systems for electrodeposition of such elements. Aluminum is an example of a metal that requires a non-aqueous electrolyte system in order to electrodeposit.

Sidelnikova *et al.*[158] demonstrated electrodeposition of aluminum on carbon fibers using both $AlBr_3$ in xylene as well as a modified Brenner electrolyte of $AlCl_3/LiAlH_4$ (1:1-3:1 molar ratios) in tetrahydrofuran/benzene (58%:42%). The latter process facilitated penetration into the fiber tow better than the former as reaction between the $LiAlH_4$ and trace amounts of moisture in the solution could be exploited to produce foaming of the electrolyte, which helps engage the inside of the tow with the electrolyte more thoroughly. To improve adhesion of the aluminum deposits to the carbon fibers (which was problematic), the fiber surfaces could be activated using a

0.1% solution of $PdCl_2$ or by working in a 10% solution of salicylic acid in tetrahydrofuran or 2% oleic acid in methanol prior to deposition. The chemistry of this process is somewhat hazardous ($LiAlH_4$ is pyrophoric, benzene is carcinogenic), however, and the entire process needs to performed under a N_2 atmosphere. As a result, an easier, less-hazardous process is desirable for industrial applications.

Aluminum electrodeposition can also be performed using electrolytes called ionic liquids.[159-161] Ionic liquids are essentially molten salts comprised solely of anions and cations that exist in a liquid phase below 100°C. Ionic liquids are typically comprised of a mixture of an organic salt and an inorganic halide, the interaction of which gives rise to a liquid-phase electrolyte system. Examples of organic salts used to prepare ionic liquids include 1-ethyl-3-methylimidazolium chloride ([EMI]Cl) and 1-butyl-1-methylpyrrolidinium bis(trifluoromethylsulfonyl) amide ([BMP]Tf_2N). To prepare an ionic liquid suitable for electrodeposition of an element, the organic salt is mixed with a halide of the element of interest for deposition, for example aluminum(III) chloride ($AlCl_3$), silicon tetrachloride ($SiCl_4$), or tantalum(V) fluoride (TaF_5).[159] Ionic liquids offer a great deal more process flexibility and stability than electrodepositing from halide salts or halide salt/hydride electrolytes in organic solvents and are less hazardous to work with. In general, ionic liquids for electrodeposition must be prepared using anhydrous salts in an anhydrous atmosphere. Once prepared, most ionic liquids, such as those based on [EMI]Cl, are moisture-sensitive and must also be used in an anhydrous atmosphere, although recently ionic liquids based on [BMP]Tf_2N and a handful of other compounds stable to moisture once mixed anhydrously have been prepared.

Electrodeposition of aluminum onto carbon fibers using an ionic liquid was explored here. A process based on an $AlCl_3$-[EMI]Cl (2:1 molar ratio) ionic liquid was selected, as ionic liquids based on [EMI]Cl are well-established.[160] At the time this work was performed (2007-2008), air- and moisture-stable ionic liquids for electrodeposition had only recently been described in the literature and as a result were not used, however such ionic liquids are now well-characterized and would likely be preferable candidates for future efforts.

Preparation of $AlCl_3$-[EMI]Cl Ionic Liquid

Preparation of $AlCl_3$-[EMI]Cl ionic liquid and subsequent electrodeposition were performed according the methods of Jiang *et al.*[160] Non-anhydrous 1-ethyl-3-methylimidazolium chloride ([EMI]Cl, Sigma-Aldrich product number 272841, >98%), anhydrous aluminum(III) chloride ($AlCl_3$, Sigma-Aldrich product number 06220, >99.0%), aluminum wire (0.58

mm diameter, Sigma-Aldrich product number 326887, >99.99%), sulfuric acid (Sigma-Aldrich product number 84718, 95-97%), phosphoric acid (Sigma-Aldrich product number 215104, 85%), nitric acid (Sigma-Aldrich product number 258113, 70%), and unsized carbon fiber tow (TohoTenax, product number HTA40 N00 12K, formerly 12KHTA-7CNS01) were used. All operations were performed inside of an inflatable glove bag under a nitrogen atmosphere. With all necessary supplies inside, the glove bag was evacuated and refilled with dry N_2 three times prior to use in order to eliminate residual atmospheric moisture. To a three-neck flask with a stir bead was added 3.00 g of [EMI]Cl (20.5 mmol). The [EMI]Cl was heated above its melting point (78-79°C) under reduced pressure to remove residual moisture from the salt. To the [EMI]Cl was then added 5.48 g of anhydrous aluminum(III) chloride (41.1 mmol) with stirring. A small amount of white gas was observed upon introduction of the $AlCl_3$, likely either HCl from hydrolysis of the $AlCl_3$ with residual moisture in the molten [EMI]Cl or Cl_2 from decomposition of the $AlCl_3$ resulting from its addition to the [EMI]Cl, which is an exothermic process. The resulting mixture was a cola-brown liquid that remained liquid upon cooling to room temperature, i.e., an $AlCl_3$-[EMI]Cl ionic liquid. Jiang *et al.* report the expected color for this ionic liquid is a faint yellow, but that heating above 160°C results in a dark brown color such as what was observed here. They hypothesized this color change was probably due to decomposition of the [EMI]Cl. Accordingly, it is believed that the EMI[Cl] in this work may have partially decomposed during dehydration of the salt and/or from a rapid temperature increase upon introduction of the $AlCl_3$ to the [EMI]Cl. Consequently, the behavior of our ionic liquid differed from what was reported by Jiang *et al.*, although conductivity measurements of our ionic liquid as a function of temperature were in good agreement with the values observed by Jiang *et al.* for this system (Figure 7.8).

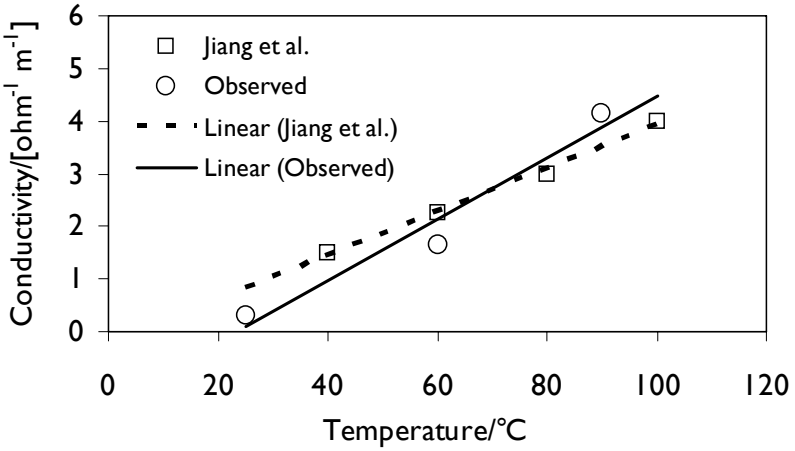

Figure 7.8 Observed and literature values for conductivity of $AlCl_3$-[EMI]Cl (2:1 molar ratio) ionic liquid as a function of temperature.

Electrodeposition from $AlCl_3$-[EMI]Cl Ionic Liquid

Aluminum working electrodes were prepared from 12-cm lengths of aluminum wire coiled to lengths of ~5 cm. Electrodes were acid-etched in 70 vol % phosphoric acid/25 vol % sulfuric acid/5 vol % nitric acid for 5 min, rinsed with deionized water, and wiped dry prior to use. Carbon fiber tow was cut into ~8-cm lengths and bonded to a steel washer with hot-melt glue at one end for ease of handling. An aluminum electrode and carbon fiber tow were then inserted into a 20-mL glass reaction vial (27 mm OD × 25 mm ID, see Figure 7.9) separated by a distance of ~1.0 cm. An open-ended glass tube (Figure 7.9) served to contain fibers in the tow to prevent short circuiting and to provide consistent spacing across depositions. The electrodes were connected to a DC power supply (Mastech HY3005) via wires soldered to copper alligator clips, with the aluminum electrode connected to the positive terminal of the power supply and the carbon fiber tow connected to the negative terminal. $AlCl_3$-[EMI]Cl ionic liquid was then transferred from the three-neck flask into the reaction vial with a syringe. The temperature of the ionic liquid was controlled through periodic warming with an electric heat gun and monitored with a type-K thermocouple dipped into the reaction vial only for taking brief readings.

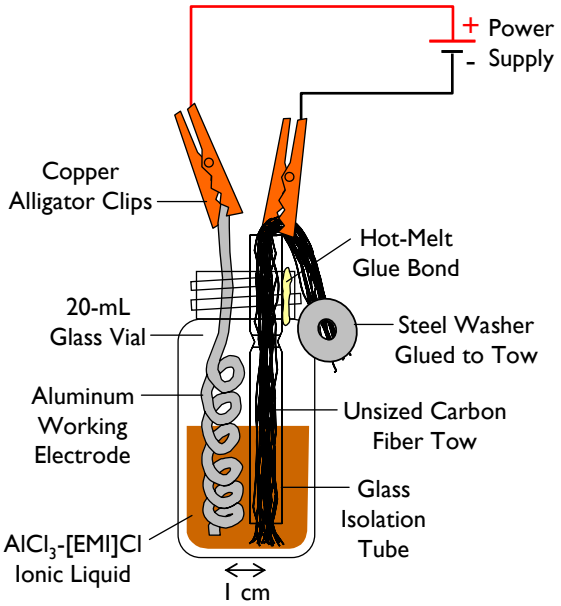

Figure 7.9 Reaction vial for electrodeposition of aluminum onto carbon fiber.

Table 7.1 summarizes experimental conditions surveyed for electrodeposition of aluminum onto unsized carbon fiber tows. No deposition occurred at 25°C with or without potential applied to the cell (as expected). Curiously, at both 60°C and 90°C (deposition temperatures suggested by Jiang *et al.*), however, deposition of aluminum was observed on

the aluminum working electrode regardless of the polarity of the potential applied to the cell (Figure 7.10) However, if the reaction medium was first heated to 90°C and potential was applied while the cell was allowed to cool to room temperature, successful deposition of aluminum onto the carbon fiber tow could be obtained (Figure 7.11). It is hypothesized that decomposition of the [EMI]Cl and/or presence of residual moisture in our ionic liquid resulted in a change in the chemistry and consequently thermodynamics (i.e., the thermovoltammogram) of our ionic liquid, thereby changing (and narrowing) the temperature window in which the desired electrochemical reaction should occur to a specific range between 90°C and 25°C. The exact temperature range over which the electrodeposition of aluminum onto the carbon fibers occurred was not clearly characterized, however.

Analysis of Electrodeposition Results

SEM imaging of successful depositions of aluminum onto carbon fibers revealed continuous, conformal films of aluminum metal were obtained on most of the fibers in the tow that had been immersed in the ionic liquid. As seen in Figure 7.11, however, a number of undesirable features were observed:

- Aluminum deposits were poorly adhered and peeled off upon handling of the fibers
- Deposits only formed on fiber surfaces directly exposed to the electrolyte leaving interfaces between fibers bundled by capillary action bare
- Morphology and grain structure of the deposited aluminum varied throughout the tow

As discussed, adhesion of aluminum to carbon fibers was addressed by Sidelnikova *et al.* by modifying the carbon fiber surface through activation and/or acid etching, however these approaches would not be suitable here as they violate the design guidelines set forth in Section 7.1 to protect tensile properties of the carbon fibers. Agitation of the bundle during deposition as described by Sidelnikova *et al.* could improve deposition onto clumped fiber surfaces. Morphology and grain structure would likely be better controlled by electrodepositing a fixed temperature, which would be facilitated by a better-characterized, higher-quality ionic liquid.

To improve the quality of the ionic liquid towards improving deposition control, $AlCl_3$-[EMI]Cl should be prepared and used in a proper dry box with properly anhydrous [EMI]Cl (now available in anhydrous form from commercial suppliers such as Sigma-Aldrich), exercising slow addition of $AlCl_3$ as to not allow the reaction medium to overheat and cause

decomposition of the [EMI]Cl. Alternatively, a moisture-stable ionic liquid such as $AlCl_3$-[BMP]Tf_2N could be used, eliminating potential complications from residual water during use. These steps were initially considered for further pursuit of electrodeposition of aluminum on carbon fibers, however as discussed below, several aspects of the initial results when taken into consideration together suggested electrodeposition would have a low probably of success for the target goal of forming conformal alumina coatings without jeopardizing fiber tensile properties.

Considerations and Conclusions

The limited adhesion of the aluminum deposits to carbon fiber observed, combined with the inherent challenges underlying uniformly coating aluminum onto the thousands of seven-micron-diameter fibers in a fiber tow, raised concerns that a substantial amount of fiber surface area would remain bare following electrodeposition, even if the process were refined. Additionally, in order to produce an alumina barrier coating from the deposited aluminum coatings, the aluminum would need to be electrooxidized, chemically oxidized, or thermally oxidized. Both processes risk oxidizing uncoated fiber surfaces, which violates the design guidelines since it jeopardizes fiber tensile properties. Additionally, should conformal, well-adhered aluminum be obtained and successfully oxidized without harming the underlying fiber, incomplete oxidation of the aluminum would result in the deleterious formation of a brittle, water-soluble carbide, Al_4C_3, at the fiber-coating interface if the fiber were heated above 400°C.[156] This is below the lowest temperatures at which CVD growth of CNTs can currently be performed and well below the temperatures typically required for growth of CNTs on alumina (>600°C). As such, the risk of either oxidizing the fiber surface or corroding the fiber surface under the barrier coating upon CVD processing seemed probable and likely to require substantial efforts to overcome.

In consideration of the aforementioned process challenges, the difficulty of preparing and using the ionic liquids for electrodeposition, and the prospects of more easily-attainable successes with other techniques, electrodeposition was not pursued further for the target application.

7.2.3. Chemical Vapor Deposition of Alumina

Chemical vapor deposition (CVD) is a useful technique for depositing ceramics, such as oxides, onto a target substrate.[162] In a typical oxide deposition process, an organometallic precursor is supplied as a vapor (possibly in conjunction with other gases such as O_2) into a heated reactor or over a heated substrate where the organometallic subsequently decomposes

to yield a solid-phase oxide. Depending on process conditions, CVD of an oxide can proceed via two reaction regimes—a mass-transport-limited regime, in which thermal decomposition of the organometallic occurs in the bulk vapor phase and results in line-of-sight precipitation of solid material from the vapor, and a surface-reaction-limited regime in which the decomposition of the organometallic occurs upon chemical and/or thermal interaction with the surface of a substrate resulting in a conformal coating. The two regimes frequently result in oxides with different phases, morphologies, surface areas, densities, and stoichiometries. For deposition of alumina on carbon fibers, surface-reaction-limited CVD of alumina is of primary interest since it has potential for forming a conformal coating and can penetrate into the interior of a tow or weave. Additionally, since the CNT growth processes of greatest interest are CVD-based, CVD of alumina barrier coatings onto carbon fibers could be generally streamlined into a single process with CNT growth and leverage the same process equipment.

Temperature/ °C	Time/ min	Applied Potential/V	Observed Current /mA	Results
25	60	0	0	No deposition, bubbles (HCl?) evolve on CF
25	60	5.0	20-30	Deposition of Al on Al electrode
60	90	5.0	80	Deposition of Al on Al electrode
60	90	-5.0	80	Black deposits on Al electrode, canary yellow water-reactive film on CF ($AlCl_3$?)
90	60	5.0	200	Deposition of Al on Al electrode
Cooling from 90 to 25*	60	5.0	Gradually decreases from 200 to 20	Electropolishing of Al electrode, deposition of Al on CF

* Potential applied continuously while reaction medium was allowed to cool to room temperature.

Table 7.1 Summary of experimental conditions surveyed for electrodeposition of aluminum on carbon fiber tows.

CVD of alumina can be performed with a number of organometallic compounds, either through decomposition of aluminum alkoxides or through decomposition of alkyl aluminum compounds in the presence of oxygen.[163]

The former are convenient as they incorporate enough oxygen in their structure to produce Al_2O_3 upon decomposition, are available as solids or liquids, and are substantially less toxic than alkyl aluminum compounds. Aluminum triisopropoxide (ATI, $Al(OC_3H_7)_3$) is an example of a solid precursor that has been used for deposition of alumina.[163-165] To use it, the compound is either sublimed or melted (melting point 128-133°C) to generate a vapor which is then delivered into the deposition chamber by a flow of an inert carrier gas such as Ar. Solid precursors such as ATI are frequently placed directly into a heated reaction chamber in proximity to the deposition target. Liquid precursors, most commonly aluminum tri-*sec*-butoxide (ATSB), can also be used[162,166,167] and have the advantages of being easier to process than solid precursors. To use them, the precursor, typically located outside of the deposition chamber, is heated to generate a vapor pressure and then delivered into the chamber by bubbling a carrier gas through the heated liquid.

In this work, three techniques for CVD of alumina onto carbon fibers were surveyed: deposition from solid-phase precursor ATI in a hot-wall reactor, deposition from liquid-phase precursor ATSB in a hot-wall reactor, and deposition from ATSB in a cold-wall reactor.

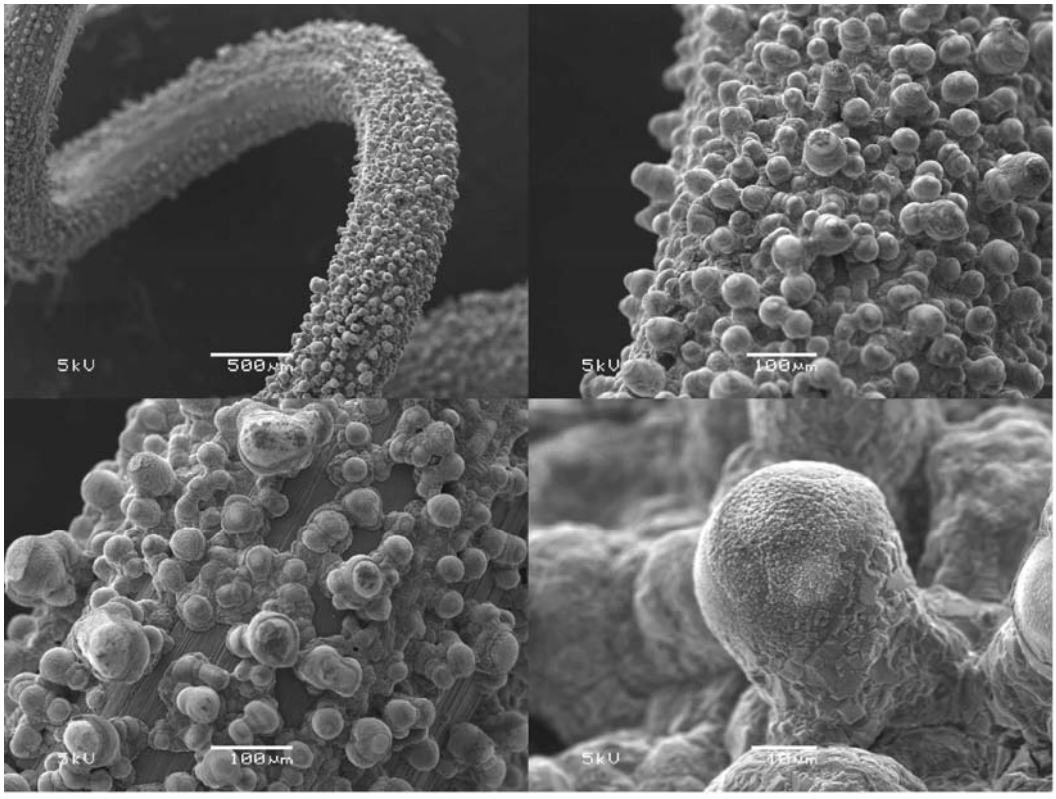

Figure 7.10 Aluminum deposits formed on the aluminum working electrode typical of several of the electrodeposition process conditions surveyed.

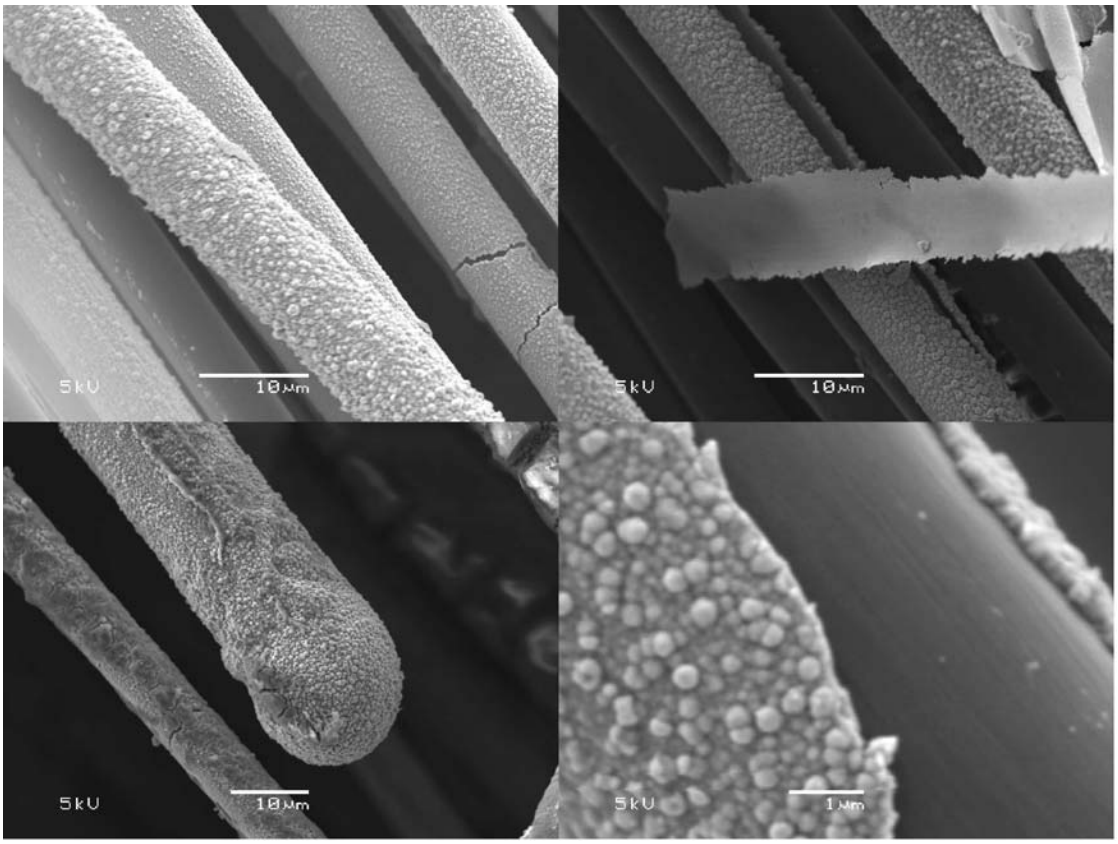

Figure 7.11 Aluminum deposits on carbon fibers formed by electrodeposition from ionic liquid: *(top left)* conformally-coated fibers exhibiting some film cracking; *(top right)* delaminated aluminum film; *(lower left)* rounded aluminum deposit formed from field lines at fiber tip; *(lower right)* detail of aluminum grain structure on carbon fiber surface.

7.2.3.1. Solid-Phase Precursor in Hot-Wall Reactor

CVD alumina from solid-phase ATI was the first alumina CVD processed evaluated as it requires no special process equipment beyond what is available in a typical CVD reactor for CNT growth. In processes investigated, a ceramic crucible is filled with a quantity of solid ATI. The crucible and a target substrate are then placed into a quartz process tube and heated with an electric clamshell furnace under a flow of an inert carrier gas such as He, N_2, or Ar. The ATI is positioned upstream of the substrate such that the carrier gas will carry ATI vapor to the substrate. It was hypothesized that by setting the temperature profile of the furnace correctly, ATI would generate vapor (either as a liquid or solid), make its way to target substrates positioned throughout the quartz tube, and decompose via a surface-reaction-limited process to yield a conformal coating of alumina over the target, here carbon fibers.

Methods, Materials, and Equipment

Aluminum triisopropoxide (ATI, ≥98%, Sigma-Aldrich product number 220418) served as the alumina precursor and was used as received. An alumina ceramic crucible (Sigma-Aldrich part number Z561738) was used to contain the ATI. Between 0.5-1.0 g of new ATI was placed in the crucible prior to each deposition. CVD of alumina was performed in a fused quartz tube (54-mm outer diameter, 50-mm inner diameter, 137-cm length) heated by a three-zone split-hinge tube furnace (Lindberg/Blue M model HT55667C, 30-cm heated zone lengths). (*Note:* Due to the distance between thermocouples in this furnace and how a 54-mm process tube sits in this furnace, reported temperatures may underestimate actual process temperatures by ~80°C as determined by calibrations performed with *in situ* thermocouple measurements). Positions of objects in the quartz tube (see Figure 7.12) are referred herein by the zone number in which the object was placed (wherein "Zone 1" is the zone on the side of the reactor in which gases enter, "Zone 2" is the center zone, and "Zone 3" is the zone on the side in which effluent exits) followed by the position in the zone in which it was placed ("Left" for the side of the zone towards gas entry, "Center" for the center, and "Right" for the side of the zone towards effluent exit). Samples placed at positions straddling two zones are denoted by "Zone X-Zone Y Boundary", where X and Y are the respective zone numbers associated with the boundary. The crucible containing ATI was placed in the center of the first zone ("Zone 1 Center") for all processes surveyed in order to facilitate control over the precursor temperature (Figure 7.12). Helium (Airgas, ultrahigh purity grade, >99.999%) was used as a carrier gas and was delivered via a computer-controlled mass flow controller (Unit model 1100A, 10 SLM capacity). Although many alumina CVD processes are conducted at reduced pressure, depositions in this work were performed at atmospheric pressure to improve potential compatibility for eventual integration with continuous CNT growth on carbon fiber substrates. Target substrates were unsized carbon fiber tow (TohoTenax, product number HTA40 N00 12K, formerly 12KHTA-7CNS01) cut to 6.5-cm lengths tied into knots at either end, and desized carbon fiber weave (Tenax-J G40-800 24K EP03) cut to sizes of either 4 cm x 18 cm or 4 cm x 6 cm. Weaves were received sized and desized by baking in air at 200°C for 30 min prior to deposition. Successful desizing was indicated by the evolution of smoke from the weave during the first 5 min of the heat treatment. Successful deposition of alumina on tows and weaves was determined by the presence of a colored thin film observable by optical microscopy at 50x magnification or below and confirmed by SEM.

CNT growth was performed on select alumina-coated and uncoated carbon fiber specimens to assess the efficacy of deposited alumina coatings

for facilitating CNT growth. First, a catalyst solution of 0.050 M $Fe(NO_3)_3 \cdot 9H_2O$ in 2-propanol (IPA) was prepared and aged with stirring for 1-2 h. Specimens were then dipped into this solution (Fe^{3+}/IPA) for ~5 min and then hung to air dry. Finally, using the same CVD equipment used for alumina deposition described above, a CVD process for growth of CNTs was performed on the specimens as follows. In a typical process, specimens were placed into a dedicated quartz process tube at Zone 3 Center. The tube was then flushed with a flow of 2070 sccm He for 10 min to displace oxygen from the tube. Next, He was turned off and a flow of 1040 sccm H_2 gas (Airgas, ultrahigh purity grade, >99.999%) was introduced. The sample was then heated to 650°C under H_2 gas over the course of ~8 min to reduce iron oxide nanoparticles on the specimen to catalytically-active iron. The sample remained at these conditions for an additional 7 min to further reduce remaining iron oxide nanoparticles. A flow of 316 sccm ethylene (Airgas, ultrahigh purity grade, >99.999%) was then added for 5 min to facilitate CNT growth. Lastly, H_2 and C_2H_4 were turned off and the sample was allowed to cool to room temperature under a flow of 2070 sccm He.

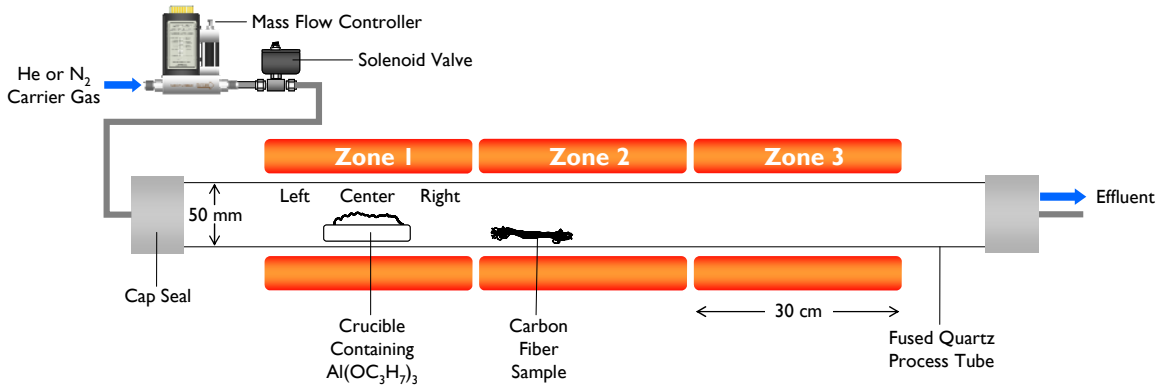

Figure 7.12 Schematic representation of setup used to perform CVD of alumina from aluminum triisopropoxide.

Results

Process conditions surveyed for deposition of alumina onto carbon fibers with ATI are summarized in Table 7.2. For reference, approximately 0.1-0.2 g of ATI was vaporized from the crucible in a typical deposition. The first process surveyed (process "Alumina CVD 1" in Table 7.2) was designed to provide an adequate temperature for generation of ATI vapor and a gradual thermal gradient to 900°C where formation and annealing of an alumina coating on a tow could occur. This process did not yield an alumina coating on the tow, however, instead resulting in bulk mass-transport-limited deposition of alumina at the end of the process tube with a region of no deposition ~1-2 cm around the fiber tow, possibly due to chemical interface

from an agent evaporating from the tow. Additionally, the remaining unsublimed ATI in the crucible turned brown, suggested decomposition of the precursor from overheating prior to vaporization. In summary, the results from this process suggested that the precursor and substrate were both too hot and that spatial variation in deposition conditions was present.

Following this, a second process ("Alumina CVD 2") was developed featuring a low precursor set point of 150°C (slightly above the melting point of ATI) and a substrate set point of 700°C. Additionally, three substrates (unsized tows) were positioned across the length of the second zone to assess spatial-dependence of the deposition. Due to proximity heating from the second zone, the zone containing the precursor was observed to be much hotter than its set point (ramping from 370°C to 495°C over the course of the 10-min soak phase of the deposition). Despite this, successful deposition of alumina was observed over most of the length of the first tow (positioned at Zone 2 Left) and was visible under a microscope and to the eye as a glossy rainbow-colored glaze. The coatings appeared well-adhered and, as observed by SEM, did not appear to crack or substantially flake off on handling of the tow. The tows positioned at Zone 2 Center and Zone 2 Right, however, did not show the presence of an alumina film, revealing the presence of a limited region (up to ~12 cm downwind of the crucible) in which deposition can be performed with this process. The absence of white or glossy deposits on the quartz tube in Zone 2 suggests that formation of the observed deposit was surface-reaction-limited.

The successfully-coated specimen from process Alumina CVD 2 and an uncoated control specimen were then dip-coated with Fe^{3+}/IPA and CVD processed for CNT growth. Following CNT growth processing the alumina-coated sample was noticeably fuzzy and matte black in color, while the control sample remained smooth and glossy black (see Figure 7.13). SEM imaging of the CNT-processed samples revealed extremely high-yield growth of aligned CNTs covering the alumina-coated tow over nearly the entire length of the tow including interior fibers (Figure 7.14). Although the aligned CNTs were longer than the design target (~100 μm vs. 10-20 μm, adjustable by changing the ethylene flow time), the areal coverage and morphology obtained are correct for the targeted fuzzy carbon fiber architecture.

Building on the promising results of the Alumina CVD 2 process, the next goal was to extend the attainable deposition range so that larger specimens, such as weaves large enough to prepare composite coupons for mechanical standards testing, could be coated with alumina. It was hypothesized that the high set point (700°C) of Zone 2 in the previous process limited the range over which the ATI vapor could survive before succumbing to homogenous gas-phase decomposition into alumina (i.e., mass-transport-limited deposition), as

white deposits were observed at the end of the quartz process tube. To adjust for these limitations, a new process (Alumina CVD 3) was devised, in which all three zones were set to 350°C (corresponding approximately to the actual temperature observed in Zone 1 during successful depositions of alumina from Alumina CVD 2). Instead of three 6.5-cm tows, a long, desized weave (4 x 18 cm) was placed across Zone 2 Left and Zone 2 Center to provide a record of the deposition range for this process. Unexpectedly, indications of an alumina coating were not observed. Subsequent dip-coating with catalyst and CVD processing for CNT growth did not yield substantial CNT growth, indicating little or no alumina on the weave. These results suggest that while 350°C may be an acceptable temperature for vaporizing the ATI precursor, it is perhaps too cold for formation of alumina on a carbon fiber substrate.

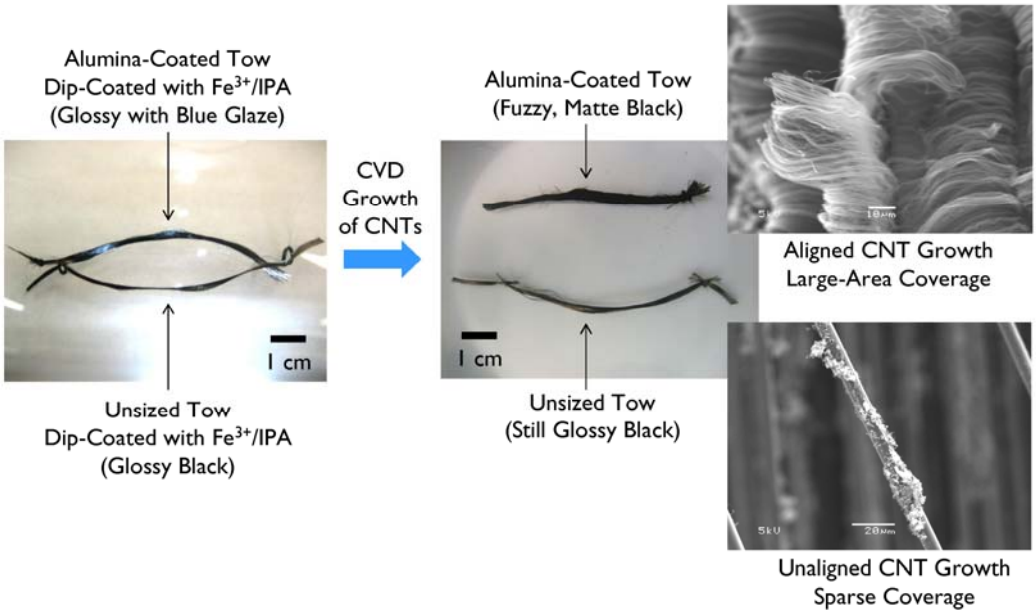

Figure 7.13 Unsized carbon fiber tow and alumina-coated carbon fiber tow from process Alumina CVD 2, both coated with iron catalyst, before and after CVD growth of CNTs.

The next process (Alumina CVD 4) tested whether or not the ATI precursor could be vaporized and transported a longer distance in the process tube across Zone 2 to a sample placed in Zone 3. The set points (Zone 1 at 150°C, Zone 2 off) were chosen to provide a temperature range of 275-450°C across the length from Zone 1 Left to Zone 2 Right which again correlated with the temperature of the precursor in the successful process Alumina CVD 2. The substrate in Zone 3 was then heated to 700°C. No alumina film observable by microscopy was found on the sample following deposition. This result suggests that residence time, not just temperature, is an important

limiting factor in the determination of the suitable deposition range downstream of the crucible.

Process Name	Sample Type and Position in Furnace[1]	Carrier, Flow Rate	Zone 1 Set Point[2] (Meas-ured)	Zone 2 Set Point[2] (Meas-ured)	Zone 3 Set Point[2] (Meas-ured)	Set Point Wait Condition (Time Taken)	Process Soak Time	Results
Alumina CVD 1	Tow at Zone 3 Center	He, 400 sccm	500°C	700°C	900°C	Until Zone 3 > 890°C (24 min)	10 min	White deposits on tube from Zone 2 Right through Zone 3 Right, no deposition in vicinity of or on tow, unsublimed ATI turned brown
Alumina CVD 2	Qty 3 tow at Zone 2 Left, Center, and Right	He, 400 sccm	150°C (ramp from 370°C-495°C)	700°C	700°C	Until Zone 3 > 690°C (17 min)	10 min	White deposits on tube from Zone 2 Right through Zone 3 Right, glossy rainbow film on sample at Zone 2 Left, other two samples unchanged
Alumina CVD 3	Desized weave (4 x 18 cm) at Zone 2 Left	He, 400 sccm	350°C	350°C	350°C	Until Zone 1 > 349°C (11 min)	10 min	No observable alumina deposition, weave curled
Alumina CVD 4	Qty 2 desized weave (4 x 6 cm) at Zone 1-Zone 2 Boundary, Zone 3 Center	He, 400 sccm	150°C (ramp from 275°C-330°C)	Off (ramp from 380°C-435°C)	700°C	Until Zone 3 > 699°C (26 min)	10 min	No observable alumina films on either weave by microscopy
Alumina CVD 2	Desized weave (4 x 6 cm) at Zone 1-Zone 2 Boundary	He, 400 sccm	150°C (ramp from 350°C-500°C)	700°C	700°C	Until Zone 3 > 690°C (17 min)	10 min	Observable rainbow gloss over 85% of weave from left side
Alumina CVD 2b	Desized weave (4 x 6 cm) at Zone 1-Zone 2 Boundary	N_2, 400 sccm	150°C (ramp from 355°C-490°C)	700°C	700°C	Until Zone 3 > 690°C (17 min)	10 min	Observable rainbow gloss over 85% of weave from left side

[1]Crucible containing ATI was placed at Zone 1 Center for all processes surveyed.
[2]Measured temperatures vary from set points when neighboring zone set points differ due to proximity heating from hotter neighboring zones. Measured temperatures listed in parentheses represent the starting and ending temperature during the soak phase of the process. Actual temperatures (based on calibration experiments) are ~80°C higher than both setpoints and measured values.

Table 7.2 Conditions surveyed for CVD of alumina onto carbon fibers with ATI.

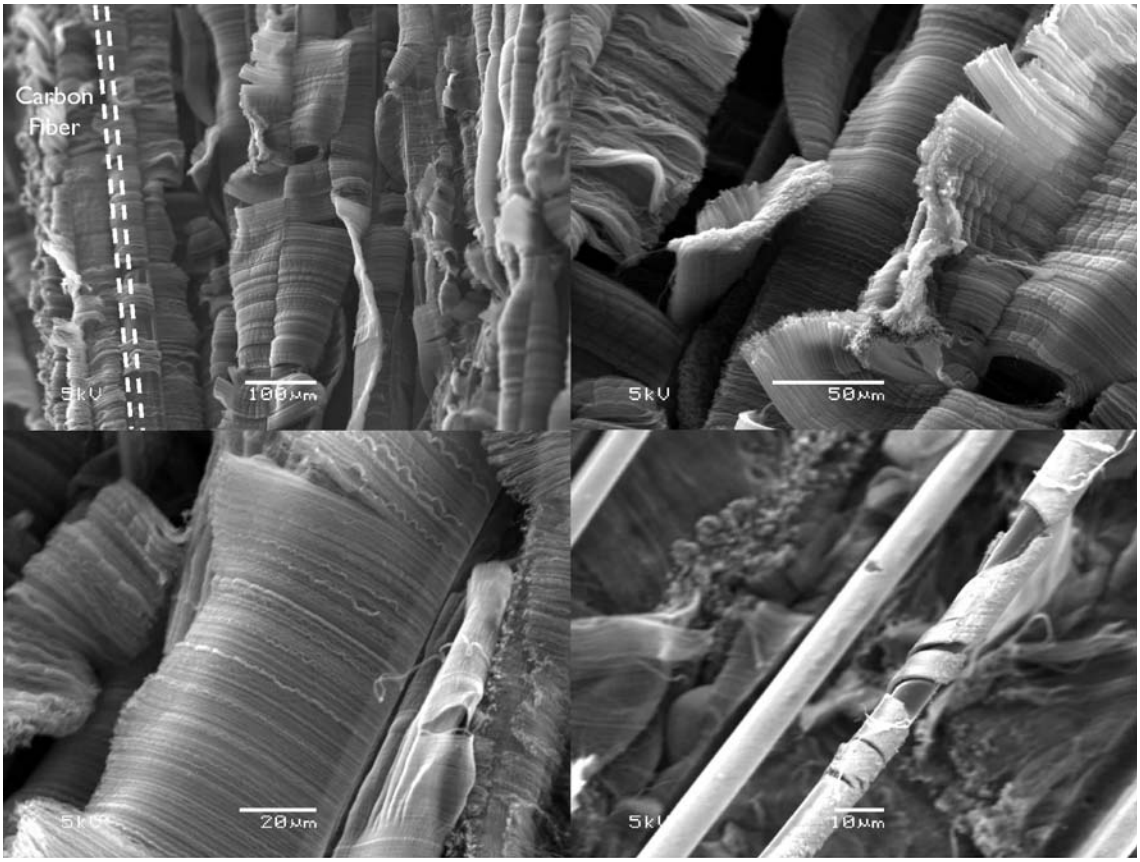

Figure 7.14 *(Top left, top right, lower left)* SEM images of aligned CNTs grown on alumina-coated carbon fibers from process Alumina CVD 2; *(lower right)* alumina-wrapped carbon fibers after mechanical delamination of CNTs.

To verify that the unsuccessful depositions in processes Alumina CVD 3 and Alumina CVD 4 were attributable to the CVD processing and not to some undetected difference between the desized weaves and the unsized tows, Alumina CVD 2 was performed again with a desized weave instead of unsized tows. Successful deposition of a glossy rainbow-colored coating was observed over 85% of the length of the weave (6 cm long) closest to the crucible (see Figure 7.15). Again, catalyst deposition and CVD processing for CNT growth of this specimen resulted in high-yield aligned CNT growth.

It was hypothesized that perhaps the light He carrier was stifling transport of usable precursor vapor and that a heavier carrier gas, such as N_2, could extend this range. Alumina CVD 2 was performed again with desized weave with a flow of N_2 in place of He (process Alumina CVD 2b). No substantial difference was observed between this process and Alumina CVD 2.

Figure 7.15 Carbon fiber weave post-CVD of alumina from ATI exhibiting a characteristic glossy rainbow glaze indicative of successful deposition.

Conclusions, Recommendations, and Next Steps

The processes surveyed here demonstrate that it is possible to deposit well-adhered alumina onto both carbon fiber tows and weaves via CVD with ATI precursor and that the target fuzzy carbon fiber architecture can be attained by providing a barrier coating deposited using a CVD process such as process Alumina CVD 2 described herein. The use of a solid precursor in a hot-wall reactor, however, makes decoupling of important process parameters such as precursor temperature, vapor temperature, vapor residence time, and substrate temperature problematic. In response to these observations, alumina CVD using an external liquid alumina precursor heated outside the tube furnace was pursued next in effort to better decouple the aforementioned process parameters and attain more scalable deposition of alumina. These experiments are described in the following section. While additional parameter space of the solid precursor in a hot-wall reactor approach could still be investigated in effort to establish larger areal coverage, other variations of alumina CVD seem more likely to enable better process control for the targeted applications.

This said, CVD of alumina from ATI in a hot-wall reactor as demonstrated here may be viable for a continuously-moving tow process in which the deposition range is unimportant (since the substrate can be continuously

passed through the deposition range at a controlled speed). Alternatively, a wide reactor in which a wide specimen is placed downwind of a wide crucible (as opposed to lengthwise downwind of the crucible as was done in this work) could enable deposition over larger areas. Another approach could be to place a large specimen above a long crucible or an array of small crucibles. Yet another approach would be to use low-pressure CVD or higher carrier flow velocities to tune residence time and thus extend the deposition range. In considering these suggestions or other efforts towards further refinement of this alumina CVD approach, issues to be considered include a several-hundred-degree difference between the optimal precursor temperature and substrate temperature, the limited deposition range for surface-reaction-limited deposition (and its proximity to the crucible), and the need to periodically or continuously replenish the moisture-sensitive ATI solid precursor as it is used up.

7.2.3.2. Liquid-Phase Precursor in Hot-Wall Reactor

In addition to solid-phase precursors like ATI, liquid-phase precursors such as aluminum tri-*sec*-butoxide (ATSB) can also be used for CVD of alumina. A few advantages to using liquid-phase precursors over solid-phase precursors include ease of control over precursor vapor pressure (done by simply heating the precursor, as the vapor pressure of a liquid is only a function of its temperature), ease of externalization of the precursor from the deposition chamber, and ability to replenish the precursor in a continuous fashion. Here deposition of alumina on carbon fiber tows and weaves with ATSB in a hot-wall reactor at atmospheric pressure was explored in effort to decouple and control critical process parameters better than with ATI under the same conditions. The goals of this effort were twofold: one, to identify a process for effectively depositing alumina on carbon fibers using ATSB as a precursor, and two, to scale such a process up for deposition on weaves towards being able to prepare specimens suitable for composites testing.

Methods and Materials

CVD of alumina from ATSB was performed using the same electric clam-shell furnace used for CVD of alumina with ATI described in Section 7.2.3.1. Set points for this system underestimate the actual process temperature by ~80°C; temperatures listed for this furnace herein are in terms of set points. To accommodate use of a liquid precursor, a special liquid-phase CVD precursor module was engineered (Figure 7.16) and connected to the furnace. This module consisted of a computer-controlled mass flow controller for delivering Ar carrier gas (Airgas, ultrahigh purity grade, >99.999%) into a computer-controlled heated bubbler containing ATSB (Sigma-Aldrich, >98%),

dubbed the Modular Reagent Bubbler (or "MRB"). Temperature feedback for controlling the temperature of the ATSB was provided by a type-K thermocouple submerged under the ATSB in the bubbler. A flexible stainless steel bellows served as a conduit between the bubbler and the quartz process tube, with a multiturn needle valve placed in-line to control the flow of vapor from the bubbler into the process tube. To prevent condensation of the precursor prior to entering the process tube, the bellows was wrapped with a flexible heat tape (BriskHeat heating tape and percentage control from McMaster-Carr, model BSAT051006, McMaster-Carr part number 3631K23, 216 W, 1/2" wide, 72" length) and heated at a setting of 35% maximum power. Similarly, a second heat tape (BriskHeat heating tape and percentage control from McMaster-Carr, model BSAT051006, McMaster-Carr part number 3631K62, 288 W, 1" wide, 48" length) was wrapped around the exposed length of the process tube and set to 25% maximum power to prevent condensation of the precursor in the section of the quartz process tube outside of the heated zones of the furnace. A photograph of the setup is shown in Figure 7.17. Unsized carbon fiber tows and sized weaves were used for deposition targets and were the same materials used in the Section 7.2.3.1. Weaves were cut to swatches of approximately 18 cm x 5 cm and were desized with a non-oxidative process by heating to a 500°C set point (580°C actual) under He for 10-15 min. Successful deposition of alumina was determined primarily through identification of a colored glaze or chalky white deposit over the specimen as observed by optical microscopy at a magnification of 50× or less and by the presence of CNTs over the specimen following dip-coating with Fe^{3+}/IPA and subsequent CVD processing for CNT growth. Catalyst dip-coating and CNT growth procedures were the same as described in the Section 7.2.3.1.

In a typical alumina CVD process, a sample was positioned at a specific location in the quartz process tube. In the case of woven specimens, a desizing procedure as described above was performed prior. Next, under a flow of He, the temperature of the sample was brought to a predetermined set point (between 270-750°C, 350-830°C actual). During this time, the bubbler containing the ATSB precursor was heated to 138°C, optionally under a flow of 50 sccm of Ar to promote homogenization of the precursor temperature. Once the sample temperature and bubbler set points had stabilized, the needle valve controlling flow from the bubbler into the quartz process tube was opened and the flow rate of Ar through the bubbler increased to initiate deposition. The system was then kept at these conditions for a predetermined soak time. Finally, flow of Ar through the bubbler was turned off, the needle valve was closed, and the sample was cooled to ambient conditions under a flow of He (at the same flow rate used in the deposition, see Table 7.3).

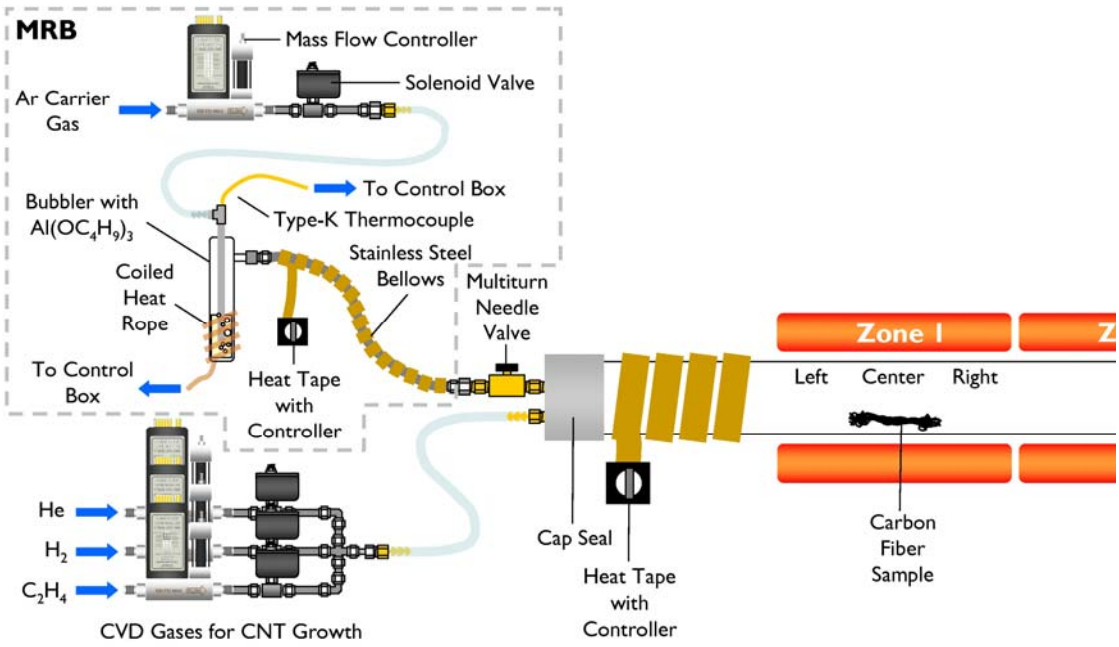

Figure 7.16 Schematic representation of setup used for performing CVD of alumina with aluminum tri-*sec*-butoxide precursor.

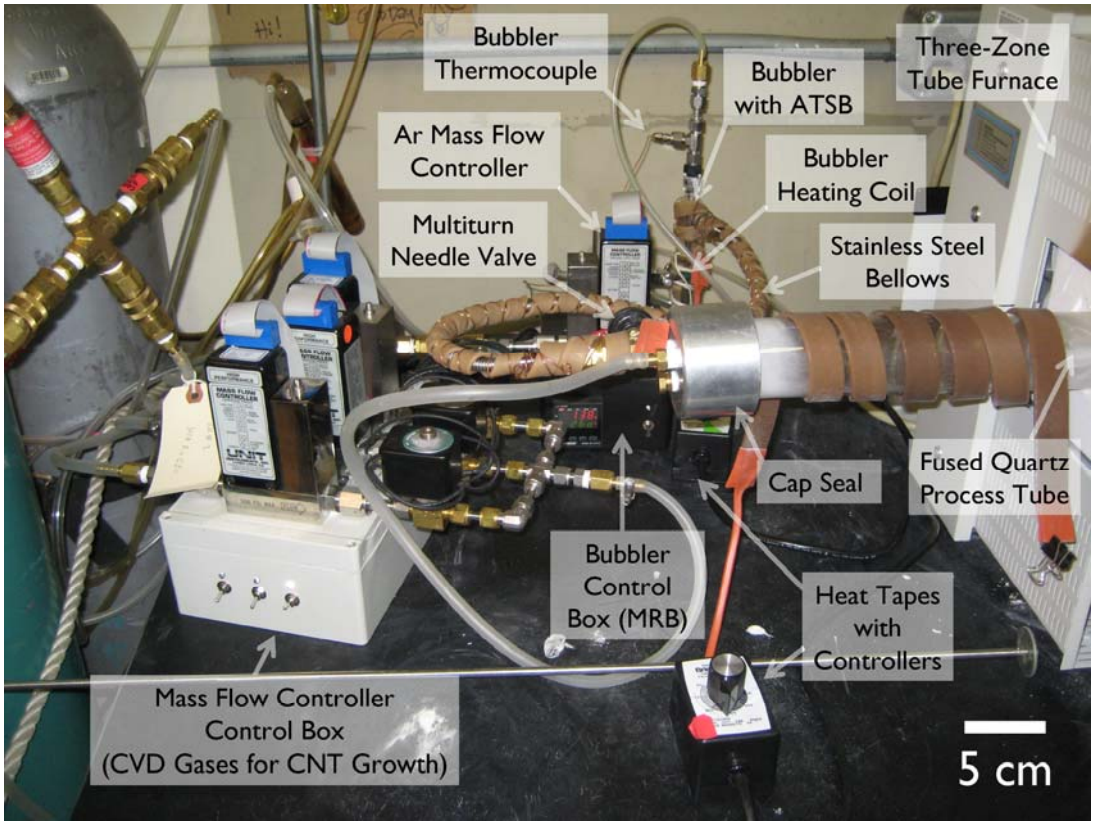

Figure 7.17 Photograph of CVD setup used for deposition of alumina from aluminum tri-*sec*-butoxide in a hot-wall reactor.

Process Name	Sample Type and Position[1]	Desizing Process (Time Taken)	CVD Temp[2]	Bulk He Flow Rate	Bubbler Flow Rate[3]	Set Point Wait Condition (Time Taken)	Process Soak Time
Alumina Liquid CVD 1	Tow at Zone 1 Center	None	750˚C	400 sccm	100 sccm	Until Zone 1 > 749˚C (9 min)	5 min
Alumina Liquid CVD 2	Tow at Zone 1 Center	None	400˚C	400 sccm	100 sccm	Until Zone 1 > 399˚C (6 min)	20 min
Alumina Liquid CVD 3	Tow at Zone 1 Center	None	330˚C	5200 sccm	1820 sccm	Until Zone 1 > 329˚C (4 min)	20 min
Alumina Liquid CVD 4	Tow at Zone 1 Center	None	330˚C	6600 sccm	1800 sccm	Preheated to 330˚C (No Wait)	20 min
Alumina Liquid CVD 5	Tow at Zone 2 Center	None	330˚C	6600 sccm	1800 sccm	Until Zone 1 > 329˚C (5 min)	20 min
Alumina Liquid CVD 6	Tow at Zone 2 Center	None	380˚C	6600 sccm	1800 sccm	Until Zone 1 > 329˚C (4 min)	20 min
Alumina Liquid CVD 7	Weave at Zone 1 Center	He at 1600 sccm, 500˚C (16 min)	380˚C	6600 sccm	1800 sccm	Until Zone 1 < 381˚C[4] and Bubbler = 138˚C[5] (13 min)	60 min
Alumina Liquid CVD 8	Weave at Zone 1-Zone 2 Boundary	He at 1600 sccm, 500˚C (17 min)	380˚C	6600 sccm	1800 sccm	Until Zone 1 < 381˚C and Bubbler = 138˚C (9 min)	60 min
Alumina Liquid CVD 9b	Weave at Zone 2 Left (0-18 cm)	He at 1600 sccm, 500˚C (16 min) earlier	300˚C	6600 sccm	1800 sccm	Until Zone 1 > 299˚C and Bubbler = 138˚C (4 min)	60 min
Alumina Liquid CVD 10	Weave at Zone 1 Left (0-18 cm)	He at 1600 sccm, 500˚C (16 min)	300˚C	6600 sccm	1800 sccm	Until Zone 1 < 305˚C and Bubbler = 138˚C (10 min)	60 min
Alumina Liquid CVD 11	Weave at Zone 2 Left (0-18 cm)	He at 1600 sccm, 500˚C (16 min)	270˚C	6600 sccm	1800 sccm	Until Zone 1 < 265˚C and Bubbler = 138˚C (9 min)	60 min
Alumina Liquid CVD 12	Small Weave Vertical Facing Gas Flow at Zone 1 Center	He at 1600 sccm, 500˚C (16 min)	300˚C	6600 sccm	1800 sccm	Until Zone 1 < 275˚C and Bubbler = 138˚C (9 min)	60 min
Alumina Liquid CVD 13	Weave Vertical but Parallel to Gas Flow at Zone 1 Left	He at 1600 sccm, 500˚C (16 min)	300˚C	6600 sccm	1800 sccm	Until Zone 1 < 275˚C and Bubbler = 138˚C (13 min)	60 min
Alumina Liquid CVD 14	Weave at Zone 1 Left (0-18 cm)	He at 1600 sccm, 500˚C (16 min)	300˚C	N_2 (not He) 6600 sccm	1800 sccm	Until Zone 1 < 275˚C and Bubbler = 138˚C (7 min)	60 min
Alumina Liquid CVD 15	Weave at Outside Furnace-Zone 1 Boundary (-8 to 13 cm)	He at 1600 sccm, 500˚C (16 min)	300˚C	6600 sccm	1800 sccm	Until Zone 1 < 275˚C and Bubbler = 138˚C (14 min)	60 min
Alumina Liquid CVD 16	Weave at Zone 1 Left (2.5-20.5 cm)	He at 1600 sccm, 500˚C (16 min)	300˚C	6600 sccm	1800 sccm	Until Zone 1 < 275˚C and Bubbler = 138˚C (6 min)	60 min
Alumina Liquid CVD 16b	Other side of weave from 16 at Zone 1 Left	None	300˚C	6600 sccm	1800 sccm	Until Zone 1 > 299˚C and Bubbler = 138˚C (6 min)	60 min
Alumina Liquid CVD 17[6]	Weave at Zone 1 Left (2.5-20.5 cm), first Side 1 then Side 2	He at 1600 sccm, 500˚C (16 min/side), done for each side of weave	300˚C	6600 sccm	1800 sccm	Until Zone 1 < 275˚C and Bubbler = 138˚C (29 min)	60 min per side

[1]Weaves were 18 x 5 cm. [2]Temperature set point during alumina deposition; actual temperature is ~80°C higher. [3]Flow of Ar carrier gas. [4]Deposition follows hotter desizing process. [5]Bubbler at 50 sccm Ar flow during warm-up to homogenize heating of ATSB. [6]CVD repeated for each side.

Table 7.3 Summary of process conditions surveyed for alumina CVD with ATSB.

Process Name	Sample Topology	Process Name	Sample Topology
Alumina Liquid CVD 7	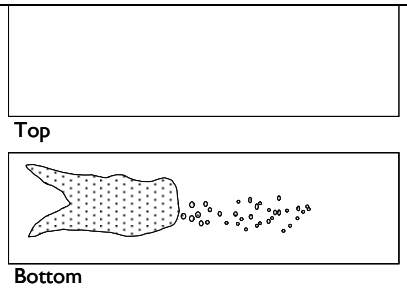	Alumina Liquid CVD 12 (Vertical Sample Facing Flow, 6 x 4.5 cm)	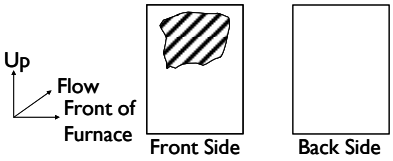
Alumina Liquid CVD 8	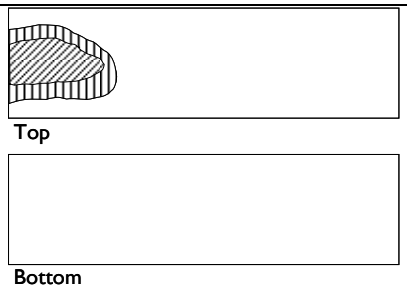	Alumina Liquid CVD 13 (Vertical Sample Parallel with Flow)	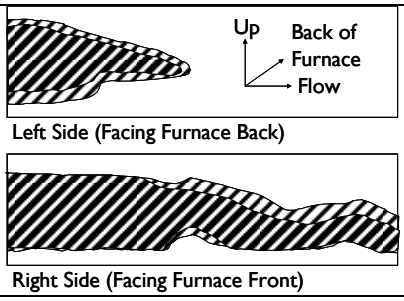
Alumina Liquid CVD 9	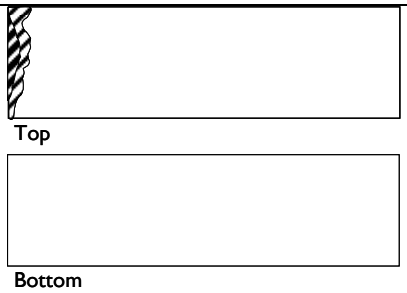	Alumina Liquid CVD 14	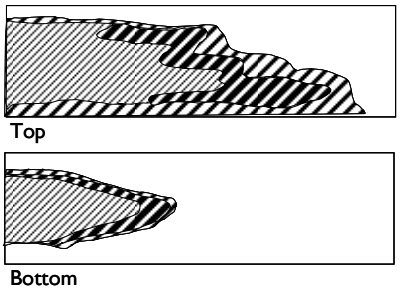
Alumina Liquid CVD 10	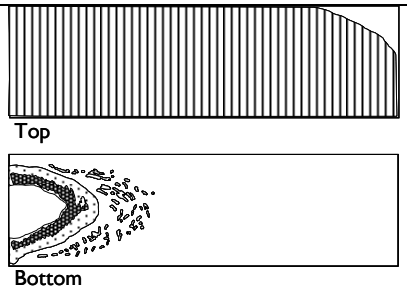	Alumina Liquid CVD 15	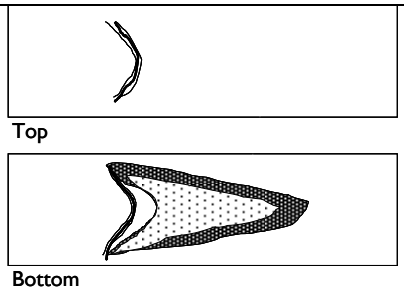
Alumina Liquid CVD 11	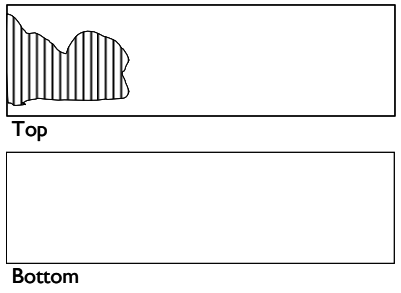	Alumina Liquid CVD 16+16b, Alumina Liquid CVD 17 (alumina only)	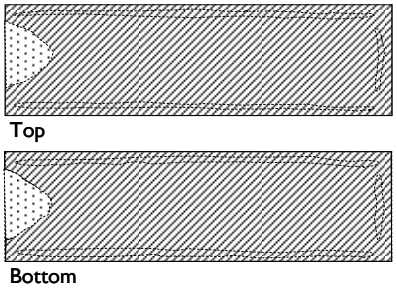

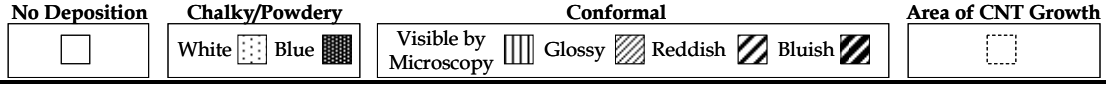

Table 7.4 Maps of alumina deposited from ATSB on weaves from each process.

Results

A summary of the process conditions surveyed for deposition of alumina in a hot-wall reactor using ATSB is provided in Table 7.3. The first six processes surveyed were conducted with tows in order to establish a rough range of conditions suitable for deposition. This was followed by a survey of another 11 sets of conditions aimed at expanding deposition coverage to 18 x 5 cm swatches of desized weaves. The topologies of alumina deposited from this second set of processes are graphically summarized in Table 7.4.

The first process surveyed, Alumina Liquid CVD 1 (Table 7.3), resulted in spontaneous fracture of fibers in the tow, demonstrating that a substrate temperature of 750°C is too hot for the target application. Alumina Liquid CVD 2, performed at 400°C, yielded no observable coating, however. In diagnosing the origins of this result, an atmospheric-pressure CVD process using ATSB with a similar reactor configuration that utilized much higher gas flow rates was found in the literature.[167] After adopting similar flow rate values into our process development, successful deposition of alumina onto tows was achieved. Positioning samples at Zone 1 Center yielded the best results for obtaining conformal coatings, although such coatings were only observable by microscopy. A few individual fibers in each tow were covered with a white, loosely-bound phase of alumina following depositions Alumina Liquid CVD 3-5, with a general white coating observable over most of the tow processed with process Alumina Liquid CVD 6 (in which the tow was positioned at Zone 2 Center at a temperature of 380°C).

Optimization of coverage was investigated by adjusting sample positions (from just before Zone 1 to Zone 2 Center), adjusting sample temperature (from 270-380°C), and adjusting sample orientation (flat, vertical facing incoming flow, vertical parallel with the flow). Flow rates were held constant at the values established in the tow study (bulk He at 6600 sccm, bubbler at 1800 sccm). Two phases of alumina were routinely observed—a chalky white and/or light-scattering-blue phase that was loosely adhered to the fibers in the weave (represented by polka-dot patterns in Table 7.4) and a glossy, sometimes colored conformal glaze similar in appearance to coatings obtained with ATI described in Section 7.2.3.1 (represented by parallel line patterns in Table 7.4). Depending on the specific process conditions, depositions were often present as parabolic or arrowhead-shaped flow patterns. Deposition of both phases seemed to be flow-mediated in part, with the chalky phase most often observed on the underside of the sample and the conformal, glossy phase most often observed on top (Figure 7.18 right). Processes Alumina Liquid CVD 12 and 13 tested whether or not this chalky phase would deposit if the weave were placed vertically instead of laying flat in the process tube and showed in fact only the conformal, glossy phase

deposits in these configurations. These results, in addition to the physical appearance and poor adhesion of the chalky phase, suggest that homogeneous decomposition of the precursor in the bulk gas flow results in formation of alumina particles (i.e., the chalky phase) which then precipitate on the relatively cooler underside of the weave.

In consideration of the target CNT growth application, process development focused on optimizing coverage of the conformal, glossy phase since it was well-adhered, similar in appearance to coatings deposited from ATI that resulted in high-quality aligned CNT growth, and appeared to be formed via a surface-reaction-limited mechanism and thus possible to extend over large sample areas. A process that results in depositions capable of covering the 18 x 5 cm weave dimensions was successfully achieved (process Alumina CVD 17), incorporating a number of process features derived throughout the process development survey. The following is a summary of recommended practices integrated in this process. Weaves should be desized under He at a temperature around 500°C for 10-15 min twice and turned over between desizings (although one longer desizing process may also suffice). The desizing temperature should be calibrated based on TGA of the weave product used and kept as low as possible to minimize damage to the fibers. The sample should lay flat with its left edge placed at a distance of ~2.5 cm past the left edge of Zone 1. The sample may extend approximately 18-20 cm past this point. A substrate temperature set point of 300°C should be used. The ATSB should be preheated to 138°C and thermally homogenized under a low flow rate of 50 sccm of He (or alternatively with a magnetic stirrer) to prevent overshooting of the target vapor pressure when the flow of Ar is boosted and deposition of alumina begins. A flow rate of 1800 sccm Ar through the bubbler supplemented by a flow rate of 6600 sccm He (or N_2 or possibly Ar) flowed directly into the process tube should be used. A deposition time of 60 min is suitable for producing a visibly observable glossy alumina coating over the weave, however the thickness of this coating may be adjusted by changing the deposition time. Finally, to achieve coverage on both sides of the weave, the sample should be flipped over and the deposition process repeated.

While the deposition area was successfully scaled to dimensions suitable for preparing alumina-coated carbon fiber weaves, the deposition processes surveyed were not substrate-selective and not very efficient. A large quantity of white alumina precipitate (a mass-transport-limited phase formed in the bulk carrier gas) deposited throughout the quartz process tube during each deposition with the majority of precipitate condensing in the unheated end of the tube. Additionally, rainbow-colored glaze was observable inside the tube along Zone 1 following several deposition processes. Also, the needle valve

used to control flow from the bubbler became progressively more difficult to actuate with each deposition performed, likely due to the accumulation of an alumina coating over the inside the valve resulting in dimensional changes of the valve's moving parts.

Samples from process Alumina Liquid CVD 16+16b (the same process as Alumina Liquid CVD 17 described above except with only one desizing process performed prior to alumina deposition) and from process Alumina Liquid CVD 17 were dip-coated with Fe^{3+}/IPA solution and CVD processed for CNT growth. As shown in Table 7.4, samples from these processes are largely coated with the conformal, glossy phase of alumina but also have small flow-pattern-shaped deposits of the chalky phase as well. High-yield CNT growth (shown with dashed lines) was observed primarily on the chalky phase patches and near sample edges (possibly due to the presence of a higher concentration of catalyst in these regions from capillary action). Unlike tows coated with alumina from deposition with ATI, catalyst does not stick well to the conformal, glossy alumina coatings deposited on the weaves. CNT growth over the entire alumina-coated weave could only be obtained by "baking on" the Fe^{3+}/IPA solution over the weave (Figure 7.18 left) and even then growth in many places was not high-yield and unaligned. This was performed by placing the weave in a bath of Fe^{3+}/IPA and condensing it into a thick orange film by forced evaporation in an oven at 80°C. Thus while large area coverage was attained, it was concluded that the alumina coatings deposited from ATSB were less wettable than those deposited from ATI. The chalky phase, however, was very wettable by the catalyst solution and did not require baking on to achieve high-yield CNT growth, possibly due to the presence of high-surface-area particles as opposed to the well-consolidated film characteristic of the glossy phase.

Conclusions, Recommendations, and Next Steps

The processes for deposition of alumina from ATSB demonstrated that full coverage over weave specimens is attainable with an atmospheric pressure process, however selectivity and control over the deposited phase and its physical properties was difficult as the feedstock temperature and substrate temperature are coupled in a hot-wall reactor. In response, a cold-wall reactor process was envisioned as a way of optimizing the properties of coatings deposited on the substrate without simultaneously generating a large quantity of a bulk-gas-phase-formed alumina phase. In the following section, development of a cold-wall reactor towards achieving this goal is described.

A process similar to Alumina Liquid CVD 17 could be tailored to give a conformal alumina phase with better wettability. An optimization of total

flow rate and furnace temperature, holding all other parameters constant, may enable large-area coverage as demonstrated here and modulation of the phase and/or morphology of the alumina coating. Alternatively, an acid-etching process or similar could be used to increase the surface area and improve the wettability of the alumina coating, although care would need to be exercised to ensure the carbon fibers are not also etched in doing so. It is important to note that one challenge underlying the use of CVD alumina barrier approaches with weaves and tows is that CNT growth tends to result on the exposed surfaces of the fibers and less so in between fibers. As a result, CVD alumina methods may best be applied in an in-line fiber manufacturing scenario.

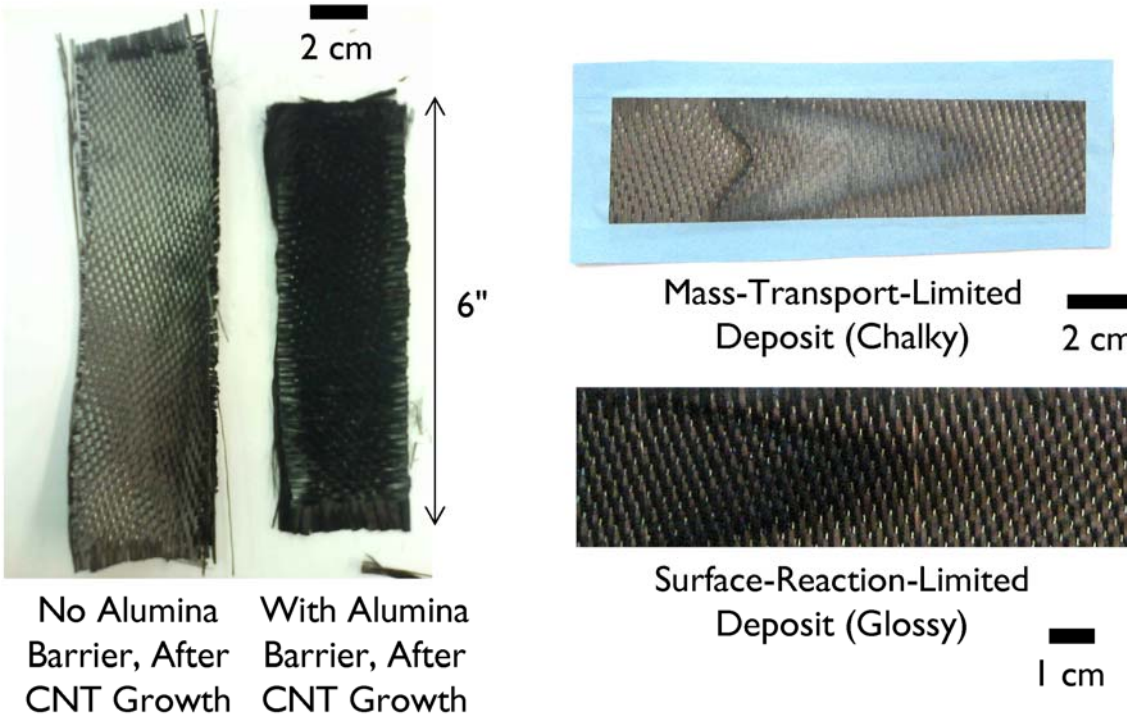

Figure 7.18 *(Left)* Photographs of desized and alumina-coated carbon fiber weaves after coating with iron catalyst and subsequent CVD growth of CNTs, where substantial CNT growth is only observed on the alumina-coated sample; *(right)* photographs comparing the two observed phases of deposited alumina.

In general, CVD of alumina with ATSB in a hot-wall reactor was successful in extending coverage of alumina coatings over the entire area of the 18 x 5 cm carbon fiber weave samples used but proved to be very cumbersome to perform. The MRB required regular maintenance including replacement of the moisture-sensitive ATSB precursor, multiple washings and bakings out of the stainless steel flex bellows, replacement of the bubbler flow control valve, and careful cleaning of the cap seals. Additionally, as the

processes surveyed generated a tremendous amount of alumina dust, quartz process tubes had to be cleaned or replaced after a dozen or so uses due to unmanageable opaque alumina build-up. In addition to the inherent coupling of critical process parameters characteristic of a hot-wall reactor, these logistical challenges complicated optimization of deposition processes (although certainly the general approach of an externalized liquid precursor enabled more flexible optimization than CVD with solid-phase ATI placed inside the reactor). It may be worthwhile to investigate CVD of alumina onto carbon fiber substrates with ATSB at atmospheric pressure in a hot-wall reactor further, however use of a more sophisticated CVD setup designed specifically for deposition of ceramic materials is highly recommended.

7.2.3.3. Liquid-Phase Precursor in Cold-Wall Reactor

To better decouple substrate temperature, precursor temperature, and gas-phase decomposition of the precursor in effort to extend the coverage of deposited alumina coatings over larger areas and control the phase of the deposited alumina, a cold-wall reactor was designed and built (Figure 7.19 and Figure 7.20). This system leveraged the MRB described in Section 7.2.3.2 for delivering precursor vapor at a temperature independent of the substrate temperature and featured an electric-cartridge-heated stainless-steel sample heater in place of the hot-wall furnace used in Sections 7.2.3.1 and 7.2.3.2. All devices in the reactor were automated to improve the accuracy of the process timing.

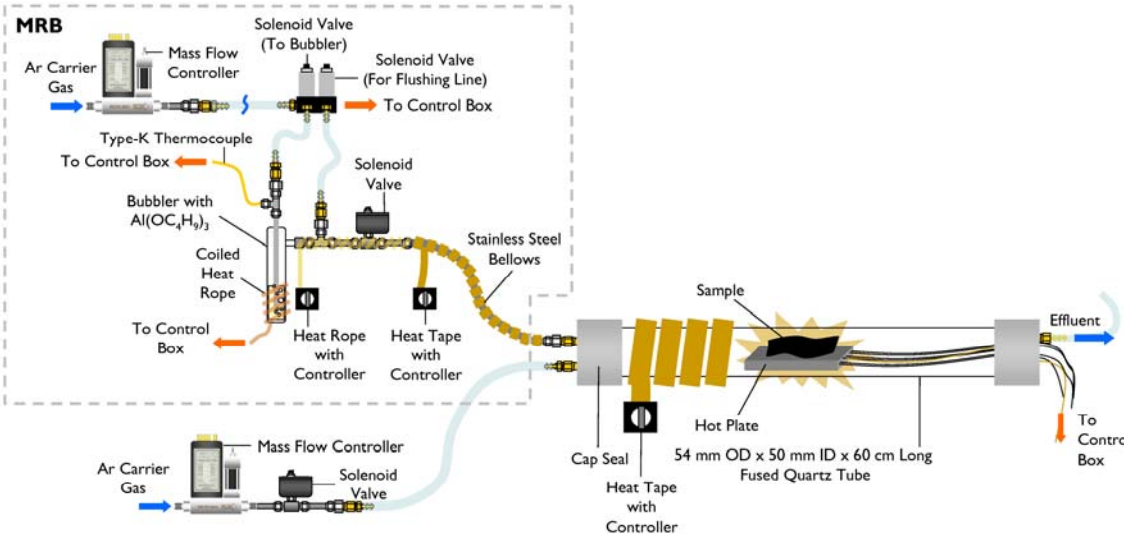

Figure 7.19 Schematic representation of cold-wall reactor designed for CVD of alumina from aluminum tri-*sec*-butoxide.

Materials and Methods

The custom cold-wall reactor shown in Figure 7.19 was used for deposition of alumina from ATSB. Ar gas (Airgas, ultrahigh purity grade, >99.999%) was used as a bulk carrier gas and for delivering ATSB vapor into the reactor. Ar gas to the bubbler could be bubbled through the ATSB or diverted around the bubbler to flush the stainless steel flex bellows of excess vapor (a key design feature to prevent clogging of the solenoid flow-control valve and bellows from accumulation of partially-hydrolyzed ATSB which plagued the hot-wall setup described in Section 7.2.3.2). An unheated fused quartz process tube (54-mm outer diameter, 50-mm inner diameter, 61-cm length) served as the reactor body. A stainless steel block (SS304, 41.0 mm × 14.2 mm × 198.5 mm) fitted with three evenly-spaced cartridge heaters (McMaster-Carr part number 3618K433, 6.35 mm diameter × 198.5 mm length, 525 W) and an embedded type-K thermocouple wire (1.5 mm diameter × 99.3 mm long) served as the sample heater. A vapor delivery manifold and stainless steel flex bellows served as the conduit for precursor vapor between the bubbler and were wrapped with a heat rope (McMaster-Carr part number 3641K23, 100 W, 1 A, 24″ length, controlled by a Payne Engineering heat rope controller from McMaster-Carr, model 18-TBP-1-10, 120 VAC, 10 A, set at ~60% maximum power) and heat tape (BriskHeat heating tape and percentage control from McMaster-Carr, model BSAT051006, McMaster-Carr part number 3631K23, 216 W, 1/2″ wide, 72″ length, 35% maximum power) to prevent condensation of the vapor before reaching the reactor. Similarly, a heat tape (BriskHeat heating tape and percentage control from McMaster-Carr, model BSAT051006, McMaster-Carr part number 3631K62, 288 W, 1″ wide, 48″ length, 25% maximum power) was wrapped around the portion of the quartz process tube before the sample heater. Power to the sample heater cartridges and continuity for the thermocouple was provided by custom-made feedthroughs fitted through the effluent cap seal. A central control box provided computer-controlled relays for all solenoid valves, the heat rope, and the heat tapes as well as a mass flow controller for the bulk Ar. The MRB used in the hot-wall reactor setup described in Section 7.2.3.2 provided a second Ar mass flow controller for delivery of Ar into the bubbler. The same as described in Section 7.2.3.2, the bubbler was filled part-way with ATSB, which served as a liquid-phase alumina precursor.

In a typical process, a tow of unsized carbon fiber (the same fiber used in Sections 7.2.3.1 and 7.2.3.2) approximately 6.5 cm long and tied into a knot at one end was placed on the sample plate. The cap seals were then fitted into place and bulk Ar was flushed through the reactor to displace oxygen (e.g., by flowing 200 sccm for 5 min). Next, the sample heater would be heated to a predetermined set point. Simultaneously, the bubbler would be warmed to

138°C under a flow of 50 sccm to homogenize thermal mixing and the heat rope/heat tapes would be turned on. Once the sample heater and bubbler set points had been reached, the flows of Ar through the bubbler and the bulk Ar were boosted and CVD of alumina began. After a predetermined soak time at these conditions, the flow of Ar through the bubbler was discontinued, the sample plate turned off, and the sample allowed to cool under a flow of bulk Ar (e.g., at 2000 sccm for ~5 min).

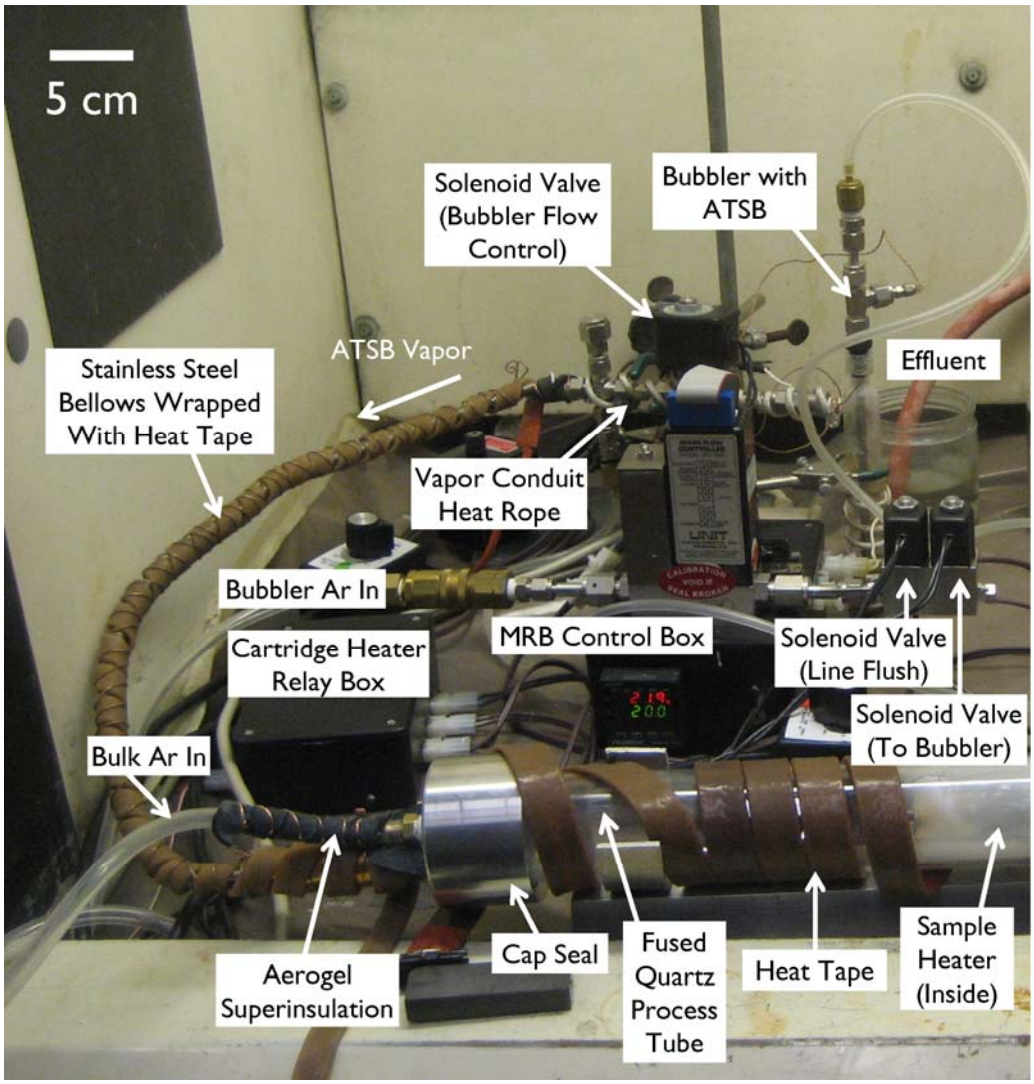

Figure 7.20 Photograph of CVD setup used for deposition of alumina from aluminum tri-*sec*-butoxide in a cold-wall reactor.

Results

A summary of process conditions surveyed for deposition of alumina with ATSB in the cold-wall reactor is provided in Table 7.5. Despite the cold-wall configuration of the CVD setup, a substantial coating of white alumina

powder resulted throughout the inside of the quartz process tube during each deposition. Deposition of alumina onto the carbon fiber tows with this system was overall not promising. No glossy or chalky coating on the tows could be observed following any of the processes surveyed, with the exception of a few isolated fibers that were well-coated with a loose white powder. The sample plate, however, would be obviously coated with alumina after each deposition, observable as a rainbow glazing over the plate that evolved with each deposition performed (Figure 7.21). SEM imaging of deposited-on samples did not reveal substantial alumina coverage other than a speckling of isolated particles along the length of the fibers in the tow (Figure 7.22). It was hypothesized that while the sample plate was hot enough for alumina deposition, thermal transport from the plate to the tow was not efficient enough to heat the tow, save a few well-contacted fibers.

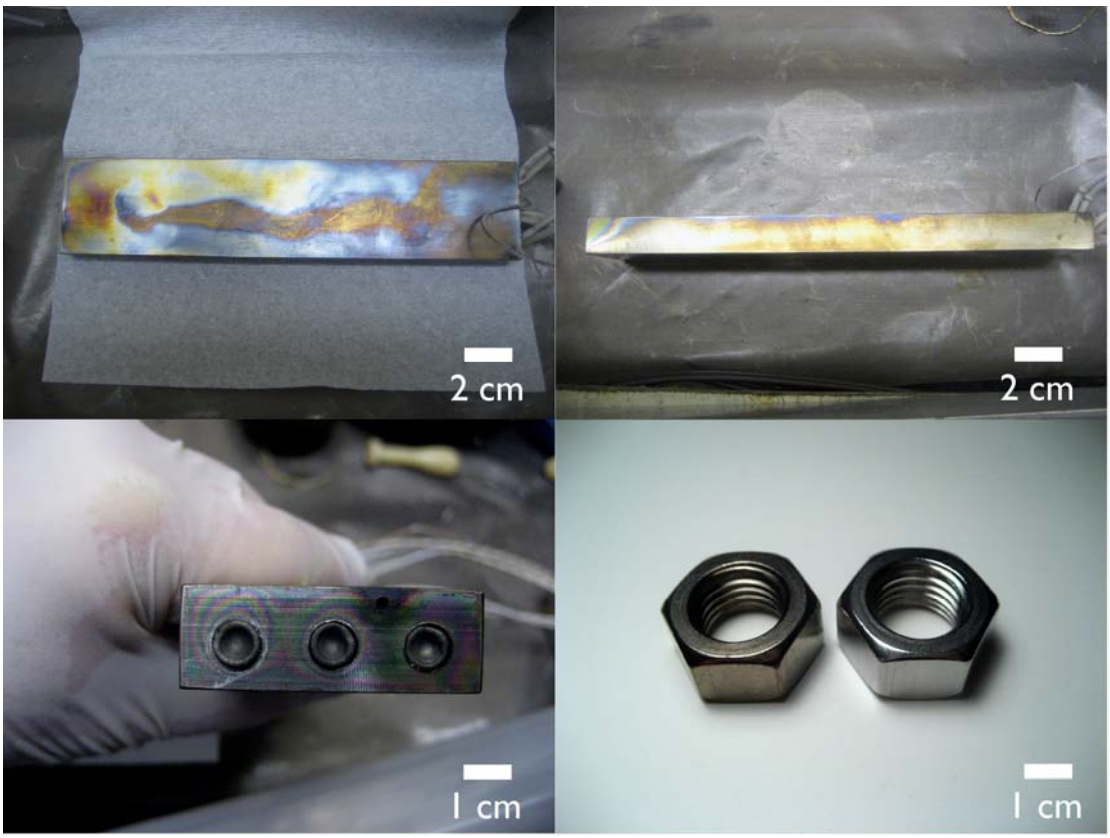

Figure 7.21 *(Top)* Glossy, rainbow-colored alumina film deposited on cold-wall reactor sample heater outlining a silhouette of previously processed tows; *(bottom left)* rings of film thickness variations in alumina coating surrounding tips of cartridges in cold-wall sample heater; *(bottom right)* alumina-coated steel nut (left) next to uncoated steel nut demonstrating the effectiveness of the alumina CVD process for thermally-conductive materials.

The next set of experiments planned focused on methods for improving thermal contact between the sample plate and tow. After a survey of only a few processes, however, the system experienced a major electrical failure due to a manufacturing defect in one of the cartridges embedded in the sample heater which caused an electrical short between the cartridge's electrical leads and damaged the temperature controller controlling the sample plate. Because of this technical setback, process development with the system was stopped until repairs could be made. Following this system failure, industrial liaisons from the carbon fiber manufacturing industry informed us that despite the use of high-temperature processing steps in the production of carbon fibers, integration of a CVD process for depositing an oxide into the carbon fiber manufacturing line would be difficult and much less preferable than solution-based coatings technologies. In consideration of this, the technical challenges regarding thermal transport into the tow, and the continued general difficulties of performing CVD of alumina, further process development was put on hold.

Conclusions, Recommendations, and Future Work

Deposition of alumina onto carbon fiber tows utilizing ATSB in a cold-wall reactor was not successful within the limited set of process conditions surveyed. Thermal transport from the sample heater to the fibers appeared to be problematic. An alternative design incorporating a short hot zone around the portion of the quartz process tube containing the sample heater could help improve heating of the tow. Joule heating through application of an electric current to the tow would be an alternative approach. A mechanical clamp could also be used to help improve thermal contact, although attempts at pinning tows down with a heavy steel nut did not improve deposition onto the tow (but did result in deposition on the nut). Yet another approach would be to use radio frequency coupling to selectively and efficiently heat a carbon fiber substrate target, which could perhaps simultaneously further aid in avoiding build-up of alumina powder due to homogenous bulk-gas-phase reactions. Further investigation with the cold-wall reactor setup may be merited, although would require more substantial further development than the other two CVD approaches surveyed.

7.2.3.4. Conclusions Regarding CVD of Alumina onto Carbon Fibers

CVD has the potential for deposition of a catalyst-wettable, well-adhered, conformal coating of alumina that facilitates high-yield, aligned CNT growth over a carbon fiber substrate. Areal coverage of deposited coatings can be modulated through process parameter optimization and decoupling,

however several factors including the phase of alumina and wettability towards Fe^{3+}/IPA catalyst precursor must be considered. Additionally, the effects of CVD of alumina on the tensile properties of carbon fibers has not been assessed and is a major cause for concern, especially for substrate temperatures in excess of 500°C, where the carbon fiber may become particularly susceptible to tensile properties degradation (as will be discussed in more detail in the following chapter). Cost is another dimension that should be considered, as CVD is energy-intensive and the organometallic alumina precursors can be costly. While CVD of alumina may not be well-suited for integration into a carbon fiber manufacturing line, the most compelling approach for growing aligned CNTs on carbon fibers surveyed during the course of this thesis was with carbon fibers coated with alumina deposited from ATI precursor in a hot-wall reactor. As such, CVD of alumina onto carbon fibers is worth following up with additional investigation, particularly to characterize effects of CVD on fiber tensile properties, however the logistical challenges of performing alumina CVD would merit investment in a more sophisticated hot-wall or cold-wall setup.

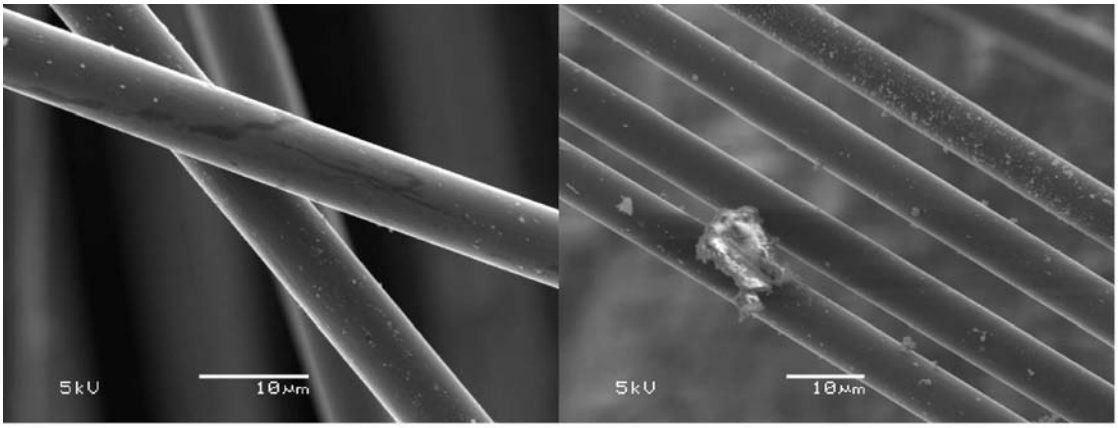

Figure 7.22 SEM images of carbon fiber tows after CVD of alumina from aluminum tri-*sec*-butoxide onto unsized carbon fibers in a cold-wall reactor revealing a sparse, thin alumina coating with particulate deposits.

7.3. Non-Covalent Functionalization of Carbon Fibers

A core problem in depositing both catalysts and barrier coatings onto carbon fibers is poor wettability of the fiber. This problem was particularly evident throughout this work, as the design guidelines established in Section 7.1 eliminated direct chemical modification of the carbon fiber surface to

improve wettability to avoid damaging the outer surface of the fiber whose microstructure provides the majority of the fiber's tensile strength.

Process Name	Sample Type	Bubbler Flow Rate	Bulk Ar Flow Rate	Sample Heater Set Point	Set Point Wait Condition (Time Taken/min)	Soak Time	Results
Test 04 Unsized CF	Unsized Tow	1600 sccm	5280 sccm	380°C	Until Sample Heater > 379°C (0:40)[1] and Bubbler[2] = 138°C (4:50)	30 min	No observable alumina coating, on tow, some stray white fibers, yellowing of sample heater, lots of bulk-phase dust
Test 05 Unsized CF	Unsized Tow	330 sccm	1056 sccm	400°C	Until Sample Heater > 379°C (3:34) and Bubbler = 138°C (5:57)	30 min	No observable alumina coating, on tow some stray white fibers, rainbow gloss over sample heater
Test 06 Unsized CF	Unsized Tow	350 sccm	1056 sccm	500°C	Until Sample Heater > 479°C (4:32) and Bubbler = 138°C (4:58)	30 min	No observable alumina coating on tow, some stray white fibers, rainbow gloss over sample heater
Test 07 Unsized CF	Unsized Tow Held Down by Steel Nut	350 sccm	1056 sccm	500°C	Until Sample Heater > 479°C (4:29) and Bubbler = 138°C (4:41)	60 min	No observable alumina coating on tow, some stray white fibers, yellow coating over nut, rainbow gloss over sample heater

[1]Maximum power duty cycle was set to 40% after this run; consequently heating times were slowed.
[2]Bubbler was warmed up under a flow of 50 sccm Ar to obtain homogenous thermal mixing of the ATSB precursor.

Table 7.5 Summary of process conditions surveyed for alumina CVD from aluminum tri-*sec*-butoxide in a cold-wall reactor.

Of the various methods for depositing alumina barrier coatings onto carbon fibers surveyed in this chapter, sol-gel and CVD show the greatest promise. CVD of alumina yielded the best CNT coverage and morphology of the two approaches, however poses difficulties with regard to integrating into a carbon fiber manufacturing line. Scalability of this process is also questionable. Sol-gel shows the potential for obtaining the desired CNT morphology (see Section 7.2.1.1), but film cracking and poor adhesion to fibers leaves a substantial percentage of fiber surfaces uncovered. Despite this drawback, the ease of processing associated with an atmosphere-compatible, solution-based deposition technique such as sol-gel makes this method promising both in terms of scalability and compatibility with existing carbon fiber manufacturing lines. Improving the wettability of the fiber towards polar species such as the ionic intermediates involved in sol-gel processing could help to reduce or eliminate cracking and delamination of sol-gel-deposited alumina films from carbon fibers despite the mass and volume loss associated with sol-gel depositions.

Additionally, direct loading of catalyst onto a fiber surface, while unlikely to produce an aligned CNT morphology, may be desirable to achieve CNT growth without the need for introducing extraneous substances (such as alumina) into the fiber architecture. This is challenging to do if the fiber surface has poor wettability. As such, development of a method for functionalizing a carbon fiber surface without chemical etching or oxidation is of great interest for both improving adhesion of sol-gel coatings and facilitating direct catalyst loading onto a fiber surface.

In this section, a method of non-covalently functionalizing carbon fibers with amphiphilic polymers derived from poly(styrene-*alt*-[maleic anhydride]) (PSMA) is explored.[168,169] In this method, PSMA is hydrolyzed to produce carboxylate derivatives. Phenyl groups extending off of the polymer backbone undergo π-π stacking with similarly-structured aromatic rings on the surface of the carbon fiber, enabling the carbon fiber surface to be coated by the polymer. Polar carboxylate moieties, also extending off of the polymer backbone, are then repelled by the carbon fiber surface and provide a polar surface functionality over the fiber. Upon heating under inert atmosphere, this polymer results in a carbon coating over the fiber that can potentially protect the underlying fiber from chemical interactions with barrier and catalyst materials. In the following subsections, the use of h-PSMA as a non-covalent functionalizing polymer and its potassium salt (K-PSMA) as a polyelectrolyte for ion exchange are investigated as methods for improving adhesion of sol-gel-derived alumina coatings and solution-deposited iron catalyst precursors to carbon fibers. These methods are then surveyed for efficacy in facilitating CNT growth.

7.3.1. Improving Adhesion of Alumina Barrier Coatings with Poly(styrene-*alt*-[maleic acid]) (h-PSMA)

Stroock *et al.* have described a method for preparing freestanding films on hydrophobic surfaces using the polymer poly(styrene-*alt*-[maleic acid]) (h-PSMA).[168] h-PSMA is produced by hydrolysis of poly(styrene-*alt*-[maleic anhydride]) (PSMA) through ring opening of maleic anhydride moieties on the polymer to yield carboxylic acid groups (Figure 7.23). The resulting amphiphilic h-PSMA polymer adsorbs and deposits onto hydrophobic surfaces from aqueous solutions by favorable hydrophobic interactions while simultaneously presenting a polar carboxylic acid functionality over the substrate surface. Carillo *et al.* adapted this technique for non-covalently functionalizing highly-oriented pyrolytic graphite (HOPG) surfaces and carbon nanotubes with polymeric films.[169] Carbon fibers, with a hydrophobic graphitic surface similar to both HOPG and CNTs, could be similarly functionalized with h-PSMA to improve adhesion of sol-gel-derived coatings, since sol-gel processing is an ionically-mediated process, i.e., relies on polar intermediates. Here h-PSMA is evaluated as a coating for reducing cracking and improving coverage of sol-gel-derived alumina coatings on carbon fibers.

Methods and Materials

Aqueous solutions with varying concentrations of h-PSMA were prepared according to the method of Stroock *et al.*[168] (see Figure 7.23). Solutions were prepared by dissolving 1.4 g, 4.2 g, or 7.0 g (corresponding to concentrations of 0.5, 1.5, and 2.5 wt%, respectively) of PSMA (Sigma-Aldrich, 99%, M_w=350,000) in 25 mL of acetone with gentle heating. The PSMA solution was then added to 300 mL of 0.3 M NaOH in deionized water with stirring and allowed to react for 3 h, after which it was acidified with 0.1 M HNO_3 to a pH of 8. The acetone in the solution was then removed with a rotary evaporator.

Unsized (i.e., never-sized), never-surface-treated carbon fiber tow (TohoTenax product number HTR40 N00 24k 1550tex) was used for substrates. (*Note:* This product was obtained through industrial liaisons and is not available commercially. The equivalent commercial version, HTA40 F22 24k 1550tex, is surface-treated and sized.) h-PSMA was coated over the fibers by dip-coating a tow in aqueous h-PSMA solution for ~5 min and subsequently allowing the tow to dry in air or blow-drying with cool air (which took ~9 min). Upon removal of the tow from h-PSMA solution the tow became noticeably stiff and hard to peel apart. To improve coating of

fibers in the inner tow, the tow could be dabbed up and down in the h-PSMA solution (as is done to clean a watercolor paintbrush) over the 5-min period.

The h-PSMA-coated fibers were next coated with a sol-gel-derived alumina or silica coating using one of the methods described in Section 7.2 and coated with catalyst for CNT growth. First, a catalyst solution of 0.050 M $Fe(NO_3)_3 \cdot 9H_2O$ in 2-propanol (IPA) was prepared and aged with stirring for 0-2 h. Solution aging time was examined as a parameter for controlling CNT diameter and density as iron oxide nanoparticles continually grow in the solution during this time frame and eventually precipitate. h-PSMA/oxide-coated fibers were subsequently dip-coated into this solution for ~5-30 min.

Finally, the h-PSMA/oxide/Fe^{3+}-coated fibers were CVD processed for CNT growth. CVD growth of CNTs was performed in a fused quartz tube (54-mm outer diameter, 50-mm inner diameter, 137-cm length) heated by a three-zone split-hinge tube furnace (Lindberg/Blue M model HT55667C, 30-cm heated zone lengths). (*Note:* Due to the distance between thermocouples in this furnace and how a 54-mm process tube sits in this furnace, reported temperatures may underestimate actual process temperatures by ~80°C as determined by calibrations performed with *in situ* thermocouple measurements). In a typical process, specimens were placed in a fused quartz process tube at the center of the third zone. The tube was then flushed with a flow of 2070 sccm He for 10 min to displace oxygen from the tube. Next, He was turned off and a flow of 1040 sccm H_2 gas (Airgas, ultrahigh purity grade, >99.999%) was introduced. The sample was then heated to 650°C under H_2 gas over the course of ~8 min to reduce iron oxide nanoparticles on the specimen to catalytically-active iron. The sample remained at these conditions for an additional 7 min to further reduce remaining iron oxide nanoparticles. A flow of 316 sccm ethylene (Airgas, ultrahigh purity grade, >99.999%) was then added for 5 min to facilitate CNT growth. Lastly, H_2 and C_2H_4 were turned off and the sample was allowed to cool to room temperature under a flow of 2070 sccm He.

Improvements in adhesion to unsized carbon fibers and reduction in cracking of sol-gel-derived coatings were assessed by FE-SEM and spatial elemental analysis by Auger spectroscopy.

Results

Unsized carbon fiber tows dip-coated with aqueous h-PSMA and uncoated control tows were analyzed by FE-SEM and Auger spectroscopy to determine if h-PSMA would readily adsorb onto a carbon fiber surface in the first place (Figure 7.24). h-PSMA-coated fibers exhibited a softer appearance than the control fibers, did not undergo substantial differential charging from the electron beam, and exhibited occasional "goopy" features protruding off

of the surface. Spatial elemental analysis by Auger revealed the presence of Na over the h-PSMA sample but no Na on the control sample. The presence of Na would be expected on an h-PSMA sample since NaOH is used to hydrolyze anhydride moieties on the PSMA precursor (Figure 7.23) and so Na^+ ions remain in solution when h-PSMA is formed and deposited. Auger analysis revealed an extensive coverage of a well-adhered conformal h-PSMA coating, disrupted only where fibers had clung together during dip-coating of the h-PSMA due to capillary action.

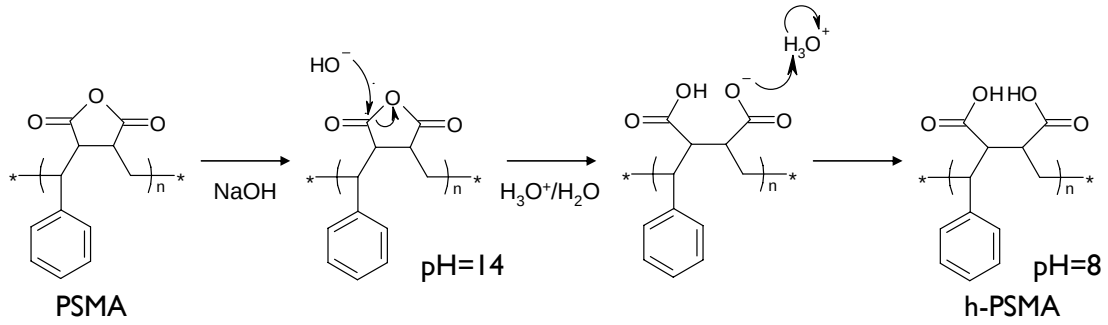

Figure 7.23 Preparation of h-PSMA from PSMA.

The efficacy of h-PSMA for improving adhesion of sol-gel-derived coatings was evaluated next. The sol-gel procedures explored in Section 7.2.1 were used in conjunction with h-PSMA-coated carbon fiber tows. Alumina coatings produced by the baked-on alkoxide technique (see Section 7.2.1.2) on bare fibers and h-PSMA-coated fibers are shown in, Figure 7.25 and Figure 7.26, respectively. A crack-laden, delaminating alumina film is observed as expected on the sample without h-PSMA leaving a substantial amount of fiber bare. With h-PSMA, however, a conformal alumina coating exhibiting substantially less cracking and substantially improved coverage over the fibers is observed. In both the control and h-PSMA-coated fibers, Auger verifies the presence of Al in the observed coatings.

The efficacy of h-PSMA for improving adhesion of silica sol-gel-derived coatings, which, as described in Section 7.2.1.3, are deposited from an alkoxide and result in a high degree of mass loss upon evaporative drying, was also investigated. Figure 7.27 shows the presence of unevenly-distributed silica deposits over carbon fibers without h-PSMA coating. Spatial elemental analysis by Auger verifies that lighter patches on the fiber surface, present as both sporadic thin films and in thick chunks, contain Si and O, whereas the surrounding dark regions only contain C, indicating these dark regions are the uncoated carbon fiber surface. On carbon fibers coated with h-PSMA (Figure 7.28), however, a well-adhered (but "gloopy") coating with uneven thickness is observed. Auger shows the presence of Si and O

over the fibers both in thicker deposits and over areas that at first glance seem to be uncoated fiber surfaces (but are actually just thin coatings). This signals that h-PSMA can also improve adhesion of alkoxide-derived gel coatings that undergo substantial mass loss upon evaporative drying due to their high pore volumes.

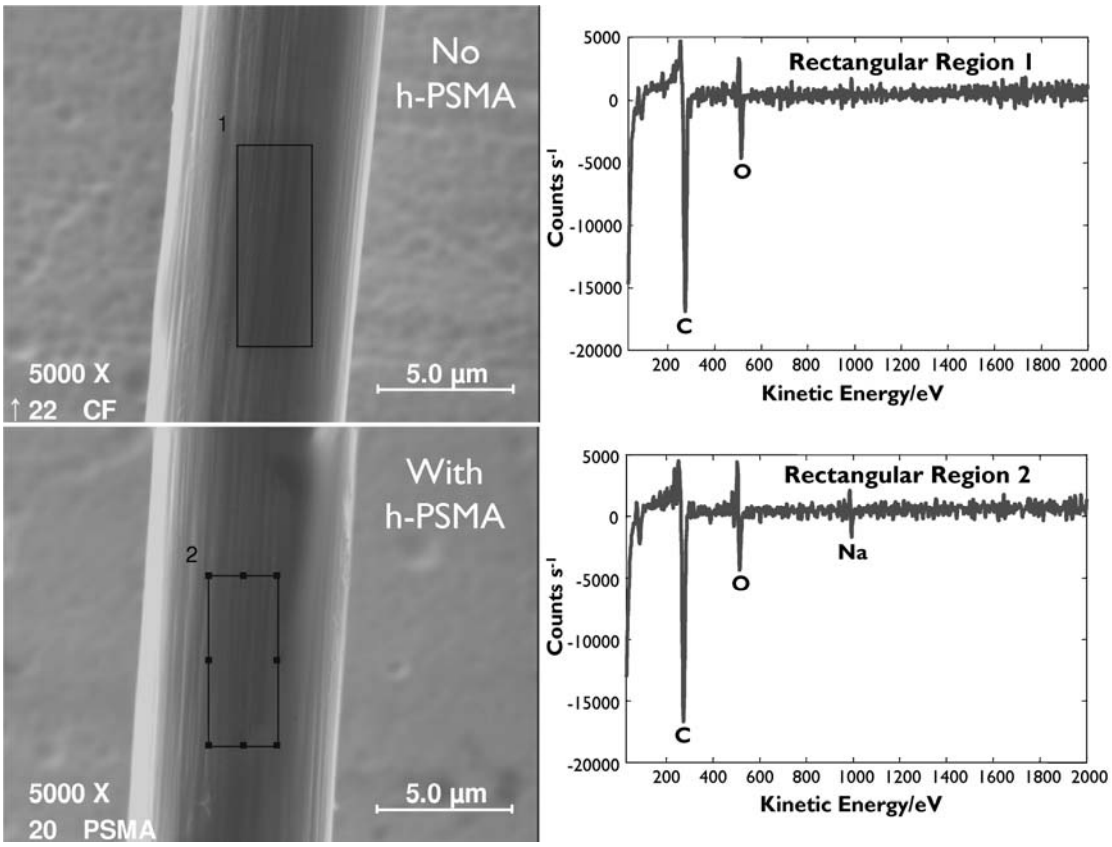

Figure 7.24 FE-SEM and Auger spectra for an unsized, uncoated carbon fiber *(top)* and an h-PSMA-coated carbon fiber *(bottom)*; the softer appearance, reduced charging, and presence of Na on the bottom fiber indicate h-PSMA is present.

Of greatest interest, however, was whether or not h-PSMA could also improve adhesion of sol-gel-derived alumina coatings prepared from propylene-oxide-assisted gelation of aluminum salts (Section 7.2.1.1). As discussed, this approach enables high-yield, aligned CNT growth, however exhibits poor adhesion and undergoes substantial volume contraction during both the gel aging phase (up to 50%) and upon evaporative drying (up to 90% of the aged gel) thereby leaving substantial areas of bare fiber. Figure 7.29 compares initially-uncoated carbon fibers covered with alumina deposits produced through this technique following dip-coating with Fe^{3+}/IPA and subsequent CNT growth by CVD against h-PSMA-coated carbon fibers covered with alumina produced through this technique. While a substantial

degree of cracking is observed over the h-PSMA-coated fibers, the coverage is noticeably improved over the control fibers.

Conclusions

h-PSMA was found to markedly improve adhesion and reduce cracking in sol-gel-derived coatings applied to unsized, never-surface-treated carbon fibers despite the mass loss associated with many sol-gel processes. This said, h-PSMA can only partially compensate for volume contraction arising from mass loss as seen for the alkoxide-derived silica and epoxide-assisted alumina coatings described above. This could be mitigated by first coating carbon fibers with h-PSMA followed by multiple sol-gel depositions (perhaps 3-4), although the resulting coating coverage would likely be quite non-uniform.

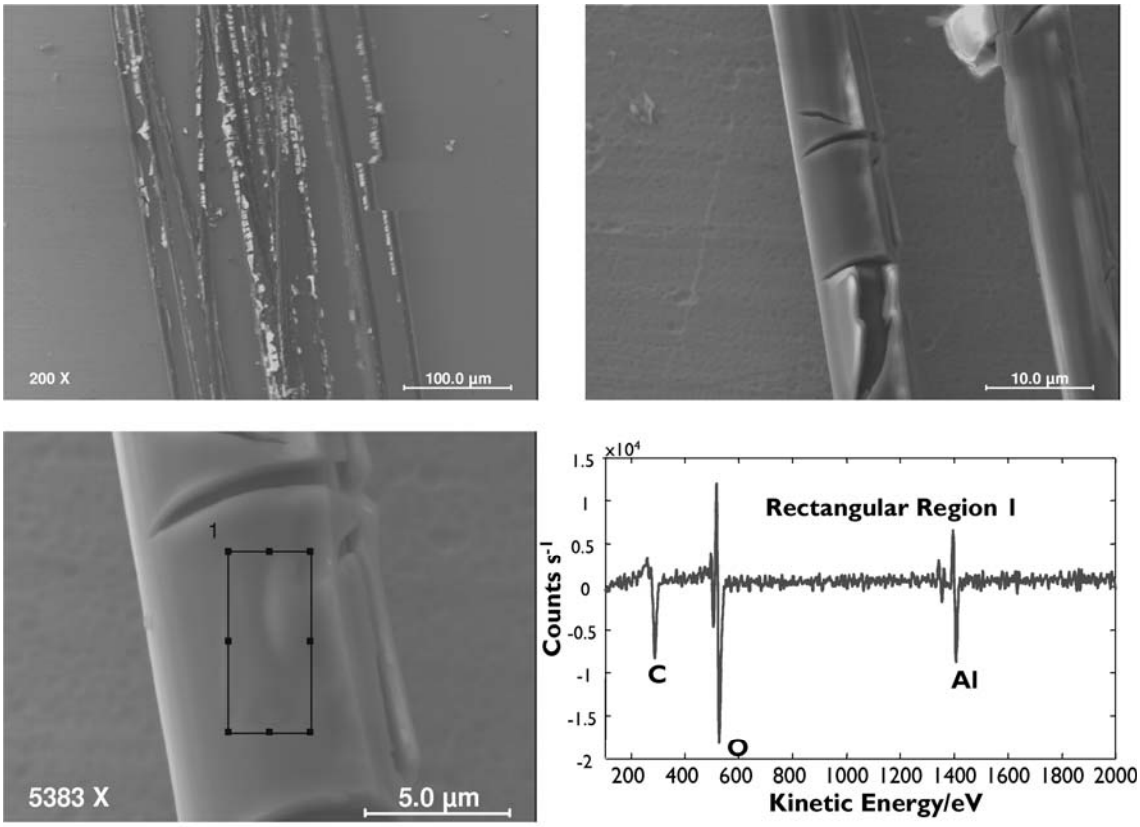

Figure 7.25 FE-SEM images and Auger spectrum of an alumina coating on a carbon fiber without h-PSMA underlayer produced with the baked-on alkoxide sol-gel process described in Section 7.2.1.2; substantial film cracking and delamination are observed, resulting in consolidated chunks of alumina rather than uniform coverage.

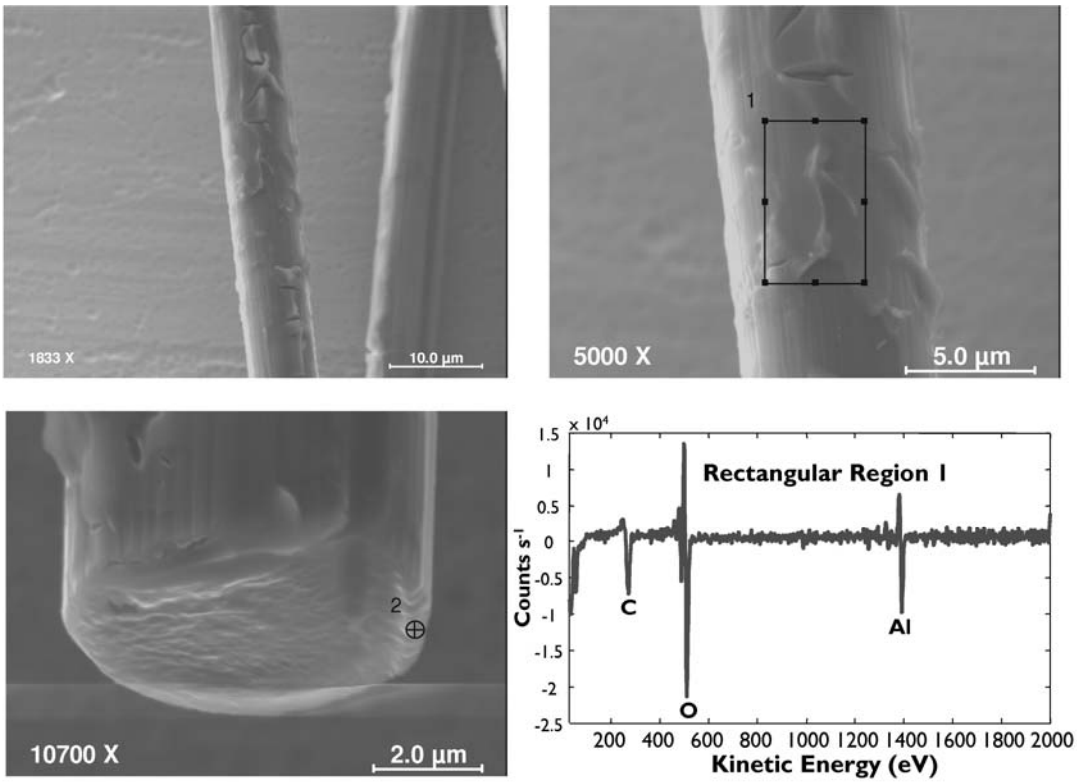

Figure 7.26 FE-SEM images and Auger spectrum of an alumina coating on a carbon fiber with h-PSMA underlayer produced with the baked-on alkoxide sol-gel process described in Section 7.2.1.2; cracking, bare spots, and delamination are substantially reduced (compare to Figure 7.25) and film coverage is consequently improved.

7.3.2. Low-Temperature CNT Growth Facilitated by Poly(styrene-*alt*-[dipotassium maleate]) (K-PSMA)

Low-temperature (<500°C) CVD growth of CNTs was recently described by Magrez *et al.*[170] In their work, oxidative dehydrogenation of acetylene by carbon dioxide over Fe-containing catalysts is shown to result in CNT growth over a wide range of temperatures. Growth of CNTs on an impressive variety of temperature-sensitive substrates is demonstrated, including wooden toothpicks(!), aluminum foil, and carbon fibers. In their methods, Fe catalyst was e-beam evaporated or physical-vapor deposited onto the substrates. The substrates were then processed by CVD using CO_2 and C_2H_2 (without a flow of H_2) in a 1:1 molar ratio at temperatures as low as 380°C.

As described in greater detail in Chapter 8, throughout the course of this work it was found that CNT growth on carbon fibers at temperatures below

500°C would be highly desirable for preserving the tensile properties of the fibers. The work of Magrez *et al.* accordingly served as inspiration that sub-500°C growth of CNTs on carbon fibers may be possible and that a method that adheres to the design guidelines set forth in Section 7.1 (namely one that does not damage the fibers pre-CVD and that does not require e-beam or PVD) could potentially be devised.

Magrez *et al.* found that the CNT growth temperature is highly dependent on the composition of the substrate supporting the Fe catalyst. For example, maximal-yield CNT growth from alumina-supported Fe was found to occur at a temperature of ~650°C. Growth from carbon-supported Fe, however, was found to be maximally effective at ~400°C. Based on these findings, we hypothesized that h-PSMA-coated carbon fibers could be dip-coated with Fe^{3+}/IPA solution and subsequently CVD processed at these low temperatures to yield CNT growth in a way that meets the design guidelines set forth in Section 7.1. Somewhat frustratingly and curiously, however, CNT growth, even with C_2H_4/H_2 at temperatures of 650-720°C, did not occur in appreciable yield on h-PSMA-coated fibers dip-coated with Fe^{3+}/IPA. Differential experimentation revealed that Fe^{3+} did not substantially adsorb onto the h-PSMA polymer on the carbon fiber surface.

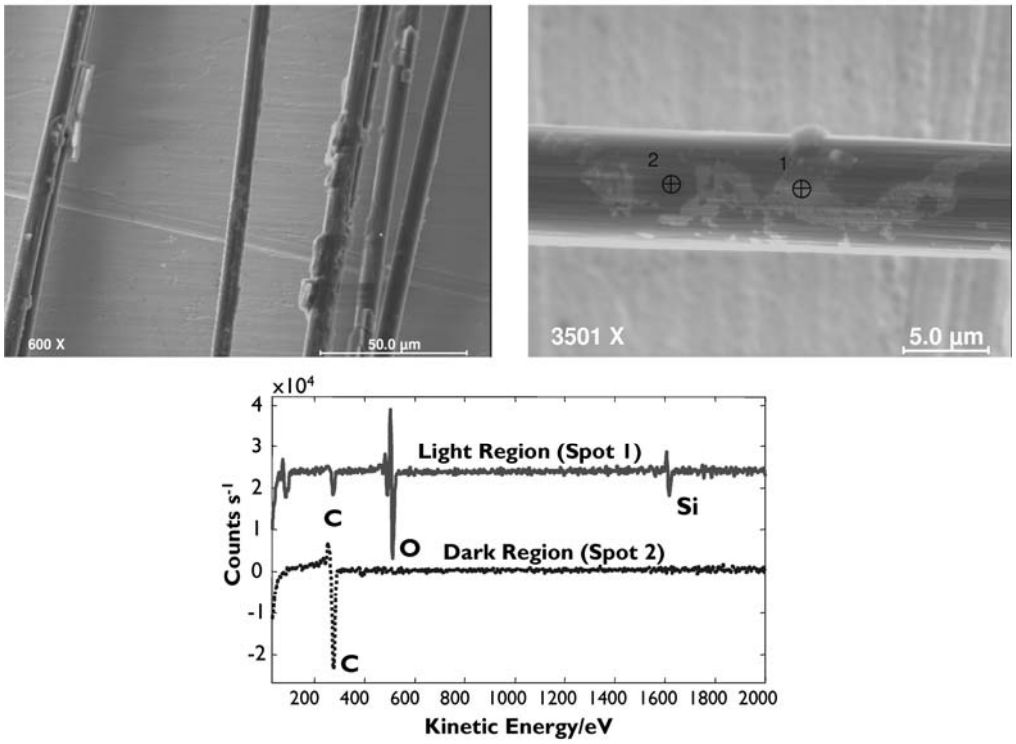

Figure 7.27 FE-SEM images and Auger spectrum of a silica coating on a carbon fiber without h-PSMA underlayer produced with the alkoxide silica sol-gel process described in Section 7.2.1.3; sparse silica coverage is observed in both thin films and loosely-adhered chunks.

It was then recognized that the carboxylic acid moieties on h-PSMA resembled the surface of phenolic resins used in ion exchange filtration, not to mention the aerogel precursors used to prepare zirconia-doped carbon aerogels described in Chapter 4. Accordingly, it was hypothesized that a K^+-salt-based ion-exchange polyelectrolyte could be prepared from h-PSMA and used to ion exchange iron onto a carbon fiber surface without damaging the carbon fiber. Furthermore, the polyelectrolyte, upon heating, would dehydrate to yield a sacrificial carbonaceous barrier that would prevent contact between resulting iron nanoparticles and the carbon fiber surface, which has been demonstrated with e-beam evaporated Fe/Al films on epoxy-coated fibers.[146]

In this section, the development and optimization of such a polyelectrolyte, poly(styrene-*alt*-[dipotassium maleate]) (K-PSMA), is described and its utility for enabling high-yield, unaligned CVD growth of CNTs on carbon fiber tows at temperatures below 500°C is demonstrated.

Methods and Materials

Various formulations for preparing K-PSMA were explored. In the method most optimal for CNT growth, a solution of 1.5 wt% h-PSMA is prepared as described in Section 7.3.1. The h-PSMA polyacid is then neutralized by stirring solid K_2CO_3 (Sigma-Aldrich part number 209619, ≥99.0%) into the solution (see Figure 7.30). At first, the K_2CO_3 simply dissolves in the solution, but upon further addition, evolution of a CO_2 fizz results. K_2CO_3 is added until CO_2 fizz no longer results upon further addition. This point corresponds to a solution pH of ~11 or ~0.79 g K_2CO_3/10.00 g 1.5 wt% h-PSMA solution. Alternative formulations were also explored. In one set of formulations, KOH was used instead of NaOH during hydrolysis of the PSMA precursor. In some of these formulations, the solution was only acidified to a pH of ~11 to test whether or not a K^+-rich solution at a pH of ~11 would result in K-PSMA or if neutralization with K_2CO_3 from a pH of 8 was required. In another set of formulations, the concentration of h-PSMA used was 0.5 wt% instead of 1.5 wt%.

Unsized (i.e., never-sized), never-surface-treated carbon fiber tow (TohoTenax product number HTR40 N00 24k 1550tex) was used for substrates. (*Note:* This product was obtained through industrial liaisons and is not available commercially. The equivalent commercial version, HTA40 F22 24k 1550tex, is surface-treated and sized.) Carbon fiber tows (~10 cm long) were cut and taped at one end with masking tape (3M 2600) for ease of handling. K-PSMA was coated over the fibers by dip-coating a tow in aqueous K-PSMA solution for ~5 min and subsequently allowing the tow to dry in air or blow-drying with cool air (which took ~9 min). Upon removal of

the tow from K-PSMA solution the tow became noticeably stiff and hard to peel apart, but less so than when coating with h-PSMA. To improve coating of fibers in the inner tow, the tow could be dabbed up and down in the h-PSMA solution (as is done to clean a watercolor paintbrush) over the 5-min period.

K-PSMA-coated fibers were then dip-coated with iron catalyst precursor solutions. In one set of formulations, 0.050 M $Fe(NO_3)_3 \cdot 9H_2O$ in 2-propanol (Fe^{3+}/IPA) was used. In subsets of these formulations, the Fe^{3+}/IPA solution was aged for 30 min, 60 min, and 90 min prior to dip-coating. Some K-PSMA-coated fibers were dip-coated before the K-PSMA deposit was dry, others were dip-coated after it was dry. Alternatively, 0.1 M aqueous $Fe(NO_3)_3$ was used to dip-coat catalyst precursor. After dip-coating with catalyst, the masking tape at the end of the tow was cut off. At this point, the tow was sufficiently stiff from and held together by its K-PSMA coating that handling of the fibers was possible without tape.

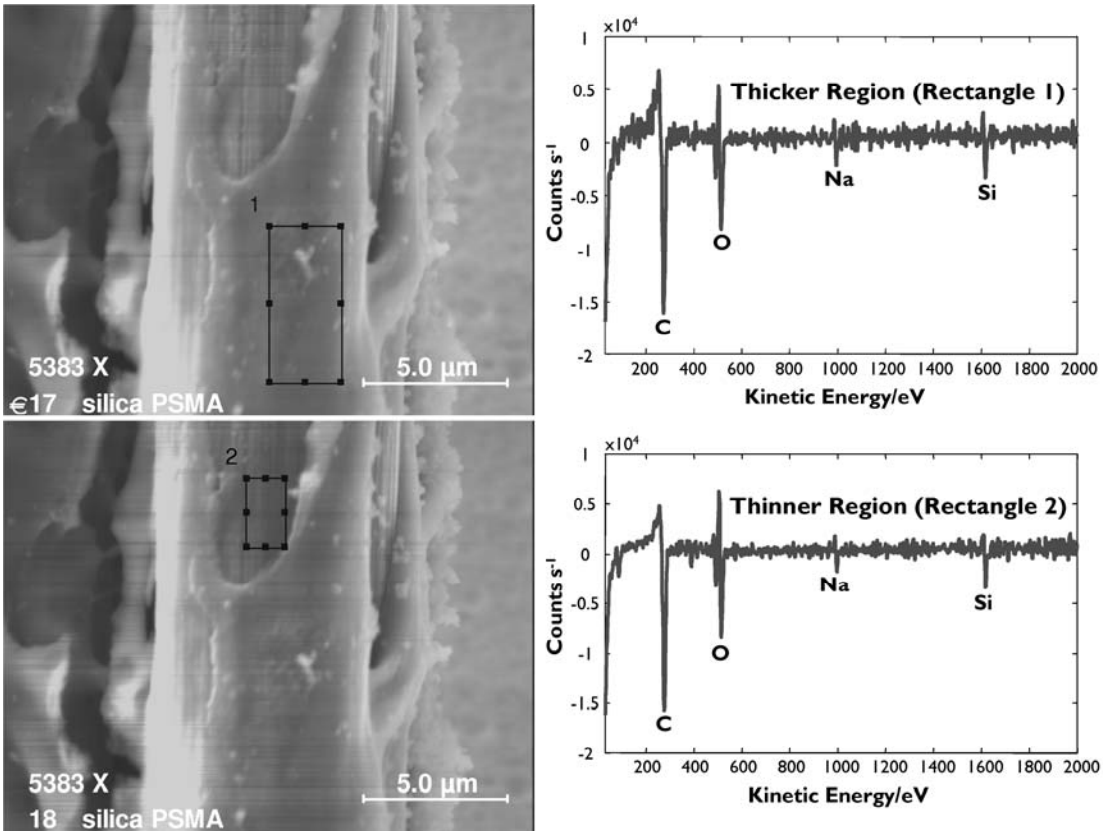

Figure 7.28 FE-SEM images and Auger spectrum of a silica coating on a carbon fiber with h-PSMA underlayer produced with the alkoxide-based silica sol-gel process described in Section 7.2.1.3; silica is present as both a thick coating *(top)* and conformal thin film *(bottom)* over the fiber surfaces.

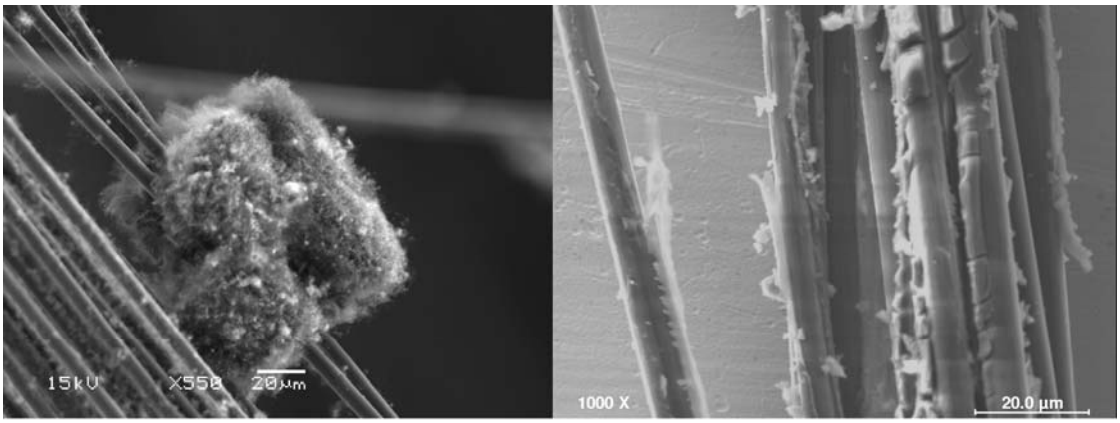

Figure 7.29 Comparison of SEM images displaying representative morphologies for carbon fibers coated with alumina from propylene oxide-assisted gelation without h-PSMA undercoating *(left, post-CNT growth)* and with h-PSMA undercoating *(right, pre-CNT growth)*; the presence of h-PSMA expands coverage of the alumina substantially despite significant (~50%) volume loss due to evaporative drying of the alumina sol-gel deposit.

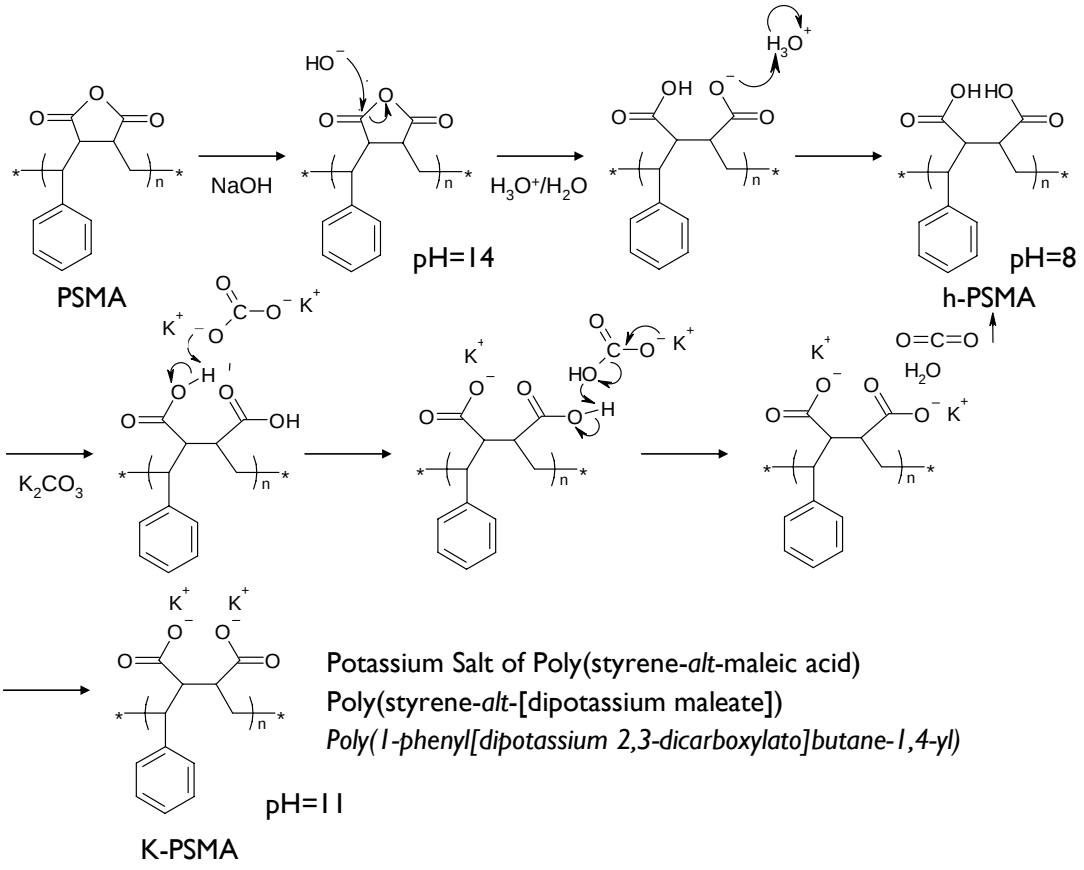

Figure 7.30 Preparation of K-PSMA polyelectrolyte from PSMA.

The Fe^{3+}/K-PSMA-coated fibers were then CVD processed for CNT growth. CVD processing was performed using the MANGO-TANGO CVD system described in Chapter 6 in a hot-wall configuration. Temperature set points reported by Magrez *et al.* were calibrated against our system's set points by comparing the optimal temperature for CNT growth established for Fe/alumina-coated wafers via the CO_2/C_2H_2 process described in Chapter 6. Based on this calibration experiment, it was determined that the temperatures reported by Magrez *et al.* underestimate the optimal growth temperature for similar substrates in our system by ~80°C. As such, the optimal growth temperature for carbon-supported iron reported by Magrez *et al.* (400°C)[170] was converted to a set point of 480°C for our system (and is believed to be more accurate, see Section 6.3.1). Samples were placed in a dedicated fused quartz process tube (25-mm outer diameter × 22-mm inner diameter × 30-cm length) and heated in an electric clam-shell tube furnace (Lindberg/Blue M MiniMite). Samples were positioned at 75% along the length of the heated zone. First, a flow of 750 sccm Ar (Airgas, ultrahigh purity grade, >99.999%) was introduced into the reactor for 2 min to displace oxygen from the process tube. Next, a flow of 400 sccm H_2 (Airgas, ultrahigh purity grade, >99.999%) was added and the Ar flow lowered to 200 sccm Ar. The samples were then heated to a set point temperature of 480°C under H_2/Ar flow to reduce and coarsen iron ions adsorbed over the coated fiber surfaces to iron nanoparticles. Once at this temperature, a flow 17 sccm CO_2 (Airgas, ultrahigh purity grade, >99.999%) and 167 sccm 10% C_2H_2 in Ar (Airgas, ultrahigh purity grade, >99.999%, acetone-free) were introduced and the H_2 and Ar deactivated. The samples were soaked under these conditions for 15 min after which a flow of 750 sccm Ar was introduced and the CO_2 and C_2H_2/Ar mixture were deactivated. The furnace was then opened and the samples were allowed to cool to ambient conditions. Between CNT growths, the quartz process tube was baked in air at 750°C for ~20 min to remove deposited organics. In one variation of this process, samples were not treated with H_2 on ramp-up to the set point temperature.

Efficacy of various K-PSMA formulations and catalyst application methods for facilitating CNT growth was assessed by the presence, areal density, and length of CNTs on tows following from CVD processing as observed by SEM.

Results

K-PSMA prepared through what proved to be the optimal process (PSMA hydrolyzed with NaOH, acidified to pH=8 with HNO_3, neutralized to pH=11 with K_2CO_3) was examined first (Figure 7.31). Short (1-3 μm), unaligned CNTs, similar to those reported by Magrez *et al.*,[46] are observed in a

significant quantity (~6-8 CNTs/μm^2) over the majority of fibers in the tow (where the fibers successfully engaged the coating solutions). As a control, an unsized tow without K-PSMA was coated with iron catalyst precursor by baking on Fe^{3+}/IPA solution and processed with the same CVD procedure (Figure 7.32). No CNTs were observed on this tow; instead, platelettes of iron presenting an observable grain structure were found delaminating from the fibers. An h-PSMA-coated tow was similarly processed and resulted in virtually no CNT growth (Figure 7.33), indicating by differential that little iron adsorbs to the h-PSMA coating and that the polyelectrolyte K-PSMA readily uptakes iron.

As the CO_2/C_2H_4 process does not require additional H_2 during CNT growth, for industrial applications it would be desirable to eliminate H_2 altogether, namely, to be able to reduce iron nanoparticles without H_2. It was hypothesized that iron nanoparticles could be formed on the K-PSMA coating without H_2 on ramp-up to the set point temperature since excess carbon provided by the K-PSMA coating could serve as a carbothermic reducing agent. The result was the formation of pointy crystalline structures ~2-3 μm across atop large oval islands of what appears to be polymer over the surface of the fibers and only very sporadic CNT growth (Figure 7.34). It was concluded that the presence of H_2 during ramp-up to the set point temperature influences the thermodynamics of the iron reduction in an important way; without it, another morphology (or possibly an iron carbide) results.

A method for improving CNT areal yield through the creation of a poly(styrene-*alt*-[iron(III) maleate]) (Fe-PSMA) coating was evaluated. In this approach, a polymer that brings Fe^{3+} with itself thereby eliminating the need for ion exchange would be coated onto the carbon fiber directly. To prepare such a polymer, a few drops of 1.5 wt% K-PSMA were added to a solution of Fe^{3+}/IPA with a Pasteur pipette. Instantly upon contact, a neutrally-buoyant orange polymer film formed in the vile. Shortly after (minutes), the solution in the vial was no longer the typical yellow-orange color characteristic of Fe^{3+}/IPA but instead virtually clear. Vigorous shaking of the vial eventually broke the polymer film into a loose, Martian-red precipitate. This experiment demonstrated K-PSMA to be a highly efficient agent for removal of iron ions from solutions and that in fact ion exchange does occur on K-PSMA-coated fiber surfaces as hypothesized, but that coating with previously-made Fe-PSMA polymer itself is not straightforward as it precipitates from solution on formation.

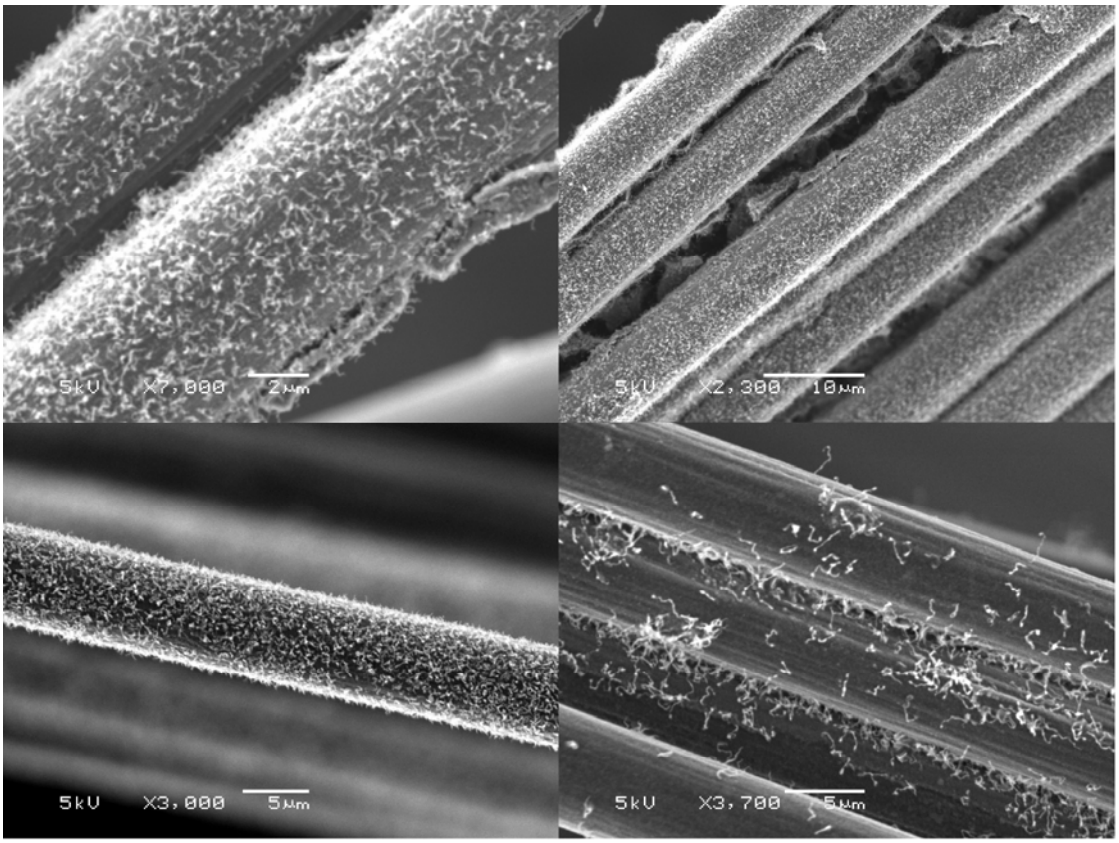

Figure 7.31 SEM images of successful growth of CNTs at 480°C on carbon fibers with K-PSMA coating (anhydride hydrolyzed by NaOH, acid neutralized with K_2CO_3, 1.5 wt %, doped with catalyst precursor with Fe^{3+}/IPA) grown via a CO_2/C_2H_2 CVD process: *(top left)* representative fiber covered with unaligned CNTs; *(top right)* overview of fuzzy fibers in tow; *(bottom left)* detail of a single fuzzy fiber; *(bottom right)* infrequent fibers in tow presenting sparser growth.

In effort to optimize CNT growth and reduce sample preparation time, the effects of dip-coating K-PSMA- and h-PSMA-coated fibers directly into catalyst solutions without drying first was evaluated (Figure 7.35). Upon dip-coating still-wet fibers (coated with either K-PSMA or h-PSMA) into Fe^{3+}/IPA solutions, a visible, orange precipitate (perhaps Fe-PSMA or similar) was observed. Following CVD processing, the orange precipitate was not observed (i.e., the iron(III) content was reduced). SEM imaging of the K-PSMA-coated sample showed no CNT growth but instead large (~10 µm) crystalline particles (assumedly Fe) over a bumpy surface (either Fe or iron carbide particles embedded in the pyrolyzed K-PSMA). The h-PSMA-coated sample was substantially featureless save the presence of a coating (probably pyrolyzed h-PSMA) also with occasional nanoscale bumps. A measurement of the pH of 0.50 M $Fe(NO_3)_3 \cdot 9H_2O$ in 2-propanol (i.e., Fe^{3+}/IPA) found this solution to be quite acidic with a pH of ~2. Likely, upon contact with the wet

K-PSMA or h-PSMA coatings, the acidic solution causes precipitation of something like Fe-PSMA in the case of K-PSMA and precipitation of just h-PSMA (with some iron intermixed with it) in the case of h-PSMA, which was determined to not absorb iron well. In the case of K-PSMA, the coating is overloaded with iron ions; upon reduction, large crystallites of iron are formed. In the case of h-PSMA, a small amount of intermixed iron results in the formation of occasional Fe-based particles (nanoscale bumps on the polymer coating).

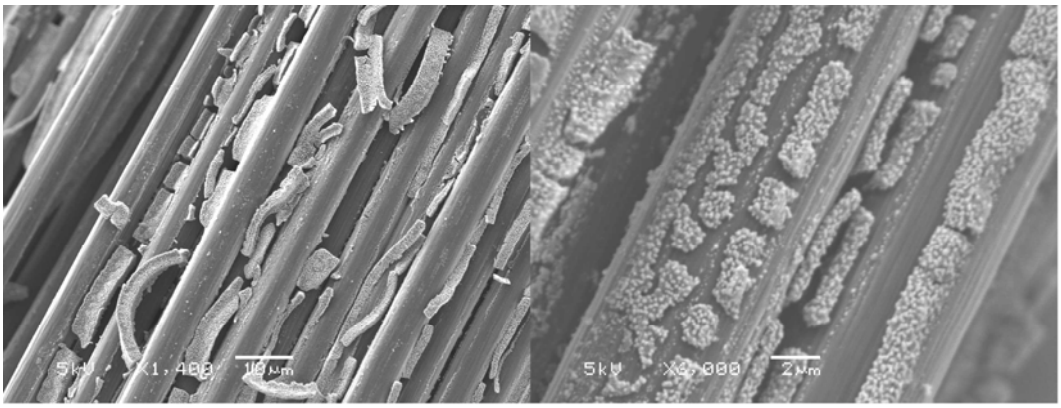

Figure 7.32 SEM images of unsized carbon fibers coated with catalyst precursor by baking on Fe^{3+}/IPA solution and subsequently CVD processed with CO_2/C_2H_2 at 480°C showing no CNT growth at any point in the tow: *(left)* metallic films delaminating from fibers; *(right)* detail of metallic deposits, revealing a coarse grain structure.

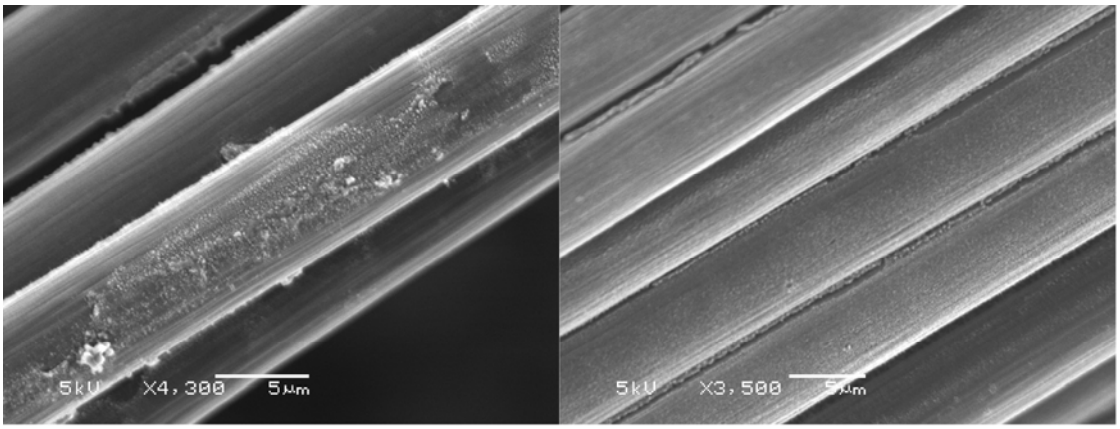

Figure 7.33 SEM images of unsized carbon fibers dip-coated with h-PSMA followed by Fe^{3+}/IPA solution and subsequently CVD processed with CO_2/C_2H_2 at 480°C showing no CNT growth anywhere in the tow.

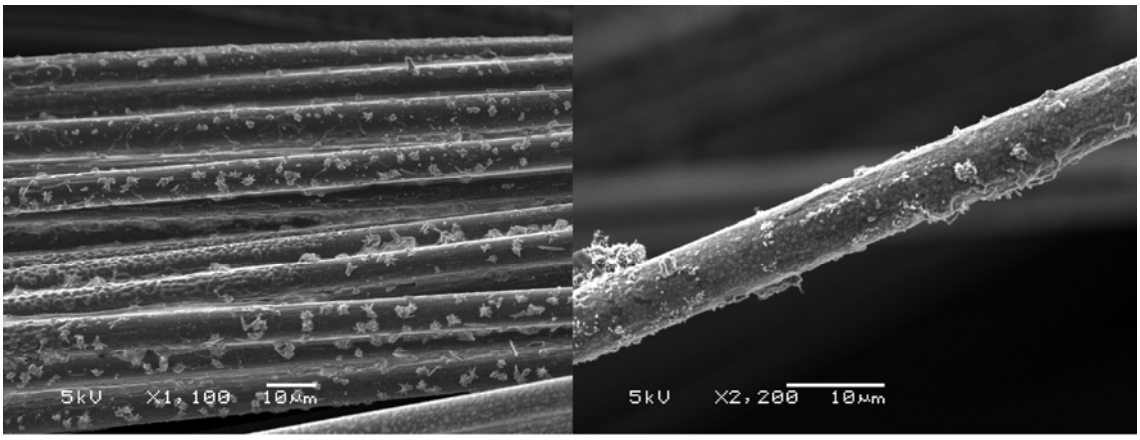

Figure 7.34 SEM images of carbon fibers coated with K-PSMA coating (anhydride hydrolyzed by NaOH, acid neutralized with K_2CO_3, 1.5 wt %, doped with catalyst precursor with Fe^{3+}/IPA) and CVD processed with CO_2/C_2H_2 at 480°C (as in Figure 7.31) but without H_2 pretreatment on ramp-up to the temperature set point, resulting in virtually no CNT growth: *(left)* unusual crystalline structures lining fibers in the tow; *(right)* isolated fiber presenting a disordered surface coating.

Dry K-PSMA-coated carbon fibers were alternatively dip-coated with aqueous 0.1 M $Fe(NO_3)_3$ to evaluate if an aqueous ion exchange would provide a superior CNT growth result over a 2-propanolic solution (Figure 7.35, bottom left). The Fe^{3+}/IPA solution is not merely a vehicle for Fe^{3+}; in fact, it is an active sol-gel polycondensation of the iron nitrate that results in a suspension of iron oxide nanoparticles. Over the course of a few hours (>2.5 h) after mixing, a red, loose precipitate forms from the Fe^{3+}/IPA solution as the growing iron nanoparticles become too large to remain in suspension and precipitate. As such, Fe^{3+}/IPA likely does not simply ion exchange K^+ for Fe^{3+} when contacted with K-PSMA but rather is believed to attach iron oxide nanoparticles to the polymer surface (like ornaments on a Christmas tree), possibly in addition to ion exchange. K-PSMA-coated carbon fibers dip-coated with aqueous Fe^{3+} yielded no CNTs, however, and instead thick polymer deposits curling off of the fibers in a way not observed with other approaches. It is believed this is Fe-PSMA, which very efficiently absorbs Fe^{3+} from the aqueous solution and forms an Fe-overloaded polymer that undergoes dimensional changes (swelling or contraction) when K^+ is exchanged for Fe^{3+}.

In further efforts to improve CNT areal yield, several variations in the K-PSMA preparation process as well as the effect of the age of the Fe^{3+}/IPA solution used were evaluated to answer questions about these two coatings. One question was whether or not K-PSMA could be produced by hydrolyzing PSMA with KOH and simply acidifying to a pH of 11 instead of hydrolyzing

with NaOH, acidifying to a pH of 8, and then rebasifying with K_2CO_3 to a pH of 11. Post-CVD SEM images of fibers prepared with coatings from this approach (Figure 7.36 right column, bottom two panels) shows CNTs form only on fibers coated with K-PSMA prepared by K_2CO_3 neutralization. As such, it was concluded that K-PSMA does not form until the PSMA is hydrolyzed, acidified, and neutralized (that is, K-PSMA is not an intermediate in the formation of h-PSMA when PSMA is hydrolyzed with KOH). Another question was whether or not K-PSMA prepared from PSMA hydrolyzed with KOH was comparable to K-PSMA prepared from PSMA hydrolyzed with NaOH (Figure 7.36 middle two panels). Surprisingly, NaOH-hydrolyzed coatings consistently gave longer CNTs than KOH-hydrolyzed coatings. This is perhaps due to solution equilibria during neutralization of h-PSMA with K_2CO_3 giving rise to a buffering effect. A third question was whether or not CNT diameter and yield was influenced by the age of the Fe^{3+}/IPA solution after mixing (t_{mix}) when K-PSMA fibers were dip-coated (Figure 7.36 left column). At t_{mix}=30 min, very few CNTs on what is otherwise a mostly uneven thick coating are observed. At t_{mix}=60 min and 90 min, CNTs are distributed in large quantity over the fiber surfaces; however, samples dip-coated with t_{mix}=90 min catalyst solutions also exhibit the presence of large (10 μm across) iron crystallites, again likely due to the presence of too much iron (from a solution containing oversized nanoparticles). As a result, t_{mix}=60 min was determined to be the best age of Fe^{3+}/IPA solution for CNT growth with K-PSMA-coated carbon fibers.

Finally, carbon fibers coated with K-PSMA from a lower concentration solution of K-PSMA (0.5 wt% instead of 1.5 wt%) were dip-coated with Fe^{3+}/IPA at t_{mix}=30 min and t_{mix}=60 min. Following CVD, fibers coated with 0.5 wt% K-PSMA solutions showed very short (<1 μm) CNTs in a density of ~1-2 CNTs/μm^2 at both t_{mix}=60 min and 90 min. Occasional patches of longer CNT growth was observed in between fibers for t_{mix}=90 min samples, possibly due to the retention of iron-rich solution from capillary action.

Additional parameter space regarding the CVD process was not pursued as the yield is only expected to be worse at lower temperatures (since 480°C is already very low for CNT growth), the growth temperature was already at the high-end of what is preferred when heating carbon fibers (discussed further in Chapter 8), and parametric studies investigating optimal gas compositions for CNT growth with CO_2/C_2H_2 (described in Chapter 6) found the conditions used here to be optimal within the scope of the studies performed.

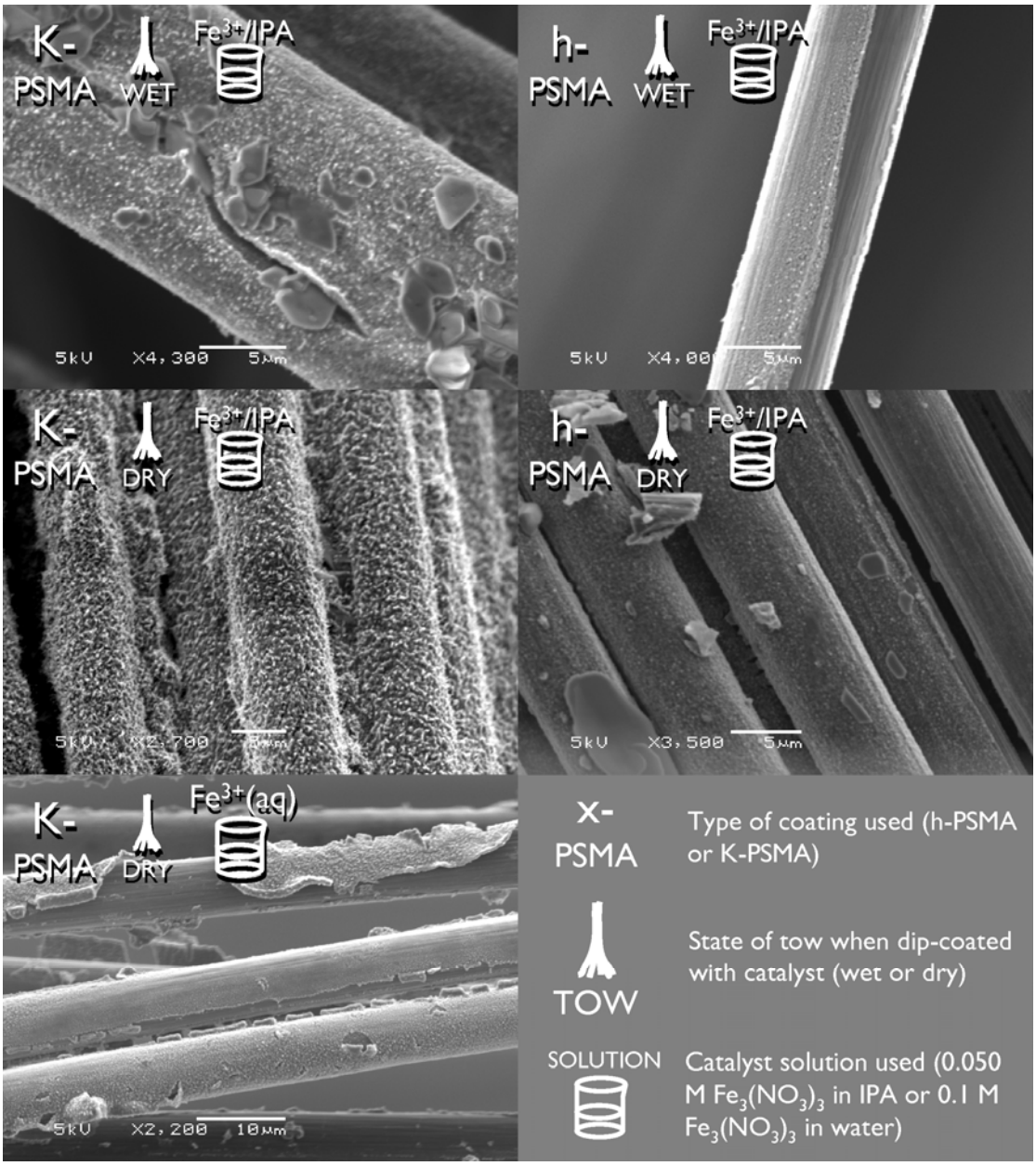

Figure 7.35 Unsized carbon fibers coated with Fe^{3+}/IPA applied onto wet K-PSMA coating *(top left)*, Fe^{3+}/IPA applied onto wet h-PSMA coating *(top right)*, Fe^{3+}/IPA applied onto dry K-PSMA coating *(middle left)*, Fe^{3+}/IPA applied onto dry h-PSMA coating *(middle right)*, and 0.1 M aqueous $Fe(NO_3)_3$ exchanged onto dry K-PSMA coating *(bottom left)* followed by CVD processing for CNT growth with CO_2/C_2H_2 at 480°C.

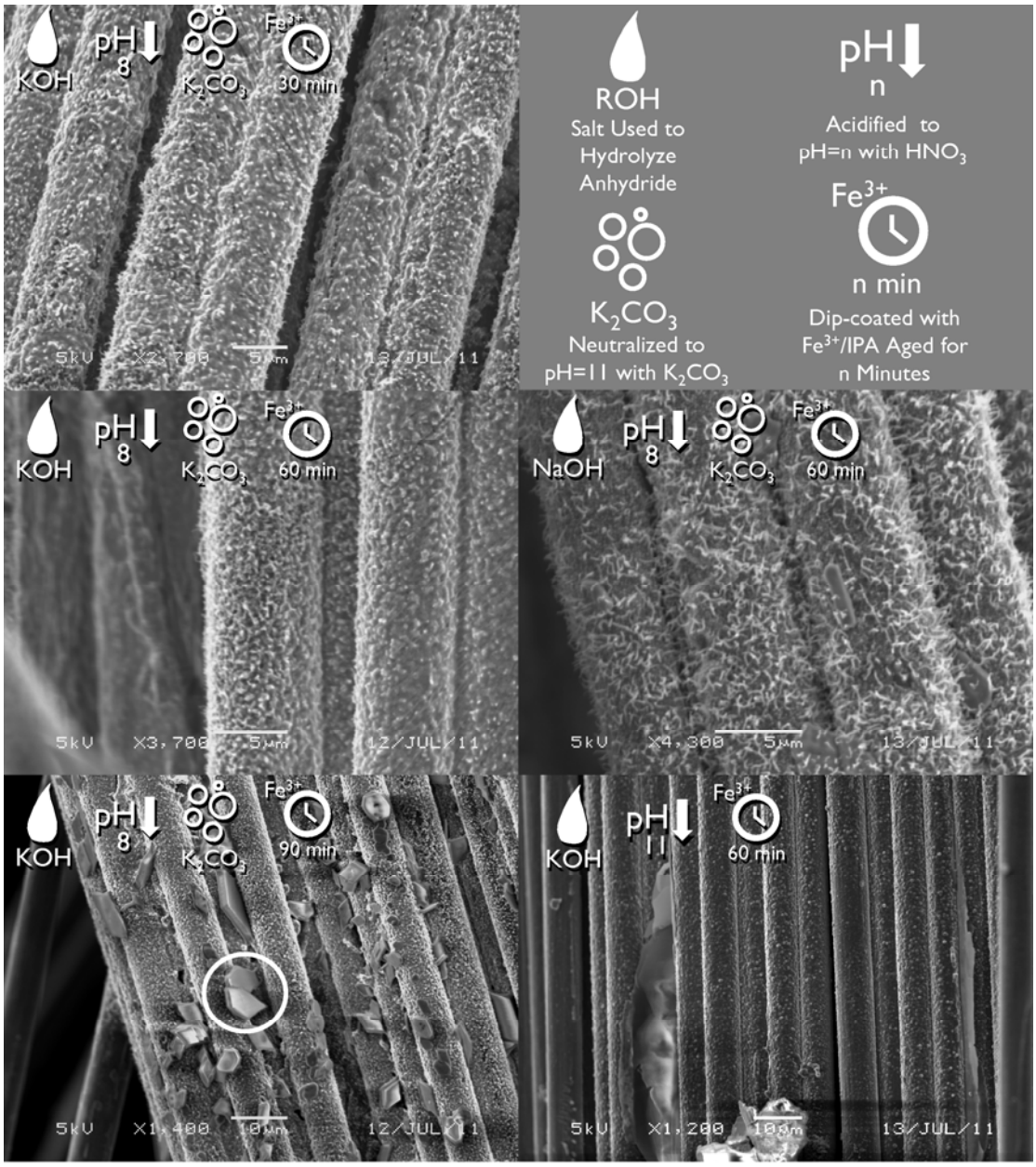

Figure 7.36 Results of CNT growth maximization study with Fe^{3+}-loaded K-PSMA on unsized carbon fibers looking at the effects of Fe^{3+}/IPA solution age *(left column)*, salt used to hydrolyze the PSMA precursor *(middle row)*, and whether or not K-PSMA forms as a function of pH or from neutralization with K_2CO_3 *(right column middle and bottom)*.

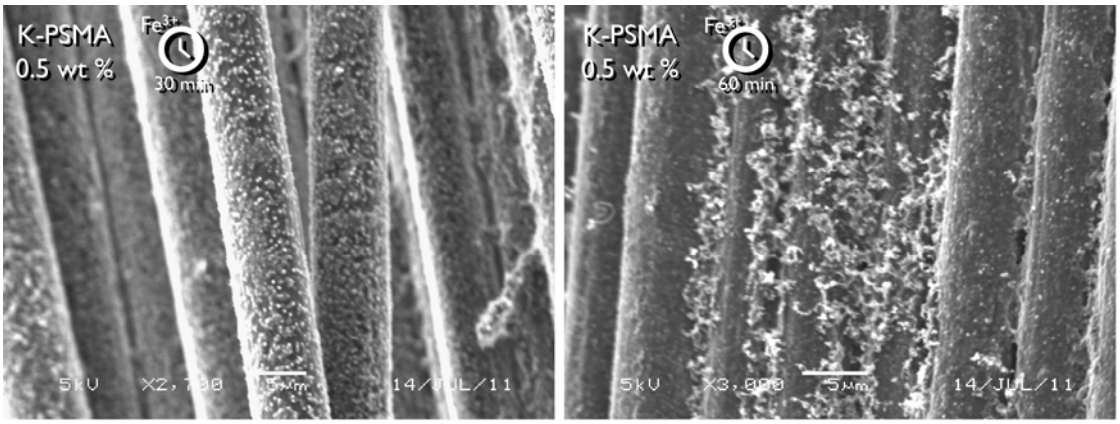

Figure 7.37 SEM images showing the effect of K-PSMA concentration on CNT growth with CO_2/C_2H_2 at 480°C: *(left)* unsized carbon fiber dip-coated with 0.5 wt % K-PSMA followed by dip-coating with Fe^{3+}/IPA aged for 30 min showing "knobby" structures over the fiber surfaces but no CNTs; *(right)* same as left but dip-coated with Fe^{3+}/IPA aged for 60 min showing very sparse CNT growth, generally between fibers.

Conclusions

CNT growth on carbon fibers can be achieved at 480°C without etching or chemically changing the carbon fiber surface and using only solution-based methods to apply coatings and catalyst precursor. K-PSMA has been shown to be an effective amphiphilic polyelectrolyte for both efficiently coating unsized carbon fibers and attaching iron ions and nanoparticles to the fiber surface. A procedure for preparing K-PSMA suitable for facilitating iron loading onto and subsequent CNT growth on unsized carbon fibers, the optimal aging time for Fe^{3+}/IPA catalyst precursor solutions, and the importance of using a H_2-pretreatment prior to CVD growth of CNTs are established.

7.3.3. Conclusions, Recommendations, and Future Work Regarding Non-Covalent Functionalization of Carbon Fibers with h-PSMA and K-PSMA

h-PSMA has been shown to be effective at improving adhesion and decreasing cracking of sol-gel-derived coatings on unsized, never-surface-treated carbon fibers. Outstanding challenges underlying the practical use of h-PSMA with sol-gel coatings include development of better methods for engaging the interior fiber surfaces of a tow, maximizing h-PSMA and sol-gel coating coverage, minimizing h-PSMA and sol-gel coating thicknesses, and improving coating uniformity. While sol-gel-derived alumina coatings prepared by propylene-oxide-assisted gelation of aluminum salts were found

to be the optimal sol-gel coating for facilitating aligned CNT growth, they also pose the challenge of obtaining uniform coverage over fiber surfaces, even with improved adhesion and reduced cracking when used in combination with an h-PSMA undercoating. Use of h-PSMA followed by multiple sol-gel depositions of alumina via the propylene oxide method could help to address this problem.

Iron ions and nanoparticles were found to not readily adsorb onto h-PSMA surfaces, requiring a different coating for direct loading of Fe onto a carbon fiber. The potassium salt of h-PSMA (K-PSMA) was found to serve as an effective polyelectrolyte for ion exchange of Fe^{3+}, enabling efficient loading of iron ions onto a carbon fiber surface.

Unaligned CVD growth employing CO_2/C_2H_4 at 480°C was found to be effective at growing CNTs on carbon fibers coated with K-PSMA and loaded with iron catalyst. This process uses 95% less gas than the standard CNT growth processes for producing fuzzy alumina cloths and does not require H_2 during CNT growth. An optimal formulation for K-PSMA and conditions for suitable iron catalyst precursor solutions were established. This is an important result, as it establishes for the first time the capability of growing CNTs on carbon fibers at a temperature below the point where untensioned carbon fibers begin to lose tensile strength and stiffness due to thermally-activated mechanochemical changes in the fibers (as established from studies discussed in Chapter 8) in a way that is compatible with carbon fiber manufacturing lines. These promising features of this approach also offer great promise to scalably grow CNTs on carbon fiber weaves without reducing the in-plane properties of the weave.

Optimization of loading K-PSMA with Fe should be further pursued. To date, it has been observed that overloading K-PSMA yields large iron particles and films, but underloading yields no CNT growth. Additionally, H_2 reduction is currently necessary prior to performing CVD growth with Fe-loaded K-PSMA. Industrially, it would be highly desirable to avoid the use of H_2 at a large scale due to its explosive properties and cost of production. Since H_2 is only necessary for reducing Fe^{3+} to iron nanoparticles in this CVD growth process, alternative H_2-free methods for including catalyst iron nanoparticles on the fiber surface should be explored. A few possibilities are a coating-based additive to enable reduction of iron ions without H_2 or coating fibers with prefabricated Fe nanoparticles (which unfortunately are notoriously difficult to keep in reduced form).

A primary advantage shared by both h-PSMA and K-PSMA is that they are both prepared in and applied from water-based solutions. This is not only appealing from scalability and toxicity perspectives, but also provides flexibility for tailoring process results. Currently, catalyst solutions used are

2-propanol-based, however use of a water-based iron oxide nanoparticle synthesis or ion exchange of K-PSMA with a dilute (<<0.1 M) solution of Fe^{3+} may give optimal results without 2-propanol. Alternatively, Fe-PSMA, which is not soluble in water or 2-propanol, could be produced in bulk (as a solid) and then dispersed in water, possibly with the aid of a surfactant. This would serve to unify K-PSMA deposition, drying of the K-PSMA coating, and loading of Fe onto the K-PSMA into one streamlined water-based process.

One concern surrounding the use of both h-PSMA and K-PSMA is the potential for fiber degradation arising from high-temperature reactions with Na^+ and K^+ ions. In the case of h-PSMA, the use of a base which results in the release of gases upon decomposition (such as NH_4OH or $(NH_4)_2CO_3$) could eliminate this problem. In the case of K-PSMA, use of such a base may be unnecessary given its application is for sub-500°C growth of CNTs, which is likely too cold for deleterious interactions between the carbon fiber and cations such as Na^+ and K^+.

Process efficiencies could be had in reducing the amount of time used for both applying K-PSMA to unsized carbon fibers and applying catalyst onto K-PSMA-coated fibers. It has been observed that adsorption of K-PSMA onto carbon fibers (as indicated in an increase in tow stiffness) occurs immediately following a few seconds of soaking in 1.5 wt% K-PSMA solution. Additionally, it has been observed that the ion exchange process between K-PSMA and solutions of aqueous Fe^{3+} and Fe^{3+}/IPA seem to occur quite fast, almost instantaneously, and that 5 min is much longer than needed to load iron ions onto the K-PSMA coating.

7.4. Conclusions

In this chapter, coatings designed to facilitate CNT growth on carbon fibers are described and evaluated. Methods for depositing alumina coatings on carbon fibers by sol-gel, electrodeposition, and CVD have been described. Methods of modifying the surface chemistry presented by a carbon fiber without chemically modifying the carbon fiber surface are demonstrated and shown to be effective in enhancing adhesion and coverage of sol-gel-derived coatings. A method for growing CNTs on carbon fibers at temperatures below 500°C is also demonstrated.

It is believed that some combination and/or formulations iteration of the methods described in this chapter should facilitate high-yield growth of aligned CNTs with uniform and complete coverage over carbon fiber tows and weaves. Sol-gel deposition employing an epoxide-assisted gelation process or CVD of alumina seem like the most promising ways of achieving aligned CNTs. Difficulties with such sol-gel coatings could be overcome by

the use of an h-PSMA coating on the fiber surface. Difficulties in getting catalyst precursor to adsorb onto CVD alumina could be overcome by a chemical modification of the alumina barrier coating.

Tremendous opportunities lie in further developing the low-temperature CNT growth on carbon fibers demonstrated with the use of K-PSMA. If aligned CNT growth can be achieved at these temperatures, or if unaligned CNTs are demonstrated to be suitably effective for achieving the desired composites application improvements, this method would perhaps be the most scalable, energy-efficient, cost-effective, gentle, and straightforward way to grow CNTs on carbon fibers.

In the following chapter, the effects of these coatings and CVD growth upon them on fiber tensile strength and stiffness are characterized at the single-fiber level to further development of fuzzy carbon fibers for structural composites.

Chapter 8

Mechanochemical Responses of Carbon Fibers to Thermochemical Processing

The goal of growing CNTs on carbon fibers is a promising vector for their delivery into carbon fiber composite architectures in a way that results in improved composite interlaminar and intralaminar shear strength, fracture toughness, as well as multifunctional properties such as electrical and thermal conductivity. In Chapter 7, several practical approaches for facilitating growth of CNTs on carbon fibers, including approaches that give rise to aligned CNTs with uniform coverage over carbon fiber surfaces, were demonstrated. Growing CNTs, however, is only the first step to achieving practical hierarchical CNT/carbon fiber composites. If the act of growing CNTs on carbon fibers results in loss of fiber tensile properties, improvements in matrix-dominated properties in derived carbon fiber composites will come at the expense of in-plane properties.

In this chapter, the effect of CNT growth on carbon fibers employing methods demonstrated in Chapter 7 on the tensile strength and modulus of unsized (i.e., never-sized), never-surface-treated carbon fibers is assessed at the single-fiber level. Great care was taken in Chapter 7 to develop coatings processes that would not overtly damage the surface chemistry of carbon fibers (where, as mentioned previously, the majority of the tensile load is transmitted) and thereby reduce tensile strength and/or stiffness of the fiber. Surprisingly, CVD growth of CNTs with these chemically-gentle processes was still found to result in substantial (upwards of 50%) loss in fiber tensile strength. Here, in a detailed study involving coating, CVD processing, and

tensile testing single carbon fibers, the origins of this degradation are identified for aerospace-grade carbon fibers. Based on these findings, methods for growing CNTs on carbon fibers that do not result in tensile property degradation are developed and demonstrated to be effective.

The work in this chapter was done in substantial collaboration with Richard Li of MIT. Mr. Li and the author acknowledge Nathan Brei for his contribution towards development of the all-graphite tensioning frame described in this chapter.

8.1. Thermochemical Processing of Single Carbon Fiber Filaments

While processing carbon fiber in tow or weave form is useful for composites applications, uneven loading of coatings arising from bundling of fibers and from capillary effects makes analysis of fibers processed in these forms precarious. It is difficult to know with confidence, for example, that observed changes in tensile properties following CNT growth are due to interactions between fiber and coating, and not because an uncoated fiber surface interacted with iron catalyst at elevated temperatures, or was damaged by a gas-phase process. Additionally, performing tensile tests with an entire tow can be misleading, since in order to do so the tow is typically brushed with resin, cured, and then pulled, smoothing out the contribution of defects throughout the tow and masking insight underlying fiber-coating interactions. Thus, to unambiguously characterize the influence of the presence of a coating on fiber properties, the fiber should be coated, thermally processed, and directly tested in isolation from other fibers.

Doing so is no small task. Commercial carbon fibers, such as the HTR-40 and AS4 fibers used in this work, are typically only 7 μm in diameter. Additionally, unsized carbon fiber abrades with itself, is sensitive to the presence of contamination when heated, and is easily electrostatically charged. In this section, methodologies developed for manipulating, coating, thermally processing, and tensioning individual 7-μm-diameter carbon fibers are described.

8.1.1. Preparation and Mounting of Carbon Fiber

The carbon fiber used in this investigation was primarily unsized (that is, never sized, as opposed to desized), never-surface-treated TohoTenax HTR40-24k (note that this unsized intermediate was specially obtained from industrial liaisons and is not commercially available; the equivalent sized commercial product is HTA40-24k). Unsized AS4 was also used in a few

studies as noted. Unsized fiber was chosen in order to eliminate possible fiber damage associated caused by desizing procedures such as thermally decomposing the sizing under inert atmosphere or interaction of the fiber with unremoved sizing. Prior to use, fibers were rinsed with acetone and evaporatively dried in air. Single fibers were carefully extracted from the 24k tow using Q-Tips®, which gently latch onto the fibers and pull them out from the other fibers. Care was taken not to stretch fibers when pulling them out to avoid pretensioning of the fiber. (Note that the force required to break a single carbon fiber is ~40-180 mN, or ~0.01-0.04 lbf, corresponding to a stretch of only ~150-300 µm.) The single fibers were then mounted into a rectangular two-piece milled graphite frame to hold them in place for handling and processing (Figure 8.1). Fibers were mounted into the frame by stringing lengthwise across the bottom half of the frame with slack on either side and then setting the top half of the frame on top. This held the fibers in place by compression. Up to five fibers could be mounted. If coatings were to be applied to the fibers, masking tape was used to hold the frame together until ready for heat treatment at which point the masking tape was peeled off and any adhesive residue was gently scrubbed from the frame with acetone.

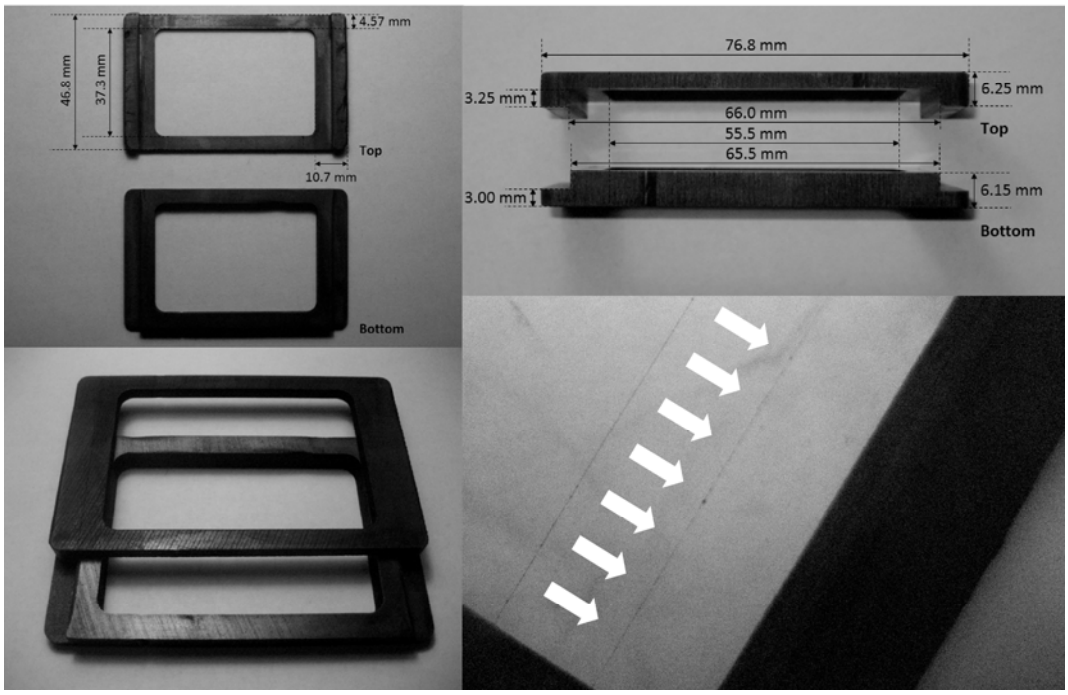

Figure 8.1 Graphite frame developed for manipulating and thermochemically processing single 7-µm-diameter carbon fibers: *(top row)* dimensions of two-piece graphite frame; *(bottom left)* demonstration of top and bottom of graphite frame illustrating clamping concept; *(bottom right)* individual Fe^{3+}/alumina/h-PSMA-coated carbon fiber after CVD processing strung in graphite frame with visible CNT clusters.

8.1.2. Application of Coatings and CVD Growth of CNTs on Single Carbon Fibers

Fibers were prepared for CVD growth of CNTs using coatings techniques developed in Chapter 7. A sol-gel-derived alumina barrier coating with iron catalyst was used to facilitate CNT growth. Sol-gel was selected as the method for depositing alumina to maximize ease of processing and probability of success. A coating of 2.5 wt% aqueous h-PSMA was put on the fiber to facilitate adhesion of the alumina coating (see Section 7.3). The alumina coating was deposited using cyclic baking of an alkoxide-derived sol (see Section 7.2.1.2 for more details).

Application of h-PSMA Coating

A solution of 2.5 wt % aqueous h-PSMA was prepared as described in Section 7.3.1. Briefly, 7.0 g of poly(styrene-*alt*-[maleic anhydride]) (PSMA, M_W=350,000, Sigma-Aldrich) was dissolved in 25 mL acetone with mild heating (up to 45°C). This solution was then added to 300 mL of 0.30 M aqueous NaOH. After 3 h, the pH was lowered to 8 with the addition of nitric acid. Finally, the acetone was removed from the solution using a rotary evaporator.

Graphite frames loaded with isolated single carbon fibers were placed into a "boat" of Parafilm® (wrapping all sides of the frame except the top) to allow for filling of the frame with liquid. Using a Pasteur pipette, 2.5 wt% aqueous h-PSMA solution was injected into the frame until the fibers were submersed (note that the frame is wetted in this process). The fibers were allowed to soak in the solution for 2 h, after which the solution was drained using a Pasteur pipette and the fibers were allowed to evaporatively dry in air overnight.

Application of Alumina Sol-Gel Coating

Graphite frames loaded with isolated single fibers were placed into a new Parafilm boat as described above. Using a Pasteur pipette, a solution containing 2.5 vol % aluminum tri-*sec*-butoxide (ATSB, Sigma-Aldrich, 97%) in 2-methoxyethanol (MeOEtOH, Sigma-Aldrich, 99%) was injected into the frame until the fibers were submersed as described above. The fibers were allowed to soak for 5 min after which they were heated at 200°C in a convection oven and cooled in air for 3 min. This process was repeated three times. The coated fibers were then allowed to dry 30 min at room temperature prior to further processing.

Application of Catalyst Precursor

A solution of 0.050 M $Fe(NO_3)_3 \cdot 9H_2O$ in 2-propanol was prepared and stirred for 1-2 h. Graphite frames loaded with isolated single fibers were

placed into a new Parafilm boat as described above. Using a Pasteur pipette, the frames were then filled with the iron nitrate solution aged no more than 2 h until the fibers were submersed. Shortly after (~5 min), the frame was drained, the fibers were allowed to dry overnight, and the Parafilm boat was removed.

CVD Processing for CNT Growth

Atmospheric thermal CVD was performed in a three-zone Lindberg/Blue M furnace with a 62-cm heated length using 54-mm outer diameter by 50-mm inner diameter fused quartz process tubes with a length of 138 cm. (Note that due to the distance between the thermocouples and samples inside a fused quartz process tube in this furnace, the furnace set point may underestimate the actual process temperature by ~80°C.) Fiber-loaded graphite frames were slid into the quartz tube and positioned between 50% and 75% of the heated length as measured from the gas intake end of the furnace. Gases used were all ultrahigh purity grade (Airgas, >99.999%). The CVD process was performed as follows. First, the tube was flushed at ambient temperature for 10 min with a flow of 2070 sccm He to displace air in the tube. Next, the flow of He was dropped to 41 sccm and 1040 sccm H_2 was added. All three zones were then ramped to a set point 650°C (corresponding to an actual process temperature of 730°C) over the course of ~7 min at which point the samples were allowed to soak under H_2 for an additional 7 min. A flow of 318 sccm C_2H_4 was then introduced for 5 min to enable CNT growth. Finally, the He flow was increased to 2400 sccm, the H_2 and C_2H_4 were turned off, and the samples were allowed to cool to ambient temperature and removed.

8.1.3. Thermochemical Processing of Single Fibers Under Tension

The role of tension during thermochemical processing of carbon fibers was evaluated using a special all-graphite tensioning frame (see Figure 8.2 left, Figure 8.3, and Figure 8.4) and screw-clamp weights. Photographs of the tensioning frame are shown in Figure 8.4. Due to concerns of chemical contamination, the frame and all fastening parts were machined exclusively out of polycrystalline graphite. Special clamp-on weights, also made of graphite, were used to impart up to 0.5 GPa of tension into single carbon fibers (Figure 8.5). A set of tungsten-core, graphite-shell weights was also produced (see Figure 8.2 right and Figure 8.6) and enabled application of tension up to 3.2 GPa.

Mounting Fibers into Tensioning Frame

A length of carbon fiber tow (~30 cm long) was cut and laid out on a clean sheet of copy paper. A "fiber grabber" tool was fashioned to extract fibers from the tow, made by rolling a piece of masking tape (3M 2600, tape type is important) onto the end of a thin wooden dowel (e.g., a toothpick) to make an ~0.5 x 1.0 cm "flag" of tape hanging off the end of the dowel with sticky side exposed. This tool was used to gently stick onto single carbon fibers in the bundle and pull them away from the tow through gentle application of torque rather than tension. This was done to minimize stretching or "pretensioning" of fibers during extraction from the tow. Next, with fiber attached to the fiber grabber, the fiber was drawn out and laid across two Parafilm-covered fiberglass blocks (~5 cm x 2.5 cm x 4.3 mm, see Figure 8.7) separated by a distance of ~18-20 cm, to which the fiber could cling electrostatically (this is the desired result). White paper could optionally be placed between the translucent Parafilm and off-white fiberglass to improve contrast of fibers placed atop the blocks. Another, thinner fiberglass block (~12 cm x 5 cm x 2.9 mm) without Parafilm was placed nearby for the next step. With a gloved finger, the end of the fiber attached to the fiber grabber tool was pressed down onto its Parafilm-covered fiberglass block and the fiber grabber twisted away and detached. With fiber strung between, the two Parafilm-covered fiberglass blocks were then picked up and carefully placed down and over the larger, thinner fiberglass plate such that the larger plate sat between the two Parafilm-covered blocks lengthwise (12-cm length) with ~3 cm space between it and each Parafilm-covered block. Once set down, the Parafilm-covered blocks were gently pulled apart to tension the fiber, noting that the fiber is capable of slipping on the Parafilm which self-corrects for and reduces concerns for overtensioning.

Next, graphite clamp weights (or heavier tungsten-core/graphite-shell clamp weights) were readied for attachment to the fibers. The clamp weights were assemblies comprised of two small blocks with dimensions of 9.5 mm x 9.5 mm x 17.8 mm joined at one end with a graphite screw to form a sandwich structure. The screw could be tightened or loosened to open a gap between the two blocks, which sit parallel to each other and perpendicular to the screw thread. Two such weight assemblies, tightened such that an ~1 mm gap was left between the two weight blocks, were placed on either side of the long fiberglass plate and pushed against the plate with gap running parallel to and under the fiber, in preparation for the fiber to be laid down into them (Figure 8.7). The two Parafilm-coated blocks were then carefully picked up and the taught fiber laid into the gaps of the two clamp weight assemblies. Once in place, the screws on the weight assemblies were screwed finger-tight resulting in clamping of the weights onto the fiber.

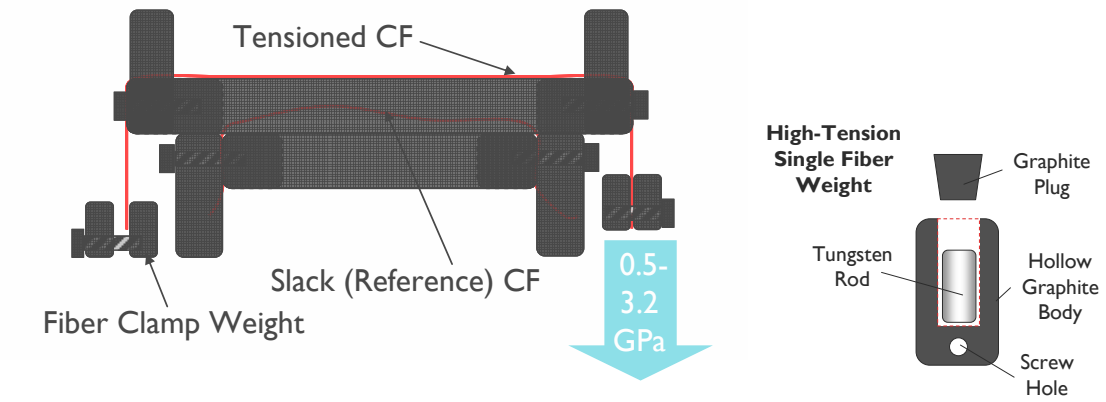

Figure 8.2 Diagram of all-graphite tensioning frame developed for thermal processing of single carbon fibers under tension *(left)* and tungsten-core/graphite-shell high-tension weight for enabling application of higher levels of tension to a fiber than with all-graphite weights.

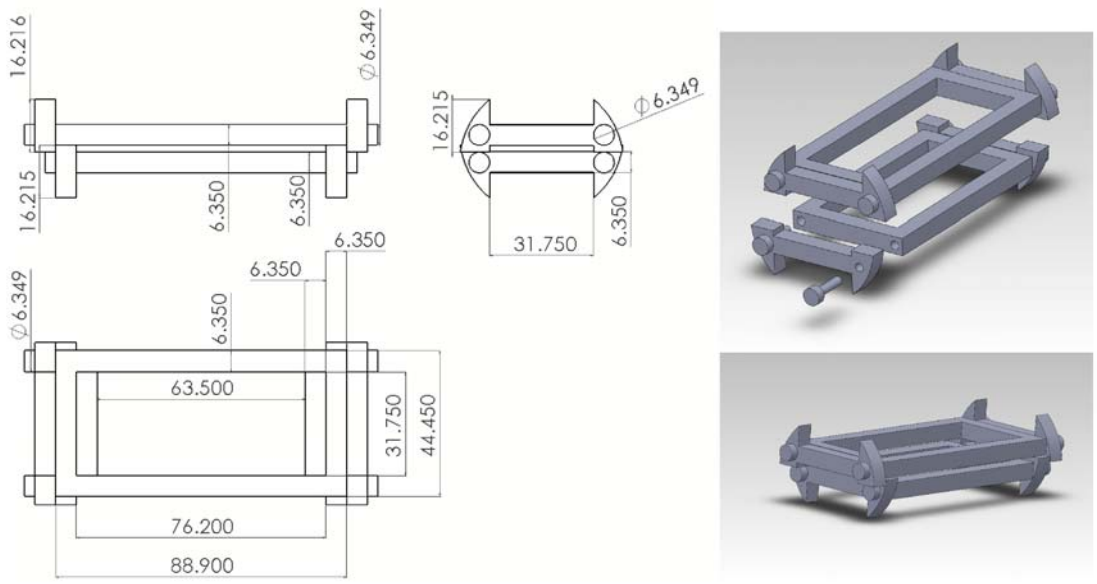

Figure 8.3 *(Left)* Dimensions (in mm) for all-graphite tensioning frame; *(upper right)* exploded view of tensioning frame components showing attachment of "horned bumpers" with threaded graphite screws; *(lower right)* assembled tensioning frame.

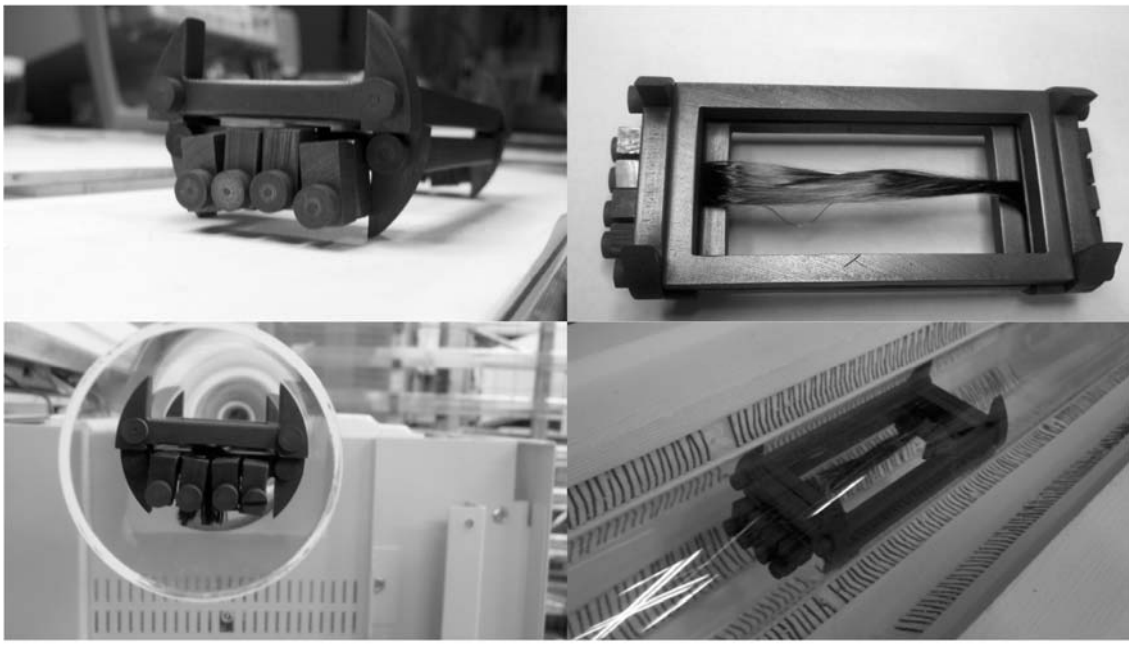

Figure 8.4 Photographs of all-graphite "horn beetle" tensioning frame: *(upper left)* four separate 7-µm-diameter tensioned carbon fibers supporting dangling tungsten-core weights; *(upper right)* untensioned tow simultaneously clamped in lower level of frame to provide reference fibers after CVD processing; *(lower left and lower right)* tensioning frame positioned in fused quartz process tube inside electric clamshell furnace ready for CVD processing.

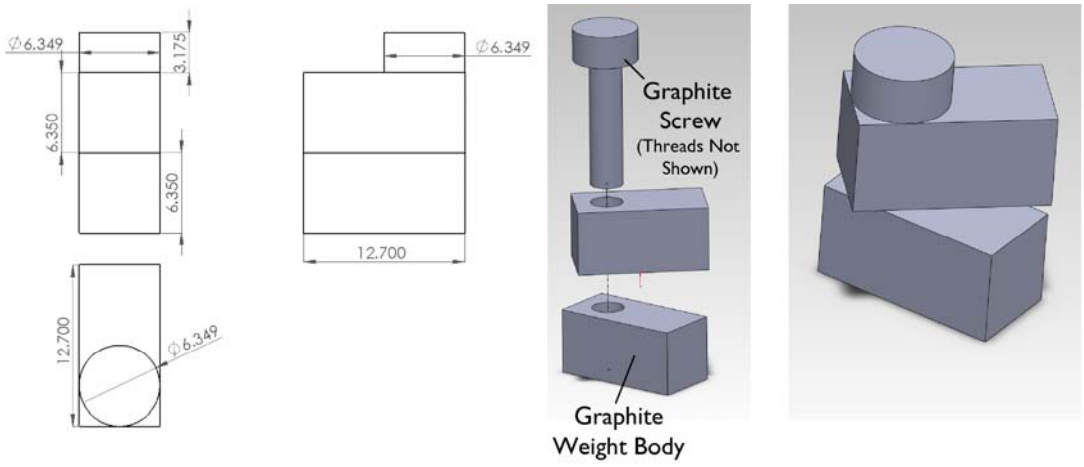

Figure 8.5 *(Left)* Dimensions (in mm) for two-piece graphite weight assemblies; *(middle)* exploded view of weight assembly; *(right)* assembled weight assembly.

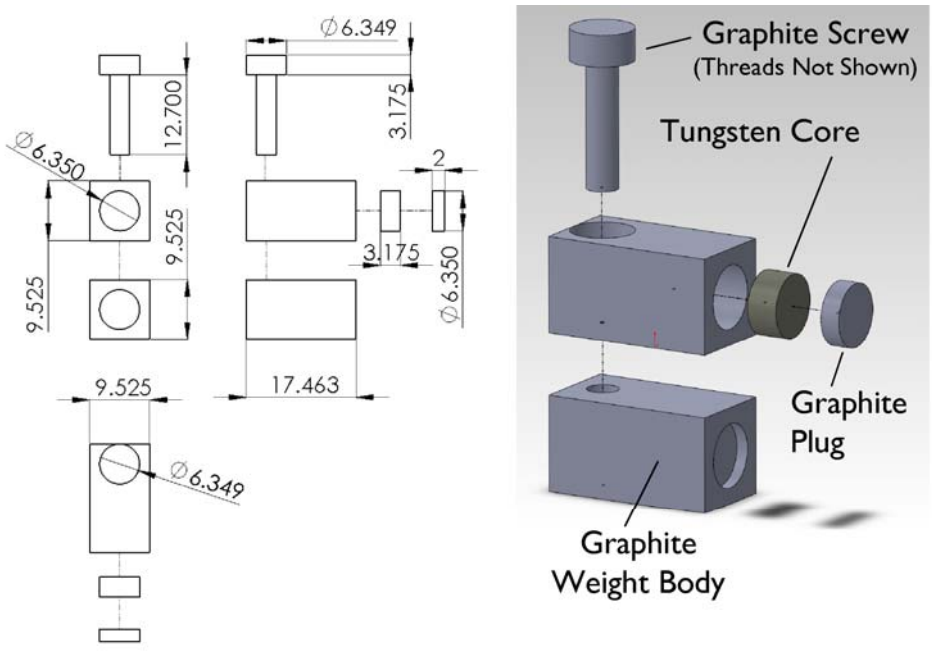

Figure 8.6 *(Left)* Dimensions (in mm) for tungsten-core weight assembly used for higher tension studies and screws used for both weight assemblies and tensioning frame; *(right)* exploded view of tungsten-core weight assembly.

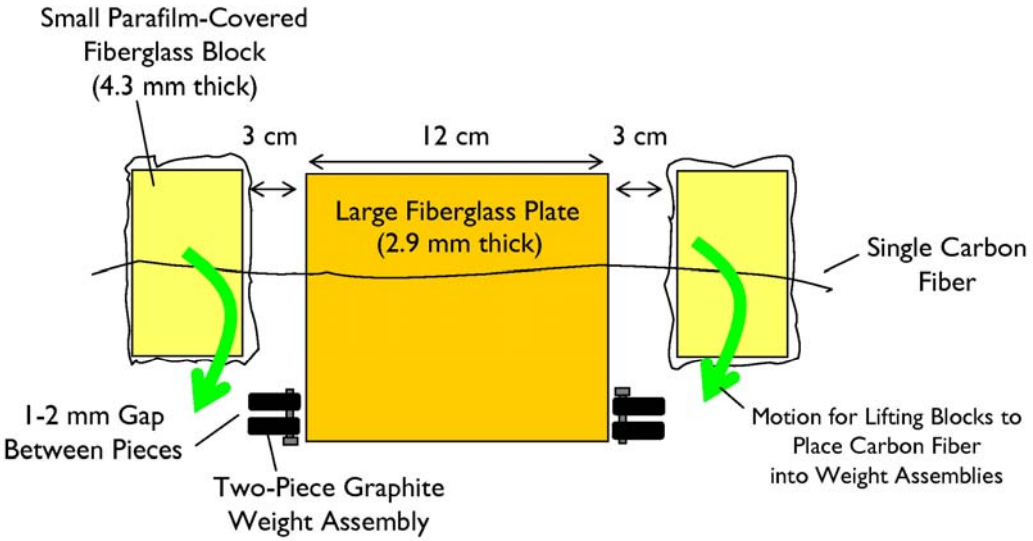

Figure 8.7 Transferring single carbon fiber into the graphite weight assemblies.

Once the clamp weights were attached, the fiber could be loaded onto the tension frame. The tension frame was placed on top of an adjustable-height lab jack to which a piece of clean white copy paper had been taped. The lab jack was then placed onto a cardboard tray which served as a semi-rigid carrying structure that helps to dampen vibration from walking when

moving the fiber-loaded frame (as described below). Two fiberglass plate "guide rails" were also taped down onto the paper to restrict sliding of the tension frame to one dimension. A 6.3-mm-thick prop block was then placed to the left of the tension frame. Pinching both of the clamp weights to pick up the fiber, the fiber-weight assembly was moved over the tension frame. Next, one clamp weight was propped up vertically (screw-side-up) on the prop block on the left side of the tension frame while the other weight was placed on its long edge atop the right side of the tension frame in such a way as to not twist the fiber. Finally (with care and skill), the right weight was carefully pulled and rotated over the right edge of the tension frame and then gently released. The prop block on the left was then carefully removed and the two weights were left dangling off either edge of the frame, holding the fiber in tension over the frame. The fiber loading process was repeated up to three more times, loading the frame with up to four fibers total. *Important: once loaded onto the frames, neither the fiber nor the weights should be touched until after processing.*

The cardboard tray under the lab jack was then carefully and slowly picked up and the lab jack with loaded tensioning frame on top was moved and placed in proximity of the tube furnace using extreme care (walking with baby steps) as to not impart dynamic loading onto the fibers. With a process tube inside the furnace, the lab jack was placed next to the furnace and raised to the height of the process tube so that the tension frame could be smoothly (but slowly) pushed into position with a push rod (see Figure 8.8).

Thermal processing was then performed per usual. Following thermal processing, the frame was pulled out of the furnace by one of its horns and placed back onto the lab jack and the fibers were removed by grabbing both weights of each fiber simultaneously, slacking the fiber, and resting it on a surface with the weights. Some fibers were found to break spontaneously during thermal processing or from bumping or vibration during loading, observable by the presence of a dropped weight next to the frame. Such fibers were no longer considered valid for tensile tests. Each fiber on the frame could be cut in half to afford two tensile test specimens.

8.1.4. Single-Fiber Tensile Testing

Single-fiber tensile tests were performed in a universal testing machine (Nano-UTM, MTS Nano Instruments) according to the ASTM D3379-75 standard.[171] This standard was selected over the ISO 1156 standard,[172] another candidate single-fiber tensile test standard, because ASTM D3379-75 factors in strain rate, which we have observed can significantly impact the measured tensile strength values for single carbon fibers.

A baseline data set for as-received fibers was established each day that tensile tests were run to normalize variations arising from machine alignment and variations in materials properties along the tow spool. As an extra validation step, conclusions regarding a sample type are drawn based on differentials run against their respective baseline dataset.

Figure 8.8 Transferring the graphite tension frame, loaded with three tensioned fibers, into the furnace via lab jack.

Sample Preparation

Testing tabs were laser-cut from tagboard to dimensions specified by the standard. Fibers were mounted on tagboard frames with epoxy. A gage length of 25 mm was used for all samples. First, a straight line was drawn down the center of the tagboard testing frame. A length of CF tow was cut and laid out on a smooth surface such as clean white copy paper. With gloved fingers, the ends of the tow were spread slightly apart. A "fiber grabber" tool was used to gently stick onto single carbon fibers in the bundle and pull them away from the tow as described earlier. The fiber grabber was used to draw a fiber over the line drawn on the testing frame. One end of the fiber was then taped down in this position on the testing frame. A second fiber grabber was then used to pull the fiber taught at other end. This end of the fiber was then taped down. Finally, each end of the fiber was glued in placed with dabs of 5-min epoxy (Devcon, product number 14250) applied by Q-Tip.

Testing Procedure

Fiber specimens were first mounted in the testing machine. *Proper vertical alignment of the tagboard frame is critical to ensure accurate and repeatable tensile measurements.* Tabs were gripped on the tagboard 25 mm away from the fiber-epoxy joints. Once mounted in the machine, the sides of the tagboard frame were separated into top and bottom halves by snipping twice on each side as to remove a section of tagboard—this ensures the top and bottom halves do not catch on each other during pulling and introduce a spike or offset in the force-displacement curve measured for the fiber from incorrect autotaring by the instrument software. Fibers were pulled at a strain rate of 400 μstrain/s which guaranteed no test took longer than 60 s to complete. A nominal fiber diameter of 7 μm was used for stress calculations (verified by SEM to be a consistent and reasonable value). Fibers typically broke at a load of ~40-180 mN and an extension of ~150-300 μm. While ideally fiber pulls would only be considered valid if the test resulted in a break in the middle of the test specimen, the extremely small diameter of the fibers and large amount of elastic energy stored at break almost always resulted in specimens springing off of the frame, making it exceedingly difficult to assess where fiber failure occurred. All fiber break test results are included in the presented data as a result and it is expected that some of the lower values of strength in particular are a result of fiber breakage near the fiber-tab interface. Elastic modulus was calculated by linear regression fit of all data points in the linear region of the stress-strain curve for a given test such that an R^2 value of 0.99 or better was obtained (data points from movement of the testing frame and non-linear behavior at the fiber break point were excluded). In some datasets, force-displacement curves exhibited a constant offset due to mistaring of the load cell (arising from momentary collision of the tagboard frame top and bottom); accordingly, this offset was subtracted from these datasets in postprocessing.

8.2. Effect of Coatings and CVD Processing on Carbon Fiber Tensile Properties

The effect of CVD processing on uncoated and coated HTR-40 carbon fibers was investigated with single-fiber tension tests. Carbon fiber strength is inherently limited by flaws in the fibers and is characterized here using a Weibull distribution.[173] The Weibull distribution represents the probability of failure for a fiber at a particular tensile load (i.e., its tensile strength). The probability of failure is given by:

$$p(x) = \begin{cases} \frac{\alpha}{\beta}\left(\frac{x}{\beta}\right)^{\alpha-1} e^{-\left(\frac{x}{\beta}\right)^{\alpha}} & x \geq 0 \\ 0 & x < 0 \end{cases} \tag{8.1}$$

where x is the parameter of interest (here tensile strength), β is the location parameter, and a is a scale factor (or "Weibull modulus"). It is assumed that fibers have random flaws distributed along them which result in fiber failure according to a weakest-link-in-chain model, and that these flaws follow Weibull-Poisson statistics. Accordingly, the location parameter can be approximated by the mean tensile strength:

$$\beta \approx \bar{x} = \bar{\sigma} \tag{8.2}$$

and the Weibull modulus, a, can be approximated as the ratio of the mean tensile strength to standard deviation in tensile strength, $S(\bar{\sigma})$:

$$\alpha \approx \frac{\bar{x}}{S} = \frac{\bar{\sigma}}{S(\bar{\sigma})}. \tag{8.3}$$

These approximations are employed in the data reported here. According to the ASTM standard used here, a minimum of 15 successful tests is required for calculation of a valid Weibull distribution;[171] as such, each condition surveyed involved preparation and testing of at least 15 samples with the exception of a few preliminary diagnostic tests (see Table 8.1). We note that the Weibull distributions presented here may be wider than the true distribution as they include all measurements regardless of fiber break point. Testing did not allow for identification of break location and it is anticipated that some fibers broke away from the center of the testing frame (e.g., at the fiber-epoxy interface). Unprocessed single-fiber tensile test datasets for select experimental conditions surveyed are provided in Appendix C. The asymmetric bias of the distributions towards lower tensile strength values with increasing number of samples tested supports this hypothesis, as more breaks at the mounting points would be included in the dataset. Weibull parameters derived from tensile tests of single alumina fibers used for CNT growth derived exclusively considering fibers with breaks in the middle of test specimens result in a comparatively narrower Weibull distribution.[174] As is observed here for carbon fibers, the Weibull distribution of alumina fibers narrows after CNT growth. Nonetheless, single-fiber tensile tests performed by Qian *et al.* with similar carbon fibers (unsized high tenacity SGL

Carbon C320.00A PAN-based fibers, ~7.5 μm diameter) gave an average tensile strength of 3,500±170 MPa for a gage length of 25 mm, which is very close to what we report here (~3,400 MPa mean tensile strength with a standard deviation of 570 MPa, see Table 8.1).[20] Additionally, Hitchon and Phillips in characterizing the tensile strength of high-tenacity carbon fibers (Courtalds reel 2CT 76B/11R, 7.9-9.5 μm diameter) reported a Weibull modulus ranging from 6.3-8.8, similar to the range we report here (6.1-6.4, Table 8.1).[175]

Single carbon fibers were coated with h-PSMA and with full Fe^{3+}/alumina/h-PSMA coating and successfully CVD processed. CNT growth on single carbon fibers was achieved with the latter coating (Figure 8.9). Mean tensile strength, tensile stiffness, and Weibull parameters for coated and uncoated fibers surveyed are summarized in Table 8.1. A comparison of the tensile strength distributions of as-received HTR-40 fibers, CVD-processed h-PSMA-coated HTR-40 fibers, and CVD-processed Fe^{3+}/alumina/h-PSMA-coated HTR-40 fibers is shown in Figure 8.10. Unexpectedly, a substantial reduction in tensile strength (~45-55%) over the as-received fibers for both coated sample types is observed. This is comparable to strength losses attributable to acid etching and CVD processing with Fe nanoparticles present directly on the carbon fiber surface![20,35] Further investigation, however, revealed that the majority of this strength loss was not due to the presence of coatings: uncoated fibers exposed to the CVD environment (i.e., run through the process used to grow CNTs but without catalyst) exhibited a substantial (~36.8%) loss in tensile strength over never-processed fibers (Figure 8.11). An additional ~28.2% loss in tensile strength past this value is observed between Fe^{3+}/alumina/h-PSMA-coated fibers and uncoated fibers following CVD processing. As a result, it was hypothesized that something in the CVD atmosphere may be corrosive to the carbon fibers, and that an additional incremental strength loss was being contributed by an aspect related to the full Fe^{3+}/alumina/h-PSMA coating (e.g., insufficient coating resulting in contact between carbon fiber and iron, etc.) Notably, CVD processing in the presence h-PSMA alone (~34% strength loss) does not seem to be more damaging than heating an uncoated carbon fiber (~30% strength loss), thus validating its use as a carbon-fiber-compatible functionalization strategy and eliminating it is a direct cause for the additional strength loss associated with use of the full coating.

One possible corrosive agent in the CVD atmosphere considered was residual oxygen in the process tube on ramp-up to the temperature set point (even though the tube is flushed with He prior to heating).[176] To test this, processes employing a 15-min H_2 dwell at a low temperature (300°C or 350°C) prior to reaching the process set point were examined. The results of these

experiments are summarized as Weibull distributions Figure 8.12 and Table 8.1. No substantial improvement in tensile strength was observed using this approach. In fact, a slight degradation is observed.

Another hypothesized source of strength loss considered was stress introduced during mounting and unmounting of the single fibers resulting in the formation of flaws prior to or during CVD processing. A set of experiments comparing the processing of fibers as tows vs. single fibers and evaluating potential stresses arising from mounting are summarized as Weibull distributions in Figure 8.13 and Table 8.1. Processing as single fibers as opposed to in tows does introduce an incremental additional amount of strength loss, possibly due to the absence of collective off-gassing behavior present in tows hypothesized to maintain a local equilibrium of gas-phase agents associated with fiber decomposition: by Le Châtlier's principle, fibers heated in the presence of a higher concentration of such agents would tend towards an equilibrium state of less decomposition. However, as the strength loss attributable to processing as single fibers is relatively minor (possibly statistically irrelevant) and is an artifact specific to this experimental procedure, it was discounted as the major source of properties degradation.

In considering the results of these experiments, the question of whether the CVD gas blends or the heating of the carbon fibers to CNT growth temperatures was responsible for the tensile strength loss incurred upon CVD processing of uncoated fibers. In the next section, the differential between these two possible causes is examined in detail.

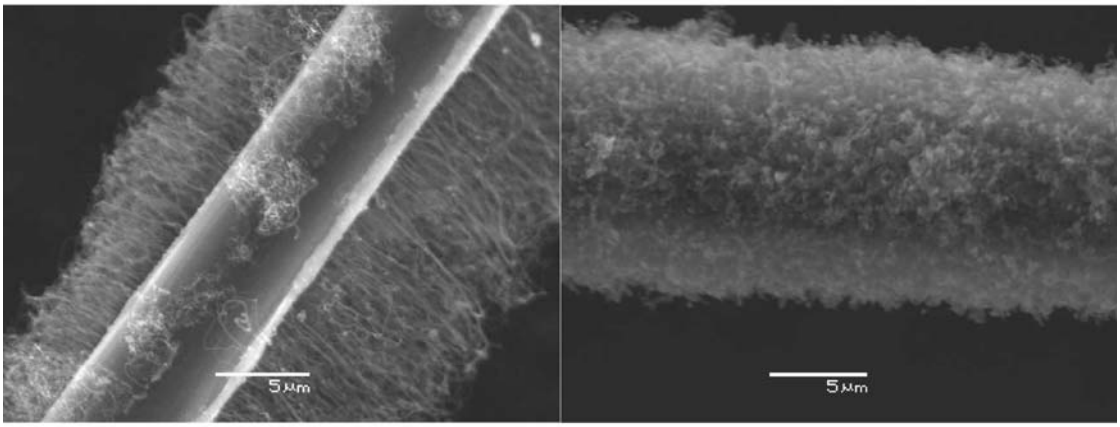

Figure 8.9 Aligned *(left)* and unaligned *(right)* CNTs grown on an individual HTR-40 carbon fiber coated with h-PSMA, alumina (from baked-on sol-gel technique described in 7.2.1.2), and Fe^{3+} with C_2H_4/H_2 at 730°C.

Sample Description	Processed as	No. of Samples[1]	$\bar{\sigma}$/GPa (= β)	S($\bar{\sigma}$)/ GPa	Weibull Modulus α	$\bar{E}$/ GPa	S($\bar{E}$)/ GPa
Unsized HTR-40, never mounted (control #1)	Tow	24	3.44	0.57	6.05	204	9.62
Unsized HTR-40, never mounted, (control #2)	Tow	12	3.26	0.51	6.37	206	12.8
Unsized HTR-40, mounted in frame and then unmounted	Single Fibers in Frame	11	3.56	0.44	8.00	203	6.81
Unsized HTR-40, CVD processed, mounted in frame	Single Fibers in Frame	19	2.25	0.50	4.48	184	11.4
Unsized HTR-40, CVD processed, unmounted (processed as tow)	Tow	10	2.76	0.55	5.04	202	11.0
Unsized HTR-40, 15 min dwell at 300°C in H_2, CVD processed, mounted	Single Fibers in Frame	9	1.71	0.55	3.09	183	12.3
Unsized HTR-40, 15 min dwell at 350°C in H_2, CVD processed, mounted	Single Fibers in Frame	10	2.09	0.58	3.61	190	9.54
h-PSMA-coated HTR-40, CVD processed, mounted	Single Fibers in Frame	10	2.16	0.36	6.01	197	8.91
Fe^{3+}/alumina/h-PSMA-coated HTR-40, CVD processed, mounted	Single Fibers in Frame	22	1.62	0.38	4.21	194	9.61

[1]A minimum of 15 valid tests is required for calculation a valid Weibull distribution.[171]

Table 8.1 Summary of single-fiber tensile test data for carbon fibers as received, after thermal processing with H_2 and subsequent CVD process suitable for CNT growth, and coated and CVD-processed.

8.3. Mechanochemical Response of Carbon Fibers to Thermal Processing in Inert Atmosphere

The surprising loss of tensile strength, as well as stiffness, caused by CVD processing of both coated and uncoated single carbon fibers revealed that the primary source of properties degradation in CNT growth on carbon fibers, at least in this work, lies in some aspect of the CVD process itself, not interactions between the fiber and the coatings used to facilitate CNT growth (the previous focus in developing strategies for minimizing properties degradation due to CNT growth).

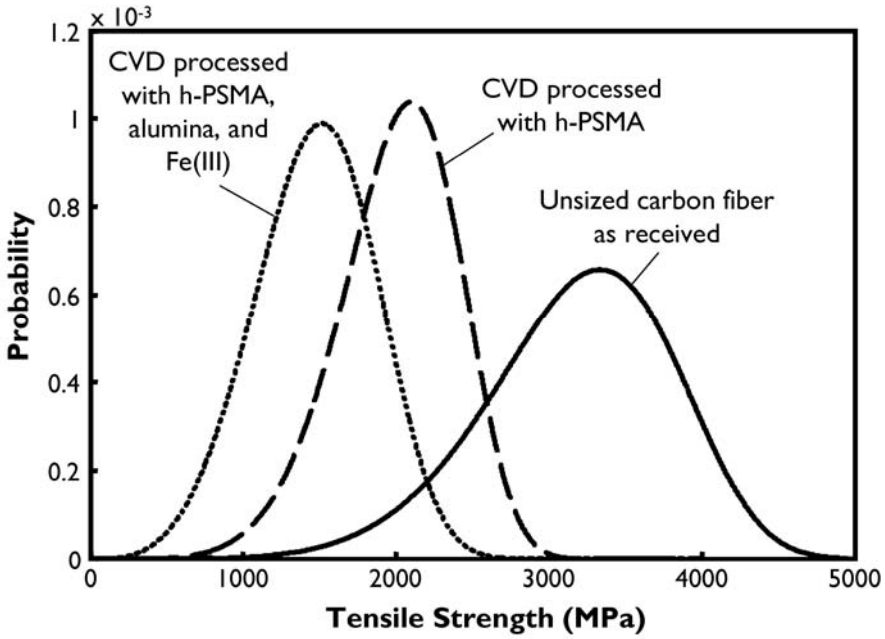

Figure 8.10 Weibull distributions calculated from single-fiber tensile tests of unsized HTR-40 carbon fibers, h-PSMA-coated HTR-40 carbon fibers after CVD processing, and Fe^{3+}/alumina/h-PSMA-coated HTR-40 carbon fibers after CVD processing.

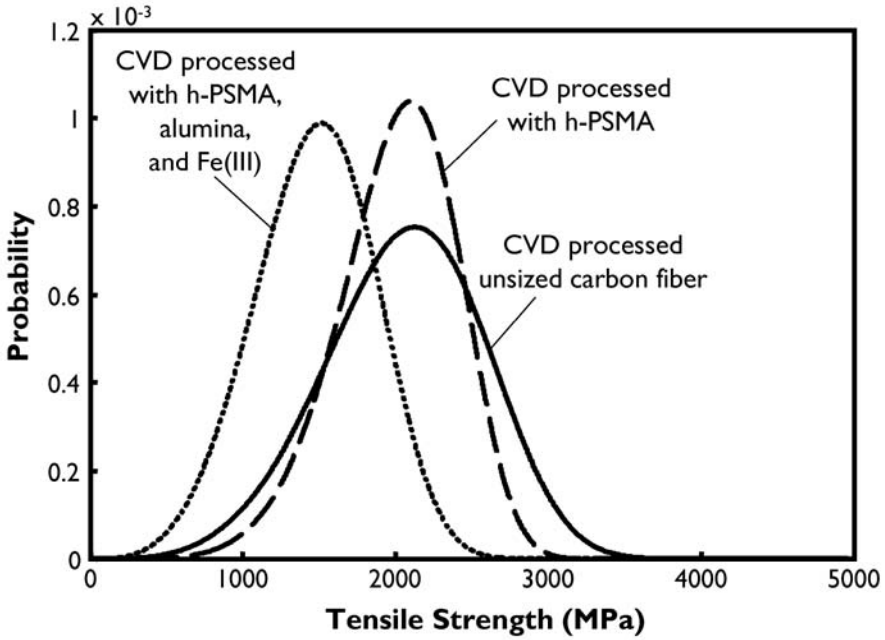

Figure 8.11 Weibull distributions calculated from single-fiber tensile tests of unsized HTR-40 carbon fibers after exposure to CVD processing, h-PSMA-coated HTR-40 carbon fibers after CVD processing, and Fe^{3+}/alumina/h-PSMA-coated HTR-40 carbon fibers after CVD processing; heat treatment, not the presence of coatings, causes the majority (30-35%) of strength loss observed.

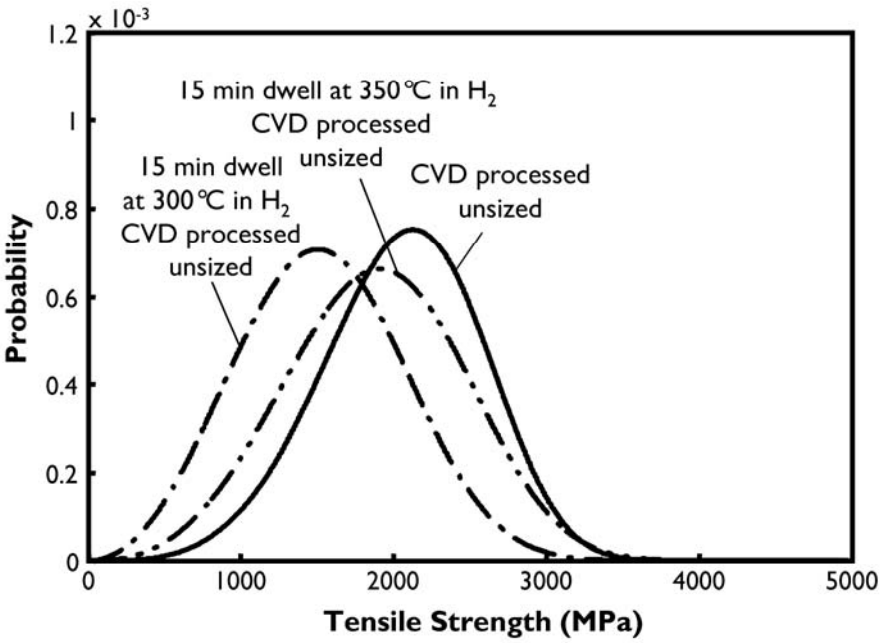

Figure 8.12 Weibull distributions calculated from single-fiber tensile tests of unsized HTR-40 carbon fibers thermally processed with and without H_2 dwell prior to being heated to 730°C in effort to quench potential residual oxygen; the H_2 dwell approach had no statistically meaningful effect.

This fascinating observation led to a series of experiments to characterize the response of carbon fibers to heating alone absent the CVD gases C_2H_4 and H_2 (Table 8.2). In one set of experiments, unsized, uncoated HTR-40 fibers were heated to 480°C, 580°C, and 730°C such that the time the fibers were at or above 480°C was equal to 18 min. (A note for historical reference: the 2" CVD furnace used in this work underestimates the actual process temperature by up to 80°C; as such the set points for these processes were 400°C, 500°C, and 650°C.) Figure 8.14 shows Weibull distributions calculated from tensile tests from samples processed under these conditions. No loss in tensile strength is observed for fibers thermally processed in He at 480°C, however substantial strength loss is observed in samples heated at 580°C, and additional strength loss over this is observed in samples heated at 730°C. Extending the length of the heat treatment has a further detrimental effect (i.e., the level of damage is not a function of temperature alone) at 580°C and 730°C, but not noticeably at 480°C. Both strength (Figure 8.15) and stiffness (Figure 8.16) are further compromised with longer treatment time at these temperatures. Thus it appears that a thermally-activated process is responsible for the observed degradation in tensile properties and occurs above 480°C.

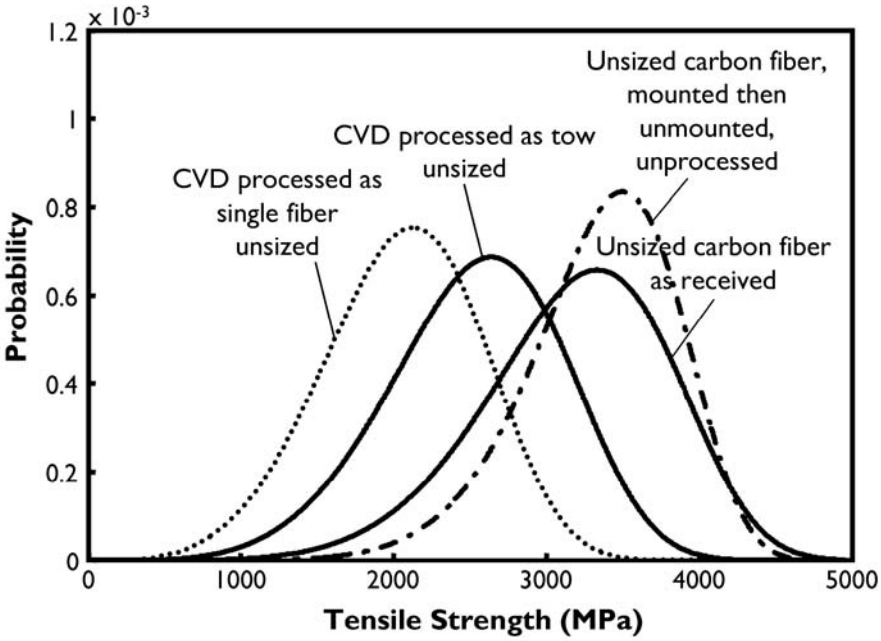

Figure 8.13 Weibull distributions calculated from single-fiber tensile tests of unsized HTR-40 carbon fibers performed to understand potential effects of manipulating carbon fibers individually (e.g., pretensioning) on tensile measurements; the thermal processing of individual fibers results in a slight reduction in measured tensile strength over processing as tows.

For practical utility, equations for predicting the tensile strength and tensile modulus of HTR-40 carbon fibers following heat treatment in inert atmosphere were fit to the data presented in Figure 8.15 and Figure 8.16:

$$\overline{\sigma}(T, t \geq 480°C) = \left(\left[-0.000241\,\text{GPa}\,°C^{-1}\,\text{min}^{-1}\right]T + \left[0.100\,\text{GPa}\,\text{min}^{-1}\right]\right)t + \left(\left[-0.000357\,\text{GPa}\,°C^{-1}\right]T + \left[4.71\,\text{GPa}\right]\right) \quad (8.4)$$

and,

$$\overline{E}(T, t \geq 480°C) = \left(\left[-0.00241\,\text{GPa}\,°C^{-1}\,\text{min}^{-1}\right]T + \left[0.683\,\text{GPa}\,\text{min}^{-1}\right]\right)t + \left(\left[-0.00317\,\text{GPa}\,°C^{-1}\right]T + \left[224.6\,\text{GPa}\right]\right) \quad (8.5)$$

where T is process temperature in °C and t is the number of minutes the sample was heated at or above 480°C.

To better characterize the nature of the hypothesized thermally-activated process, thermogravimetric analysis (TGA) was performed with HTR-40

fibers in He atmosphere (3 mg chopped fiber per run). TGA of fibers at a constant heating rate of 100°C min^{-1} (comparable to what is encountered during CNT growth in the CVD furnace) reveals a sudden change in mass-loss rate beginning at 550°C (Figure 8.17). Similarly, TGA over the course of 60 min at constant temperatures of 400°C, 500°C, and 650°C (Figure 8.18) reveal that time-dependent mass loss only occurs at 650°C.

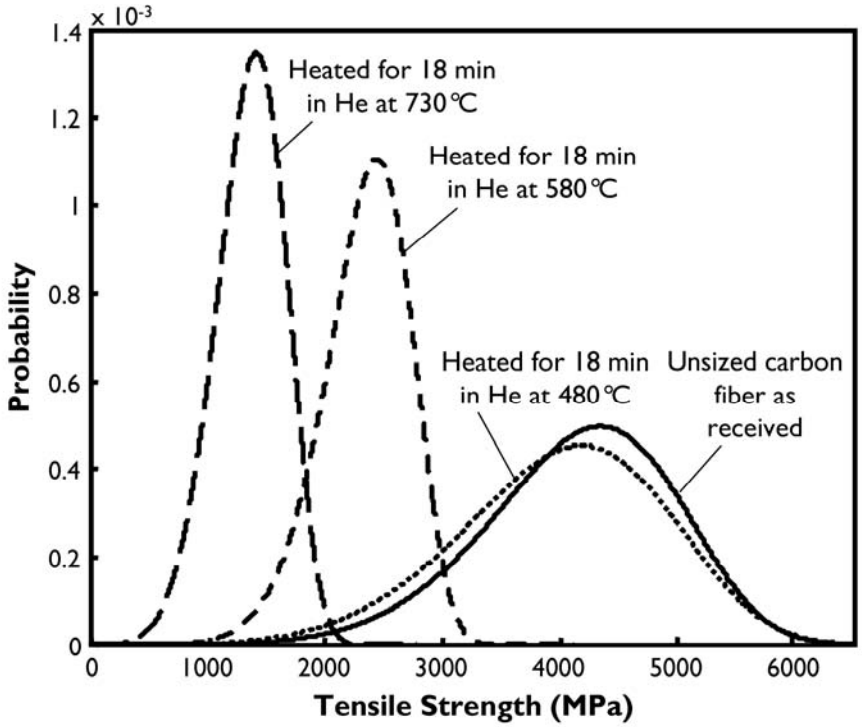

Figure 8.14 Weibull distributions calculated from single-fiber tensile tests of unsized HTR-40 carbon fibers as received and after heat treatment in He atmosphere at 480°C, 580°C, and 730°C (heating times indicated refer to length of time that fibers spent at or above 480°C, here 18 min).

To verify the observed results were not peculiar to the specific TohoTenax product that the majority of this study focused on, single-fiber tension tests were performed with heat-treated AS4 fibers as well. Breaking strength (Figure 8.19) and tensile stiffness (Figure 8.20) for unsized AS4 as received and after heat treatment in He at 480°C, 580°C, and 730°C shows similar temperature-dependent declines in these properties, although less severe below 600°C than HTR-40. Thus the observed responses of the HTR-40 carbon fibers are not isolated to this specific product but rather are generally relevant to ex-PAN carbon fibers.

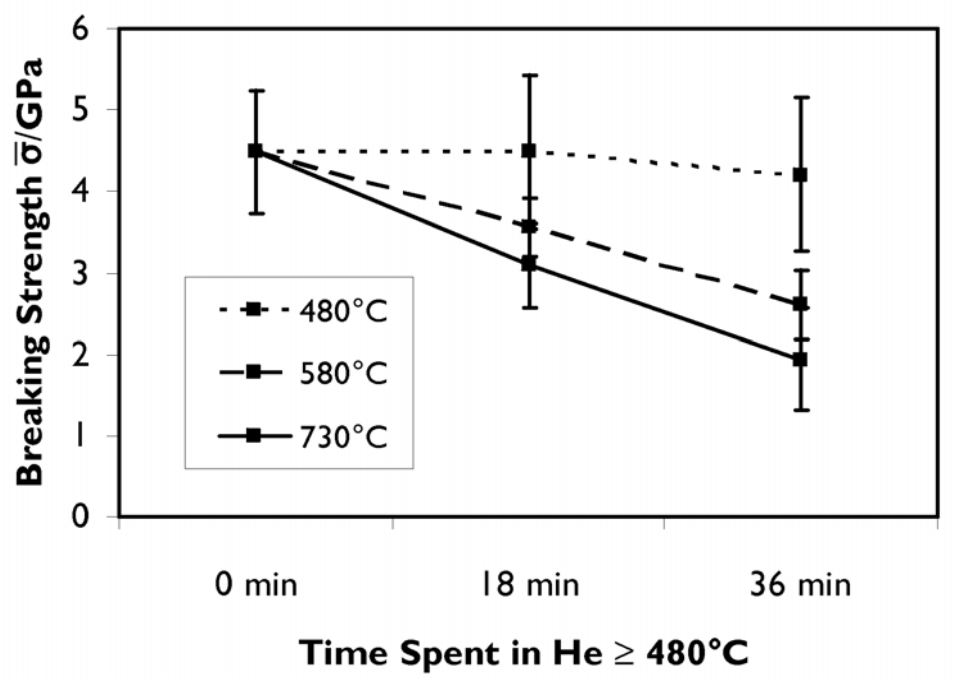

Figure 8.15 Losses in mean breaking strength of heat-treated HTR-40 fibers as a function of temperature and time spent at or above 480°C.

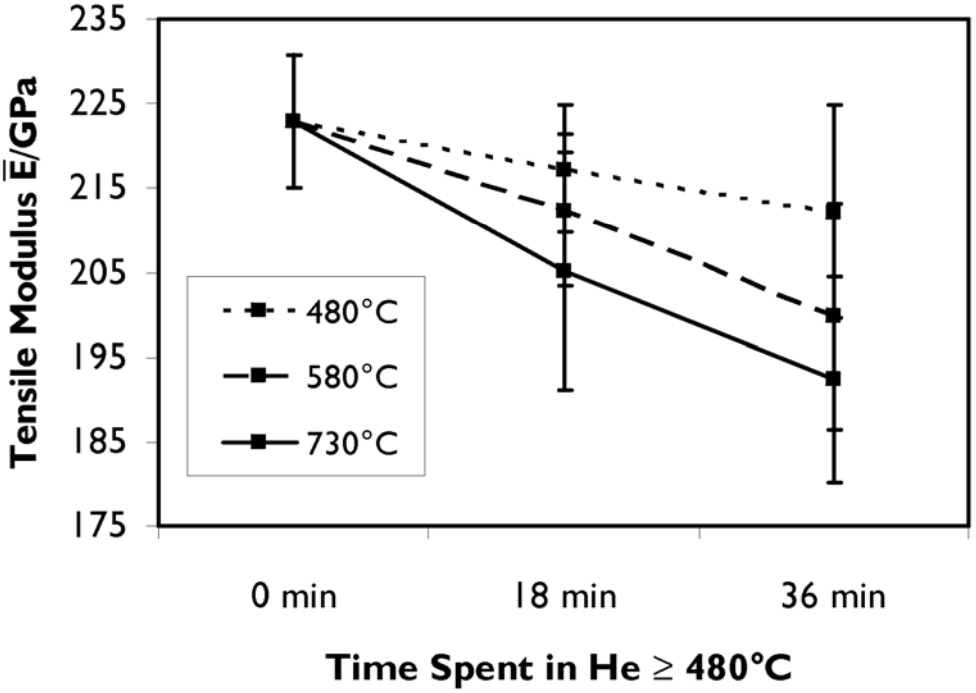

Figure 8.16 Decrease in mean tensile modulus of HTR-40 carbon fibers as a function of temperature and time spent at or above 480°C.

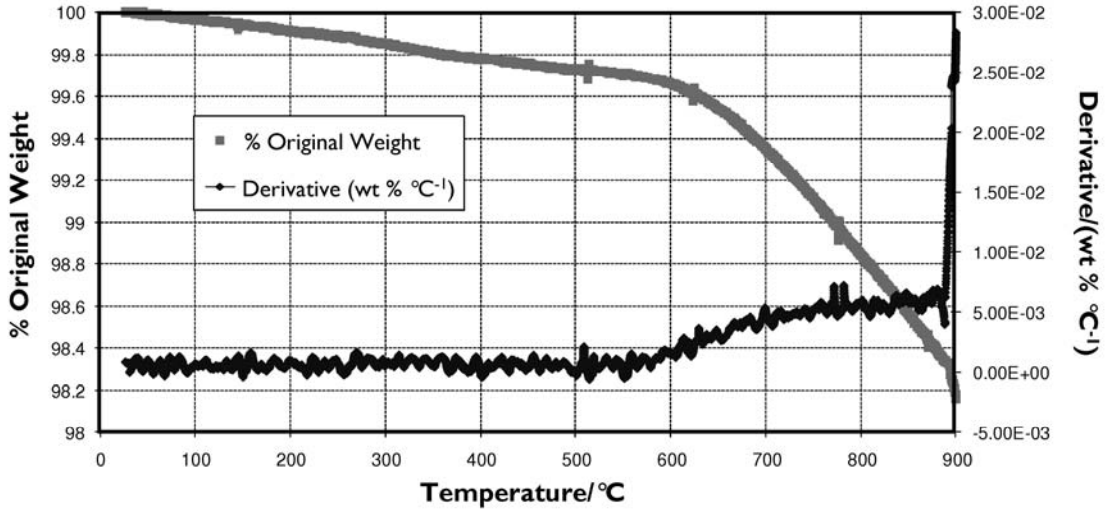

Figure 8.17 Thermogravimetric analysis of HTR-40 unsized carbon fibers at constant heating rate, showing a thermally-activated process beginning around 550°C; this suggests that these carbon fibers can be thermally processed below 550°C without undergoing mass loss.

Drawing on these results, it was further hypothesized that this mass loss may be correlated with a loss of HCN, the major by-product generated in the pyrolysis of poly(acrylonitrile)-derived carbon fibers such as HTR-40 and AS4. In-line mass spectrometry with adequate capability to differentiate the release of this from CO (which is another expected by-product and has the same mass number as HCN) was not available. Instead, a surface analysis using Auger spectroscopy was performed to detect changes in the nitrogen-to-carbon ratio present on the carbon fiber surface: if HCN is being volatilized, N must be present in the carbon fiber, and if it is coming off, a decrease in its concentration should be measurable. Figure 8.21 shows the C:N ratio measured by Auger spectroscopy of unsized HTR-40 fibers as received and after thermal processing in He at 480°C, 580°C, and 730°C. A measurable, temperature-dependent loss of N is clearly observed. Notably, the largest drop in N content occurs between the as-received fibers and the fibers heat-treated at 480°C, even though strength and (generally) stiffness are preserved at this temperature.

HTR-40 fibers before and after thermal processing in He at 730°C (Figure 8.22). The as received fibers display a superposition of two phases of graphite—one with a very small domain size (tens of nm, the broad peaks at 44° 2-θ and 53° 2-θ) and one with larger domain sizes (hundreds of nm, the sharp peaks at 44° 2-θ and 53° 2-θ and possibly an accentuated feature at 25.7° 2-θ). The disappearance of the phase associated with the larger graphite domain sizes upon heat treatment in He at 730°C, in combination with the

chemical changes on the carbon fiber surface observed by Auger spectroscopy, suggests that a microstructural rearrangement within the carbon fiber occurs beginning at 550°C, wherein the minor strength-bearing phase (the highly-oriented surface shell of the fiber) restructures leaving a weaker phase (the less-oriented interior core of the fiber) as the primary load-bearing continuity.

Herein lies a fascinating prospect: the inherent mechanochemical coupling of fiber strength with chemical aspects of the fiber's microstructure. Extending this, one of the most critical dimensions in the parameter space of carbon fiber manufacture is the role of tension during various phases of production—in fact, in the case of most ex-PAN carbon fibers, the fiber is tensioned to significant fractions of its breaking strength during production. Tensioning is an important aspect of imparting high tensile strength in graphitic fibers. Thus, not only do chemical changes affect the mechanical properties of carbon fibers, but mechanical forces can be used to direct the chemical evolution of the fiber microstructure.

This begs an important question: *why is it that the carbon fibers lose strength at temperatures well within the range in which they were manufactured?* One critical difference between the environment in which the carbon fibers are manufactured and the environment encountered in the CVD system is the absence of tension in the fibers while hot. In the next section, the role of tension during heat treatment in He and CVD processing for CNT growth is examined at the single-fiber level.

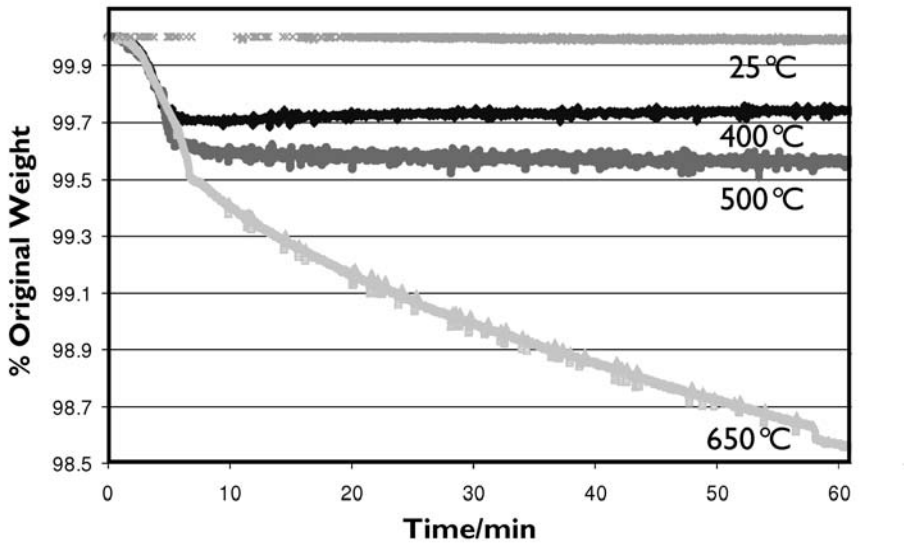

Figure 8.18 Thermogravimetric analysis of unsized HTR-40 carbon fibers in He atmosphere held at room temperature, 400°C, 500°C, and 650°C showing steady mass loss at 650°C.

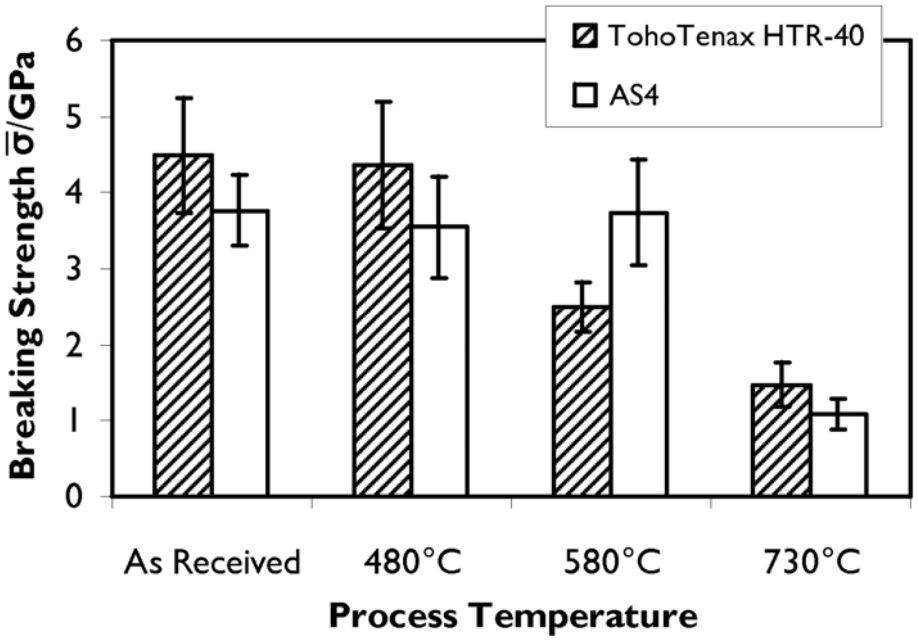

Figure 8.19 Comparison of mean breaking strengths measured for HTR-40 and AS4 carbon fibers after thermal processing in He at various temperatures, verifying strength loss at CVD conditions is not specific to one specific carbon fiber type.

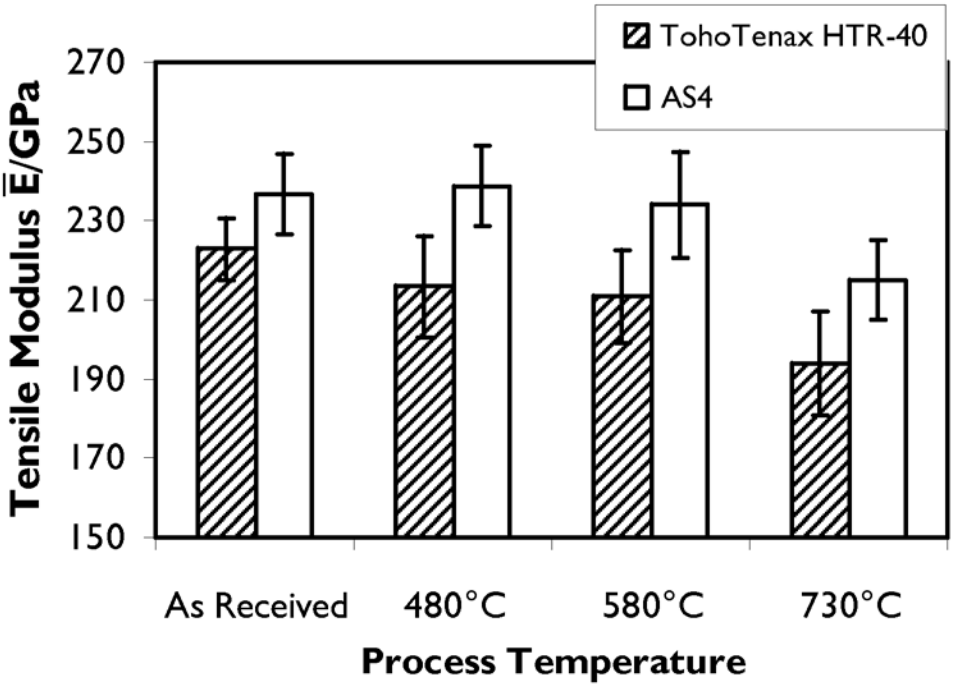

Figure 8.20 Comparison of mean tensile modulus measured for HTR-40 and AS4 carbon fibers after thermal processing in He at various temperatures; both show a reduction in modulus at CVD growth temperatures.

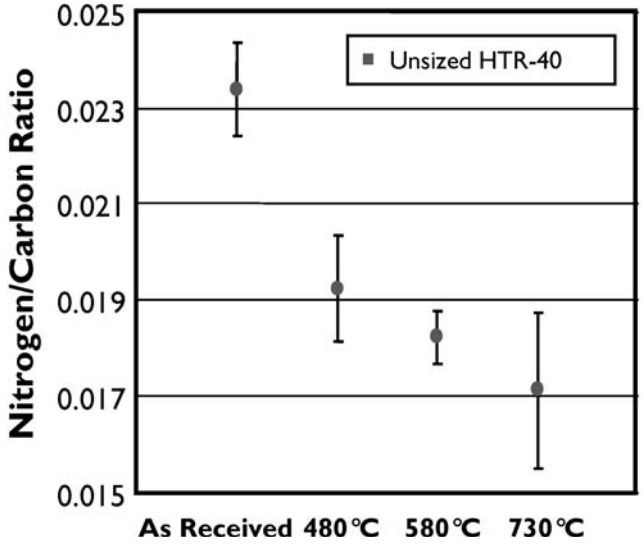

Figure 8.21 Carbon fiber surface nitrogen-to-carbon ratio as measured by Auger spectroscopy for HTR-40 fibers as received and heat treated in He at 480°C, 580°C, and 730°C.

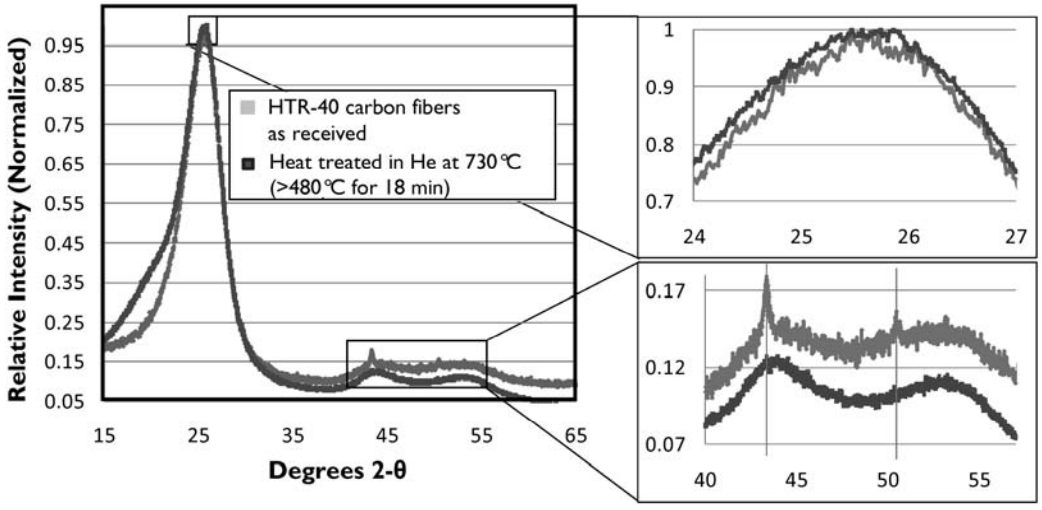

Figure 8.22 X-ray diffraction pattern for unsized HTR-40 carbon fibers as received (light gray trace) and after heat treatment in He at 730°C (dark gray trace); two phases of graphite are superimposed prior to heat treatment, possibly attributable to a bulk fiber core graphite phase and a separate surface graphite phase, which disappears on heat treatment.

Sample Description	Processed as	No. of Samples[1]	$\bar{\sigma}$/ GPa (= β)	S($\bar{\sigma}$)/ GPa	Weibull Modulus α	$\bar{E}$/ GPa	S($\bar{E}$)/ GPa
Temperature Study, TohoTenax HTR-40							
Unsized HTR-40	Tow	19	4.49	0.75	5.96	223	7.88
Unsized HTR-40, 480°C in He, 10 min at set point	Tow	19	4.37	0.83	5.27	213	12.9
Unsized HTR-40, 580°C in He, 10 min at set point	Tow	18	2.50	0.34	7.42	211	11.9
Unsized HTR-40, 730°C in He, 10 min at set point	Tow	20	1.47	0.28	5.30	194	13.1
Temperature Study, AS4							
Unsized AS4	Tow	19	3.77	0.46	8.11	237	10.2
Unsized AS4, 480°C in He, 18 min ≥ 480°C	Tow	17	3.55	0.66	5.34	239	9.99
Unsized AS4, 580°C in He, 18 min ≥ 480°C	Tow	20	3.74	0.69	5.40	234	13.3
Unsized AS4, 730°C in He, 18 min ≥ 480°C	Tow	18	1.09	0.20	5.41	215	10.2
Temperature vs. Time Study							
Unsized HTR-40, 480°C in He, 18 min ≥ 480°C	Tow	20	4.49	0.94	4.76	217	7.54
Unsized HTR-40, 580°C in He, 18 min ≥ 480°C	Tow	20	3.56	0.36	9.97	212	8.96
Unsized HTR-40, 730°C in He, 18 min ≥ 480°C	Tow	20	3.09	0.52	5.94	205	14.0
Unsized HTR-40, 480°C in He, 36 min ≥ 480°C	Tow	20	4.20	0.95	4.44	212	12.6
Unsized HTR-40, 580°C in He, 36 min ≥ 480°C	Tow	19	2.61	0.43	6.11	200	13.3
Unsized HTR-40, 730°C in He, 36 min ≥ 480°C	Tow	18	1.94	0.63	3.07	192	12.2

[1]A minimum of 15 valid tests is required for computation of a valid Weibull distribution.[171]

Table 8.2 Summary of single-fiber tensile test data for carbon fibers thermally processed in He atmosphere as a function of temperature and time.

To gain insights about microstructural changes throughout the bulk of the fiber (the interior core), X-ray diffraction (XRD) was performed on unsized

8.4. Thermochemical Processing of Carbon Fibers Under Tension

Tension is a critical aspect in the production of ex-PAN carbon fibers. Here, we reintroduce tension into already-manufactured HTR-40 carbon fibers to evaluate the role of this parameter on fiber tensile strength and stiffness during heat treatment. Tension was applied to single carbon fibers using the all-graphite tensioning frame described in Section 8.1.3. Determination of the maximum level of tension that could be reliably applied to single carbon fibers for thermal processing was not straightforward. Carbon fibers of a given length exhibit polydispersity in their tensile strengths and so the maximum applicable tension for a given length of fiber varies from specimen to specimen and is not knowable in advance of tensile testing. Let Ξ represent the tension applied to a single fiber. The maximum applicable tension is, at a minimum, less than the fiber's breaking strength by some increment, and in practice, may be even less due to limitations arising from gripping, dynamic loading, and variations in material quality. For simplicity, we set the maximum tension that can be practicably applied to a fiber, $\bar{\Xi}$, equal to the mean breaking strength measured for fibers of the same type as determined by single-fiber tensile tests. The tension applied to a fiber can then be expressed as a proportion of the approximate maximum applicable tension with the dimensionless ratio $\frac{\Xi}{\bar{\Xi}}$. Here, single fiber loadings of $\frac{\Xi}{\bar{\Xi}}$ = 0.12, $\frac{\Xi}{\bar{\Xi}}$ = 0.45, and $\frac{\Xi}{\bar{\Xi}}$ = 0.75 were investigated. At tensions of $\frac{\Xi}{\bar{\Xi}}$ = 0.75, less than 1 in 10 fibers survived thermal processing, and so this level of tension was not studied in depth (in fact, this level of tension likely serves more as a mechanism for selecting out the highest strength fibers from a set of fibers than a method for tensioning the fibers).

Figure 8.23 shows Weibull distributions calculated from tension tests performed on unsized HTR-40 fibers as received and after heat treatment at 730°C (at or above 480°C for 18 min) with $\frac{\Xi}{\bar{\Xi}}$ = 0.12 and $\frac{\Xi}{\bar{\Xi}}$ = 0.45 (Table 8.3). The application of a low level of tension ($\frac{\Xi}{\bar{\Xi}}$ = 0.12) was found not only to preserve carbon fiber tensile stiffness and strength upon thermal processing at 730°C but possibly also to enhance tensile strength. Interestingly, however, the higher level of tension resulted in ~10% loss in tensile strength, although this is still a 20-25% improvement in strength retention compared with untensioned thermal processing of fibers.

In conclusion, application of a low level of tension is a viable strategy for preserving fiber strength and stiffness during CNT growth on carbon fibers.

Sample Description	Processed as	No. of Samples[1]	$\bar{\sigma}$/ GPa (= β)	S($\bar{\sigma}$)/ GPa	Weibull Modulus α	$\bar{E}$/ GPa	S($\bar{E}$)/ GPa
Low Tension Study							
Unsized HTR-40, untensioned,730°C in He, 18 min ≥ 480°C	Tow on Tension Frame	20	3.91	1.07	3.66	214	17.6
Unsized HTR-40, tensioned (12% max Ξ), 730°C in He, 18 min ≥ 480°C	Single Fibers on Tension Frame	21	4.46	0.72	6.23	215	10.7
Moderate Tension Study							
Unsized HTR-40	Tow	19	3.46	0.79	4.40	212	12.5
Unsized HTR-40, tensioned (45% max Ξ), 730°C in He, 18 min ≥ 480°C	Single Fibers on Tension Frame	24	3.10	0.71	4.36	202	11.6

[1]A minimum of 15 valid tests are required for computation of a valid Weibull distribution.[171]

Table 8.3 Summary of single-fiber tensile test data for carbon fibers thermally processed in He atmosphere under tension as single fibers and control samples processed untensioned as tows.

8.5. Growth of CNTs on Carbon Fibers Below Strength-Loss Threshold Temperature

Informed by tensile strength and stiffness measurements of heat-treated fibers and TGA showing a process activation at 550°C, if it were possible to grow CNTs below 550°C (500°C conservatively), tension would not be needed to preserve carbon fiber tensile properties. Here, the method of low-temperature CNT growth employing CO_2/C_2H_2[46] in combination with Fe^{3+}-loaded K-PSMA as demonstrated in Section 7.3.2 is used to grow CNTs on HTR-40 carbon fibers at 480°C, well below the critical temperature threshold of 550°C (see Section 7.3.2 for process details). Briefly, fibers were coated with K-PSMA (from h-PSMA initially acidified with NaOH to a pH of 8 then neutralized with K_2CO_3 to a pH of 11) and dip-coated with 0.050 M Fe^{3+}/IPA solution aged for 60 min. The fibers were then processed in a 1" CVD furnace first under 400 sccm hydrogen on ramp-up to 480°C to reduce the Fe^{3+} to iron nanoparticles and then 17 sccm CO_2/167 sccm 10% C_2H_2 in Ar for 15 min to grow CNTs by oxidative dehydrogenation. Full process details for the preparation of K-PSMA, preparation of the carbon fibers, and CVD processing are presented in Section 7.3.2.

Table 8.4 summarizes tension tests performed on unsized HTR-40 and CVD-processed Fe^{3+}/K-PSMA-coated HTR-40 fibers (see Figure 7.36 middle right panel for a representative SEM). Incredibly, CNTs were obtained and no changes in breaking strength or tensile modulus are observed.

In conclusion, CNT growth has been achieved on high-performance carbon fibers without resulting in degradation of fiber tensile properties.

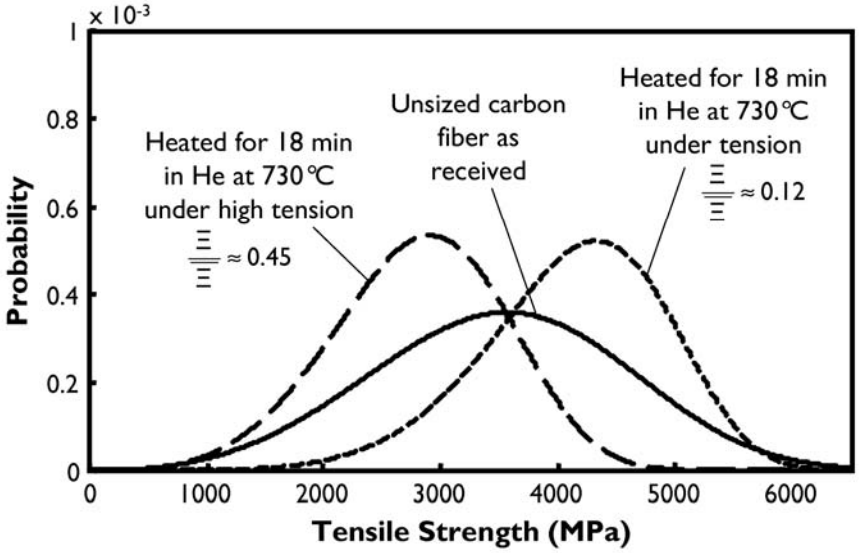

Figure 8.23 Weibull distributions calculated from single-fiber tensile tests of unsized HTR-40 carbon fibers compared with HTR-40 carbon fibers tensioned to 12% and 45% of maximum practicably applicable level of tension and heat treated in He at a typical CNT growth temperature of 730°C; application of low-level tension enables preservation of tensile strength at temperatures where severe strength degradation is otherwise expected.

Sample Description	Processed as	No. of Samples[a]	$\bar{\sigma}$/ GPa (= β)	S($\bar{\sigma}$)/ GPa	Weibull Modulus α	$\bar{E}$/ GPa	S($\bar{E}$)/ GPa
Unsized HTR-40[b]	Tow	19	3.46	0.79	4.40	212	12.5
K-PSMA/Fe^{3+} on HTR-40, CO_2/C_2H_2 CVD at 480°C	Tow	20	3.88	0.85	4.55	213	13.2

[a]A minimum of 15 valid tests is required for calculation of a valid Weibull distribution.[171]
[b]Repeat of listing from Table 8.3; served as control for moderate tension study and CNT growth study.

Table 8.4 Summary of single-fiber tensile test data for carbon fibers coated with Fe^{3+}-loaded K-PSMA CVD processed for CNT growth with CO_2/C_2H_2, and as-received control samples.

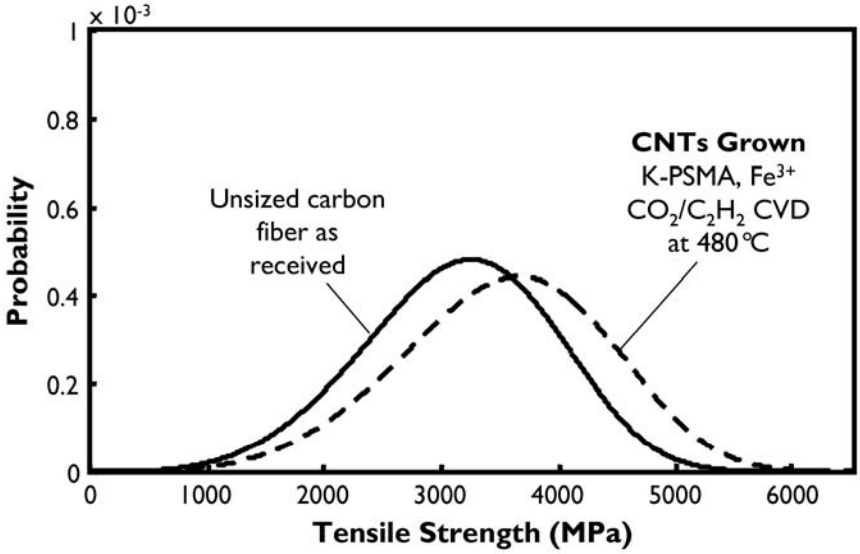

Figure 8.24 Weibull distributions calculated from single-fiber tensile tests of baseline unsized HTR-40 carbon fibers and HTR-40 fibers coated with Fe^{3+}-loaded K-PSMA coating that were subsequently CVD processed for CNT growth with CO_2/C_2H_2 at 480°C; no strength or modulus degradation is observed.

8.6. Conclusions and Future Work

Two important discoveries emerged from this study. First, it is possible to compensate for tensile strength and stiffness loss in carbon fibers due to heating by tensioning the fibers during the heat treatment. A fiber-type-specific critical threshold temperature exists above which tension is a recommended solution. A microstructural process becomes thermally active in carbon fibers at some temperature which likely depends on the chemical and microstructural composition of the fiber. For HTR-40 fibers that temperature is ~550°C. Above this temperature, chemical and microstructural changes are free to occur. Application of tension guides the evolution of these changes, perhaps invoking alignment and overlap of graphenic ribbons throughout the surface of the fiber increasing fiber modulus and strength. Upon cooling, this microstructural state is kinetically trapped as is, and only when heated above the critical threshold temperature again does restructuring resume. In essence, there is an energetically favorable state that becomes accessible above this critical temperature, creating mobility throughout the internal structure of the fiber that permits reshaping of the microstructure, to the benefit or detriment of strength and stiffness properties, through the application or absence of stress. The degradation of tensile properties above this temperature is found to be time-dependent, however, which provides an opportunity of minimizing

properties degradation by minimizing the time samples are exposed to such temperatures, should tension not be practicable, such as in the case of growing CNTs on a weave.

Second, growth of CNTs on carbon fibers employing CVD with CO_2/C_2H_2 and Fe^{3+}-loaded K-PSMA coatings has been achieved at 480°C and demonstrated not to result in loss of tensile strength or stiffness. This provides, possibly for the first time, a viable way of growing CNTs on carbon fibers that, although not aligned, may be suitable for composites applications without compromising in-plane properties. Further process optimization and scale-up to composite-level specimens should be pursued.

Finally, ex-PAN carbon fibers, specifically TohoTenax HTR-40 and AS4 fibers, have been characterized in the context of a mechanochemical system. The interplay among temperature, time, and tension when these fibers are heated above their characteristic critical threshold temperatures has been explored at the single-fiber level and provides some insights of what to expect from carbon fibers at these conditions.

Chapter 9

Conclusions and Recommendations

This thesis successfully addressed the engineering goal of developing methods for growing CNTs on carbon fibers that simultaneously preserve fiber properties, addressed the scientific goal of building an understanding of relevant catalyst-substrate and CVD environment-substrate interactions in the CNT-carbon fiber system, and resulted in the novel discovery of CNT growth and graphitization of amorphous carbon employing nanoparticulate oxides.

At the start of this work, examples of methods for preparing CNT-coated carbon fibers had been already reported in the literature (more are published every few months), however only a few of these reports had characterized effects on the mechanical properties of the underlying fiber and none had described a scalable, industrially viable method that simultaneously takes into consideration in-plane properties of derivative composites—i.e., there was no broader context. By analyzing these approaches, development and implementation of new processes for CNT growth on carbon fibers to maximize the probability of preserving fiber tensile properties was pursued. This led to the development of methods for applying barrier coatings, improving wettability of carbon fibers, and performing growth of CNTs without employing techniques known to damage carbon fibers. Considering not only scientific but also manufacturing aspects of the target engineering goal, processes that not only meet the technical needs of the engineering goal but that are viable for laboratory- and commercial-scale operations have been demonstrated. Development of these processes was enabled by science-based diagnostics including surface chemistry characterizations and single-fiber tensile testing providing a powerful model of carbon fibers as a mechanochemical system and elucidating specific degrees of freedom for materials engineering of CNT-coated carbon fibers.

Also prior to this thesis, the working model for CVD growth of CNTs that was generally accepted by most practicing CNT researchers did not accommodate for phenomena such as growth of CNTs from an oxide. Today, contributions described in this thesis, in conjunction with recent works from other groups, have established the possibility of oxide-based CNT growth as an accepted aspect of the broader model of thermal CVD growth of CNTs. It is interesting, however, that despite reports of successful CNT growth employing oxides other than zirconia and the purported "high activity" of these oxides as CNT "catalysts", widespread adoption of oxides for CNT growth has not been observed. Indeed, the understanding of CNT growth with oxide nanopositors has been predisposed by a well-established legacy of CNT growth employing other approaches, and a lack of rigor in, and open-mindedness about, how oxide-facilitated growth works. The use of *in situ* metrology is especially powerful in this arena and has informed and validated the observations made in this work. However powerful *in situ* observations may be, though, further *objective and rigorous differential experimentation* is still required to properly elucidate growth mechanisms. Despite the knowledge that zirconia could enable CNT growth by CVD, the availability of *in situ* XPS during CNT growth, and TEM of CNTs attached to zirconia nanoparticles, no good method for practically using zirconia was available, even after performing the broad parametric study described in Chapter 5. It is only now (perhaps) after careful thinking and differential experimentation that the "missing parameters" of zirconia-based CNT growth are coming to light, despite *in situ* data being available the entire time, namely, that the presence of high-surface-area amorphous carbon may play important role.

Following is a summary of the contributions made in the course of this thesis work and recommendations for the direction of future efforts on these topics.

9.1. Summary of Thesis Contributions

Oxide-Mediated Growth of CNTs and Graphitization of Amorphous Carbon

It has been conclusively demonstrated that nanoparticulate zirconia is a non-metallic and non-carbidic substance that catalyzes, or somehow else enables, both single-wall and multiwall CNT growth by CVD as well as graphitization of amorphous carbon. It was shown that zirconia remains in an oxidized state during CNT growth, a phenomenon never previously observed. The stability of zirconia in the presence of solid-state carbon was also verified by XRD and XPS methods, and its propensity to restructure amorphous carbon around itself into graphitic nanoshells was identified for

the first time. It is now believed that these two phenomena are not circumstantial nor only tangentially related, but rather that CNTs grow from a zirconia nanoparticle, in some fashion, through an intermediate step involving the formation of nanoshells around itself.

Critical Parameters for Enabling Practical Use of Zirconia for CNT Growth

A broad study to characterize the response of zirconia-based CNT growth to multiple parametric vectors typically effective at increasing CNT yield from legacy-catalyst-based processes led to the deduction that one more of the zirconia nanoparticles, substrates, or overall CVD approaches surveyed was not optimized, and that whatever beneficial aspects that enable a minority of nanoparticles on a wafer surface to result in CNT growth was not present in a high concentration and/or yet controlled, i.e., was not one of the parametric vectors investigated. In probing which of these areas to target future investigations, it appears that the decision to optimize growth on oxide supports was the major source of null results, and that high-surface-area carbon substrates such as carbon aerogels facilitate high-yield activity. Further work to understand and utilize this for practical application is required and is underway. This study also verified that predictable, albeit low-yield, growth of CNTs from zirconia derived from different sources could be attained, providing further validation of results to date despite a large body of null results catalogued.

New Advanced CVD System for Enhancing CNT Growth and Photocatalytic CVD

A new modular CVD system engineered to accommodate emerging needs in the investigation of CNT growth from oxide nanopositors was designed, constructed, and calibrated in part. New opportunities at the intersection of carbon feedstock engineering and photocatalysis-mediated CVD are now possible with this system. Other aspects of the system including a decoupling of temperatures for gas processing and substrate processing, a construction designed to eliminate influences of trace water and oxygen from growth processes, and the ability to quantitatively remove contamination from the growth chamber promise to elucidate sources of variability in legacy CVD processes and better control them.

Oxide Barrier Coatings for Carbon Fibers

A survey of techniques for coating ("disguising") carbon fibers with alumina barrier coatings was conducted and the most promising approaches from this survey were iterated to distill practical methods. Both CVD of alumina employing the precursor aluminum triisopropoxide and sol-gel deposition of high-surface-area alumina (when used in conjunction with the amphiphilic polymer h-PSMA as an adhesion enhancing undercoating) were

shown to be effective methods for coating carbon fibers with well-adhered alumina that facilitates growth of aligned CNTs when used in conjunction with Fe catalysts and CVD processed for CNT growth.

Low-Temperature Growth of CNTs on Carbon Fibers to Preserve Fiber Tensile Properties

Furthermore, a novel amphiphilic polyelectrolyte, K-PSMA, was developed and demonstrated as a method of loading Fe catalyst onto a carbon fiber with otherwise poor wettability without damaging the carbon fiber. Fe-loaded K-PSMA-coated carbon fibers were then demonstrated to yield uniform density of unaligned CNTs when processed at only 480°C with CVD based on oxidative dehydrogenation of acetylene (CO_2/C_2H_2).

Tensioning Fibers Can Preserve Fiber Tensile Properties During Growth of CNTs

A detailed effort to characterize the effects of the coatings approaches developed at the single-fiber level was then performed, opening an investigation into the fundamental mechanochemical nature of carbon fibers. Carbon fibers, specifically TohoTenax HTR-40 and an AS4 aerospace-grade fiber, were found to undergo substantial (~50%) tensile strength loss and experience a reduction in tensile stiffness from simply being heated above a critical threshold temperature characteristic of the carbon fiber type in inert atmosphere (~550°C for HTR-40). If instead these fibers are placed under a tension of ~12% mean breaking strength, however, tensile strength and stiffness are both preserved. These discoveries enable two degrees of freedom for engineering practical approaches for CNT growth: one, using a CVD process that allows for CNT growth below the critical threshold temperature of the fiber used, and two, placing the fiber under tension and using CVD processes that require higher temperatures. In the case of application to weaves, the former may be preferable. In the case of in-line carbon fiber manufacturing, the latter is preferable, as the number of CVD processes available is much larger and growth of aligned CNTs has not yet been demonstrated with a low-temperature CVD process.

9.2. Recommendations for Future Work

This thesis lends itself to divergence into two future research areas: further optimization, reduction to practice, and extension of the work performed with CNT growth on carbon fibers, and further exploration, characterization, and reduction to practice of CNT growth with oxide nanopositors.

9.2.1. Future Work with CNT Growth on Carbon Fibers

Scale-Up of K-PSMA/Low-Temperature CVD Method

Growth of CNTs on carbon fibers in a way that preserves fiber properties was demonstrated for the first time in this thesis by employing low-temperature CVD with CO_2 and C_2H_2 on Fe-loaded K-PSMA-coated carbon fibers. The methods described herein are ready for scale-up to weaves, coupons for mechanical properties standards testing, and possibly a proof-of-concept manufacturing line. Further characterization and optimization of the approach is merited, for example, minimizing the K-PSMA thickness, maximizing CNT density, and optimizing CVD processing towards aligned or pseudo-aligned growth. This method shows great promise, especially for substrates or manufacturing approaches that do not permit or easily permit tension (such as weaves).

Integration of Tensioning, Alumina Barrier Coating into Continuous Process

Tensioning carbon fibers when heating carbon fibers post-manufacture was identified and demonstrated as a way of preserving fiber properties during high-temperature CVD growth of CNTs in this thesis. Use of a reel-to-reel CVD processing system that would enable controllable tensioning of a fiber tow during CNT growth is a logical next step in scaling this up. Such a setup could also allow exploration of applying alumina by CVD with aluminum triisopropoxide (located in a short hot zone through which the tensioned tow would pass) while under tension as a way to conformally deposit a barrier coating suitable for high-yield aligned CNT growth throughout the interior of a tow without degradation of fiber tensile properties. The reel-to-reel system could also be extended to allow for sequential dip-coating processes with h-PSMA, an alumina sol-gel process (such as one employing propylene-oxide-assisted gelation of aluminum(III) chloride), a catalyst precursor bath of 0.050 M $Fe(NO_3)_3 \cdot 9H_2O$ in 2-propanol, and then entering into an open-entry atmospheric CVD furnace.

Characterization of the CNT-Fiber Interface

Outstanding questions include the strength of the CNT-substrate interface with both the low-temperature CVD/K-PSMA process and with CNTs grown on alumina-coated carbon fibers. The strength of this interface could be measured using microanalytical techniques similar to the single-fiber testing performed in this work or via fragmentation testing. Effects of the presence of intermediary coatings on the thermal and electrical conductivity of composites prepared with fuzzy carbon fibers produced through one of the methods described herein are also topics of relevance. Considering the

permanence of coatings following CNT growth, methods for depositing such coatings may need to be optimized to reduce the quantity and improve the coverage of the coating materials.

Extension of Methods for CNT Growth on Carbon Fibers to Advanced Composites and Polymers

In addition to growth of CNTs on carbon fibers themselves, the methods described herein should be immediately extensible to growth of CNTs on other carbon-based substrates such as carbon/carbon composites, graphite, and glassy carbon, as well as other ceramics such as silicon carbide. Carbon/carbon composites prepared with fuzzy carbon fibers are also an interesting prospect for tribological materials and thermal protection systems for spacecraft with enhanced thermal and wear characteristics. It is also interesting to consider if low-temperature CNT growth employing CO_2/C_2H_2 used in conjunction with K-PSMA or a similar technology could be used to grow CNTs on advanced *polymer* fibers and matrix materials as well; although 480°C is hotter than the melting point of most polymers, perhaps a workaround such as short residence time at 480°C or optimization for growth at less than 480°C could be devised.

Multifunctional and Sensory Carbon Fibers

The coatings technologies described in this thesis could also be extended to materials other than alumina and iron nanoparticles to install novel functionalities onto carbon fibers. For example, sol-gel-deposited lead zirconium titanate (PZT) piezoelectric coatings could be conformally deposited on h-PSMA-coated carbon fibers and allow for installation of a structural health monitoring functionality into composite architectures. PZT, as an oxide, may serve the dual role of also being a suitable support for CNT growth with iron catalysts; as such, PZT-coated carbon fibers could also be coated with aligned CNT arrays achieving multifunctional benefits. K-PSMA-coated carbon fibers could be further derivatized with other surface functionalities to facilitate attachment of various functional nanostructures for biological sensing applications, resistance against chemical exposure, or enhanced non-destructive evaluation via infrared or ultraviolet imaging.

Additionally, emerging high-tensile-strength CNT-based fibers would benefit from an additional circumferential aligned CNT component for application in advanced CNT-fiber composites similar to carbon fibers, since regardless of improvements in in-plane properties afforded by CNT fibers, matrix-dominated shortcomings still need to be mitigated.

9.2.2. Future Work with Oxide Nanopositors

Development of Oxide Nanoparticles as a Practical Tool for CVD Growth of CNTs

Immediate future work should focus on improving yield with monodisperse zirconia further so that more rigorous *in situ* experimentation can be performed, including *in situ* TEM during CNT growth, to reveal the mechanisms of CNT growth from oxide nanoparticles. This may entail engineering of high-surface-area amorphous carbon materials and thin films on silicon wafers for use as supports with zirconia and possibly methods of encapsulating zirconia nanoparticles with a pyrolyzable polymer or carbon shell in advance of deposition onto a substrate for CNT growth to avoid the need for an amorphous carbon support. Further *in situ* XPS is merited as well, as is XRD to see if nanoparticle phase is an important facet of the solid-state graphitization and CNT growth processes.

A parametric exploration of non-oxide substrates for use in combination with oxide nanopositors such as zirconia is warranted. High-surface-area amorphous carbon seems to be one promising candidate; perhaps others exist as well. The effects of substrate surface area and composition should be characterized.

Other nanoparticulate oxides and non-oxides should be evaluated as well. Reliable production of monodisperse oxide nanoparticles of high purity is an outstanding need that hindered this work. Laser ablation methods may be promising.

Towards Diameter and Chirality Control

With the ability to control nanoparticle diameter and composition more precisely, it is predicted that control over both CNT outer diameter *and* inner diameter could be achieved with oxides, as the diffusivity of carbon through oxides is much less than through metals. Along these lines, oxide nanoparticles can be rendered into a variety of shapes such as rods and tetrapods and are stable as these shapes at CVD growth temperatures, suggesting that novel non-circular cross-section CNTs could be produced.

Photocatalytic CVD Employing Oxides

A large parameter space surrounding photocatalytic CVD is left to explore. Engineered zirconia and titania nanoparticles coupled with CVD and exposure to ultraviolet can be investigated in the near future with the new CVD system developed in this thesis. Roles of dopants and solid state acidity are variables of interest for this work.

Characterization of Gas-Phase Species Important in CNT Growth with Oxides

Parameter space in the area of alkyne-assisted growth of CNTs from zirconia and other oxide nanoparticles is also within reach in the near term and may be a promising approach to enhancing CNT yield from these nanopositors.

Applications for Electronics and CMOS-Compatible Processing

Extension of lessons learned from this thesis and in future work regarding oxide-based CNT growth could be extended to metal-free synthesis of large-area graphene for nanoelectronics and sensors.

9.3. Conclusions

In summary, this thesis:

- Demonstrated the CVD growth of CNTs employing a nanoparticulate oxide (zirconia) for the first time, and that CNT growth by thermal CVD is not limited to only metallic catalysts (Chapter 4)
- Demonstrated the solid-state conversion of amorphous carbon into graphitic nanoshells employing zirconia (Chapter 4)
- Showed that zirconia remains in an oxidized state during CVD growth of CNTs (Chapter 4)
- Surveyed a large parameter space of process conditions in CVD growth of CNTs employing zirconia nanoparticles showing that most of that parameter space has little effect in enhancing CNT yield (Chapter 5)
- Showed that thermal pretreatment of zirconia nanoparticles with solid-state, high-surface-area amorphous carbon prior to CVD enables dramatic enhancement in CNT yield in CNT growth employing zirconia (Chapter 5)
- Described a new versatile CVD system that eliminates wetted polymers, expands gas feedstocks, decouples gas-conditioning and substrate process temperature, and enables introduction of ultraviolet light and light-based spectroscopy during CVD (Chapter 6)
- Demonstrated methods for applying alumina barrier coatings to and enhancing the wettability of high-performance carbon fibers without employing techniques known to damage fiber tensile properties (Chapter 7)

- Demonstrated a method for loading Fe onto the surface of a carbon fiber without etching the fiber surface made possible through the polyelectrolyte K-PSMA (Chapter 7)
- Demonstrated low-temperature growth of CNTs on Fe-loaded K-PSMA-coated carbon fibers, well below the temperature where the tensile properties of carbon fibers begin to degrade (Chapter 7)
- Identified that the major origin of tensile properties degradation during CVD growth of CNTs on carbon fiber is due simply to heating, and that there exists a threshold temperature (~550°C for one fiber investigated here) where tensile property degradation begins (Chapter 8)
- Identified and demonstrated that the application of tension during CVD growth of CNTs on carbon fibers can prevent tensile property degradation above the threshold degradation temperature (Chapter 8)

These contributions can now serve as a foundation for the development of fuzzy carbon fiber based composite architectures with viable potential for aerospace engineering applications.

Discoveries made during the course of this thesis have also brought to light an important lesson regarding the nature of scientific discovery worth voicing. Now more than ever, we as scientists must keep our observation skills keen and our minds open so that when the universe presents us with subtle clues about its workings, we pay attention and probe deeper. Several of the findings in this thesis were first met by other researchers with great skepticism because of their unexpected, and in some cases even counter-expected, nature.

In conclusion, it is the hope of the author that the contributions provided during the course of this thesis will serve to enable enhanced materials technologies that will have a broad impact on energy usage and enhance aerospace vehicle performance as to further ensure the perpetuation of our society and to enable us to extend the presence of our society to space.

Appendix A

Select CVD Process Scripts

This appendix provides a selection of process scripts used to perform various CVD processes described in this thesis. The scripts were used with a natural language processing program that controlled the various CVD systems described in this thesis (for CNT growth, alumina deposition, and general thermal processing); as such, the code below can be read, interpreted, and executed without a computer as written. A single quotation mark (') indicates the text to the right is a comment and should not be executed. Line wrapping is indicated with an indent on the line containing the continued text. Commands to turn on or off "log" are a signal to the computer to start or stop recording process measurements.

The following select scripts, of particular relevance to the work performed in this thesis, are included below:

- **A1.** CVD Growth of CNTs with Zirconia, 2" Furnace ("ZrO2Growth2009-02-19_g2.txt"), Chapter 4 and Chapter 5
- **A2.** CVD Growth of CNTs with Zirconia, 1" Furnace ("ZrO2Growth2010-04-16_g2.txt"), Chapter 4 and Chapter 5
- **A3.** CVD Growth of CNTs with CO_2/C_2H_2 for Fe/Al_2O_3 Substrates, MANGO-TANGO ("CO2 acetylene growth vC2.txt"), Chapter 7
- **A4.** CVD Growth of CNTs with CO_2/C_2H_2 for Fe on Carbon Substrates Including Carbon Fibers, MANGO-TANGO ("CO2 acetylene growth vCF-480.txt"), Chapter 7 and Chapter 8
- **A5.** Alumina CVD with Aluminum Triisoproxide, 2" Furnace ("AluminaCVD_2.txt"), Chapter 7

- **A6.** Two-Sided Alumina CVD with Aluminum Tri-*sec*-butoxide Precursor for Carbon Fiber Weaves, 2" Furnace with MRB Attached ("AluminaLiquidCVD_17.txt"), Chapter 7
- **A7.** Quartz Tube Bake Out, 2" Furnace ("BakeOut.txt"), throughout thesis
- **A8.** Quartz Tube Bake Out, 1" Furnace ("Bakeout.txt"), throughout thesis
- **A9.** Quartz Tube Bake Out, MANGO-TANGO ("bake out.txt"), throughout thesis

A1. CVD Growth of CNTs with Zirconia, 2" Furnace ("ZrO2Growth2009-02-19_g2.txt")

```
'ZrO2 Growth Script g
'Standard Growth, Two Samples, 30 Minute Growth
'10/05/2007
'Stevie Steiner

turn log on
set helium to 400 sccm
set hydrogen to 1600 sccm
set ethylene to 400 sccm
turn helium on
turn hydrogen on
sync zones
set zone 1 to 680 deg C
turn zone 1 on
wait until zone 1 temperature > 679 deg C
turn ethylene on
wait for 30 minutes
turn ethylene off
set helium to 2400 sccm
turn hydrogen off
turn zone 1 off
wait until zone 1 temperature < 450 deg C
email ssteiner@mit.edu with a message saying "Growth is
   done."
wait until zone 1 temperature < 150 deg C
turn helium off
turn log off
```

A2. CVD Growth of CNTs with Zirconia, 1" Furnace ("ZrO2Growth2010-04-16_g2.txt")

```
'ZrO2 Growth Script g2 1" Furnace Edition
'Standard 30 Minute Growth
'04/16/2009
'Stevie Steiner

turn log on
set helium to 100 sccm
set hydrogen to 400 sccm
set ethylene to 100 sccm
```

```
turn helium on
wait 2 min
turn hydrogen on
set zone 1 to 750 deg C
turn zone 1 on
wait until zone 1 temperature > 749 deg C
turn ethylene on
wait for 30 minutes
turn ethylene off
set helium to 600 sccm
turn hydrogen off
turn zone 1 off
wait until zone 1 temperature < 450 deg C
email ssteiner@mit.edu with a message saying "Growth is
   done."
wait until zone 1 temperature < 150 deg C
turn helium off
turn log off
```

A3. CVD Growth of CNTs with CO_2/C_2H_2 for Fe/Al_2O_3 Substrates, MANGO-TANGO ("CO2 acetylene growth vC2.txt")

```
wait 3 sec
start hydrogen oled, argon oled, carbon dioxide oled,
   acetylene oled

'Warn user
alert user of explosive hazard

'Flush tube
set argon to 750 sccm
turn argon on
open argon to preheater
wait 2 min

'Reduction
set preheater to 720 deg C
turn preheater on
set argon to 100 sccm
set hydrogen to 400 sccm
turn hydrogen on
open hydrogen to preheater
'Get other gases ready
set co2 to 17 sccm
set acetylene to 167 sccm
wait until preheater temperature > 718 deg C
close hydrogen to preheater
turn hydrogen off
set preheater to 740 deg C
'Stabilize com reading
wait 5 sec
wait until preheater temperature > 738 deg C

'Start CNT growth
turn acetylene on
open acetylene to preheater
close argon to preheater
```

```
turn argon off
turn co2 on
open co2 to preheater
wait 15 min

'Stop growth
close acetylene to preheater
turn acetylene off
turn argon on
open argon to preheater
close co2 to preheater
turn co2 off

'Flush out tube to cool
set argon to 750 sccm
turn preheater off
'Stabilize readings so logic proceeds normally (need to
   eliminate data spikes)
wait 5 sec
notify "Open the preheater"
wait until preheater temperature < 200 deg C
close argon to preheater
turn argon off
alert
turn log off
```

A4. CVD Growth of CNTs with CO_2/C_2H_2 for Fe on Carbon Substrates Including Carbon Fibers, MANGO-TANGO ("CO2 acetylene growth vCF-480.txt")

```
'CO2/Acetylene Growth vCF-480
'06/28/2011
'By Stevie Steiner
'Growth with CO2/acetylene on CF loaded with Fe on K-PSMA
   at 480 deg C
'Sample at 3/4 length

'Start recording measurements
turn log on

'Warn user
alert user of explosive hazard

'Flush tube
set argon to 750 sccm
turn argon on
open argon to preheater
wait 2 min

'Reduction
set preheater to 480 deg C
turn preheater on
set argon to 100 sccm
set hydrogen to 400 sccm
turn hydrogen on
open hydrogen to preheater
'Get other gases ready
set co2 to 17 sccm
```

```
set acetylene to 167 sccm
wait until preheater temperature > 478 deg C
close hydrogen to preheater
turn hydrogen off
'set preheater to 480 deg C
''Stabilize com reading
'wait 5 sec
wait until preheater temperature > 478 deg C

'Start CNT growth
turn acetylene on
open acetylene to preheater
close argon to preheater
turn argon off
turn co2 on
open co2 to preheater
wait 15 min

'Stop growth
close acetylene to preheater
turn acetylene off
turn argon on
open argon to preheater
close co2 to preheater
turn co2 off

'Flush out tube to cool
set argon to 750 sccm
turn preheater off
'Stabilize readings so logic proceeds normally (need to
   eliminate data spikes)
wait 5 sec
notify "Open the preheater"
wait until preheater temperature < 200 deg C
close argon to preheater
turn argon off
alert
turn log off
```

A5. Alumina CVD with Aluminum Triisoproxide, 2" Furnace ("AluminaCVD_2.txt")

```
'Alumina CVD Version 2
'Deposition of Al(C3H7O)3
'Place Al(C3H7O)3 in alumina combustion boat in center of
   Zone 1
'Sigma-Aldrich part number Z561738-1EA
'Place substrates along Zone 2 and Zone 3

turn log on
set helium to 400 sccm
turn helium on
wait for 5 min
unsync zones
set zone 1 to 150 deg C
set zone 2 to 700 deg C
set zone 3 to 700 deg C
turn zone 1 on
```

```
turn zone 2 on
turn zone 3 on
wait until zone 3 temperature > 690 deg C
wait 10 min
turn zone 3 off
turn zone 2 off
turn zone 1 off
wait until zone 2 temperature < 150 deg C
turn helium off
notify "Please wait until temperature is below 50 deg C
   before opening tube."
turn log off
```

A6. Two-Sided Alumina CVD with Aluminum Tri-*sec*-butoxide Precursor for Carbon Fiber Weaves, 2" Furnace with MRB Attached ("AluminaLiquidCVD_17.txt")

```
'Alumina CVD from Al(OC4H9)3 Liquid Precursoor
'07/30/2008
'By Stevie Steiner

'Sample between 1" and 7" from left side of Zone 1

'Initialize
lock pause button
turn log on

'Start flushing
set helium to 1600 sccm
turn helium on

'Desize
sync zones
set zone 1 to 500 deg C
turn zone 1 on
wait until zone 1 temperature > 499 deg C
wait for 10 min
alert section is finished

'Desize bottom
turn zone 1 off
wait until zone 1 temperature drops below 200 deg C
turn helium off
notify "Flip sample over."
pause
turn helium on
turn zone 1 on
wait until zone 1 temperature > 499 deg C
wait for 10 min
alert section is finished

'Initialize alumina CVD
set zone 1 to 270 deg C
notify "Open furnace."
pause
wait until zone 1 temperature drops below 275 deg C
set helium to 6600 sccm
set bubbler to 50 sccm
```

```
notify "Close furnace and open bubbler valve."
pause
set zone 1 to 300 deg C
turn bubbler on
notify "Wait until zone 1 temperature is 300 deg C and
   bubbler is at 138 deg C, and then click dismiss."
pause

'Start alumina CVD
set bubbler to 1800 sccm
wait for 60 min
turn bubbler off

'Flush and cool down
set he to 500 sccm
turn zone 1 off
alert section is finished

'Flip sample over and deposit on bottom
wait until zone 1 temperature < 200 deg C
turn helium off
notify "Close bubbler valve.  Flip sample over.  Replace
   end cap and open bubbler valve again."
pause
set helium to 6600 sccm
set bubbler to 50 sccm
set zone 1 to 300 deg C
turn zone 1 on
turn bubbler on
notify "Wait until zone 1 temperature is 300 deg C and
   bubbler is at 138 deg C, and then click dismiss."
pause

'Start second alumina CVD
set bubbler to 1800 sccm
wait for 60 min
turn bubbler off

'Flush and cool down
set he to 500 sccm
turn zone 1 off

'Finish up
alert that process is finished
email ssteiner@mit.edu with a message saying "Open furnace"
wait until zone 1 temperature < 200 deg C
turn helium off
turn log off
```

A7. Quartz Tube Bake Out, 2” Furnace (“BakeOut.txt”)

```
'Bake Out v1.0
'10/03/2007
'Stevie Steiner

turn log on
set zone 1 to 800 deg C
sync zones
turn zone 1 on
```

```
wait until the zone 1 temperature > 799 deg C
turn zone 1 off
wait until the zone 1 temperature < 250 deg C
turn log off
```

A8. Quartz Tube Bake Out, 1" Furnace ("Bakeout.txt")

```
'Bake Out
'04/17/2010
'By Stevie Steiner

turn log on
set zone 1 to 800 deg C
turn zone 1 on
wait until zone 1 temperature > 799 deg C
turn zone 1 off
wait until zone 1 temperature < 400 deg C
turn log off
```

A9. Quartz Tube Bake Out, MANGO-TANGO ("bake out.txt")

```
'Bake Out
'06/19/2011
'By Stevie Steiner

turn log on
alert user of toxic hazard
set zone 1 to 750 deg C
turn zone 1 on
wait until zone 1 temperature > 748 deg C
notify "Slide the tube over"
turn zone 1 off
wait 5 sec
notify "Open furnace"
wait until zone 1 temperature < 200 deg C
alert
turn log off
```

Appendix B

MANGO Parts List

This appendix provides a list of parts, part numbers, and vendors for constructing a MANGO control box such as that described in Chapter 6.

Subsystem	Part Description	Vendor Part Number	Vendor	Quantity
Circuit Boards				
MFC/DAQ Mainboard				2
	Aalborg-Aalborg MFC/DAQ Lid Mount Mainboard	Aalborg-Aalborg MFC/DAQ Lid Mount Mainboard	Express PCB (Custom)	1
	DB-15 Female (Receptacle), PCB Mount	A34066-ND	Digikey	2
	6-pin (2x3) Male Header, 0.1" Pitch	609-2845-ND	Digikey	1
	2-pin 0.1" Pitch Header (for Power)	WM4200-ND	Digikey	1
	34-pin (2x17) 0.1" Pitch Receptacle	S9199-ND	Digikey	1
	NI DAQ USB-6008 OEM Board Only Kit (No Enclosure)	193132-02	National Instruments	1
	4-40 Machine Screw, 1/4" Long	91249A105	McMaster-Carr	8
LED Driver Board				2
	LED Driver Board	LED Driver Board	Express PCB (Custom)	1
	MOSFET	IRLD014PBF-ND	Digikey	8
	Resistor, 100 Ohm	S100QCT-ND	Digkey	6
	Resistor, 470 Ohm	S470QCT-ND	Digkey	8

	6-pin (2x3) Male Header, 0.1" Pitch	609-2845-ND	Digkey	2
	8-pin (2x4) Male Header 0.1"	609-3530-ND	Digkey	1
	2-pin Male Header 0.1" (for Switch)	A26543-ND	Digkey	1
	4-40 Machine Screw, 1/4" Long	91249A105	McMaster-Carr	8
LED Board				2
	LED Panel Mount Board	LED Panel Mount Board	Express PCB (Custom)	1
	3-Color LEDs	754-1492-ND	Digikey	2
	8-pin (2x4) Male Header 0.1"	609-3530-ND	Digkey	1
	2-pin 0.1" Pitch Header (for Power)	WM4200-ND	Digikey	1
Relay (Solenoid/SSR) Board				2
	Relay (Solenoid/SSR) Lid Mount Board	Relay (Solenoid/SSR) Lid Mount Board	Express PCB (Custom)	1
	Solenoid Connector Male Receptacle PCB-Mount	A29693-ND	Digikey	2
	SSR 4-SIP 3A 60VDC Max 0.02 A Min 3-10 V On	CC1139-ND	Digikey	4
	6-pin (2x3) Male Header, 0.1" Pitch	609-2845-ND	Digikey	1
	2-pin 0.1" Pitch Header (for Power)	WM4200-ND	Digikey	1
	4-40 Machine Screw, 1/4" Long	91249A105	McMaster-Carr	8
Special Cables				
Solenoid Cable				8
	Mating Connector for Solenoid Cable	A29361-ND	Digikey	1
	Receptacle Inserts for Solenoid Cable Connector	A29224-ND	Digikey	4
	16-20 Gauge Wire			
	DIN Connector	DIN Connector for Series 3900 Solenoid Valve	Spartan Scientific	1
MFC/DAQ Mainboard to LED Driver Board Cable				2
	6-Pin Receptacle IDC	609-2841-ND	Digikey	2

6-Conductor Ribbon Cable, 5 ft. (Need 17 Inches per Cable)	MC06G-5-ND	Digikey	1
Relay Board to LED Driver Board Cable			2
6-Pin Receptacle IDC	609-2841-ND	Digikey	2
6-Conductor Ribbon Cable, 5 ft. (Need 21 Inches per Cable)	MC06G-5-ND	Digikey	1
LED Board to LED Driver Board Cable			2
8-Pin Receptacle IDC	609-3568-ND	Digikey	2
10-Conductor Ribbon Cable, 5 ft. (4-inch Length, Use Only 8 Conductors)	MC10G-5-ND	Digikey	1
24 VDC or 5 VDC Power to Board Cable			6
2-Pin Connector Housing	WM2011-ND	Digikey	1
Crimp Pin for Housing	WM1114CT-ND	Digikey	2
Spade Connector, 22-26 Gauge	A27415-ND	Digikey	1
22-30 Gauge Wire			
Switch to LED Driver Board Cable			2
2-Pin Locking Connector	A26921-ND	Digikey	1
Crimp Pin for Housing, 22-26 Gauge	A34242-ND	Digikey	2
22-26 Gauge Wire			
Mass Flow Controller to MFC/DAQ Mainboard Cable			4
DB-15 Female IDC	HFM15H-ND	Digikey	1
DB-15 Male IDC	HMM15H-ND	Digikey	1
20-Conductor Ribbon Cable, 5 ft. (Need 6 Inches per Cable, Use Only 15 Conductors)	MC20G-5-ND	Digikey	1
Micro OLED Labels			
Micro OLED Display			4

	Micro OLED-96-G1-GFX Smart 96x64 OLED Display with SD Slot, Serial Connection Type (Runs as Standalone Unit)	Micro OLED-96-G1-GFX	Saelig	1
	Serial to Mini USB Adapter for Micro OLED Display, Micro USB-MB5 Tiny CP2102-based USB to Serial Board	Micro USB-MB5	Saelig	1
	M2 Machine Screw, Flathead 5 mm Long x 0.4 mm Pitch, 90° Head Angle	91420A002	McMaster-Carr	16
	M2 Nut	90695A025	McMaster-Carr	16
	M2 Washer	90097A080	McMaster-Carr	16
Front Switches				
Switch				4
	SPST Flatted Metal Lever Toggle Switch, Rated 6 A at 125VAC, Mounts in 1/4" Hole.	275-634	RadioShack	1
Power				
Power Entry				1
	IEC Appliance Inlet C14 with Filter, Circuit Breaker TA45 (Recessed)	DF12	Schurter	1
	M3 Screws, <= 3.3 Diameter Flathead Machine Screws, 90° Head Angle	91698A306	McMaster-Carr	4
	M3 Nuts	91828A211	McMaster-Carr	4
	Standard IEC Power Cable			
Power Exit				1

	4787 GST PG07: IEC Appliance Outlet F, Screw-on Mounting, Front Side, Solder Terminal	4787	Shurter (http://www.estore.schurter.com/estore/merchant.ihtml?cid=277&step=2)	1
	M3 Screws, <= 3.3 Diameter Flathead Machine Screws, 90° Head Angle	91698A306	McMaster-Carr	4
	M3 Nuts	91828A211	McMaster-Carr	4
Power Supply				1
	Power Supply 90~132VAC, 180~264 VAC Input, 24V@8.33A, 5V@30A DC Outputs, 320 W, 6" L x 4" W x 1.5" H	102-2000-ND	Digikey	1
	8-32 Machine Screws, 0.25" Long Pan Head	91772A190	McMaster-Carr	4
	Rubber Washers, 0.062" Thick	90130A009	McMaster-Carr	4
Data				
Data Acquisition and Control				1
	USB-6008 12-bit Multifunction DAQ	USB-6008 OEM	National Instruments	2
USB Entry				1
	USB B Female to A Female Panel Mount	U09-AF-BF	Trinet USA (Call 909-598-8818, www.trinetusa.com, cablingsys.com, contact wliu@cablingsys.com)	1
	4-40 Flat Machine Screws, Flathead, Length 7/16", 82° Head Angle	91771A109	McMaster-Carr	2
	4-40 Nut	96537A120	McMaster-Carr	2
USB Exit				1

	USB A Female to B Female Panel Mount	U09-AF-BF	Trinet USA (http://www.trinetusa.com/images/spec_sheets/usb/U09-AF-BF.pdf)	1
	4-40 Flat Machine Screws, Flathead, 1.4-1.5" Long	91771A119	McMaster-Carr	2
	4-40 Nut	96537A120	McMaster-Carr	4
	USB A Male to B Male Coupler	U05-AM-BM	Trinet USA (http://www.trinetusa.com/images/spec_sheets/usb/U05-BM-BM.pdf)	1
USB Hub				1
	10-Port USB Hub, Input USB B F, Output 10 USB A F, 5 VDC Power Supply	33189	Dealextreme.com (http://www.dealextreme.com/p/10-port-usb-2-0-hub-with-external-power-source-100-240v-ac-adapter-33189)	1
	8-32 Machine Screw, 0.25" Long Pan Head	91772A190	McMaster-Carr	3
	L-Bracket, With Slotted Bottom Hole	534-4337	Mouser	1
USB Cables				4
	6" USB A to Mini USB B Cable	YYI1-DE4087	Tiger Direct	1
	Long USB A to USB B Cable			
Structures				
MFC Rapid Mount System				4
	6-32 Pan Head Screws, 1/4" Long	90604A144	McMaster-Carr	2
	L-bracket	611K-ND	Digikey	1
	Thumb Screw	90772A384	McMaster-Carr	1
	Washer	90945A716	McMaster-Carr	2
	Rubber Grommet	9311K3	McMaster-Carr	2
Wire Management			Non-Unit Subsystem, Order All Below	
	2X2 Barrier Block	A98514-ND	Digikey	2
	2X3 Barrier Block	A98515-ND	Digikey	1
	8-32 Screws, 7/16" Long	91772A193	McMaster-Carr	12

	Adhesive Back Wire Clip, 0.63" by 0.63"	RP617-ND	Digikey	25
	Adhesive Back Wire Clip, 0.56" by 1"	RP392-ND	Digikey	25
Gas Management				
Mass Flow Controllers				
	Mass Flow Controller, Stainless Steel Body, 24 VDC, 1/4" Compression Connection, 0-5 VDC Input and Output	GFC17S-VADN4-C0A (specify calibration gas, o-ring, and flow range)	Aalborg	4
Solenoid Valves				
	Stackable Solenoid Valves, Stainless Steel Body, 1/8" NPT Connections	Series 3900	Spartan Scientific	8

Appendix C

Select Single-Fiber Tensile Test Data

This appendix provides the complete, unprocessed single-fiber tensile test datasets for select experiments detailed in Chapter 8. Included are tensile test data for:

- **C1.** Unsized HTR-40 Baseline (Table 8.3)
- **C2.** Unsized HTR-40, 730°C in He, 18 min ≥ 480°C (Table 8.3)
- **C3.** Unsized HTR-40, tensioned (12% max Ξ), 730°C in He, 18 min ≥ 480°C (Table 8.3)
- **C4.** K-PSMA/Fe^{3+} on HTR-40, CO_2/C_2H_2 CVD at 480°C (Table 8.4)

C1. Unsized HTR-40 Baseline

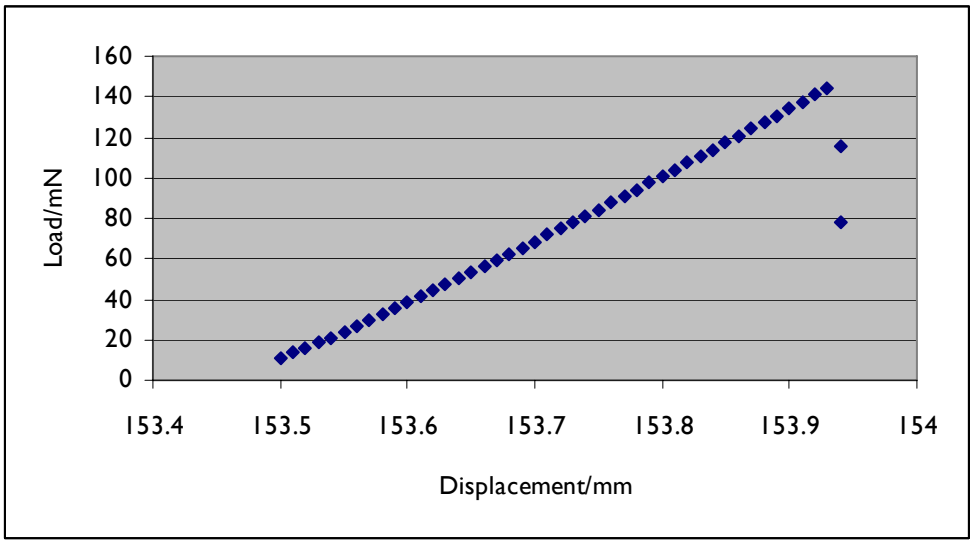

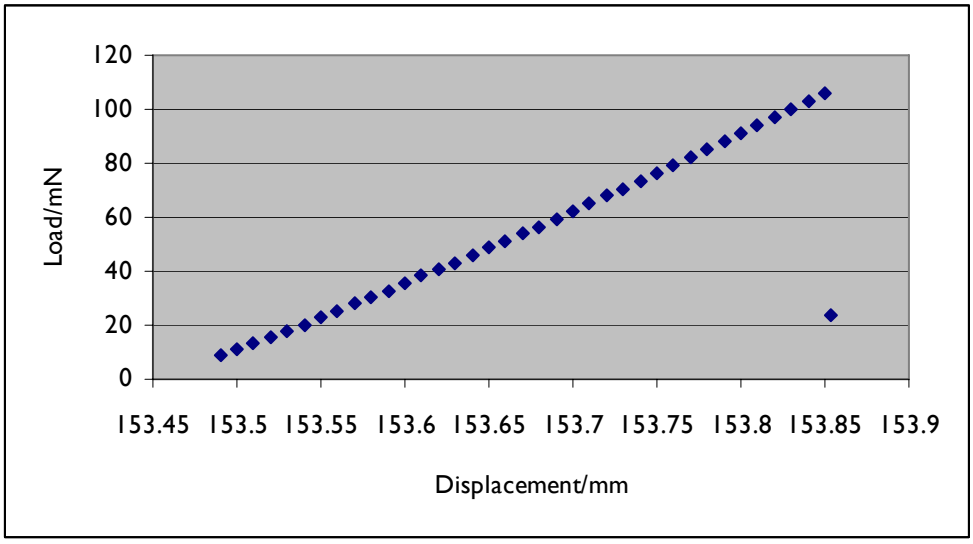

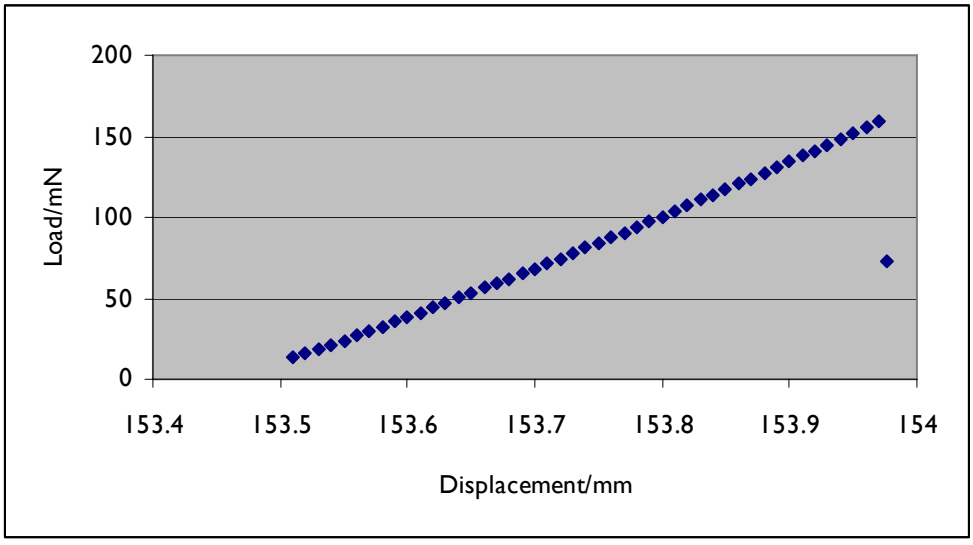

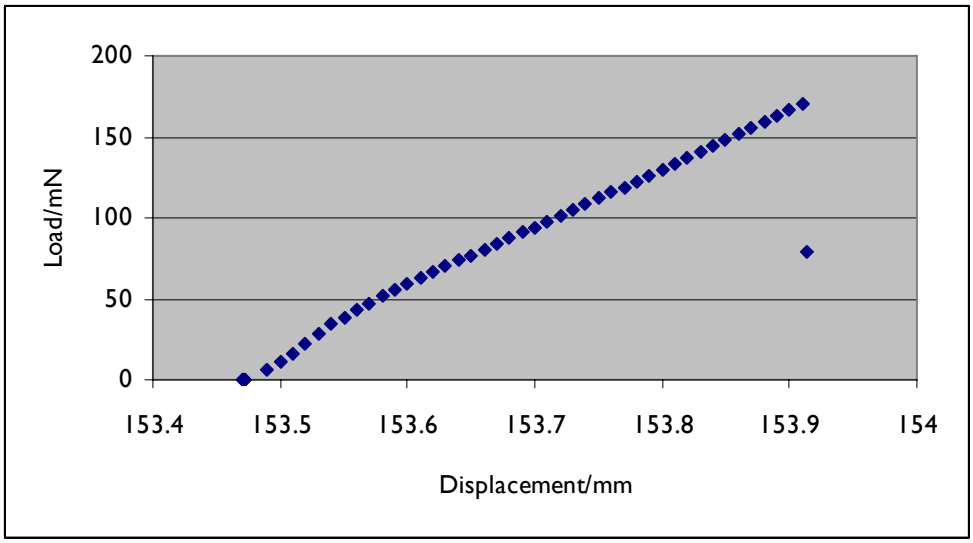
200
150
100
50
0
Load/mN
153.4
153.5
153.6
153.7
153.8
153.9
154
Displacement/mm

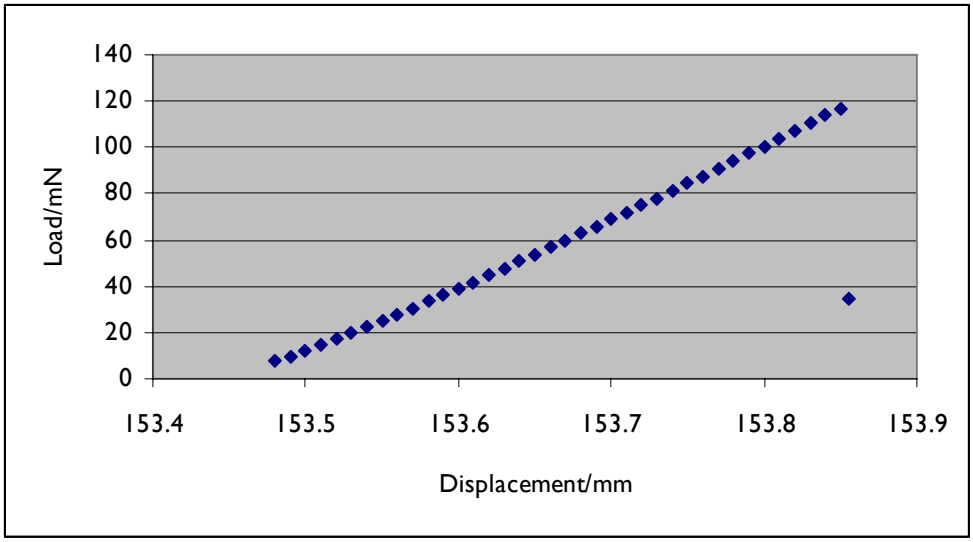
140
120
100
80
60
40
20
0
Load/mN
153.4
153.5
153.6
153.7
153.8
153.9
Displacement/mm

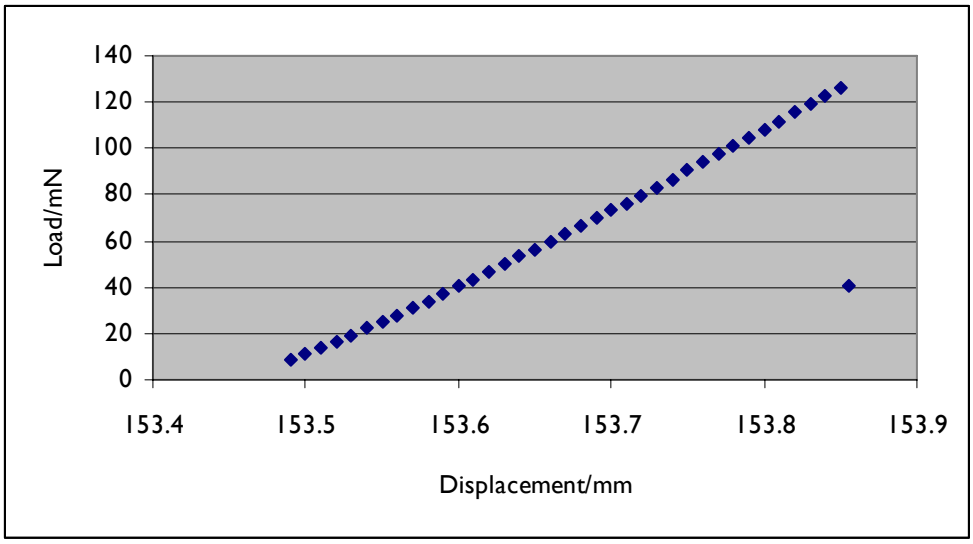
140
120
100
80
60
40
20
0
Load/mN
153.4
153.5
153.6
153.7
153.8
153.9
Displacement/mm

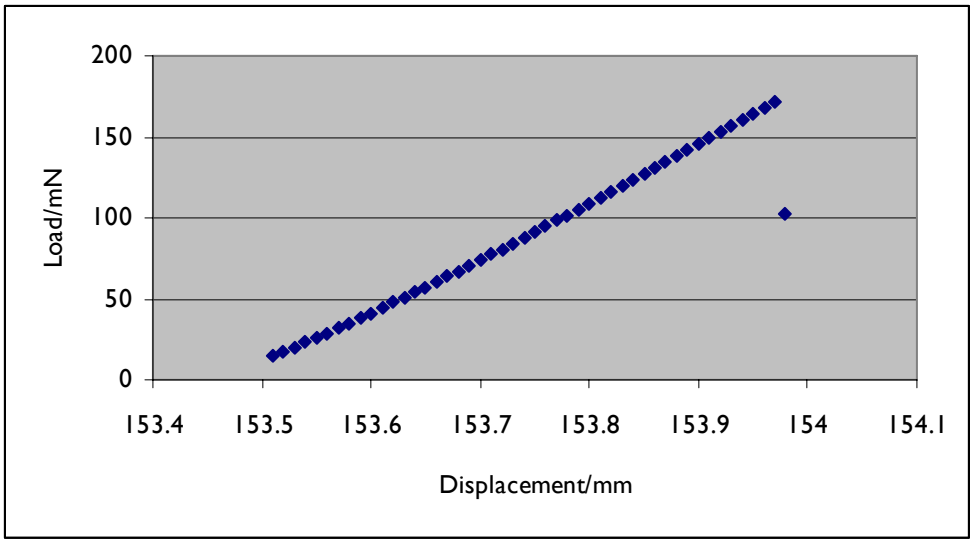
200
150
100
50
0
Load/mN
153.4
153.5
153.6
153.7
153.8
153.9
154
154.1
Displacement/mm

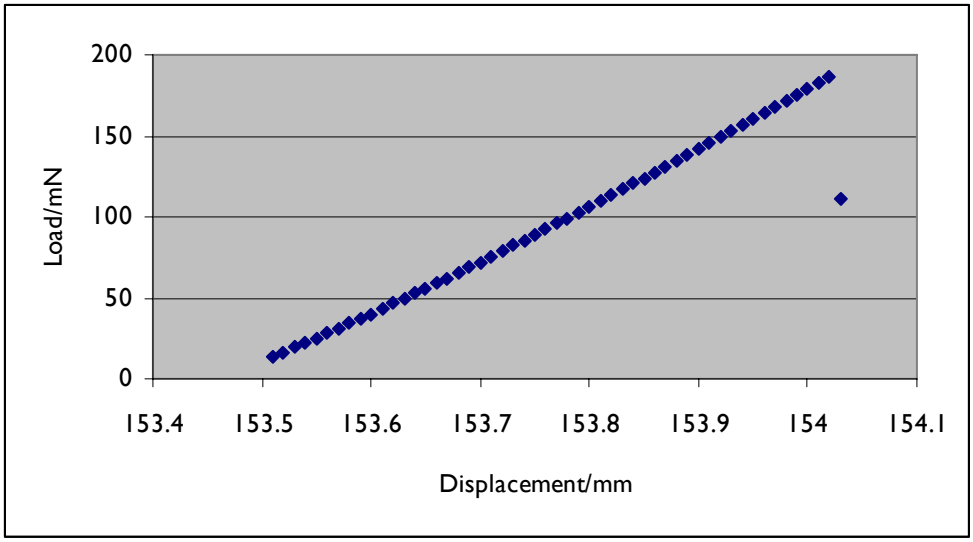
200
150
100
50
0
Load/mN
153.4
153.5
153.6
153.7
153.8
153.9
154
154.1
Displacement/mm

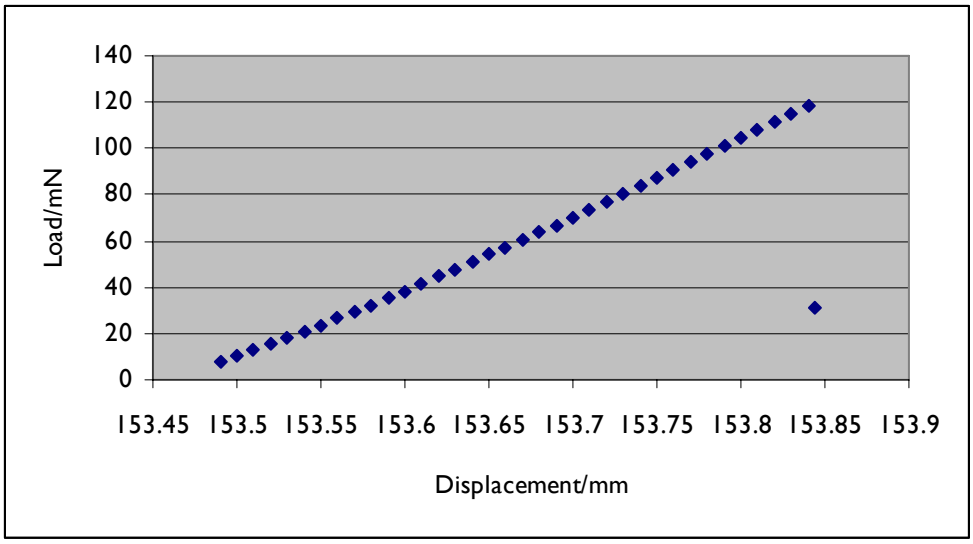
140
120
100
80
60
40
20
0
Load/mN
153.45
153.5
153.55
153.6
153.65
153.7
153.75
153.8
153.85
153.9
Displacement/mm

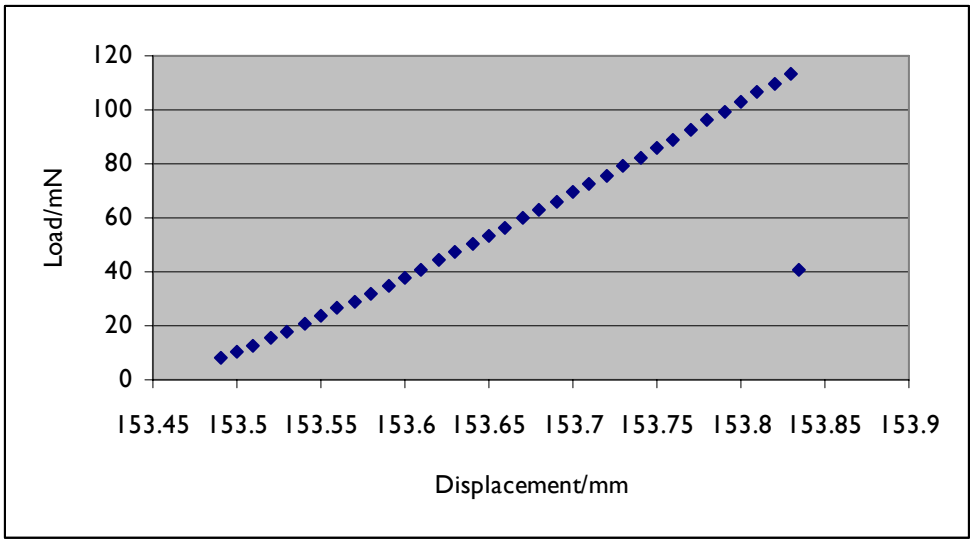
120
100
80
60
40
20
0
Load/mN
153.45
153.5
153.55
153.6
153.65
153.7
153.75
153.8
153.85
153.9
Displacement/mm

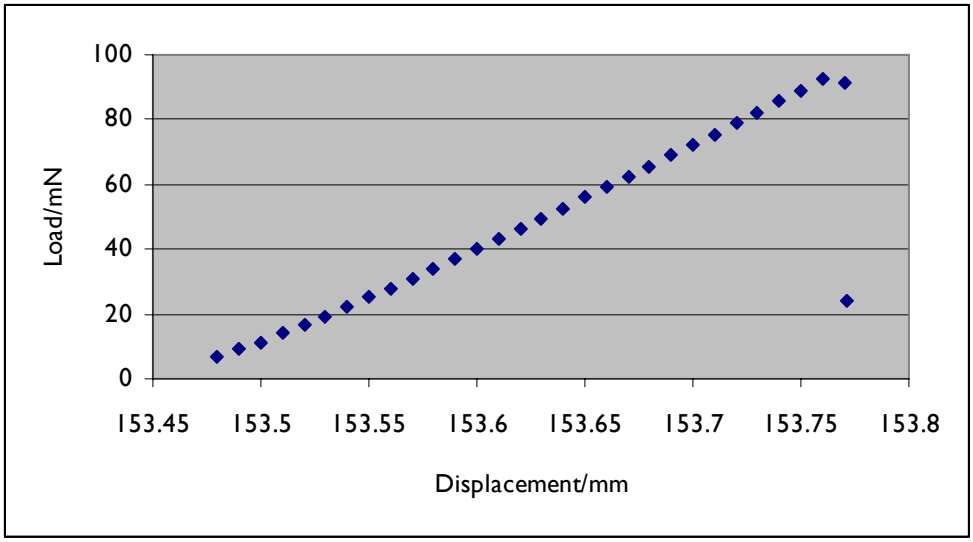
100
80
60
40
20
0
Load/mN
153.45
153.5
153.55
153.6
153.65
153.7
153.75
153.8
Displacement/mm

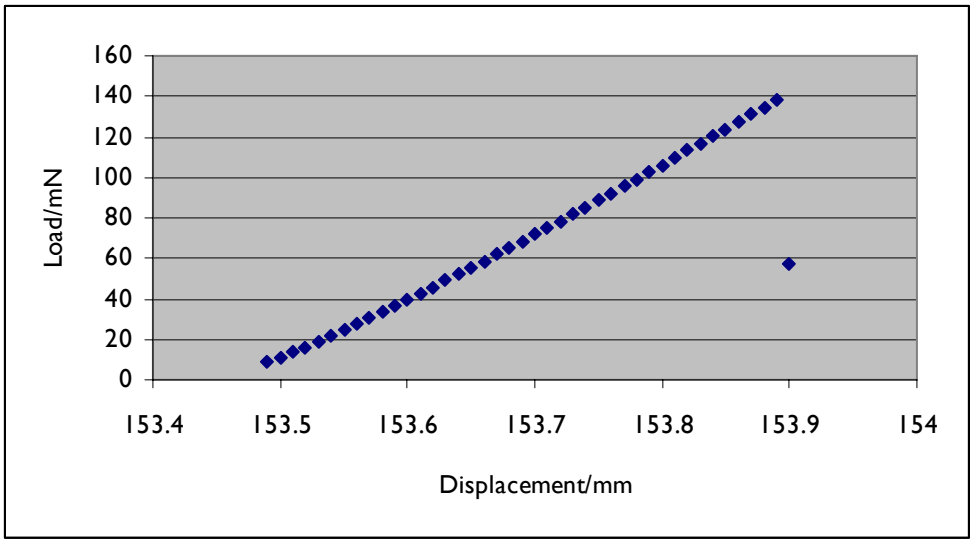
160
140
120
100
80
60
40
20
0
Load/mN
153.4
153.5
153.6
153.7
153.8
153.9
154
Displacement/mm

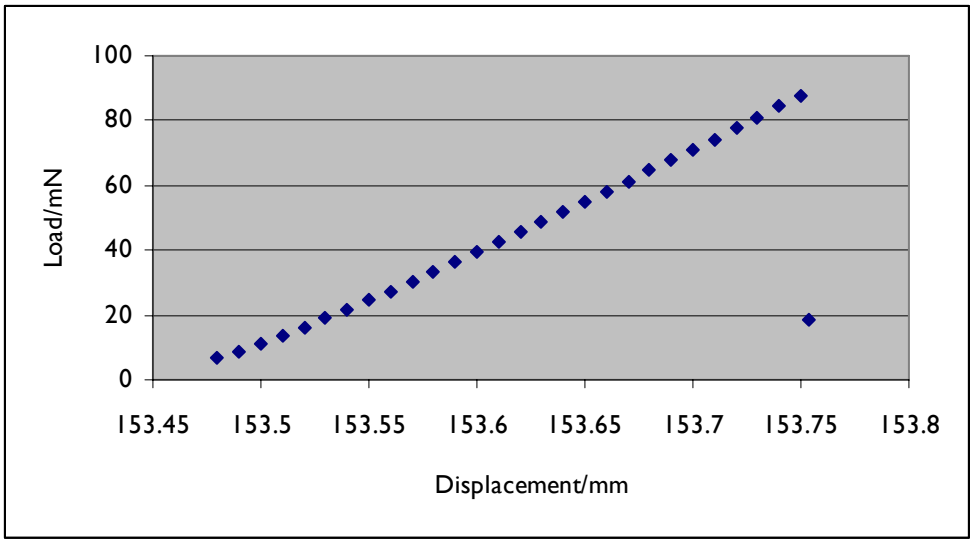
100
80
60
40
20
0
Load/mN
153.45
153.5
153.55
153.6
153.65
153.7
153.75
153.8
Displacement/mm

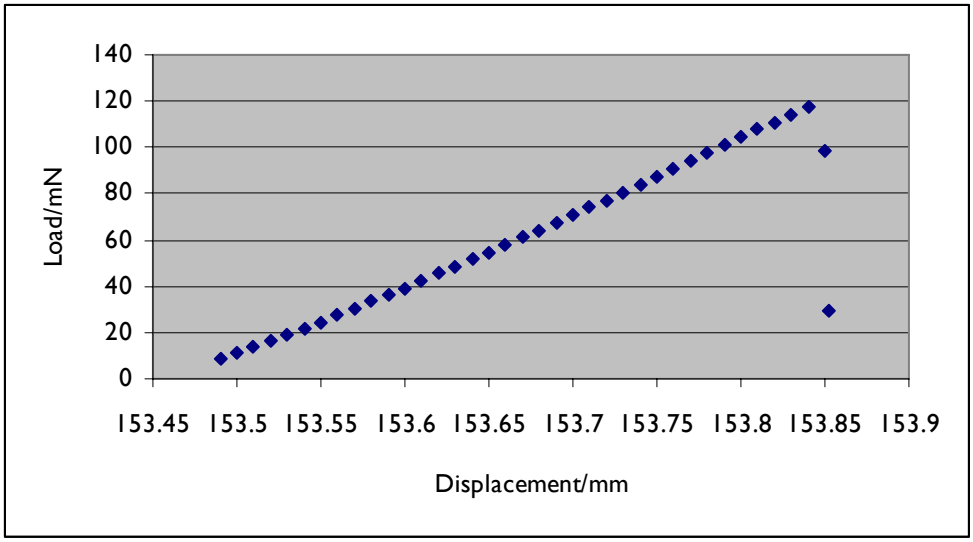
140
120
100
80
60
40
20
0
Load/mN
153.45
153.5
153.55
153.6
153.65
153.7
153.75
153.8
153.85
153.9
Displacement/mm

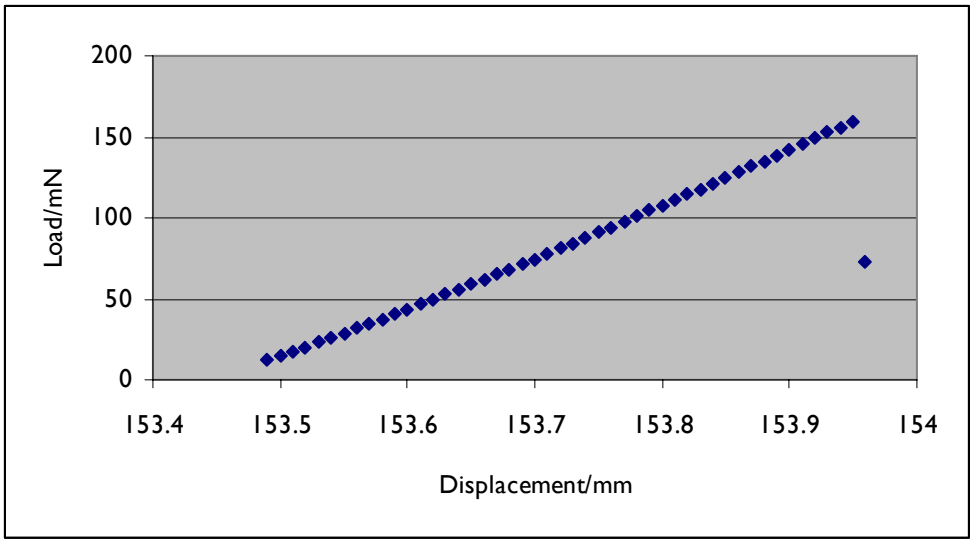
200
150
100
50
0
Load/mN
153.4
153.5
153.6
153.7
153.8
153.9
154
Displacement/mm

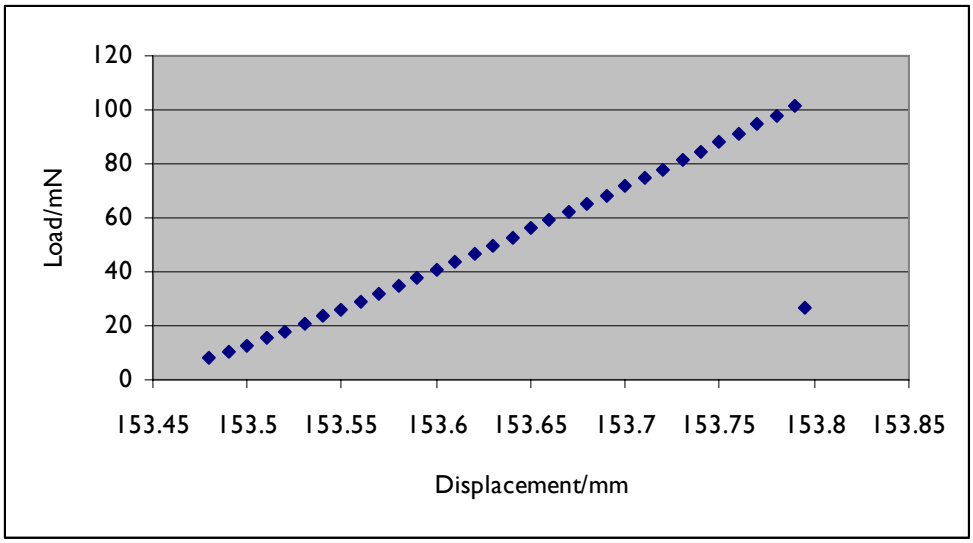
120
100
80
60
40
20
0
Load/mN
153.45
153.5
153.55
153.6
153.65
153.7
153.75
153.8
153.85
Displacement/mm

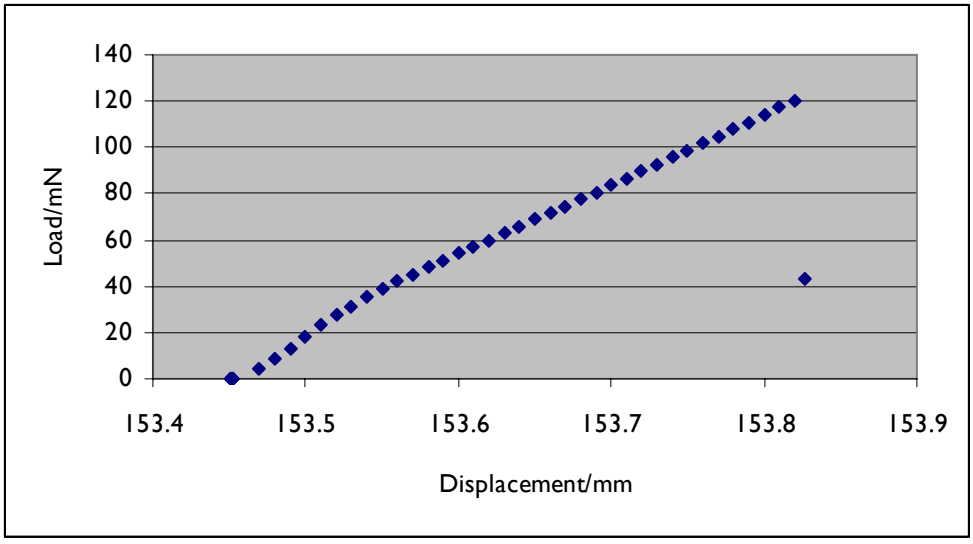
140
120
100
80
60
40
20
0
Load/mN
153.4
153.5
153.6
153.7
153.8
153.9
Displacement/mm

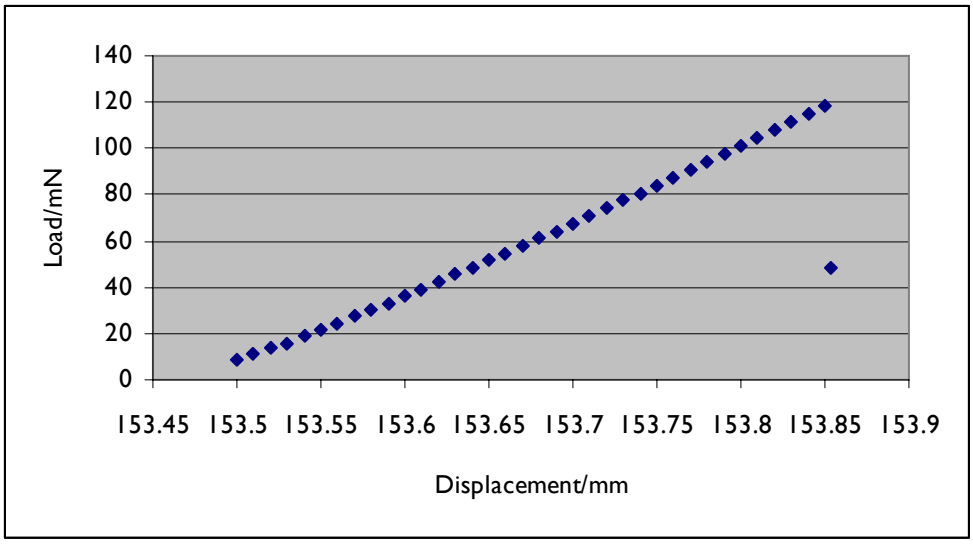
140
120
100
80
60
40
20
0
Load/mN
153.45
153.5
153.55
153.6
153.65
153.7
153.75
153.8
153.85
153.9
Displacement/mm

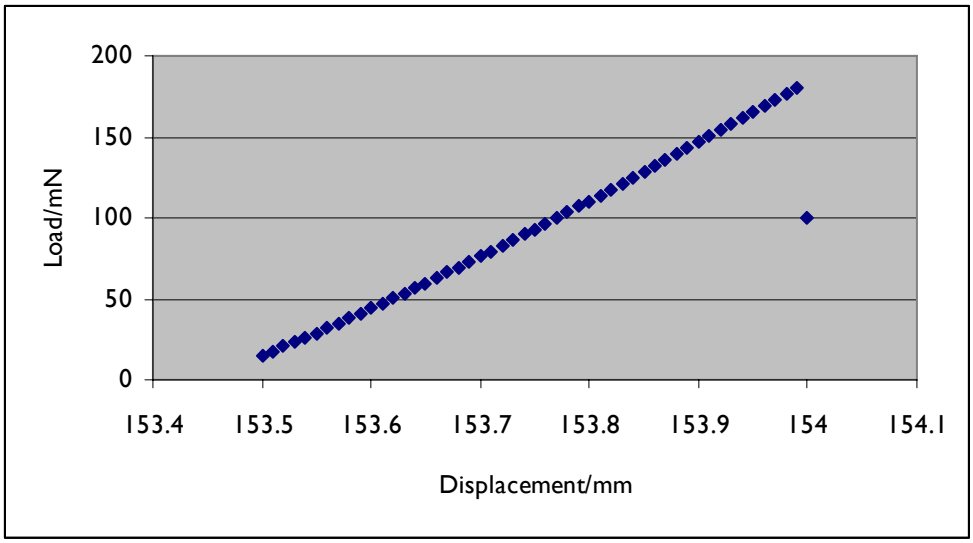

C2. Unsized HTR-40, 730°C in He, 18 min ≥ 480°C

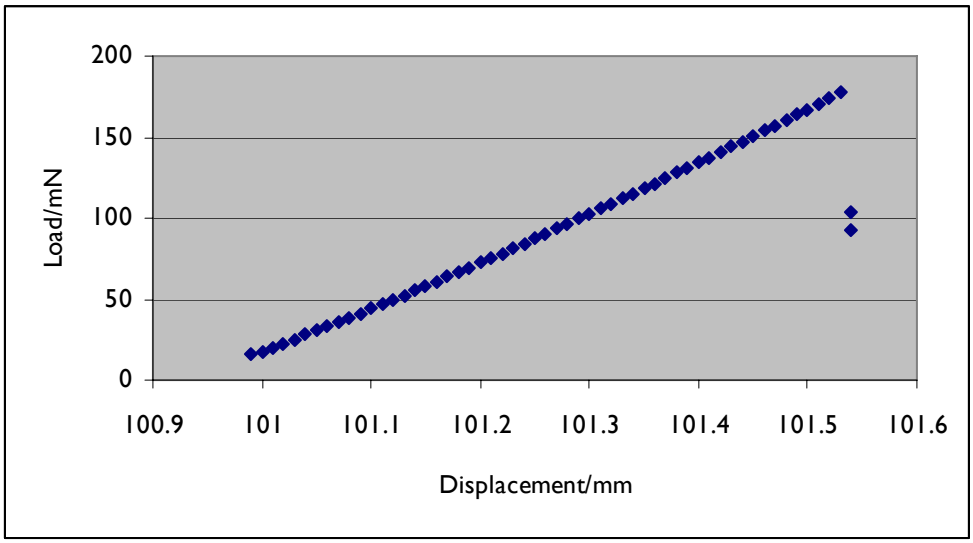

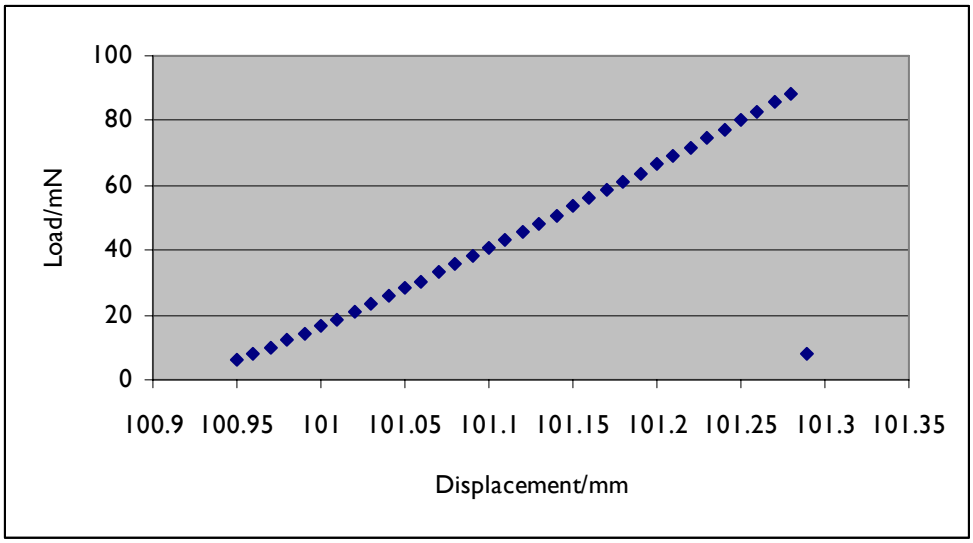
100
80
60
40
20
0
Load/mN
100.9
100.95
101
101.05
101.1
101.15
101.2
101.25
101.3
101.35
Displacement/mm

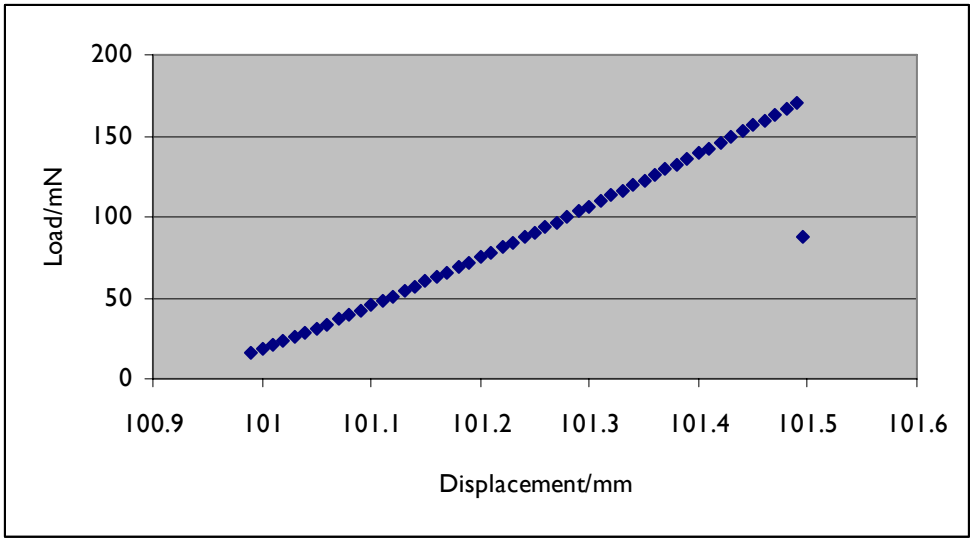
200
150
100
50
0
Load/mN
100.9
101
101.1
101.2
101.3
101.4
101.5
101.6
Displacement/mm

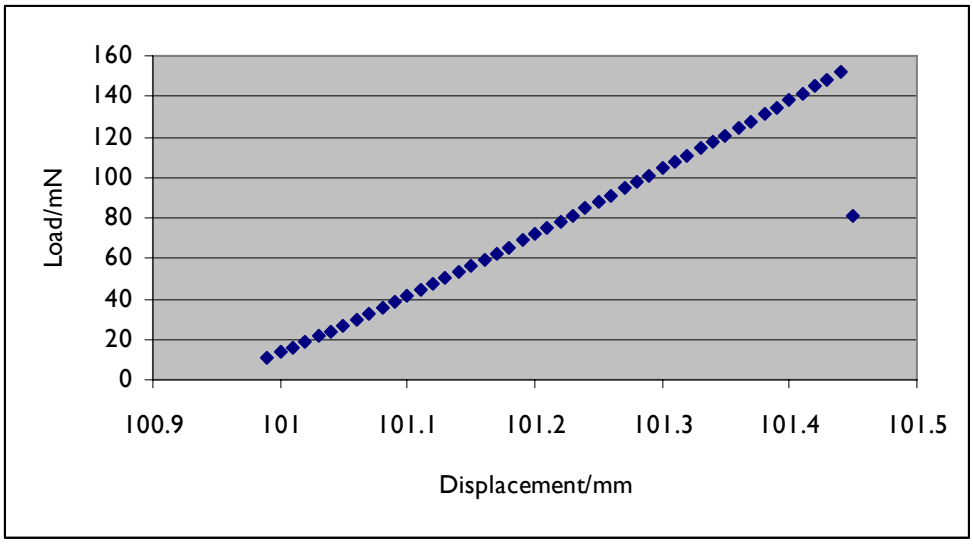
160
140
120
100
80
60
40
20
0
Load/mN
100.9
101
101.1
101.2
101.3
101.4
101.5
Displacement/mm

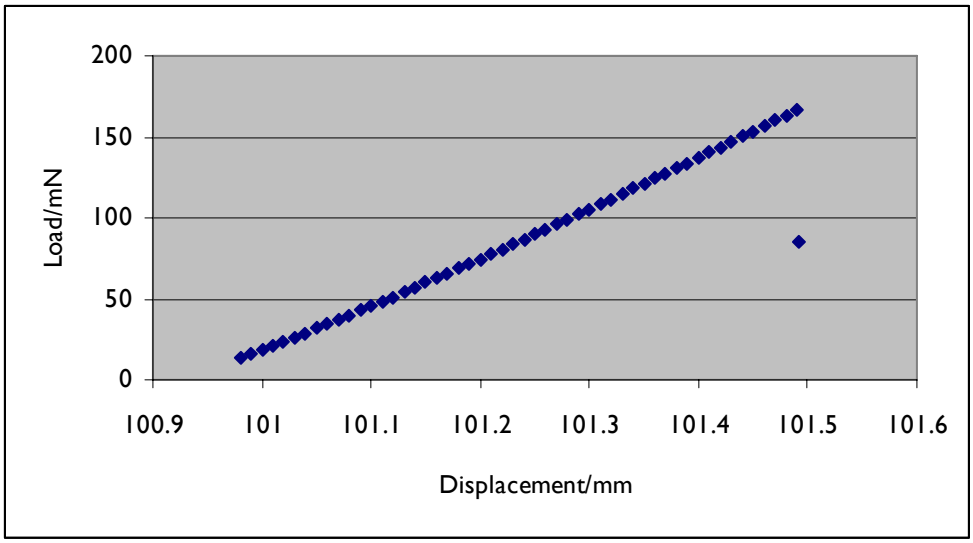
200
150
100
50
0
Load/mN
100.9
101
101.1
101.2
101.3
101.4
101.5
101.6
Displacement/mm

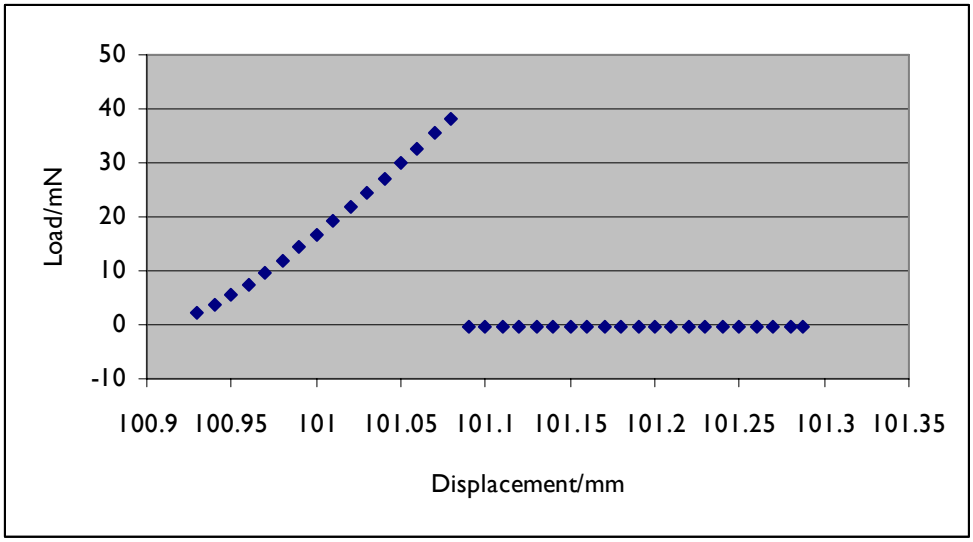
50
40
30
20
10
0
-10
Load/mN
100.9
100.95
101
101.05
101.1
101.15
101.2
101.25
101.3
101.35
Displacement/mm

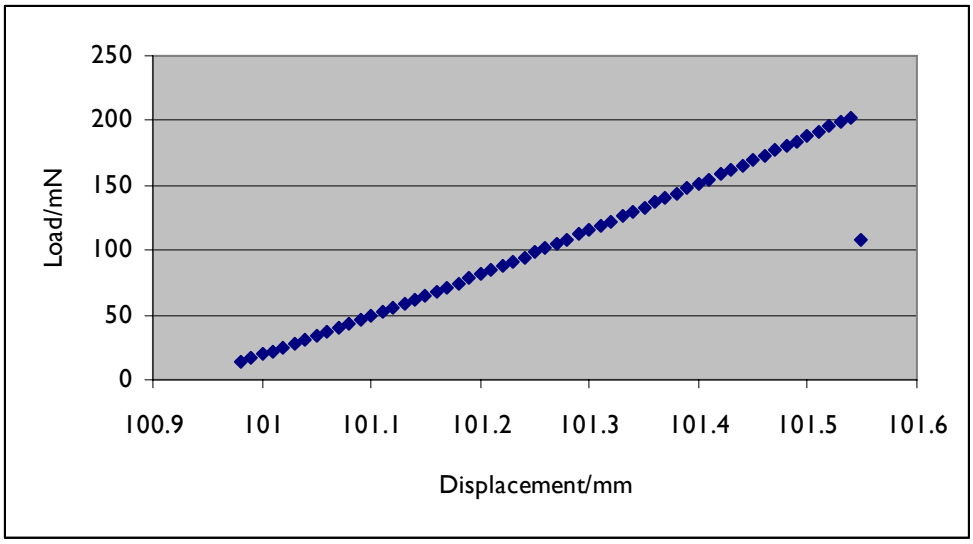
250
200
150
100
50
0
Load/mN
100.9
101
101.1
101.2
101.3
101.4
101.5
101.6
Displacement/mm

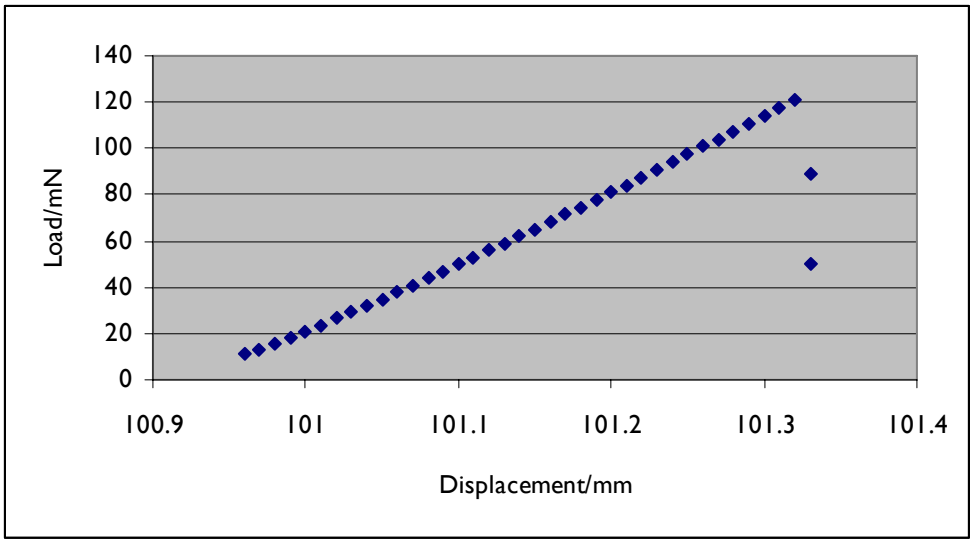
140
120
100
80
60
40
20
0
Load/mN
100.9
101
101.1
101.2
101.3
101.4
Displacement/mm

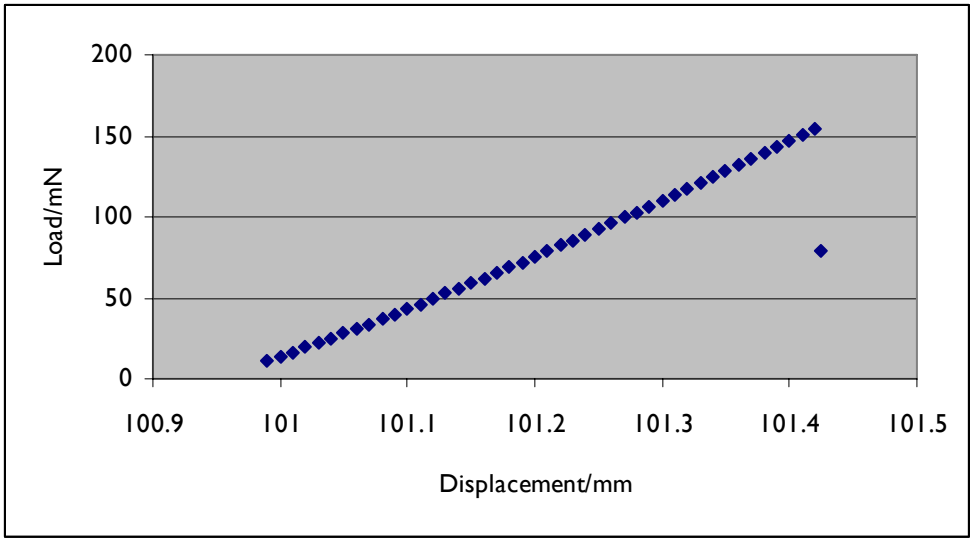
200
150
100
50
0
Load/mN
100.9
101
101.1
101.2
101.3
101.4
101.5
Displacement/mm

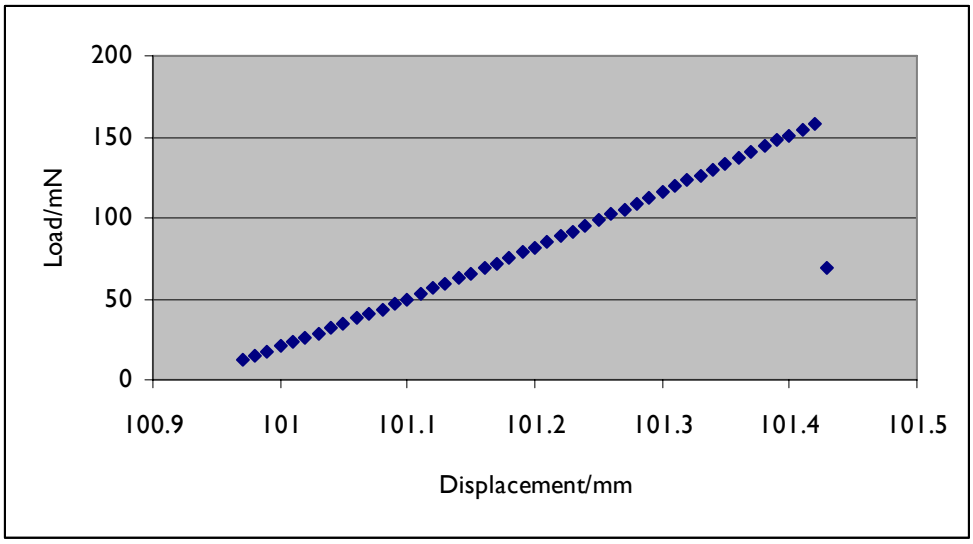
200
150
100
50
0
Load/mN
100.9
101
101.1
101.2
101.3
101.4
101.5
Displacement/mm

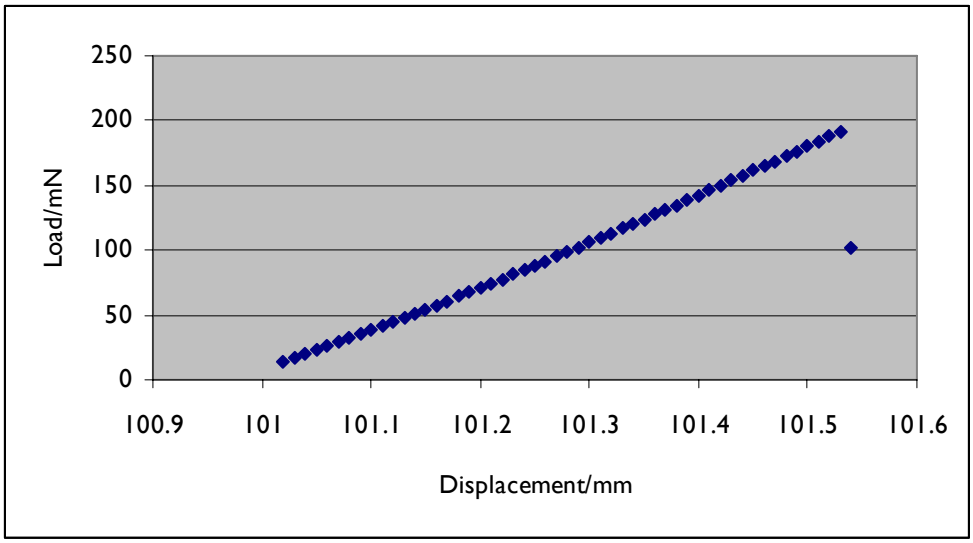
250
200
150
100
50
0
Load/mN
100.9
101
101.1
101.2
101.3
101.4
101.5
101.6
Displacement/mm

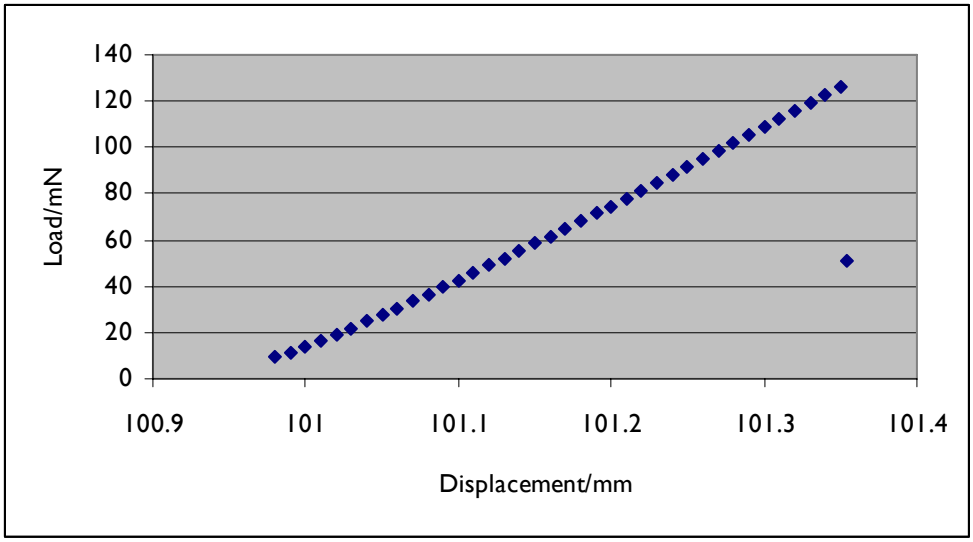
140
120
100
80
60
40
20
0
Load/mN
100.9
101
101.1
101.2
101.3
101.4
Displacement/mm

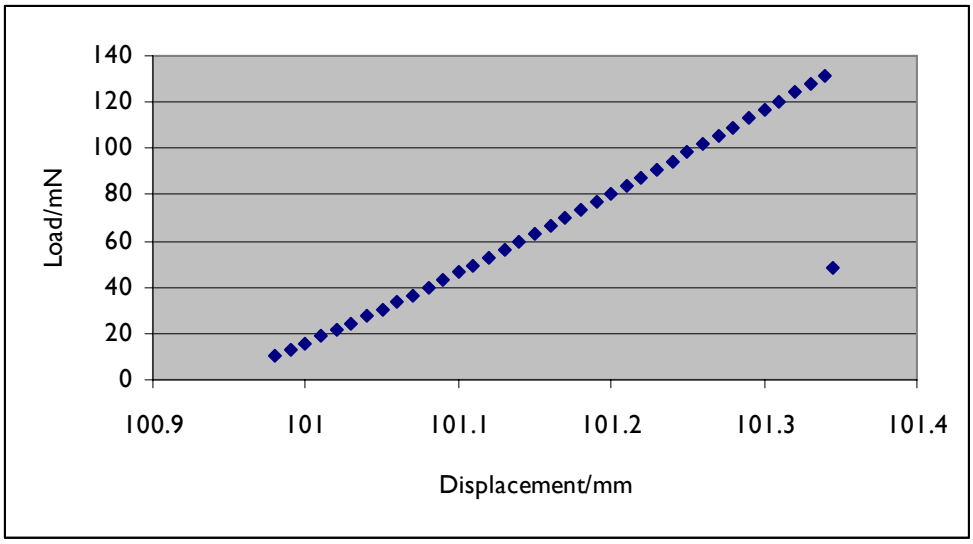
140
120
100
80
60
40
20
0
Load/mN
100.9
101
101.1
101.2
101.3
101.4
Displacement/mm

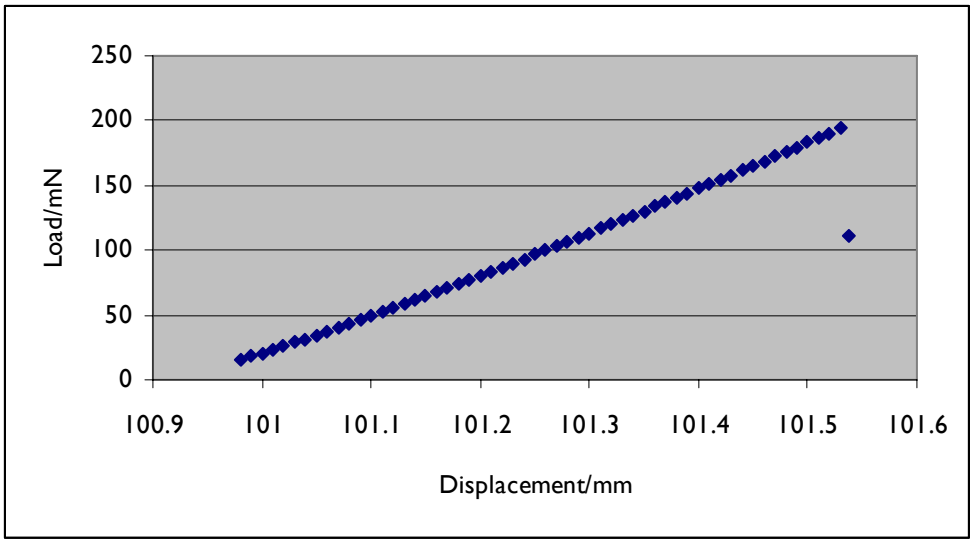
250
200
150
100
50
0
Load/mN
100.9
101
101.1
101.2
101.3
101.4
101.5
101.6
Displacement/mm

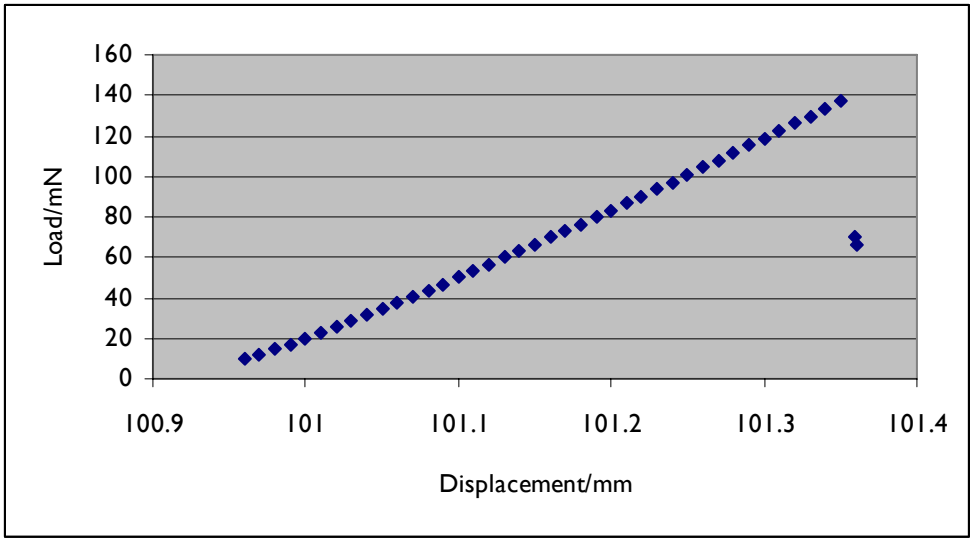
160
140
120
100
80
60
40
20
0
Load/mN
100.9
101
101.1
101.2
101.3
101.4
Displacement/mm

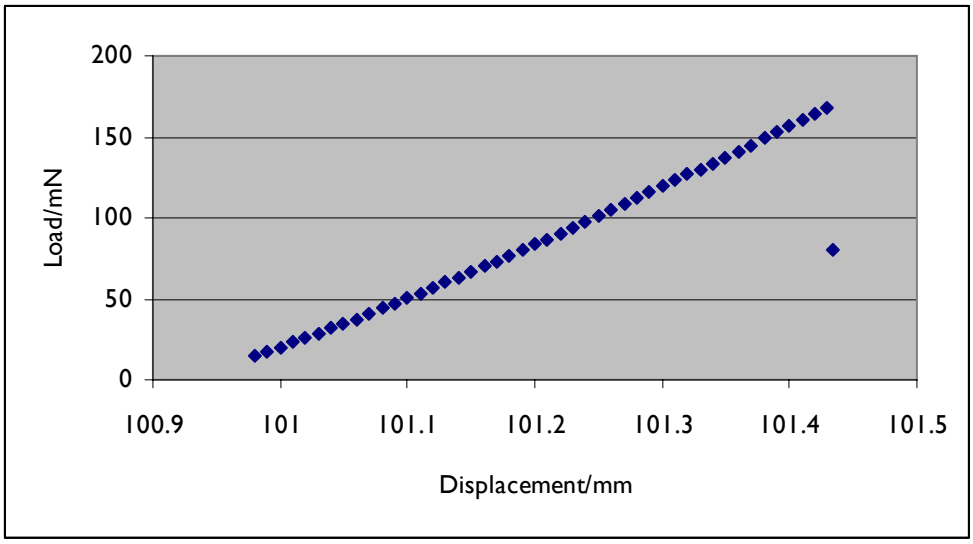
200
150
100
50
0
Load/mN
100.9
101
101.1
101.2
101.3
101.4
101.5
Displacement/mm

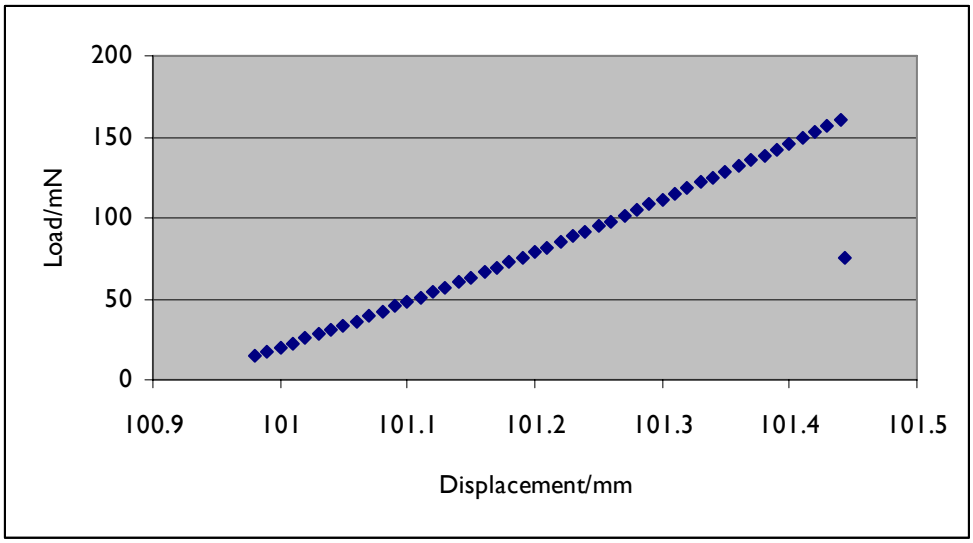
200
150
100
50
0
Load/mN
100.9
101
101.1
101.2
101.3
101.4
101.5
Displacement/mm

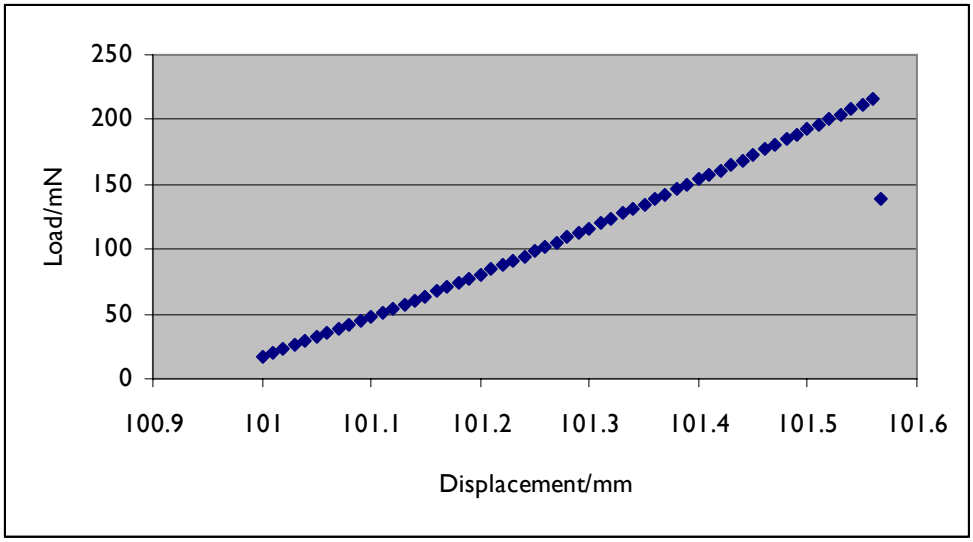
250
200
150
100
50
0
Load/mN
100.9
101
101.1
101.2
101.3
101.4
101.5
101.6
Displacement/mm

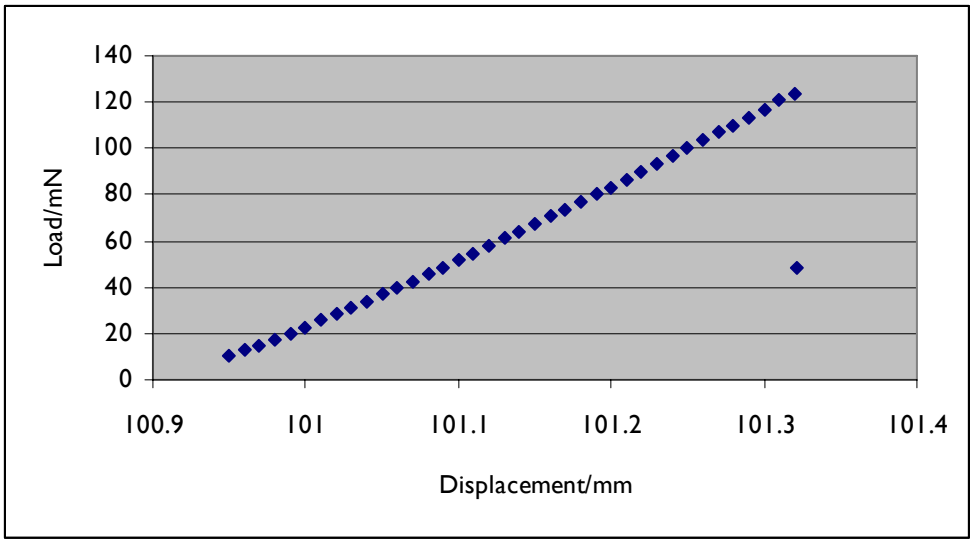
140
120
100
80
60
40
20
0
Load/mN
100.9
101
101.1
101.2
101.3
101.4
Displacement/mm

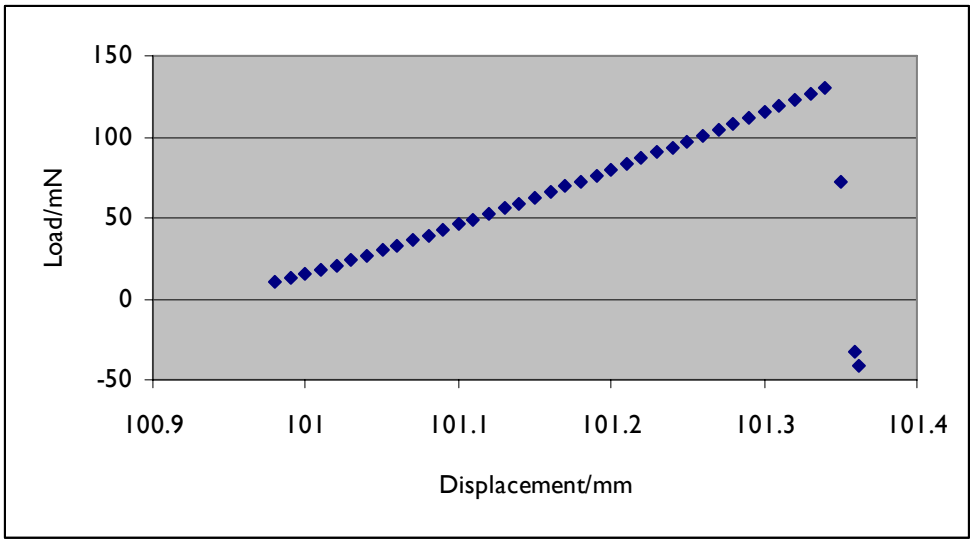

C3. Unsized HTR-40, tensioned (12% max Ξ),730°C in He, 18 min ≥ 480°C

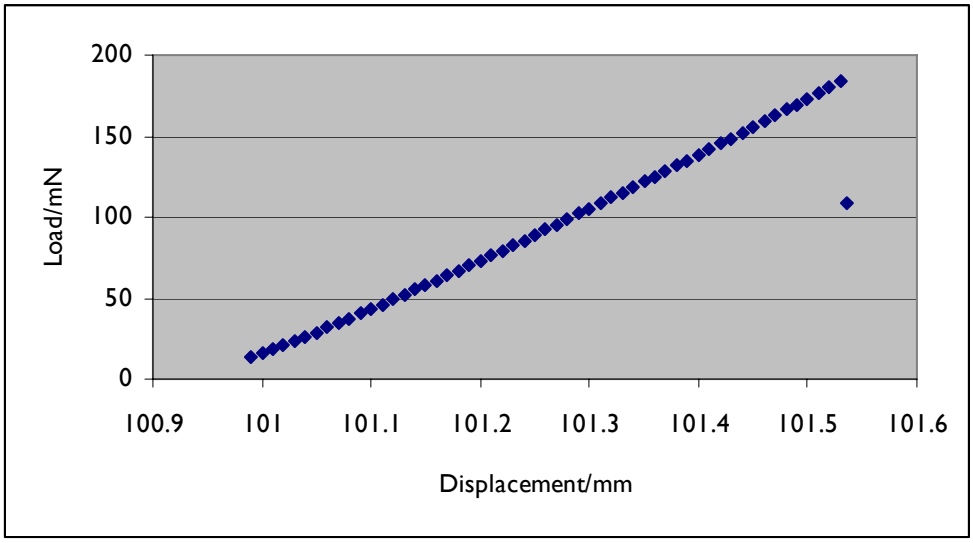

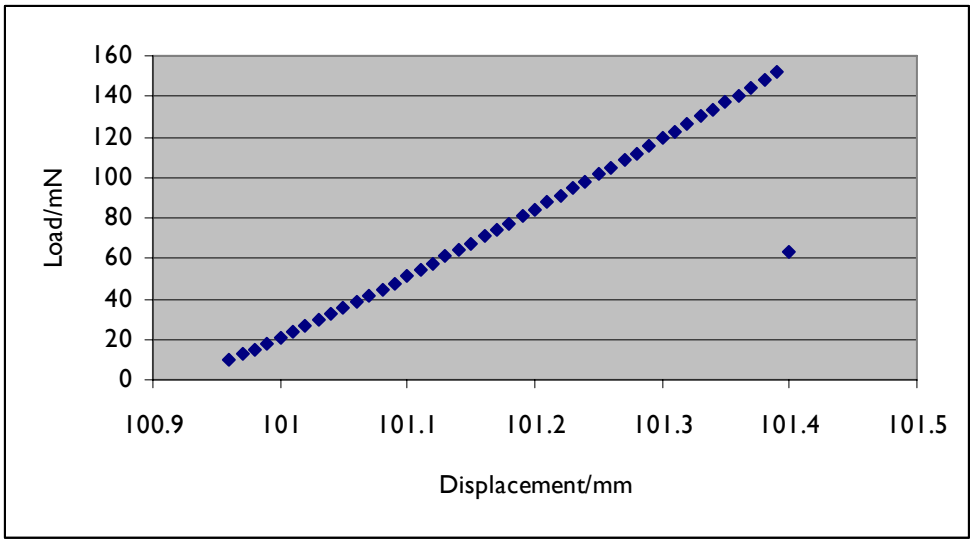
160
140
120
100
80
60
40
20
0
Load/mN
100.9
101
101.1
101.2
101.3
101.4
101.5
Displacement/mm

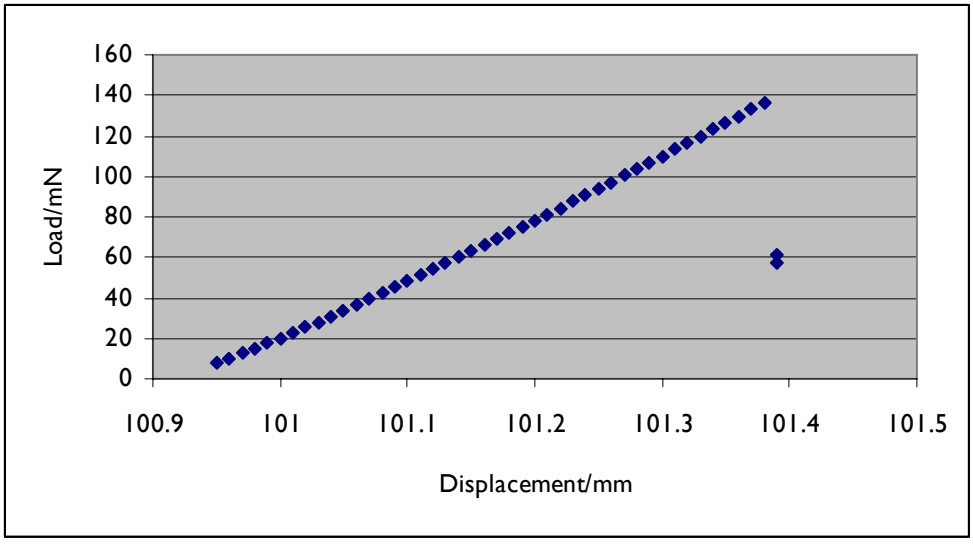
160
140
120
100
80
60
40
20
0
Load/mN
100.9
101
101.1
101.2
101.3
101.4
101.5
Displacement/mm

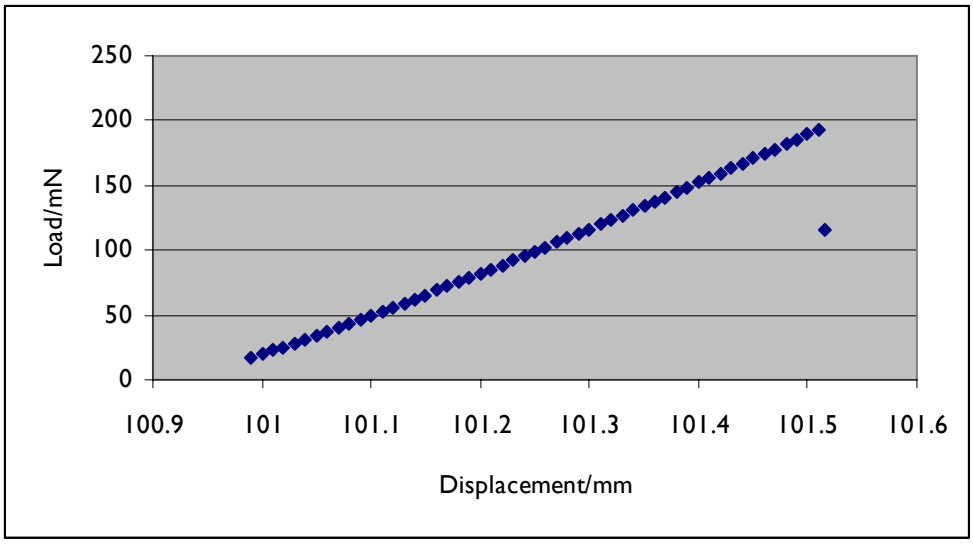
250
200
150
100
50
0
Load/mN
100.9
101
101.1
101.2
101.3
101.4
101.5
101.6
Displacement/mm

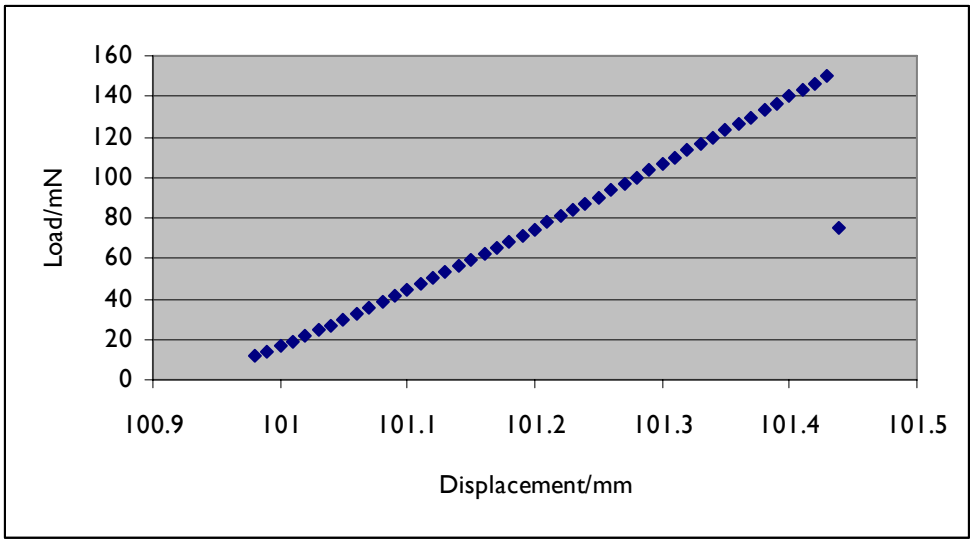
160
140
120
100
80
60
40
20
0
Load/mN
100.9
101
101.1
101.2
101.3
101.4
101.5
Displacement/mm

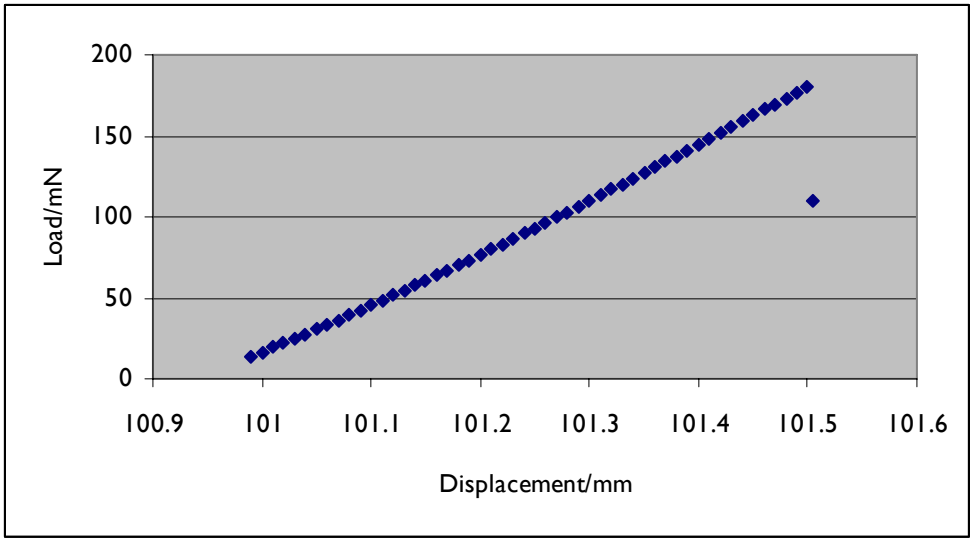
200
150
100
50
0
Load/mN
100.9
101
101.1
101.2
101.3
101.4
101.5
101.6
Displacement/mm

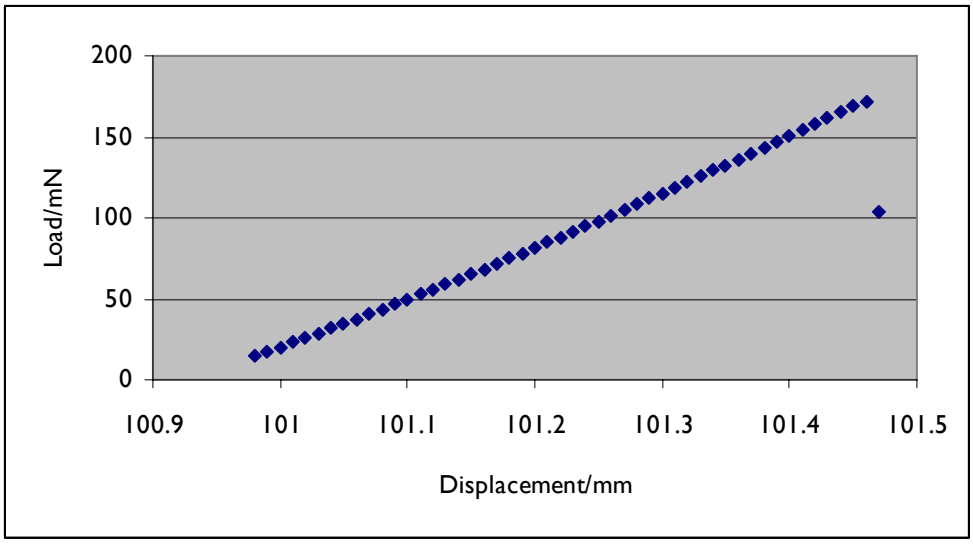
200
150
100
50
0
Load/mN
100.9
101
101.1
101.2
101.3
101.4
101.5
Displacement/mm

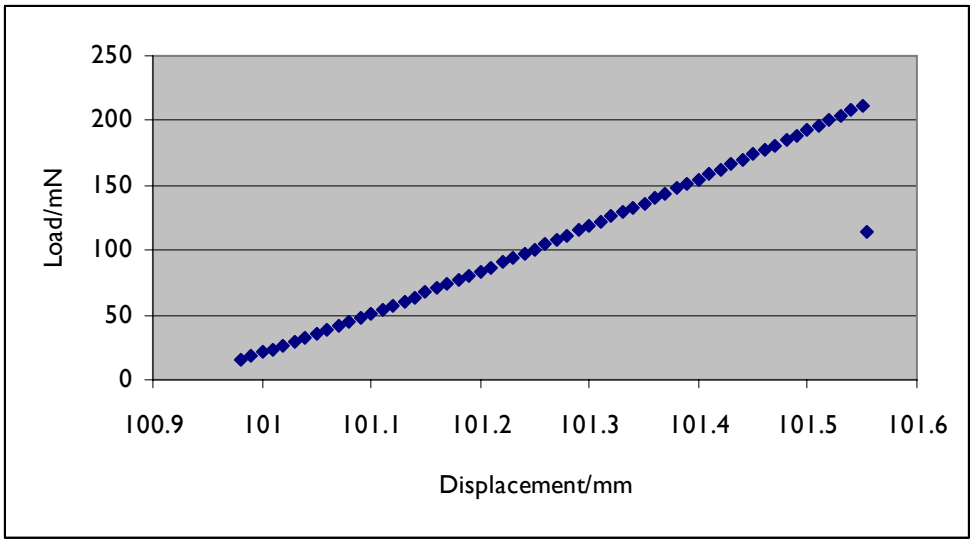
250
200
150
100
50
0
Load/mN
100.9
101
101.1
101.2
101.3
101.4
101.5
101.6
Displacement/mm

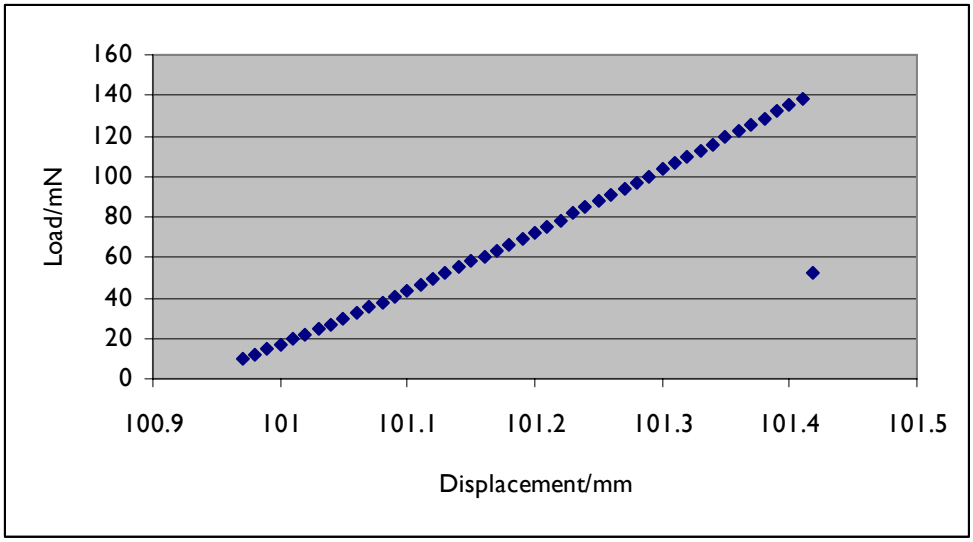
160
140
120
100
80
60
40
20
0
Load/mN
100.9
101
101.1
101.2
101.3
101.4
101.5
Displacement/mm

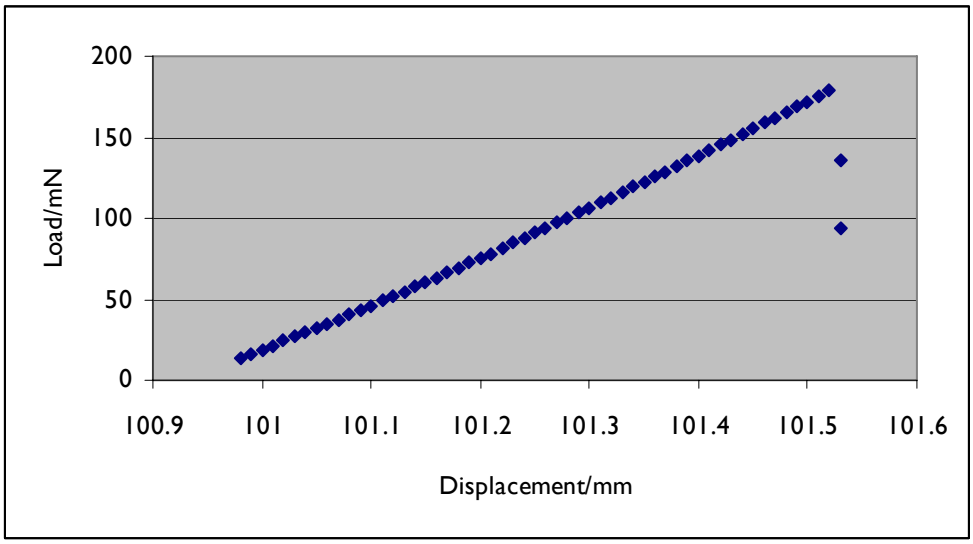
200
150
100
50
0
Load/mN
100.9
101
101.1
101.2
101.3
101.4
101.5
101.6
Displacement/mm

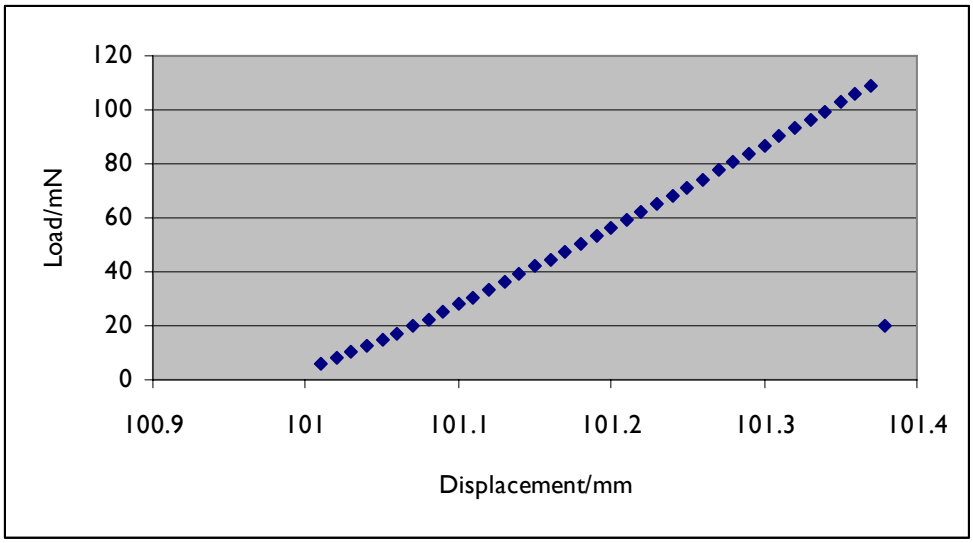
120
100
80
60
40
20
0
Load/mN
100.9
101
101.1
101.2
101.3
101.4
Displacement/mm

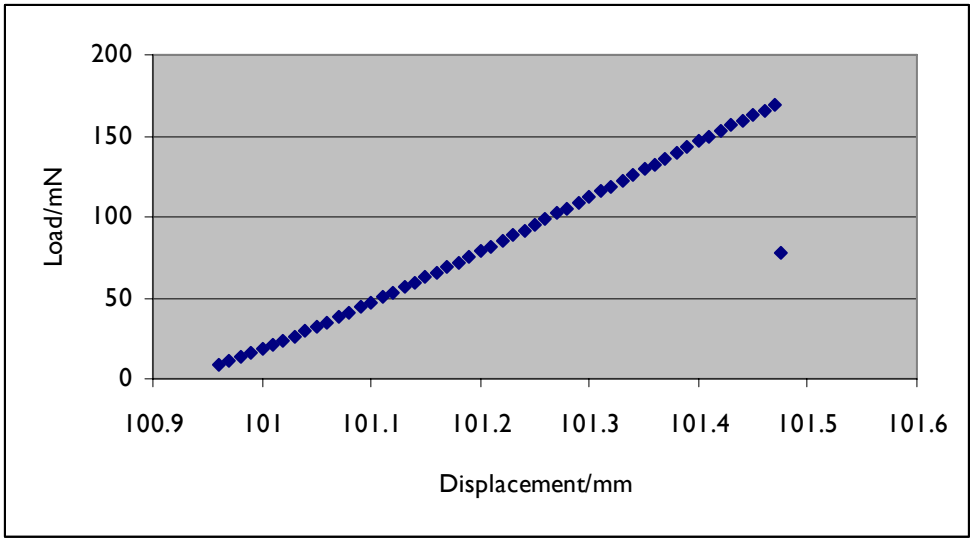
200
150
100
50
0
Load/mN
100.9
101
101.1
101.2
101.3
101.4
101.5
101.6
Displacement/mm

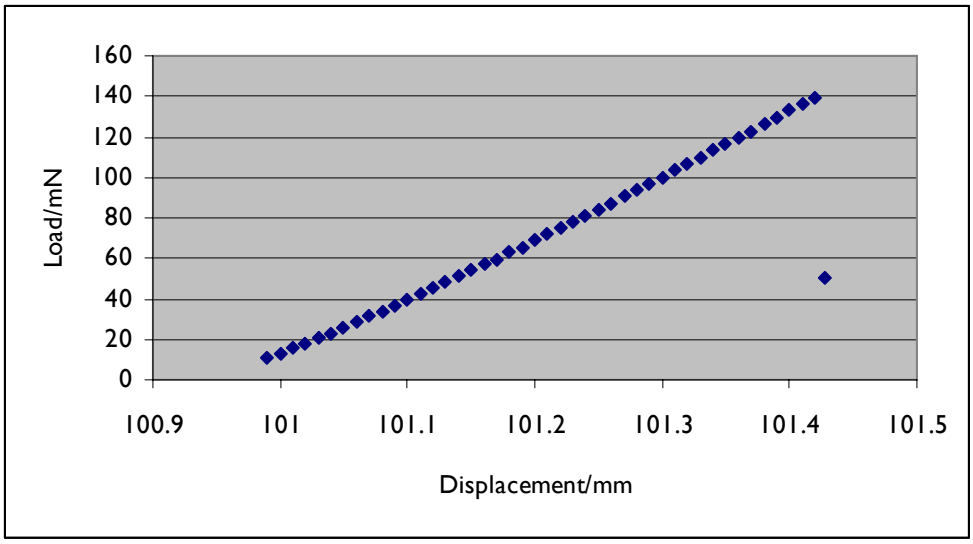
160
140
120
100
80
60
40
20
0
Load/mN
100.9
101
101.1
101.2
101.3
101.4
101.5
Displacement/mm

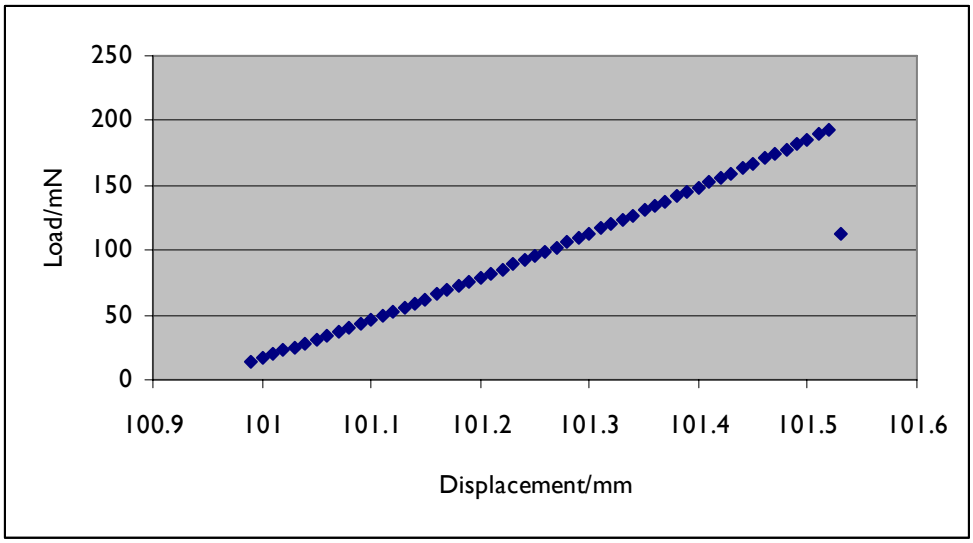
250
200
150
100
50
0
Load/mN
100.9
101
101.1
101.2
101.3
101.4
101.5
101.6
Displacement/mm

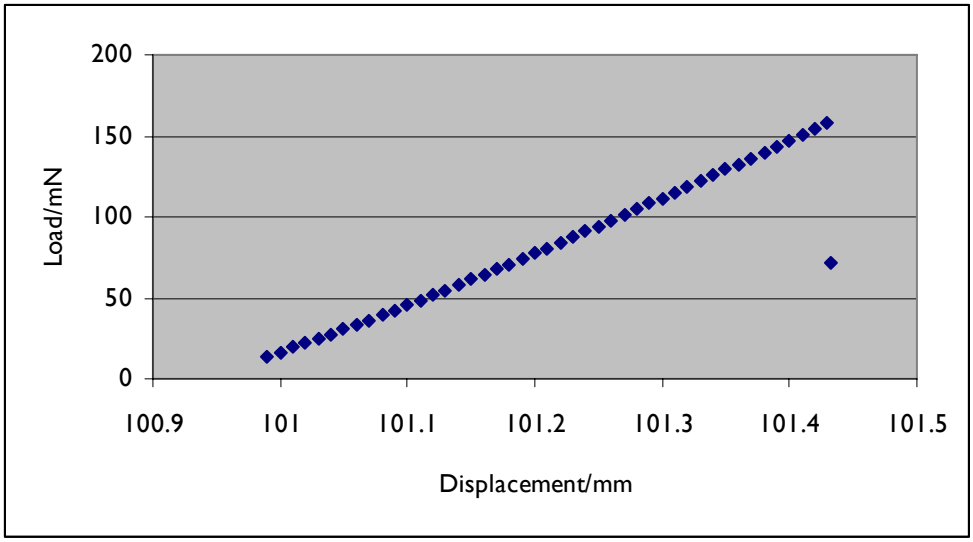
200
150
100
50
0
Load/mN
100.9
101
101.1
101.2
101.3
101.4
101.5
Displacement/mm

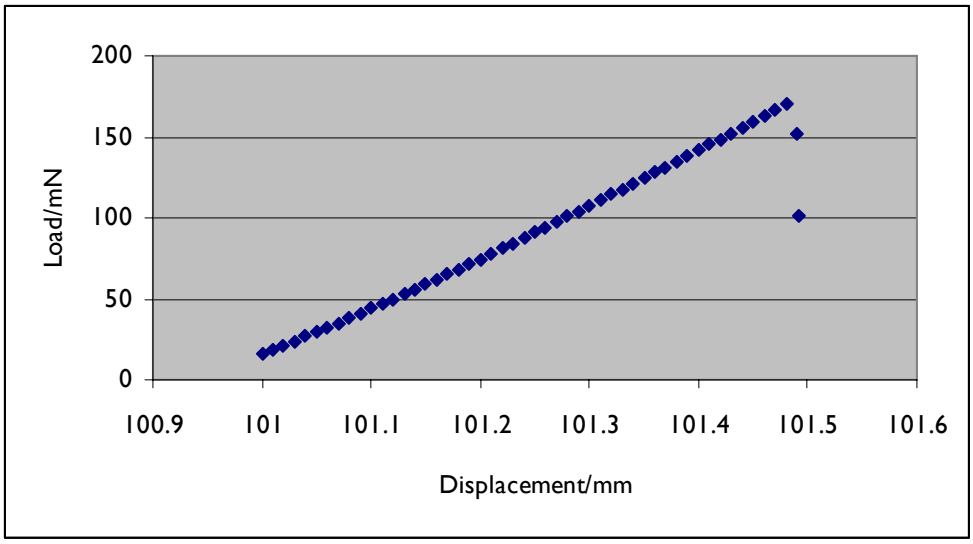
200
150
100
50
0
Load/mN
100.9
101
101.1
101.2
101.3
101.4
101.5
101.6
Displacement/mm

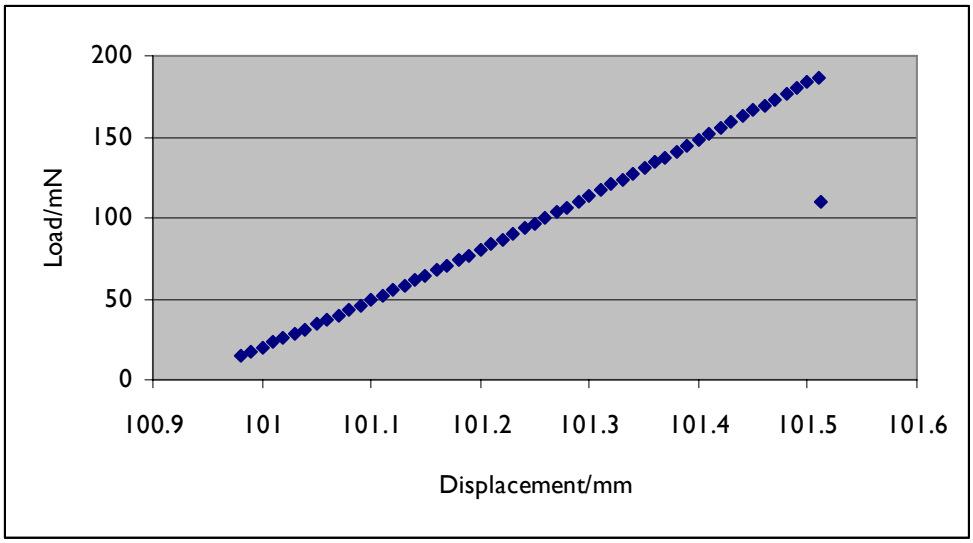
200
150
100
50
0
Load/mN
100.9
101
101.1
101.2
101.3
101.4
101.5
101.6
Displacement/mm

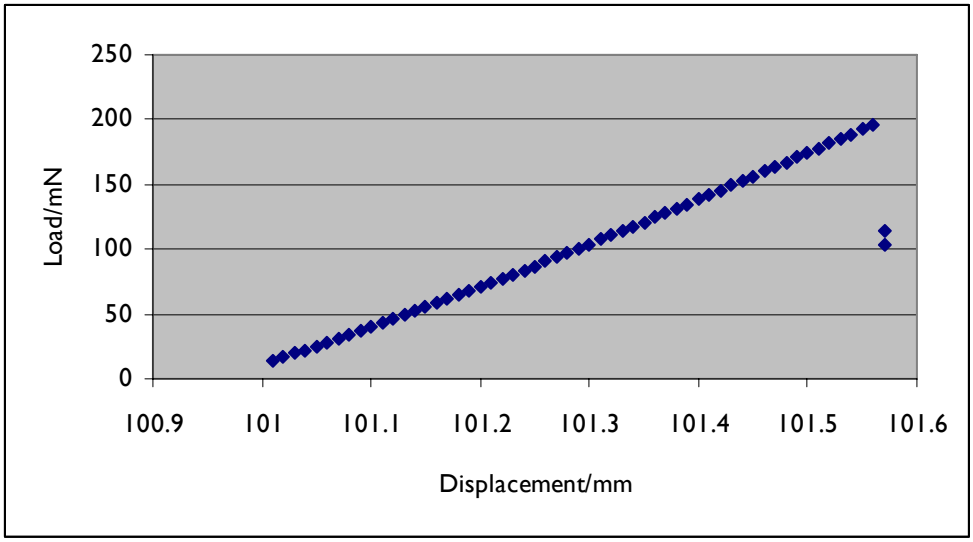
250
200
150
100
50
0
Load/mN
100.9
101
101.1
101.2
101.3
101.4
101.5
101.6
Displacement/mm

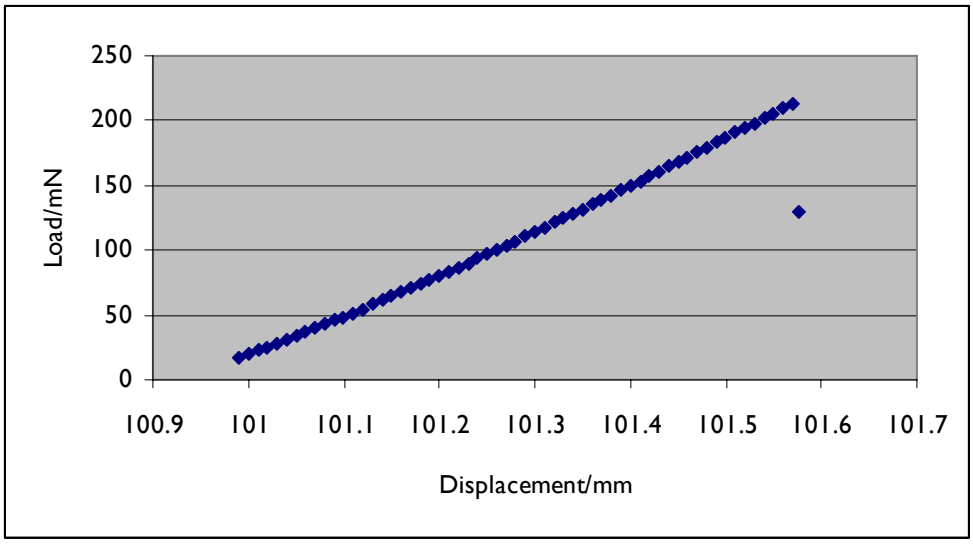
250
200
150
100
50
0
Load/mN
100.9
101
101.1
101.2
101.3
101.4
101.5
101.6
101.7
Displacement/mm

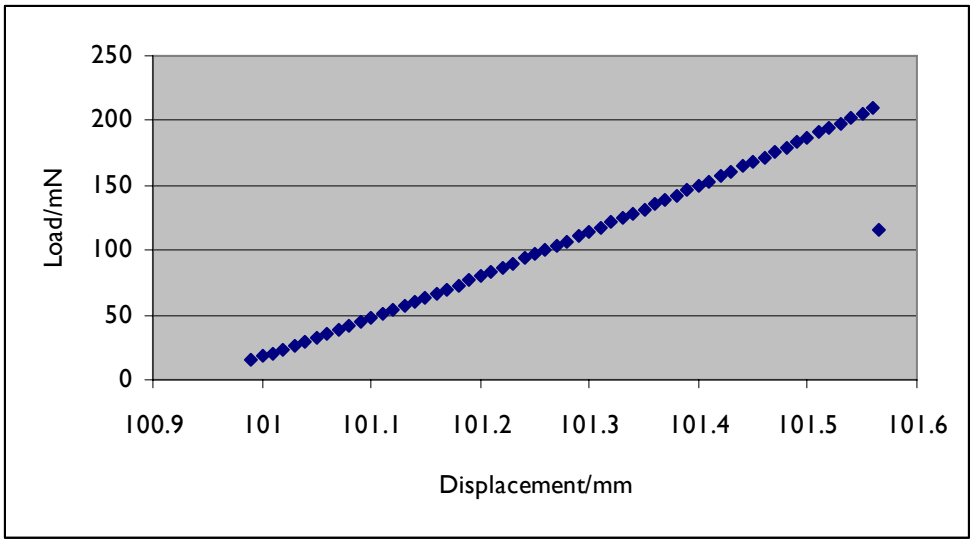
250
200
150
100
50
0
Load/mN
100.9
101
101.1
101.2
101.3
101.4
101.5
101.6
Displacement/mm

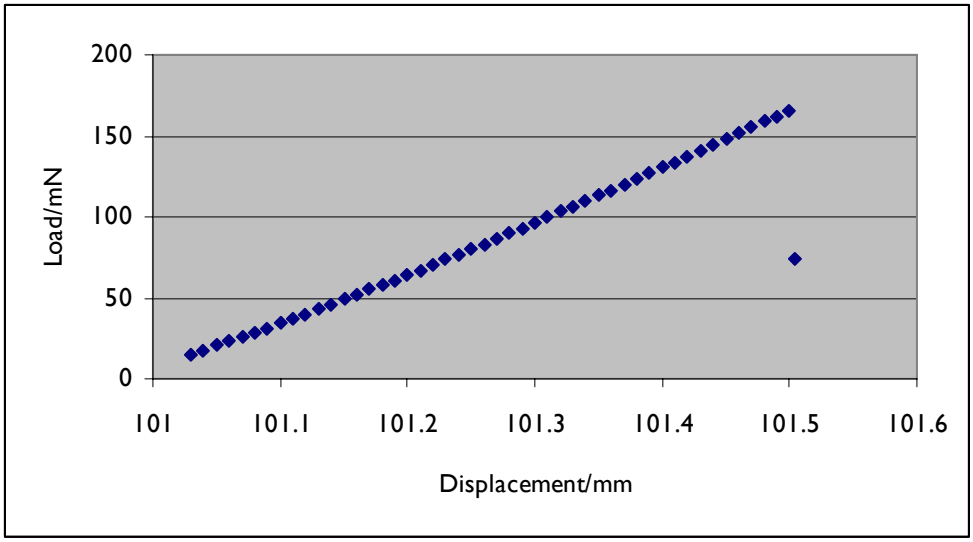
200
150
100
50
0
Load/mN
101
101.1
101.2
101.3
101.4
101.5
101.6
Displacement/mm

C4. K-PSMA/Fe^{3+} on HTR-40, CO_2/C_2H_2 CVD at 480°C

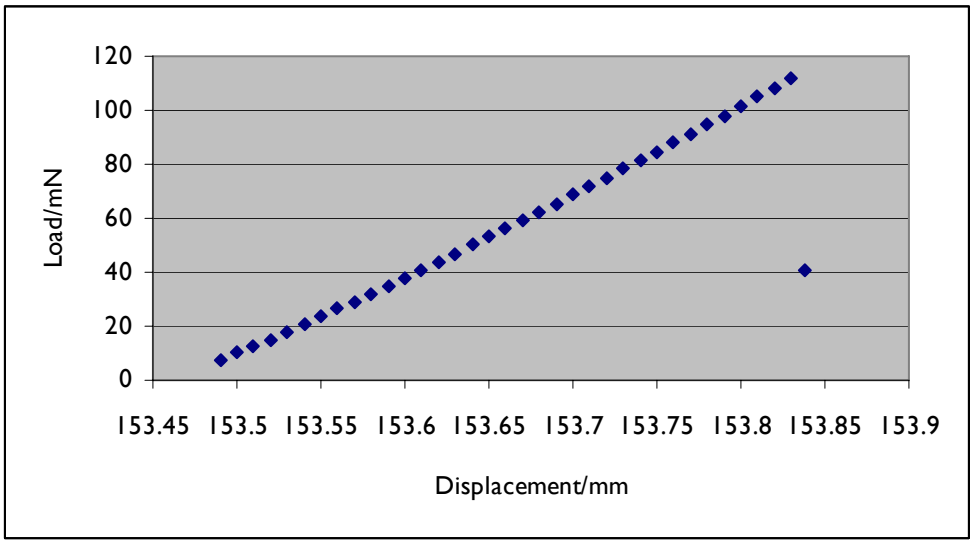

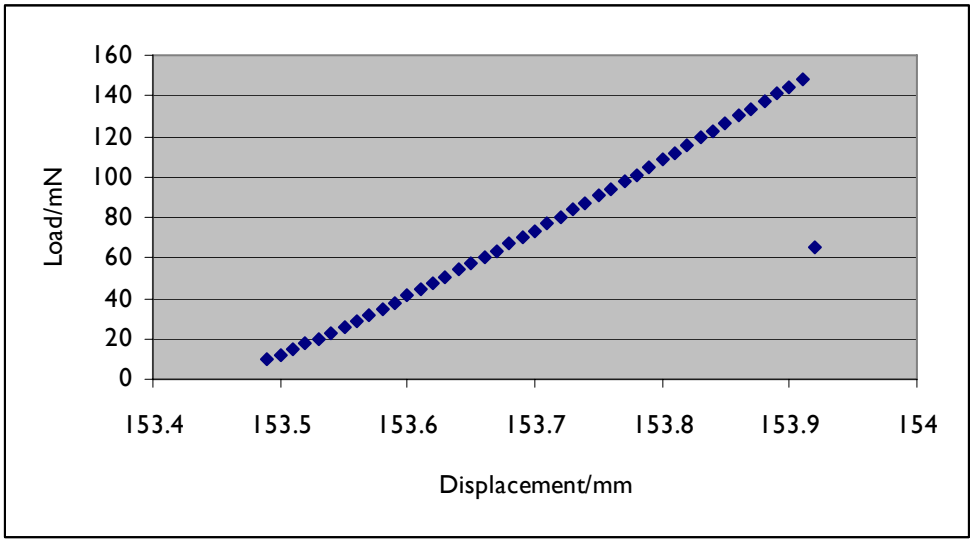

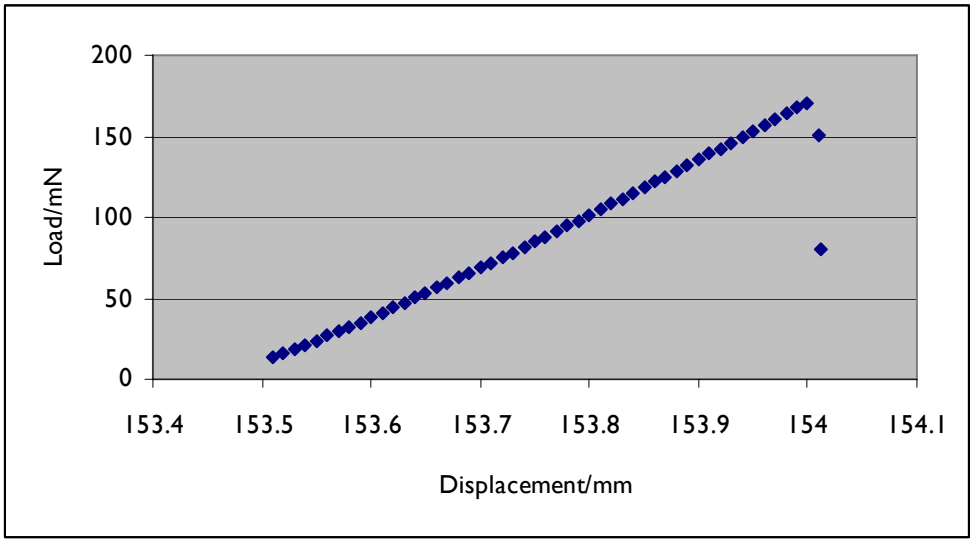

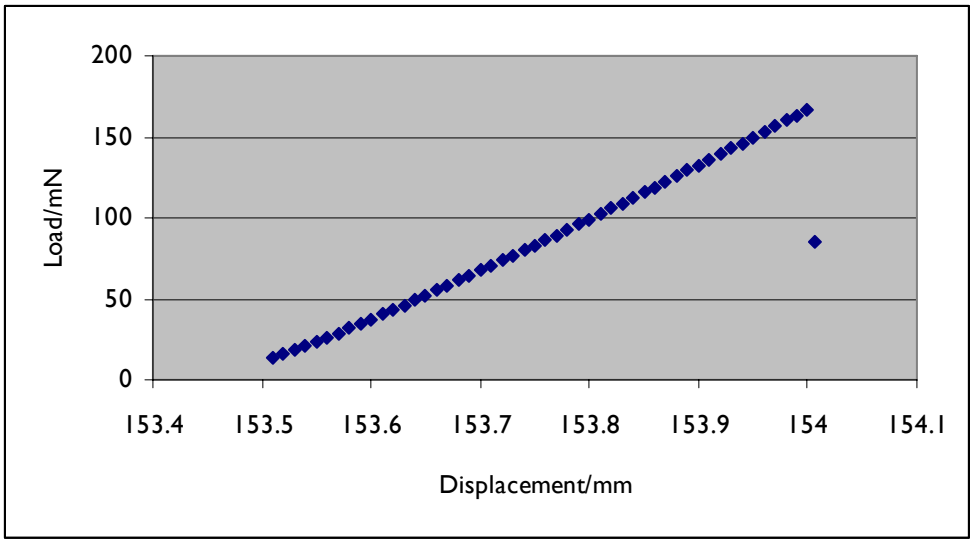
200
150
100
50
0
Load/mN
153.4
153.5
153.6
153.7
153.8
153.9
154
154.1
Displacement/mm

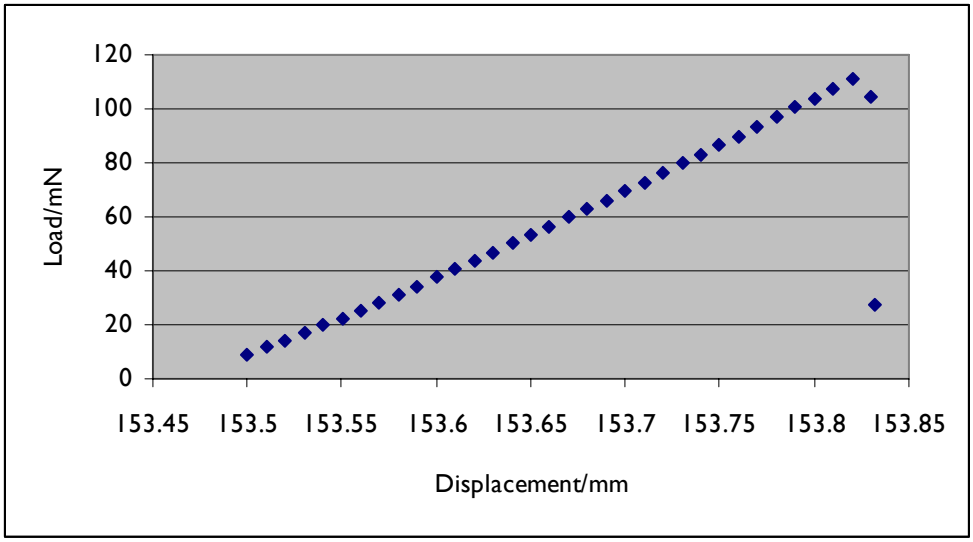
120
100
80
60
40
20
0
Load/mN
153.45
153.5
153.55
153.6
153.65
153.7
153.75
153.8
153.85
Displacement/mm

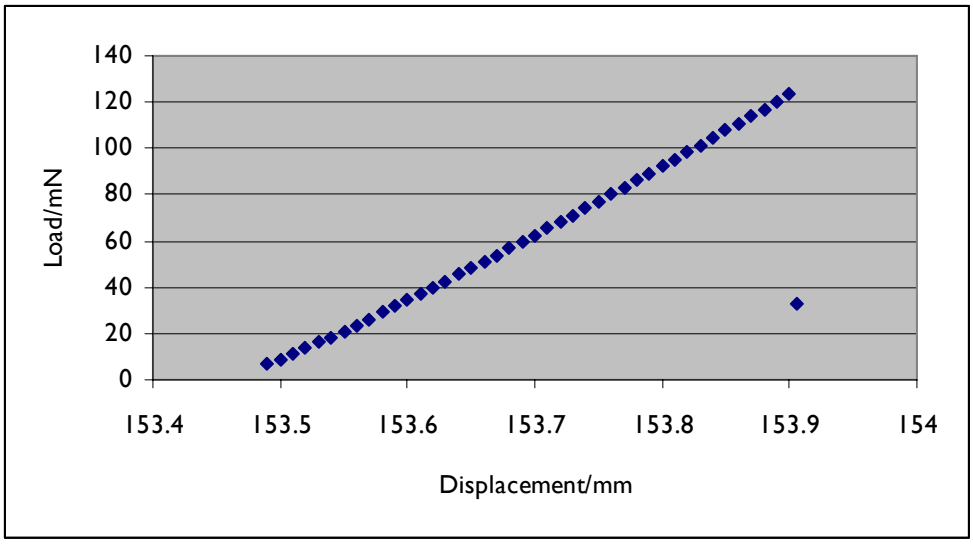
140
120
100
80
60
40
20
0
Load/mN
153.4
153.5
153.6
153.7
153.8
153.9
154
Displacement/mm

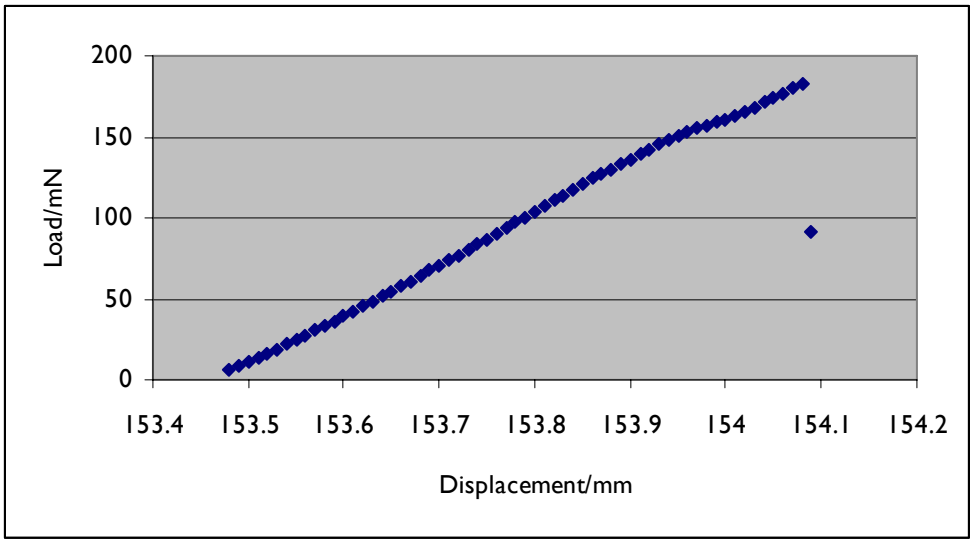
200
150
100
50
0
Load/mN
153.4
153.5
153.6
153.7
153.8
153.9
154
154.1
154.2
Displacement/mm

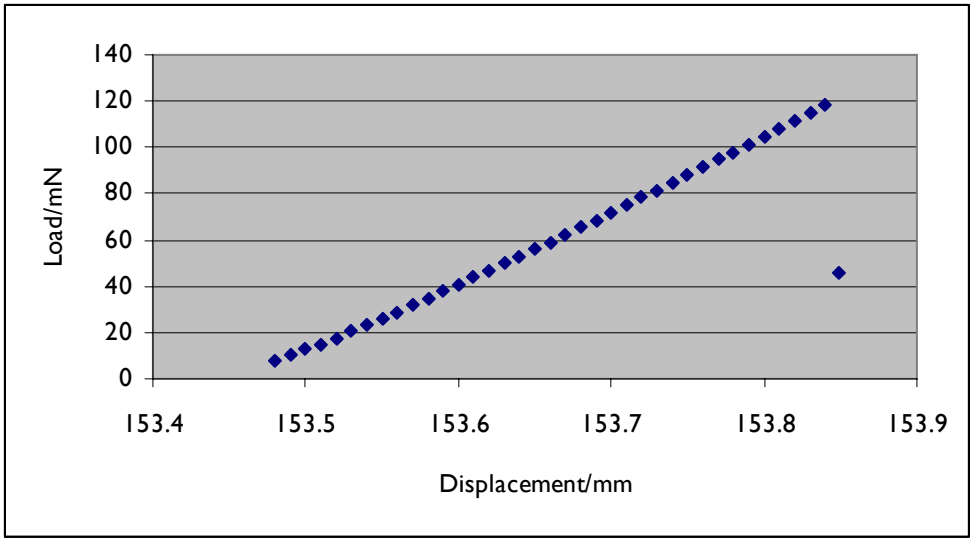
140
120
100
80
60
40
20
0
Load/mN
153.4
153.5
153.6
153.7
153.8
153.9
Displacement/mm

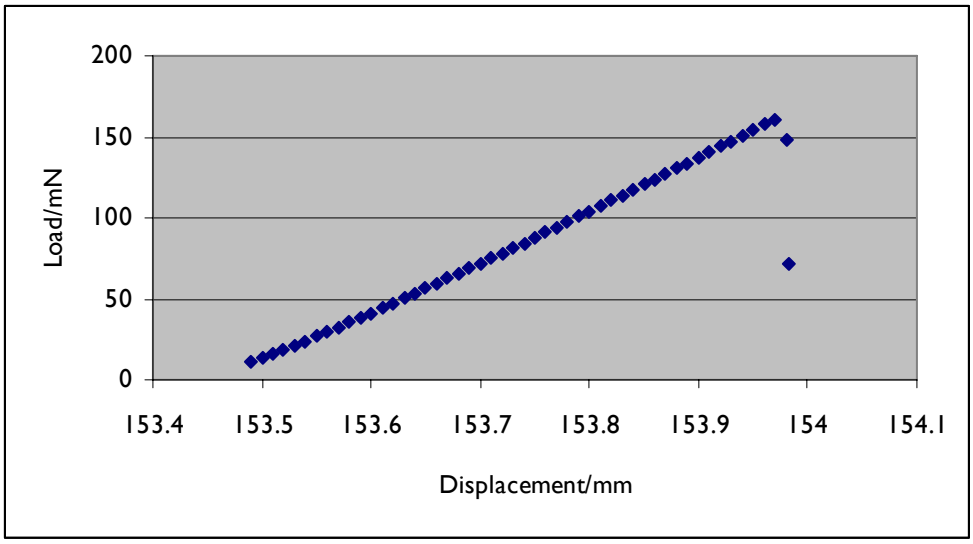
200
150
100
50
0
Load/mN
153.4
153.5
153.6
153.7
153.8
153.9
154
154.1
Displacement/mm

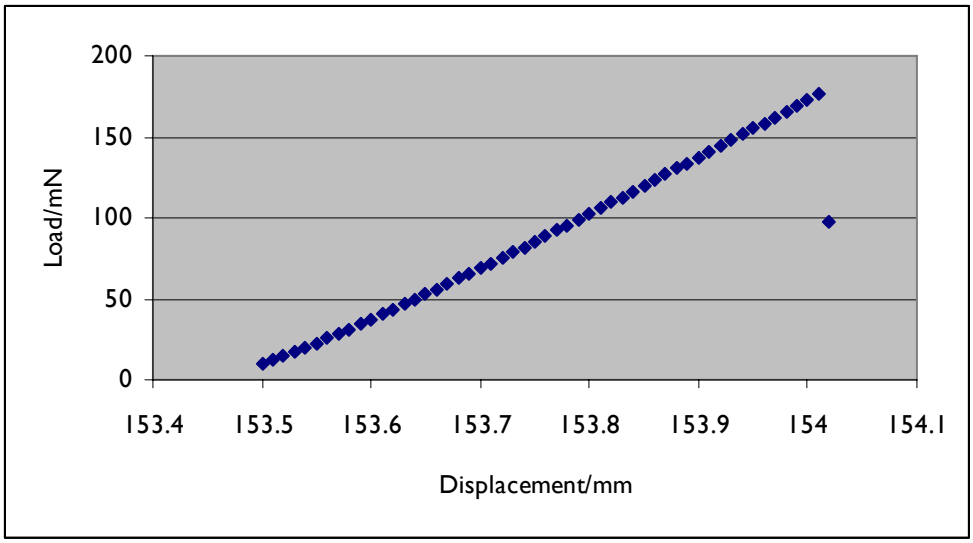
200
150
100
50
0
Load/mN
153.4
153.5
153.6
153.7
153.8
153.9
154
154.1
Displacement/mm

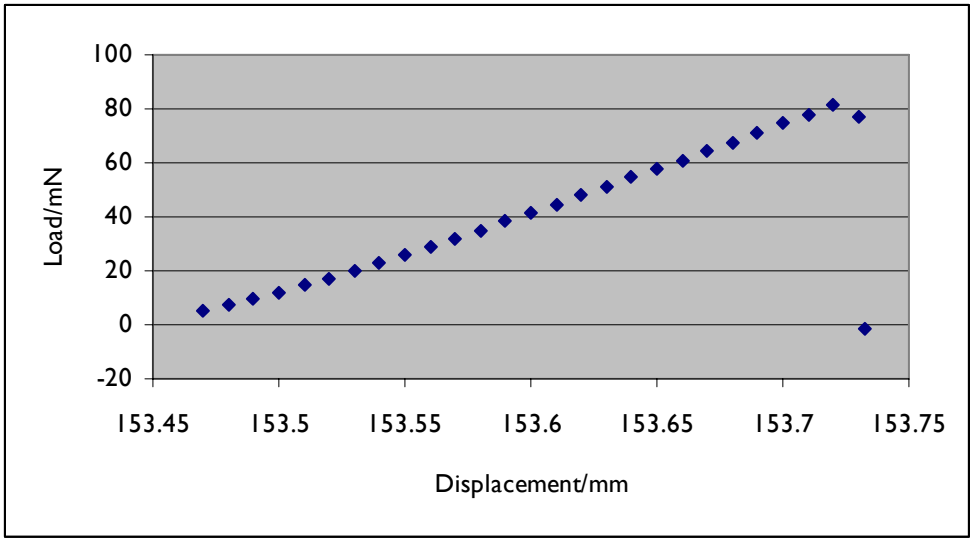
100
80
60
40
20
0
-20
Load/mN
153.45
153.5
153.55
153.6
153.65
153.7
153.75
Displacement/mm

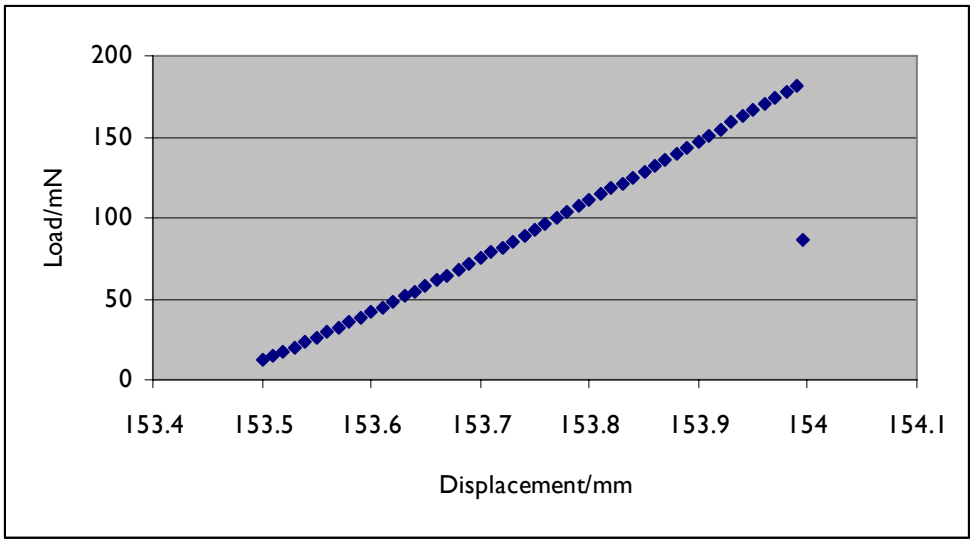
200
150
100
50
0
Load/mN
153.4
153.5
153.6
153.7
153.8
153.9
154
154.1
Displacement/mm

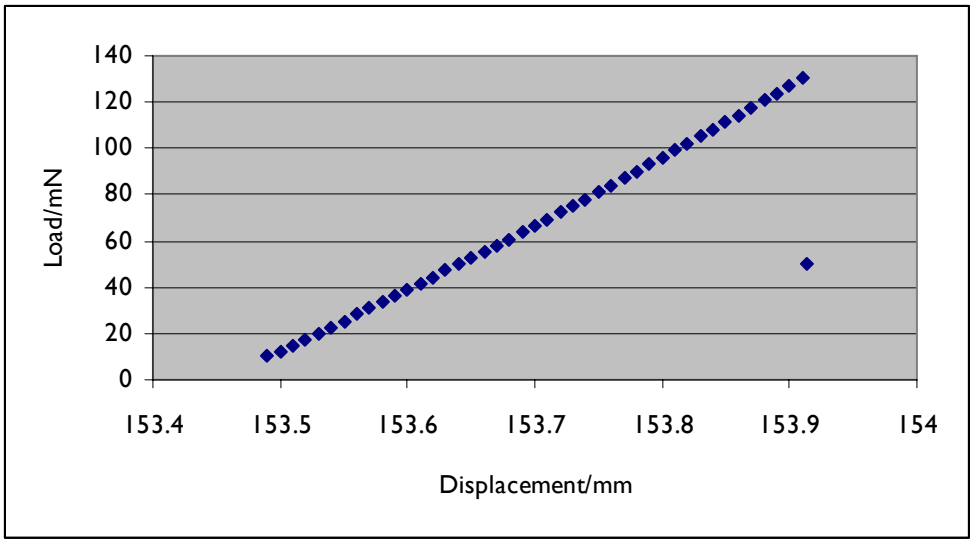
140
120
100
80
60
40
20
0
Load/mN
153.4
153.5
153.6
153.7
153.8
153.9
154
Displacement/mm

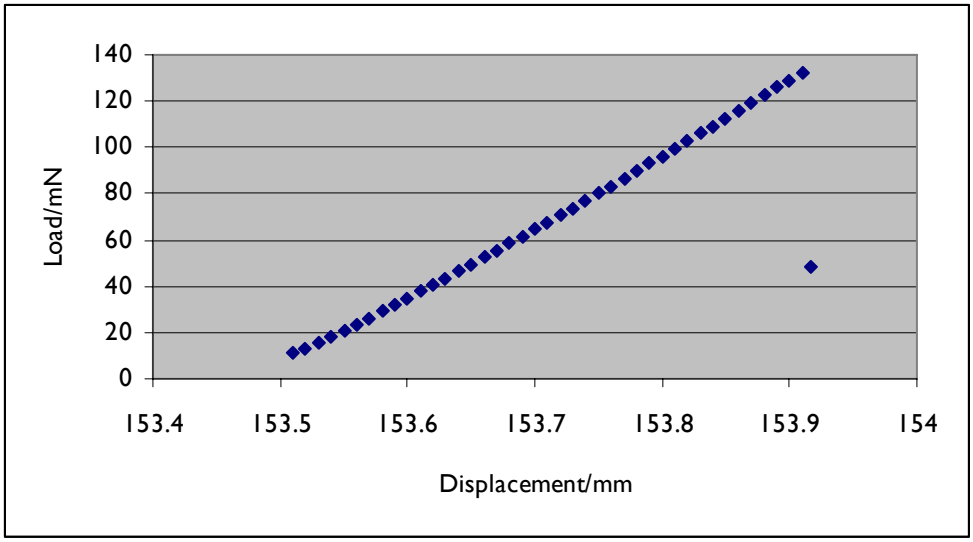
140
120
100
80
60
40
20
0
Load/mN
153.4
153.5
153.6
153.7
153.8
153.9
154
Displacement/mm

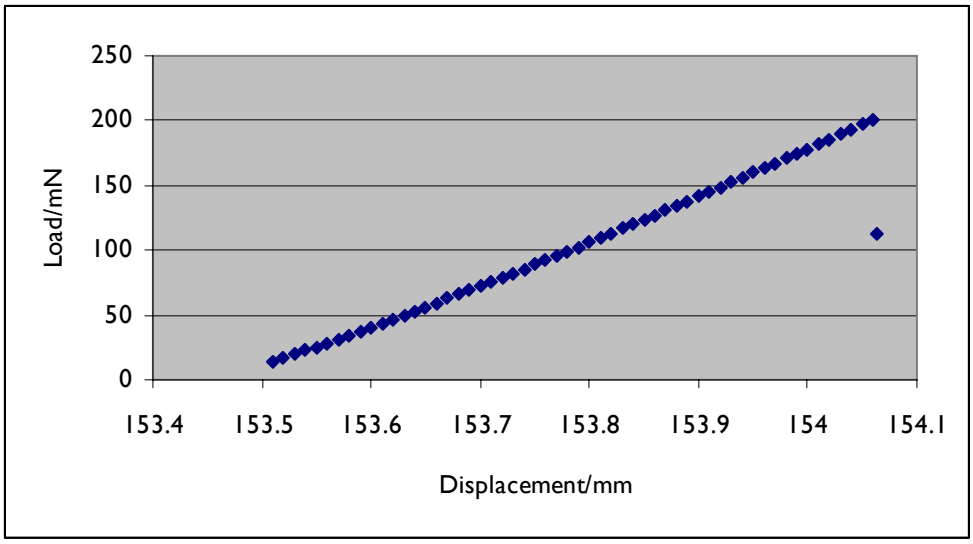
250
200
150
100
50
0
Load/mN
153.4
153.5
153.6
153.7
153.8
153.9
154
154.1
Displacement/mm

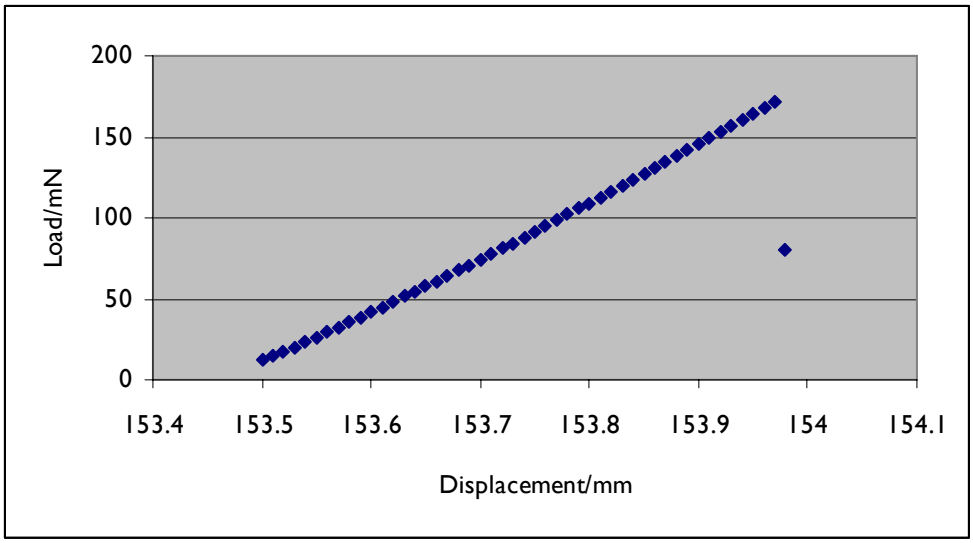
200
150
100
50
0
Load/mN
153.4
153.5
153.6
153.7
153.8
153.9
154
154.1
Displacement/mm

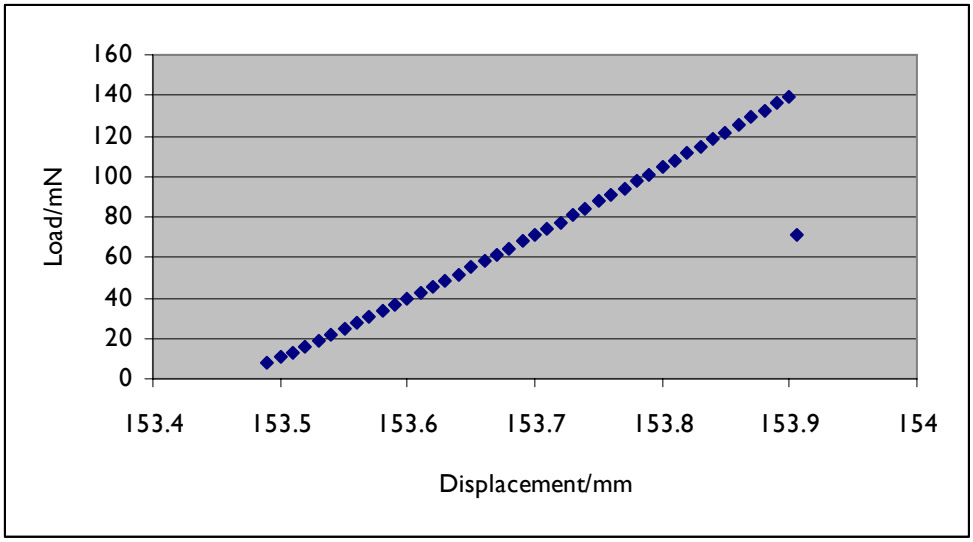
160
140
120
100
80
60
40
20
0
Load/mN
153.4
153.5
153.6
153.7
153.8
153.9
154
Displacement/mm

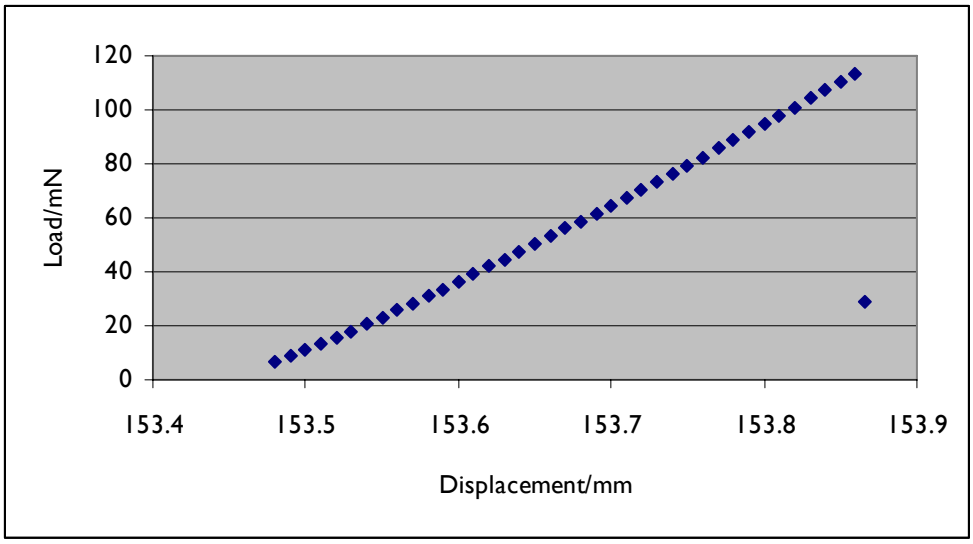
120
100
80
60
40
20
0
Load/mN
153.4
153.5
153.6
153.7
153.8
153.9
Displacement/mm

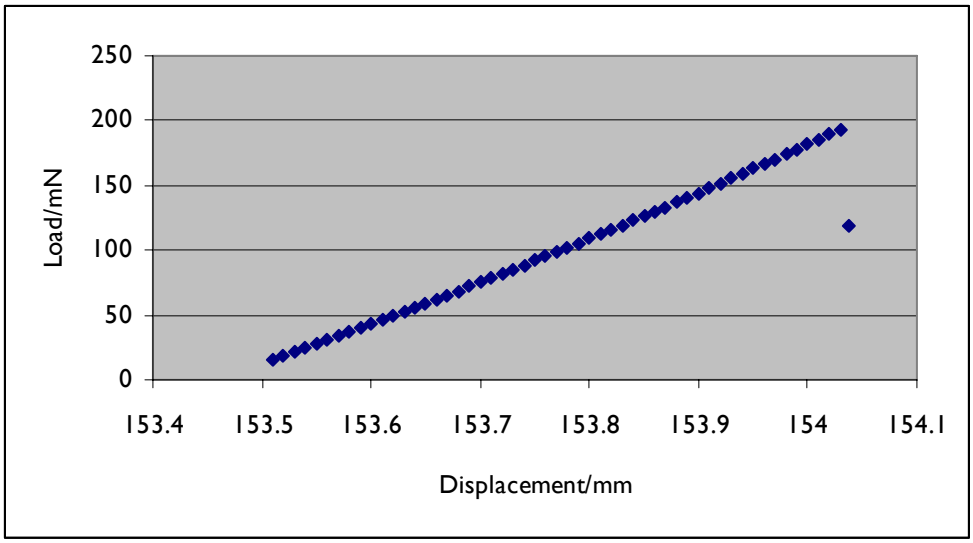
250
200
150
100
50
0
Load/mN
153.4
153.5
153.6
153.7
153.8
153.9
154
154.1
Displacement/mm

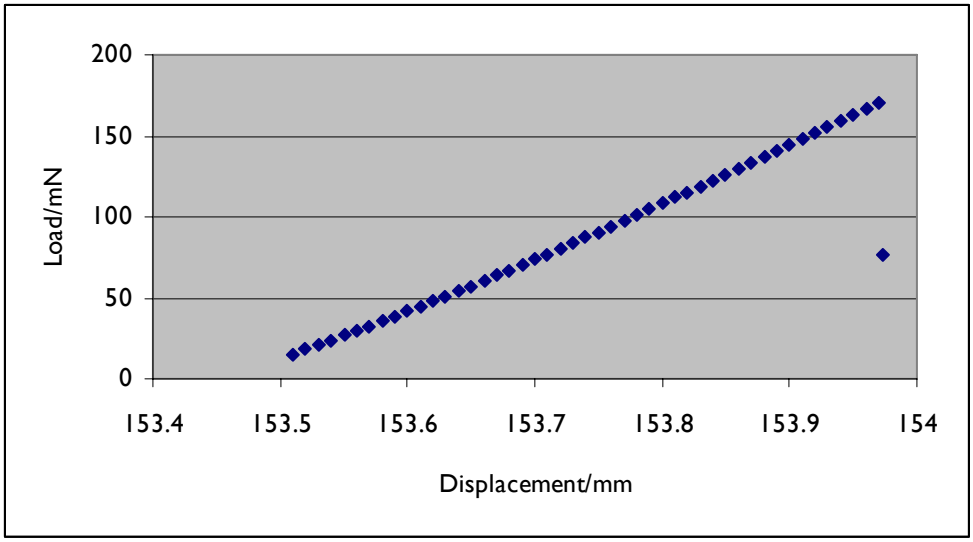
200
150
100
50
0
Load/mN
153.4
153.5
153.6
153.7
153.8
153.9
154
Displacement/mm

References

[1] Wicks, S. S.; Guzman de Villoria, R.; Wardle, B. L. *Composites Science and Technology* **2010**, *70*, 20-28.

[2] Garcia, E. J.; Wardle, B. L.; Hart, A. J.; Yamamoto, N. *Composites Science and Technology* **2008**, *68*, 2034-2041.

[3] Wicks, S. S.; Guzmán de Villoria, R.; Barber, D. M.; Wardle, B. L. *AIAA-2009-2386, Proceedings of the 50th AIAA Structures, Structural Dynamics, and Materials Conference*, Palm Springs, CA, May 4-7, 2009.

[4] Yamamoto, N.; Hart, A. J.; Garcia, E. J.; Wicks, S.; Duong, H. M.; Slocum, A. H.; Wardle, B. L. *Carbon* **2009**, *47*, 551-556.

[5] Baker, A.; Dutton, S.; Kelly, D. *Composite Materials for Aircraft Structures*; Second ed.; American Institute of Aeronautics and Astronautics, **2004**.

[6] Morgan, P. *Carbon Fibers and Their Composites*; CRC Press, **2005**.

[7] Tong, L.; Mouritz, A. P.; Bannister, M. K. *3D Fibre Reinforced Polymer Composites*; Elsevier, **2002**.

[8] Gojny, F. H.; Wichmann, M. H. G.; Köpke, U.; Fiedler, B.; Schulte, K. *Composites Science and Technology* **2004**, *64*, 2363-2371.

[9] Qiu, J.; Zhang, C.; Wang, B.; Liang, R. *Nanotechnology* **2007**, *18*, 275708.

[10] Bekyarova, E.; Thostenson, E. T.; Yu, A.; Kim, H.; Gao, J.; Tang, J.; Hahn, H. T.; Chou, T.-W.; Itkis, M. E.; Haddon, R. C. *Langmuir* **2007**, *23*, 3970-3974.

[11] Bekyarova, E.; Thostenson, E. T.; Yu, A.; Itkis, M. E.; Fakhrutdinov, D.; Chou, T.-W.; Haddon, R. C. *J. Phys. Chem. C* **2007**, *111*, 17865-17871.

[12] Zhua, J.; Imamb, A.; Cranec, R.; Lozanod, K.; Khabasheskue, V. N.; Barreraf, E. V. *Composites Science and Technology* **2007**, *67*, 1509-1517.

[13] Veedu, V. P.; Cao, A.; Li, X.; Ma, K.; Soldano, C.; Kar, S.; Ajayan, P. M.; Ghasemi-Nejhad, M. N. *Nature Materials* **2006**, *5*, 457-462.

[14] Garcia, E. J.; Wardle, B. L.; Hart, A. J. *Composites Part A: Applied Science and Manufacturing* **2008**, *39*, 1065-1070.

[15] Dzenis, Y. *Science* **2008**, *319*, 419–420.

[16] Adhikari, K.; Hubert, P.; Simard, B.; Johnston, A. *47th AIAA Structures, Dynamics, and Materials Conference Proceedings*, Newport, RI, May 1–4, 2006.

[17] Thakre, P. R.; Zhu, J.; Barrera, E. V. *47th AIAA Structures, Dynamics, and Materials Conference Proceedings* Newport, RI, May 1–4, 2006.

[18] Blanco, J.; Garcia, E. J.; Guzmán de Villoria, R.; Wardle, B. L. *Journal of Composite Materials* **2009**, *43*, 825-842.

[19] Kepple, K. L.; Sanborn, G. P.; Lacasse, P. A.; Gruenberg, K. M.; Ready, W. J. *Carbon* **2008**, *46*, 2026-2033.

[20] Qian, H.; Bismarck, A.; Greenhalgh, E. S.; Kalinka, G.; Shaffer, M. S. P. *Chemistry of Materials* **2008**, *20*, 1862-1869.

[21] Sager, R. J.; Klein, P. J.; Lagoudas, D. C.; Zhang, Q.; Liu, J.; Dai, L.; Baur, J. W. *Composites Science and Technology* **2009**, *69*, 898–904.

[22] Mathur, R. B.; Chatterjee, S.; Singh, B. P. *Composites Science and Technology* **2008**, *68*, 1608-1615.

[23] Garcia, E. J.; Hart, A. J.; Wardle, B. L. *AIAA Journal* **2008**, *46*, 1405-1412.

[24] Dupuis, A.-C. *Progress in Materials Science* **2005**, *50*, 929.

[25] Kong, J.; Cassell, A. M.; Dai, H. *Chemical Physics Letters* **1998**, *292*, 567-574.

[26] Hofmann, S.; Blume, R.; Wirth, C. T.; Cantoro, M.; Sharma, R.; Ducati, C.; Haevecker, M.; Zafeiratos, S.; Schnoerch, P.; Oestereich, A.; Teschner, D.; Albrecht, M.; Knop-Gericke, A.; Schloegl, R.; Robertson, J. *The Journal of Physical Chemistry C* **2009**, *113*, 1648.

[27] Hofmann, S.; Sharma, R.; Ducati, C.; Du, G.; Mattevi, C.; Cepek, C.; Cantoro, M.; Pisana, S.; Parvez, A.; Cervantes-Sodi, F.; Ferrari, A. C.; Dunin-Borkowski, R.; Lizzit, S.; Petaccia, L.; Goldoni, A.; Robertson, J. *Nano Letters* **2007**, *7*, 602-608.

[28] Mattevi, C.; Hofmann, S.; Cantoro, M.; Ferrari, A. C.; Robertson, J.; Castellarin-Cudia, C.; Dolafi, S.; Goldoni, A.; Cepek, C. *Physica E: Low-Dimensional Systems & Nanostructures* **2008**, *40*, 2238-2242.

[29] Downs, W. B.; Baker, R. T. K. *Carbon* **1991**, *29*, 1173-1179.

[30] Simon, R. A.; Naval Ordnance Lab (White Oak MD) *Silicon Carbide Whiskers on Carbon Fibers to Improve Resin Adhesion*; Ft. Belvoir Defense Technical Information Center, **1973**.

[31] Garcia, R.; Naval Air Development Center (Warminster PA) Aircraft and Crew Systems Technology Directorate *Methods of Improving the Matrix Dominated Performance of Composite Structures: A Technical Review*; Ft. Belvoir Defense Technical Information Center, **1983**.

[32] Garcia, R.; Evans, R. E.; Palmer, R. J. *Structural Property Improvements Through Hybridized Composites ASTM Special Technical Publication* **1987**, *937*, 397-412.

[33] Yamashita, S.; Hatta, H.; Takei, T.; Sugano, T. *Journal of Composite Materials* **1992**, *26*, 1254-68.

[34] Wang, W. X.; Takao, Y.; Matsubara, T.; Kim, H. S. *Composites Science and Technology* **2002**, *62*, 767-774.

[35] Downs, W. B.; Baker, R. T. K. *Journal of Materials Research* **1995**, *10*, 625-633.

[36] TohoTenax Corporation, "Properties of Filament", <http://www.tohotenax.com/tenax/en/products/st_property.php>, Retreived Mar 11, 2011.

[37] Zhang, Q.; Liu, J.; Sager, R.; Dai, L.; Baur, J. *Composites Science and Technology* **2009**, *69*, 594–601.

[38] Cesano, F.; Bertarione, S.; Scarano, D.; Zecchina, A. *Chemistry of Materials* **2005**, *17*, 5119-5123.

[39] Chen, L.-H.; AuBuchon, J. F.; Chen, I.-C.; Daraio, C.; Ye, X.-R.; Gapin, A.; Jin, S.; Wang, C. M. *Applied Physics Letters* **2006**, *88*, 033103.

[40] Qu, L.; Zhao, Y.; Dai, L. *Small* **2006**, *2*, 1052-1059.

[41] He, X.; Zhang, F.; Wang, R.; Liu, W. *Carbon* **2007**, *45*, 2559–2563.

[42] Li, J.; Steigerwalt, E. S.; Sambandam, S.; Lu, W.; Lukehart, C. M. *Chemistry of Materials* **2007**, *19*, 6001-6006.

[43] Laachachi, A.; Vivet, A.; Nouet, G.; Doudou, B. B.; Poilâne, C.; Chen, J.; bai, J. B.; Ayachi, M. H. *Materials Letters* **2008**, *62*, 394-397.

[44] Fan, Z.; Wu, C.; Chen, J. *Carbon* **2008**, *46*, 365–389.

[45] Kim, H. S.; Kim, B.; Lee, B.; Chung, H.; Lee, C. J.; Yoon, H. G.; Kim, W. *J. Phys. Chem. C Lett.* **2009**, *113*, 17983–17988.

[46] Magrez, A.; Seo, J. W.; Smajda, R.; Korbely, B.; Andresen, J. C.; Mionic, M.; Casimirius, S.; Forro, L. *ACS Nano* **2010**, *4*, 3702-3708.

[47] Garcia, E. J.; Hart, A. J.; Wardle, B. L.; Slocum, A. H. *Nanotechnology* **2007**, *18*, 165602/1-165602/11.

[48] Dresselhaus, M. S.; Dresselhaus, G.; Sugihara, K.; Spain, I. L.; Goldberg, H. A. *Graphite Fibers and Filaments*; Springer-Verlag, **1988**.

[49] Oya, A.; Marsh, H. *Journal of Materials Science* **1982**, *17*, 309-322.

[50] Yamada, M.; Kawana, M.-A.; Miyake, M. *Applied Catalysis, A: General* **2006**, *302*, 201-207.

[51] Wong, Y. M.; Wei, S.; Kang, W. P.; Davidson, J. L.; Hofmeister, W.; Huang, J. H.; Cui, Y. *Diamond and Related Materials* **2004**, *13*, 2105-2112.

[52] Wang, X.; Yue, W.; He, M.; Liu, M.; Zhang, J.; Liu, Z. *Chemistry of Materials* **2004**, *16*, 799-805.

[53] Lee, C. J.; Lyu, S. C.; Kim, H.-W.; Park, J. W.; Jung, H. M.; Park, J. *Chemical Physics Letters* **2002**, *361*, 469-472.

[54] Yuan, D.; Ding, L.; Chu, H.; Feng, Y.; McNicholas, T. P.; Liu, J. *Nano Letters* **2008**, *8*, 2576-2579.

[55] Steiner III, S. A.; Baumann, T. F.; Bayer, B. C.; Blume, R.; Worsley, M. A.; MoberlyChan, W. J.; Shaw, E. L.; Schloegl, R.; Hart, A. J.; Hofmann, S.; Wardle, B. L. *Journal of the American Chemical Society* **2009**, *131*, 12144-12154.

[56] Bhaviripudi, S.; Mile, E.; Steiner, S. A., III; Zare, A. T.; Dresselhaus, M. S.; Belcher, A. M.; Kong, J. *Journal of the American Chemical Society* **2007**, *129*, 1516-1517.

[57] Lee, S. Y.; Yamada, M.; Miyake, M. *Carbon* **2005**, *43*, 2654-2663.

[58] Takagi, D.; Hibino, H.; Suzuki, S.; Kobayashi, Y.; Homma, Y. *Nano Letters* **2007**, *7*, 2272-2275.

[59] Takagi, D.; Homma, Y.; Hibino, H.; Suzuki, S.; Kobayashi, Y. *Nano Letters* **2006**, *6*, 2642-2645.

[60] Steiner III, S. A. Master's Thesis, Massachusetts Institute of Technology, **2006**.

[61] Ritschel, M.; Leonhardt, A.; Elefant, D.; Oswald, S.; Buchner, B. *The Journal of Physical Chemistry C* **2007**, *111*, 8414-8417.

[62] Zhou, W.; Han, Z.; Wang, J.; Zhang, Y.; Jin, Z.; Sun, X.; Zhang, Y.; Yan, C.; Li, Y. *Nano Letters* **2006**, *6*, 2987-2990.

[63] Okamoto, H.; Massalaski, T. B. *Bulletin of Alloy Phase Diagrams* **1984**, *5*, 378-379.

[64] Shunk, F. A.; *Constitution of Binary Alloys, Second Supplement*, McGraw-Hill: New York, **1969**, p 155.

[65] Takagi, D.; Kobayashi, Y.; Homma, Y. *Journal of the American Chemical Society* **2009**, *131*, 6922-6923.

[66] Hafner, J. H.; Bronikowski, M. J.; Azamian, B. R.; Nikolaev, P.; Rinzler, A. G.; Colbert, D. T.; Smith, K. A.; Smalley, R. E. *Chemical Physics Letters* **1998**, *296*, 195-202.

[67] Murakami, Y.; Miyauchi, Y.; Chiashi, S.; Maruyama, S. *Chemical Physics Letters* **2003**, *377*, 49-54.

[68] Lee, S.-Y.; Yamada, M.; Miyake, M. *Carbon* **2005**, *43*, 2654-2663.

[69] Oya, A.; Marsh, H. *Journal of Materials Science* **1982**, *17*, 309-322.

[70] Mattevi, C.; Wirth, C. T.; Hofmann, S.; Blume, R.; Cantoro, M.; Ducati, C.; Cepek, C.; Knop-Gericke, A.; Milne, S.; Castellarin-Cudia, C.; Dolafi, S.; Goldoni, A.; Schloegl, R.; Robertson, J. *The Journal of Physical Chemistry C* **2008**, *112*, 12207-12213.

[71] Nishimura, K.; Okazaki, N.; Pan, L. J.; Nakayama, Y. *Japanese Journal of Applied Physics, Part 2: Letters* **2004**, *43*, L471-L474.

[72] Sharma, R.; Moore, E.; Rez, P.; Treacy, M. M. J. *Nano Letters* **2009**, *9*, 689-694.

[73] Li, X.; Zuo, X.; Yuan, G.; Brown, A.; Westwood, A.; Brydson, R.; Rand, B. *Journal of Physics: Conference Series* **2005**, *26*, 308-311.

[74] Rümmeli, M. H.; Kramberger, C.; Grüneis, A.; Ayala, P.; Gemming, T.; Büchner, B.; Pichler, T. *Chemistry of Materials* **2007**, *19*, 4105-4107.

[75] Liu, H.; Takagi, D.; Ohno, H.; Chiashi, S.; Chokan, T.; Homma, Y. *Applied Physics Express* **2008**, *1*, (014001-1)-(014001-3).

[76] Esconjauregui, S.; Whelan, C. M.; Maex, K. *Carbon* **2008**, *47*(3), 659-669.

[77] Liu, B.; Ren, W.; Gao, L.; Li, S.; Pei, S.; Liu, C.; Jiang, C.; Cheng, H.-M. *Journal of the American Chemical Society* **2009**, *131*, 2082-2083.

[78] Huang, S.; Cai, Q.; Chen, J.; Qian, Y.; Zhang, L. *Journal of the American Chemical Society* **2009**, *131*, 2094-2095.

[79] United States Geological Survey. *Mineral Commodity Summaries* **2008**, 192-193.

[80] Sacks, M. D.; Wang, C.-A.; Yang, Z.; Jain, A. *Journal of Materials Science* **2004**, *39*, 6057-6066.

[81] Baumann, T. F.; Fox, G. A.; Satcher, J. H., Jr.; Yoshizawa, N.; Fu, R.; Dresselhaus, M. S. *Langmuir* **2002**, *18*, 7073-7076.

[82] Baumann, T. F.; Fu, R.; Cronin, S.; Dresselhaus, G.; Dresselhaus, M. S.; Satcher, J. H., Jr. *Langmuir* **2005**, *21*, 2647-2651.

[83] Steiner III, S. A.; Baumann, T. F.; Satcher, J. H., Jr.; Kong, J.; Dresselhaus, M. S. *Langmuir* **2007**, *23*, 5161-5166.

[84] Trace cation analysis (available from Sigma-Aldrich): Ca ≤100 mg/kg; Cd ≤5 mg/kg; Co ≤5 mg/kg; Cr ≤10 mg/kg; Cu ≤5 mg/kg; Fe ≤10 mg/kg; K ≤50 mg/kg; Mg ≤5 mg/kg; Mn ≤5 mg/kg; Na ≤50 mg/kg; Ni ≤5 mg/kg; Pb ≤10 mg/kg; Ti ≤50 mg/kg; Zn ≤5 mg/kg.

[85] McTaggart, F. K. *Nature* **1961**, *191*, 1192.

[86] Berger, L.-M.; Gruner, W.; Langholf, E.; Stolle, S. *International Journal of Refractory Metals and Hard Materials* **1999**, *17*, 235-243.

[87] *Phase Diagrams for Zirconium and Zirconia Systems*; Ondik, H. M.; McMurdie, H. F., Eds.; American Ceramics Society, **1998**.

[88] Morant, C.; Sanz, J. M.; Galán, L.; Soriano, L.; Rueda, F. *Surface Science* **1989**, *218*, 331-345.

[89] Guittet, M. J.; Crocombette, J. P.; Gautier-Soyer, M. *Physical Review B* **2000**, *63*.

[90] Dzhurinskii, B. F.; Gati, D.; Sergushin, N. P.; Nefedov, V. I.; Salyn, Y. V. *Russian Journal of Inorganic Chemistry* **1975**, *20*, 2307-2314.

[91] Barr, T. L. *Journal of Physical Chemistry* **1978**, *82*, 1801-1810.

[92] Briggs, D.; Seah, M. P. *Practical Surface Analysis*; Second Edition ed.; John Wiley & Sons, **1993**, Vol. 1.

[93] Ebert, H.; Knecht, M.; Muhler, M.; Helmer, O.; Bensch, W. *Journal of Physical Chemistry* **1995**, *99*, 3326-3330.

[94] Won, Y. S.; Kim, Y. S.; Varanasi, V. G.; Kryliouk, O.; Anderson, T. J.; Sirimanne, C. T.; McElwee-White, L. *Journal of Crystal Growth* **2007**, *304*, 324-332.

[95] Balaceanu, M.; Braic, M.; Braic, V.; Vladescu, A.; Negrilaa, C. C. *Journal of Optoelectronics and Advanced Materials* **2005**, *7*, 2557-2560.

[96] Moulder, J. F.; Stickle, W. F.; Sobol, P. E.; Bomben, K. D. *Handbook of X-Ray Photoelectron Spectroscopy*; Physical Electronics, Inc.

[97] Plata, D. L.; Hart, A. J.; Reddy, C. M.; Gschwend, P. M. *Environmental Science and Technology* **2009**, *43*, 8367-8373.

[98] Okita, A.; Suda, Y.; Oda, A.; Nakamura, J.; Ozeki, A.; Bhattacharyya, K.; Sugawara, H.; Sakai, Y. *Carbon* **2007**, *45*, 1518-1526.

[99] Stein, S. E.; Fahr, A. *J. Phys. Chem.* **1985**, *89*, 3714-3725.

[100] Plata, D. L.; Meshot, E. R.; Reddy, C. M.; Hart, A. J.; Gschwend, P. M. *ACS Nano* **2010**, *4*, 7185-7192.

[101] Plata, D. L. PhD Thesis, PhD Thesis, Massachusetts Institute of Technology, **2009**.

[102] Saito, R.; Grüneis, A.; Samsonidze, G. G.; Brar, V. W.; Dresselhaus, G.; Dresselhaus, M. S.; Jorio, A.; Cançado, L. G.; Fantini, C.; Pimenta, M. A.; Filho, A. G. S. *New Journal of Physics* **2003**, *5*, 157.1-157.15.

[103] Kurti, J.; Zolyomi, V.; Kertesz, M.; Sun, G. *New Journal of Physics* **2003**, *5*, 125.1-125.21.

[104] Zyuzin, D. A.; Cherepanova, S. V.; Moroz, E. M.; Burgina, E. B.; Sadykov, V. A.; Kostrovskii, V. G.; Matyshak, V. A. *Journal of Solid State Chemistry* **2006**, *179*, 2965-2971.

[105] Pekala, R. W.; Alviso, C. T.; LeMay, J. D. *Journal of Non-Crystalline Solids* **1990**, *125*, 67-75.

[106] Matched to Inorganic Crystal Structure Database (ICSD) reference pattern file PDF00-049-1642 (ICDD Powder Diffraction File 4+); see Tomaszewski, H.; Godwod, K. *Journal of the European Ceramic Society* **1995**, *15*, 17.

[107] Matched to Inorganic Crystal Structure Database (ICSD) reference pattern file PDF00-037-1484 (ICDD Powder Diffraction File 4+); see McMurdie, H. F.; Morris, M.; Evans, E.; Paretzkin, B.; Wong-Ng, W.; Hubbard, C. R. *Powder Diffraction* **1986**, *1*, 265-275.

[108] Fu, R.; Yoshizawa, N.; Dresselhaus, M. S.; Dresselhaus, G.; Satcher, J. H., Jr.; Baumann, T. F. *Langmuir* **2002**, *18*, 10100-10104.

[109] Maitre, A.; Lefort, P. *Actualité Chemie* **1999**, *5*, 35-41.

[110] Gaskell, D. R. In *Encyclopedia of Materials: Science and Technology*; Elsevier: 2001, p 5481-5486.

[111] Kong, J.; Soh, H. T.; Cassell, A. M.; Quate, C. F.; Dai, H. *Nature* **1998**, *395*, 878-881.

[112] Bachilo, S. M.; Balzano, L.; Herrera, J. E.; Pompeo, F.; Resasco, D. E.; Weisman, R. B. *Journal of the American Chemical Society* **2003**, *125*, 11186-11187.

[113] Hart, A. J.; Slocum, A. H. *Journal of Physical Chemistry B* **2006**, *110*, 8250-8257.

[114] Maruyama, S.; Kojima, R.; Miyauchi, Y.; Chiashi, S.; Kohno, M. *Chemical Physics Letters* **2002**, *360*, 229-234.

[115] Noda, S.; Hasegawa, K.; Sugime, H.; Kakehi, K.; Zhang, Z.; Maruyama, S.; Yamaguchi, Y. *Japanese Journal of Applied Physics, Part 2: Letters & Express Letters* **2007**, *46*, L399-L401.

[116] Wal, R. L. V.; Ticich, T. M.; Curtis, V. E. *Carbon* **2001**, *39*, 2277-2289.

[117] Hauffe, K. *DECHEMA Monographien* **1956**, *26*, 301-32.

[118] Satterfield, C. N. *Heterogeneous catalysis in industrial practice*; 2nd Ed. ed.; McGraw-Hill, New York, **1991**.

[119] Freund, H.-J. *Surface Science* **2007**, *601*, 1438-1442.

[120] Miller, T. M.; V.H.Grassian *Catalysis Letters* **1997**, *46*, 213-221.

[121] Tomishige, K.; Sakaihori, T.; Ikeda, Y.; Fujimoto, K. *Catalysis Letters* **1999**, *58*, 225-229.

[122] Singhal, S. C.; Kendall, K. *High Temperature Solid Oxide Fuel Cells: Fundamentals, Design, and Applications*; Elsevier Advanced Technology, **2003**.

[123] Buffat, P.; Borel, J.-P. *Physical Review A* **1976**, *13*, 2287-2296.

[124] Gupta, S. K.; Talati, M.; Jha, P. K. *Materials Science Forum* **2008**, *570*, 132-137.

[125] Canty, E. G.; Lu, Y.; Meadows, R. S.; Shaw, M. K.; Holmes, D. F.; Kadler, K. E. *Journal of Cell Biology* **2004**, *165*, 553-563.

[126] Joo, J.; Yu, T.; Kim, Y. W.; Park, H. M.; Wu, F.; Zhang, J. Z.; Hyeon, T. *Journal of the American Chemical Society* **2003**, *125*, 6553-6557.

[127] Bhaviripudi, S.; Reina, A.; Qi, J.; Kong, J.; Belcher, A. M. *Nanotechnology* **2006**, *17*, 5080-5086.

[128] Mulik, S.; Sotiriou-Leventis, C.; Leventis, N. *Chemistry of Materials* **2007**, *19*, 6138-6144.

[129] Maillard, M.; Motte, L.; Ngo, A. T.; Pileni, M. P. *Journal of Physical Chemistry B* **2000**, *104*, 11871-11877.

[130] Rabani, E.; Reichman, D. R.; Geissler, P. L.; Brus, L. E. *Nature* **2003**, *426*, 271-274.

[131] Gole, J.; Burda, C.; Fedorov, A.; White, M. *Reviews on Advanced Materials Science* **2003**, *5*, 265-269.

[132] Miller, T. M.; Grassian, V. H. *Catalysis Letters* **1997**, *46*, 213-221.

[133] Li, J.; Zeng, H. C. *Journal of the American Chemical Society* **2007**, *129*, 15839-15847.

[134] Li, Q.; Shang, J. K. *Journal of the American Chemical Society* **2008**, *91*, 3157-3172.

[135] Liu, B.; Ren, W.; Liu, C.; Sun, C.-H.; Gao, L.; Li, S.; Jiang, C.; Cheng, H.-M. *ACS Nano* **2009**, *3(*11*),* 3421-3430.

[136] Carp, O.; Huisman, C. L.; Reller, A. *Progress in Solid State Chemistry* **2004**, *32*, 33-177.

[137] Kitiyanan, A.; Ngamsinlapasathian, S.; Pavasupree, S.; Yoshikawa, S. *Journal of Solid State Chemistry* **2005**, *175*, 1044-1048.

[138] Durr, M.; Rosselli, S.; Yasuda, A.; Nelles, G. *Journal of Physical Chemistry B* **2006**, *110*, 21899-21902.

[139] Nishimura, O.; Yabe, K. *X-sen Bunseki no Shinpo (Japanese)* **1991**, *22*, 201-10.

[140] Han, S.; Yu, T.; Park, J.; Koo, B.; Joo, J.; Hyeon, T.; Hong, S.; Im, J. *Journal of Physical Chemistry B* **2004**, *108*, 8091-8095.

[141] Wardle, B. L.; Saito, D. S.; Garcia, E. J.; Hart, A. J.; Guzman de Villoria, R.; Verploegen, E. A. *Advanced Materials* **2008**, *20*, 2707-2714.

[142] Cebeci, H.; Guzman de Villoria, R.; Hart, A. J.; Wardle, B. L. *Composites Science and Technology* **2009**, *69*, 2649-2656.

[143] Hata, K.; Futaba, D. N.; Mizuno, K.; Namai, T.; Yumura, M.; Iijima, S. *Science* **2004**, *306*, 1362-1364.

[144] Yamada, T.; Maigne, A.; Yudasaka, M.; Mizuno, K.; Futaba, D. N.; Yumura, M.; Iijima, S.; Hata, K. *Nano Letters* **2008**, *8*, 4288-4292.

[145] Hart, A. J.; van Laake, L.; Slocum, A. H. *Small* **2007**, *3*, 772-777.

[146] Kim, H. S.; Kim, B.; Lee, B.; Chung, H.; Lee, C. J.; Yoon, H. G.; Kim, W. *Journal of Physical Chemistry C* **2009**, *113*, 17983–17988.

[147] Gonzaga de Resende, V.; Freire Antunes, E.; de Oliveira Lobo, A.; Antônio Lima Oliveira, D.; Jesus Trava-Airoldi, V.; José Corat, E. *Carbon* **2010**, *48*, 3655-3658

[148] Louchev, O. A.; Sato, Y.; Kanda, H. *Applied Physics Letters* **2002**, *80*, 2752-2754.

[149] Brinker, C. J.; Scherrer, G. W. *Sol-Gel Science: The Physics and Chemistry of Sol-Gel Processing*; Academic Press, **1990**.

[150] Aerogel.org, "What is Aerogel?" <http://www.aerogel.org/?p=3>, Retreived Aug 16, 2011.

[151] Magrez, A.; Smajda, R.; Seo, J. W.; Horvath, E.; Ribic, P. R.; Andresen, J. C.; Acquaviva, D.; Olariu, A.; Laurenczy, G.; Forro, L. *ACS Nano* **2011**, *5*, 3428-3437.

[152] Yoldas, B. E. *Journal of Materials Science* **1975**, *10*, 1856-60.

[153] Gash, A. E.; Tillotson, T. M.; Satcher, J. H., Jr.; Hrubesh, L. W.; Simpson, R. L. *Journal of Non-Crystalline Solids* **2001**, *285*, 22-28.

[154] Baumann, T. F.; Gash, A. E.; Chinn, S. C.; Sawvel, A. M.; Maxwell, R. S.; Satcher Jr., J. H. *Chemistry of Materials* **2005**, *17*, 395-401.

[155] Hübert, T.; Svobod, S.; Oertel, B. *Surface Coatings and Technology* **2006**, *201*, 487-491.

[156] Zeng, Q. *Journal of Applied Polymer Science* **1998**, *70*, 177-183.

[157] Poco, J. F.; Satcher, J. H.; Hrubesh, L. W. *Journal of Non-Crystalline Solids* **2001**, *285*, 57-63.

[158] Sidelnikova, S. P.; Sherstkina, V. N.; Yagubets, A. N. *Nauk (Russian)* **1979**, 69-74.

[159] Zein El Abedin, S.; Endres, F. *Accouts of Chemical Research* **2007**, *40*, 1106-1113.

[160] Jiang, T.; Chollier Brym, M. J.; Dubé, G.; Lasia, A.; Brisard, G. M. *Surface Coatings and Technology* **2006**, *201*, 1-9.

[161] Zein El Abedin, S.; Moustafa, E. M.; Hempelmann, R.; Natter, H.; Endres, F. *ChemPhysChem* **2006**, *7*, 1535-1543.

[162] Haanappel, V. A. C.; van Corbach, H. D.; Hofman, R. *High Temperature Materials and Processes* **1996**, *15*, 245-262.

[163] Fournier, J.; DeSisto, W.; Brusasco, R.; Sosnowski, M.; Kershaw, R.; Baglio, J.; Dwight, K.; Wold, A. *Materials Research Bulletin* **1988**, *23*, 31-36.

[164] Gleizes, A. N.; Vahlas, C.; Sovar, M.-M.; Samélor, D.; Lafont, M.-C. *Chemical Vapor Deposition* **2007**, *13*, 23-29.

[165] Sovar, M.-M.; Samélor, D.; Gleizes, A.; Alphonse, P.; Perisanu, S.; Vahlas, C. *Advanced Materials Research* **2007**, *23*, 245-248.

[166] Haanappel, V. A. C.; van Corbach, H. D.; Fransen, T.; Gellings, P. J. *Thin Solid Films* **1993**, *230*, 138-144.

[167] Haanappel, V. A. C.; van Corbach, H. D.; Fransen, T.; Gellings, P. J. *Surface Coatings and Technology* **1994**, *63*, 145-153.

[168] Stroock, A. D.; Kane, R. S.; Weck, M.; Metallo, S. J.; Whitesides, G. M. *Langmuir* **2003**, *19*, 2466-2472.

[169] Carrillo, A.; Swartz, J. A.; Gamba, J. M.; Kane, R. S.; Chakrapani, N.; Wei, B.; Ajayan, P. M. *Nano Letters* **2003**, *3*, 1437-1440.

[170] Magrez, A.; Seo, J. W.; Smajda, R.; Korbely, B.; Andresen, J. C.; Mionic, M.; Casimirius, S.; Forro, L. *ACS Nano* **2010**, *4*.

[171] ASTM International, *Standard Test Method for Tensile Strength and Young's Modulus for High-Modulus Single-Filament Materials*, ASTM D3379-75, **1989**.

[172] International Standards Organization, *Carbon Fibre – Determination of the Tensile Properties of Single-Filament Specimens*, ISO 11566, **1996**.

[173] Harlow, E. G.; Phoenix., L. *Journal of Composite Materials* **1978**, *12*, 195-214.

[174] Garcia, E. J.; Hart, A. J.; Wardle, B. L.; Slocum, A. H. *Proceedings of the 47th AIAA/ASME/ASCE/AHS/ASC Structures, Structural Dynamics, and Materials Conference, 1-4 May 2006, Newport, Rhode Island*. **2006**.

[175] Hitchon, J. W.; Phillips, D. C. *Fibre Science and Technology* **1979**, *12*, 217-233.

[176] Saito, K.; Ogawa, H. *Proceedings of the 31st International SAMPE Symposium* April 7-10, 1986.